Lithium Niobate Nanophotonic Circuits for Information Processing

Thesis by
Ryoto Sekine

In Partial Fulfillment of the Requirements for the
Degree of
Doctor of Philosophy

CALIFORNIA INSTITUTE OF TECHNOLOGY
Pasadena, California

2025
Defended June 27, 2024

Ryoto Sekine
ORCID: 0000-0001-6135-8581

To my grandfather,
Ryoji Baba
and my parents,
Kyoko Sekine & *Toshitaka Sekine*

ACKNOWLEDGEMENTS

When I applied to the Nonlinear Photonics Group at Caltech, I did not know any optics, yet alone nonlinear optics. Although I had taken advanced E&M in my undergraduate physics classes, **P** was still very much proportional to **E**. Thus I cannot thank my PhD advisor, Alireza Marandi, enough for taking a leap of faith in a student who clearly knew so little about his field of research. It is also thanks to him that I have been able to be a part of an incredible team, on a mission to develop a new optical platform. We built everything from scratch, and although the material we work with still holds many surprises, it is remarkable to look back and see how far we have come. This was all only possible with the guidance of Alireza.

Three individuals who were with me through thick and thin are Dr. Luis Ledezma, now Professor Qiushi Guo, and, still a Mr., Robert M. Gray. I am indebted to Luis for teaching me how to design nanophotonic components; he is truly to blame for my video game addictions to both Lumerical and SNOW (Simulator for Nonlinear Optical Waveguides). Qiushi, I cannot thank enough for his patience in mentoring me and demonstrating the level of dedication it takes to conduct meaningful research. Robby has taught me everything I know about OPO dynamics and has saved me from the brink of giving up on experiments on countless occasions. Beyond the lab, Robby has my gratitude for being a patient roommate for many years and a great teammate on the soccer pitch. I could not have asked for a better friend to navigate graduate school with.

In terms of mentors, I cannot thank Jin-Sung Kim enough for teaching me all I know about nanofabrication while I was an undergraduate at Princeton University. Although he might be appalled at some of our current procedures, I now appreciate the value of a person of his caliber teaching me his best practices. For this level of mentorship, I also owe a great deal of gratitude to my advisor at the time, Professor Steven Lyon, for providing such a golden opportunity. Speaking of mentors, I would like to express my gratitude to Professors Azita Emami, Scott Cushing, and Axel Scherer for serving on my committee and for their insightful questions and suggestions. Scott will get another mention soon for all of our fruitful collaborations.

From the Nonlinear Photonics Group, I have many others to thank as well. Rajveer Nehra's enthusiasm for everything quantum was infectious. Midya Parto was always willing to discuss my questions about computing architectures. If Nicolas Englebert wasn't sending me cycling memes, he was teaching me about the zoo of solitons. I am also very grateful to Luis Costa, Saman Jahani, Myoung-Gyun Suh, and Joong Hwan Bahng for looking after me even after moving on from the group.

I have been blessed to work with a diverse team of graduate students. Gordon Li has always kept me grounded in my enthusiasm for optical computing, and Benjamin Gutierrez is nearly the only reason I have not given up on lasers, despite them being one of the devices with the worst fabrication yield. I cannot wait to see where Selina Zhou will take the nanophotonic PPLN on sapphire platform. I have also enjoyed many discussions with Arkadev Roy, Mingchen Liu, Christian Leefmans, James

Williams, Elina Sendonaris, Thomas Zacharias, Rithvik Ramesh, and Maximilian Shen.

During my graduate studies, I had the opportunity to mentor a few exceptional students. I say mentor, but by the end, they were all teaching me something, which I take with a sense of pride. First and foremost are Nathan Harper and Emily Hwang from the Scott Cushing group at Caltech. These two always came to me with questions or unwittingly 'changed' fabrication procedures, forcing me to reevaluate everything I thought I knew. Also on this list is Parthorn Ammawat. I cannot quite believe how lucky I was to stumble across such a talented undergraduate, but now I cannot imagine doing research without him. Jennifer Solgaard is another exceptional undergraduate who learned my chip coupling technique so quickly that I am now ashamed to admit how long it took me to discover.

I have also enjoyed collaborations outside of the *Nonlinear Photonics Group*. Working with Scott Diddams' group at UC Boulder and Ryan Briggs at JPL on the UV-Vis frequency comb project was a pleasure. During a visit to JPL, I met Frank Greer and learned about atomic layer etching, which sparked another project focused on developing a more precise way of etching lithium niobate. This project is now in the capable hands of Ivy Chen in the Austin Minnich group.

I would also like to express my gratitude to everyone I have interacted with during my graduate studies through my association with Alireza. His connections afforded me the opportunity to meet Dr. Hiroki Takesue and witness the impressive 100k node Ising Machine in person. Alireza's reputation also facilitated interactions up and down the manufacturing chain, allowing us to speak directly with wafer manufacturers and redefine what it means to be nonlinear optics grade. Additionally, through Alireza, I interned at PINC Technologies, gaining valuable insights into the challenges that industries face with the nanophotonic PPLN platform.

During my graduate studies, I spent a significant amount of time in various cleanrooms. I would like to thank the staff at KNI, UCLA, and MDL for their patience and support over the years. I am especially grateful to Alessandro Maggi for being on the night watch and always willing to come to the rescue.

I am also grateful to the Ezoe Memorial Recruit Foundation for their support, which began at the end of my undergraduate studies and continued throughout my graduate studies. Their rigorous annual exams led me to meet Professor Hidetoshi Nishimori. After nearly flunking his interview in my first year, I made sure to prepare thoroughly for his grilling sessions, which ultimately led to an invitation to present at his Workshop on Quantum Annealing in Tokyo in 2023.

Additionally, I thank the Quad Fellowship for their generous funding and for inviting me to help establish and shepherd the Quad Investors Network's, Quantum Center of Excellence. Through this initiative, I had the wonderful opportunity to work closely with Dr. Cathy Foley (the Chief Scientist of Australia), Professor Ajay Kumar Sood (the Principal Scientific Adviser to the Government of India), Professor Hiroaki Aihara (the Executive Vice President of the University of Tokyo), Dr. Celia Merzbacher (the Executive Director of the Quantum Economic Development Consortium), and Karl Mehta (Chairman Emeritus of the Quad Investors Network), to name a few. The discussions among co-chairs and task forces, which informed

our recommendations to the Quad governments and prominent public and private stakeholders, offered invaluable insights into how government, industry, start-ups, and academia collaborate to shape scientific policies.

Graduate school has had its ups and downs, and I certainly could not have made it to the finish line without the help of all my friends. I owe special thanks to Arjuna Subramanian, Komron Shayegan, and Jared Sisler for pulling me out of the lab for cycling adventures. No matter how daunting a project seemed, it always felt much more achievable after a healthy dose of cycling up the switchbacks to Mt. Baldy or tackling the Circle of Doom with the Lollipop for extra credit.

Lastly, I extend my deepest gratitude to my family for their continuous support. My sister, Yukina, has always been there in times of crisis, and I am indebted to my parents, Kyoko and Toshitaka, for providing me with all the opportunities to succeed in life. Who knows, if it were not for my father's insistence, I may have ended up in economics rather than in nonlinear optics.

ABSTRACT

In today's world, electronic information processors are ubiquitous. This dissertation explores an alternative paradigm of processing information using nanophotonics. We develop and investigate nanophotonic lithium niobate circuits leveraging strong $\chi^{(2)}$ nonlinearity for information processing. We demonstrate promising performance of nanophotonic circuits as building blocks of unconventional computing architectures that exploit the rich classical and quantum dynamics inherent to optics. Additionally, we introduce a new class of ultrafast nanophotonic sources, enabling novel opportunities for information processing. Ultimately, this dissertation puts forth the building blocks of next generation ultrafast photonic information processors in lithium niobate nanophotonics which may lead to photonic advantage.

PUBLISHED CONTENT AND CONTRIBUTIONS

[1] **Ryoto Sekine**†, Robert M. Gray†, Luis Ledezma, Selina Zhou, Qiushi Guo, and Alireza Marandi. "Multi-octave frequency comb from an ultra-low-threshold nanophotonic parametric oscillator". In: *arXiv* (2023). URL: https://arxiv.org/abs/2309.04545.
R.S. conceived the project, designed and fabricated the device, performed part of the optical characterization, and lead the writing of the manuscript.
† denotes equal contributions.

[2] Rajveer Nehra†, **Ryoto Sekine**†, Luis Ledezma, Qiushi Guo, Robert M. Gray, Arkadev Roy, and Alireza Marandi. "Few-cycle vacuum squeezing in nanophotonics". In: *Science* 377.6612 (2022), pp. 1333–1337. URL: https://www.science.org/doi/abs/10.1126/science.abo6213.
R.S. fabricated the device, contributed to the optical characterization, and participated in the writing of the manuscript.
† denotes equal contributions.

[3] Qiushi Guo†, **Ryoto Sekine**†, Luis Ledezma†, Rajveer Nehra, Devin J. Dean, Arkadev Roy, Robert M. Gray, Saman Jahani, and Alireza Marandi. "Femtojoule femtosecond all-optical switching in lithium niobate nanophotonics". In: *Nature Photonics* 16.9 (Sept. 2022), pp. 625–631. URL: https://doi.org/10.1038/s41566-022-01044-5.
R.S. developed the measurement techniques, assisted the fabrication development, and participated in writing of the manuscript.
† denotes equal contributions.

[4] Luis Ledezma†, **Ryoto Sekine**†, Qiushi Guo†, Rajveer Nehra, Saman Jahani, and Alireza Marandi. "Intense optical parametric amplification in dispersion-engineered nanophotonic lithium niobate waveguides". In: *Optica* 9.3 (Mar. 2022), pp. 303–308. URL: https://opg.optica.org/optica/abstract.cfm?URI=optica-9-3-303.
R.S. performed the measurements, assisted the fabrication development, and participated in writing of the manuscript.
† denotes equal contributions.

[5] Gordon H.Y. Li†, **Ryoto Sekine**†, Rajveer Nehra†, Robert M. Gray†, Luis Ledezma, Qiushi Guo, and Alireza Marandi. "All-optical ultrafast ReLU function for energy-efficient nanophotonic deep learning". In: *Nanophotonics* 12.5 (2023), pp. 847–855. URL: https://doi.org/10.1515/nanoph-2022-0137.
R.S. fabricated and phase-matched the device, and developed a new facet-polishing procedure.
† denotes equal contributions.

[6] Robert M. Gray†, **Ryoto Sekine**†, Luis Ledezma, Gordon H. Y. Li, Selina Zhou, Arkadev Roy, Midya Parto, and Alireza Marandi. "Large-scale time-multiplexed nanophotonic parametric oscillators". In: *arXiv* (2024). URL:

https://arxiv.org/abs/2405.17355.
R.S. designed and fabricated the device, assisted the measurements, and contributed to developing the all-to-all coupled network architecture.
† denotes equal contributions.

[7] **Ryoto Sekine**†, Robert Gray†, Luis Ledezma, Qiushi Guo, and Alireza Marandi. "Sync-pumped femtosecond OPO based on dispersion-engineered nanophotonic PPLN with 3-octave spectrum". In: *Conference on Lasers and Electro-Optics*. Optica Publishing Group, 2022, SM5K.2. URL: https://opg.optica.org/abstract.cfm?URI=CLEO_SI-2022-SM5K.2.
R.S. participated in the conception of the project, characterized the device, and lead the writing of the manuscript.
† denotes equal contributions.

[8] Qiushi Guo, Benjamin K. Gutierrez, **Ryoto Sekine**, Robert M. Gray, James A. Williams, Luis Ledezma, Luis Costa, Arkadev Roy, Selina Zhou, Mingchen Liu, and Alireza Marandi. "Ultrafast mode-locked laser in nanophotonic lithium niobate". In: *Science* 382.6671 (2023), pp. 708–713. URL: https://www.science.org/doi/abs/10.1126/science.adj5438.
R.S. contributed to the fabrication development and part of the optical characterization.

[9] Nathan A. Harper†, Emily Y. Hwang†, **Ryoto Sekine**, Luis Ledezma, Christian Perez, Alireza Marandi, and Scott K. Cushing. "Highly efficient visible and near-IR photon pair generation with thin-film lithium niobate". In: *Optica Quantum* 2.2 (Apr. 2024), pp. 103–109. URL: https://opg.optica.org/opticaq/abstract.cfm?URI=opticaq-2-2-103.
R.S. mentored the lead authors and participated in the writing of the manuscript.

[10] Emily Hwang†, Nathan Harper†, **Ryoto Sekine**, Luis Ledezma, Alireza Marandi, and Scott Cushing. "Tunable and efficient ultraviolet generation with periodically poled lithium niobate". In: *Optics Letters* 48.15 (Aug. 2023), pp. 3917–3920. URL: https://opg.optica.org/ol/abstract.cfm?URI=ol-48-15-3917.
R.S. mentored the lead authors and participated in the writing of the manuscript.

[11] Ivy I. Chen, Jennifer Solgaard, **Ryoto Sekine**, Azmain A. Hossain, Anthony Ardizzi, David S. Catherall, Alireza Marandi, James R. Renzas, Frank Greer, and Austin J. Minnich. "Directional atomic layer etching of MgO-doped lithium niobate using sequential exposures of H_2 and SF_6 plasma". In: *arXiv* (2023). URL: https://arxiv.org/abs/2310.10592.
R.S. participated in the conception of the project, played a supporting role in the measurements, and assisted in the writing of the manuscript.

[12] **Ryoto Sekine**†, Robert Gray†, Luis Ledezma, Selina Zhou, Qiushi Guo, and Alireza Marandi. "Multi-octave frequency comb from a nanophotonic parametric oscillator". In: *Optica Nonlinear Optics Topical Meeting 2023*. Optica Publishing Group, 2023, W3A.5. URL: https://opg.optica.org/abstract.cfm?URI=NLO-2023-W3A.5.

R.S. conceived the project, designed and fabricated the device, performed part of the optical characterization, and lead the writing of the manuscript. † denotes equal contributions.

[13] **Ryoto Sekine**†, Robert Gray†, Luis Ledezma, Selina Zhou, Qiushi Guo, and Alireza Marandi. "Two-octave frequency comb from a nanophotonic parametric oscillator". In: *Conference on Lasers and Electro-Optics*. Optica Publishing Group, 2023, SW4G.2. URL: https://opg.optica.org/abstract.cfm?URI=CLEO_SI-2023-SW4G.2.
R.S. conceived the project, designed and fabricated the device, performed part of the optical characterization, and lead the writing of the manuscript. † denotes equal contributions.

[14] Midya Parto, Gordon Li, **Ryoto Sekine**, Robert Gray, Luis Ledezma, James Williams, and Alireza Marandi. "An optical neural network based on nanophotonic optical parametric oscillators". In: *Conference on Lasers and Electro-Optics*. 2024, STu3P.7.
R.S. aided the measurement and assisted the fabrication of the device.

TABLE OF CONTENTS

Acknowledgements iv
Abstract vii
Published Content and Contributions viii
Table of Contents x
List of Illustrations xiii
List of Tables xvii
Nomenclature xviii
Chapter I: Introduction 1
1.1 Photonic Information Processing: When Nanophotonics Meets Strong Nonlinearity 1
1.2 Light-Matter Interactions Paving the Way to Nanophotonic PPLN . . 4
1.3 The Nuts & Bolts of Nanophotonic PPLN 10
1.4 Summary of Contributions & Thesis Overview 14
References 22
Chapter II: Intense, Broadband, Phase-Sensitive Gain 34
2.1 Abstract 34
2.2 Introduction 34
2.3 Device Design and Fabrication 36
2.4 Results and Discussion 39
2.5 Conclusion 41
2.6 Supplementary Information 42
References 51
Chapter III: All-Optical Ultrafast ReLU Function for Energy-Efficient Nanophotonic Deep Learning 56
3.1 Abstract 56
3.2 Introduction 56
3.3 Methods 57
3.4 Results 59
3.5 Discussion 63
3.6 Conclusion 67
3.7 Supplementar Information 67
References 76
Chapter IV: Femtojoule, Femtosecond All-Optical Switch 80
4.1 Abstract 80
4.2 Introduction 80
4.3 Results 82
4.4 Discussion 89
4.5 Methods 91
4.6 Supplementary Information 92

References . . . 116
Chapter V: Few-Cycle Vacuum Squeezing in a Nanophotonic Circuit . . . 121
5.1 Abstract . . . 121
5.2 Introduction . . . 121
5.3 Results . . . 122
5.4 Conclusion . . . 129
5.5 Supplementary Information . . . 129
References . . . 152
Chapter VI: Multi-Octave Frequency Comb from an Ultra-Low-Threshold Nanophotonic Parametric Oscillator . . . 155
6.1 Abstract . . . 155
6.2 Introduction . . . 155
6.3 Operating Principle and Design . . . 158
6.4 Experimental Results . . . 160
6.5 Conclusion and Discussion . . . 162
6.6 Methods . . . 162
6.7 Supplementary Information . . . 164
References . . . 185
Chapter VII: Large-Scale Time-Multiplexed Nanophotonic Parametric Oscillators . . . 192
7.1 Abstract . . . 192
7.2 Introduction . . . 192
7.3 Results . . . 193
7.4 Outlook . . . 199
References . . . 201
Chapter VIII: Outlook . . . 204
8.1 Large Scale Information Processors . . . 204
8.2 New Lasers ↔ New Nonlinear Optics . . . 209
References . . . 211

LIST OF ILLUSTRATIONS

Number		*Page*
1.1	Timeline of photonics leading up to Nanophotonic PPLN	3
1.2	Fabrication overview	10
1.3	Mode engineering	11
1.4	QPM engineering	11
1.5	Dispersion engineering	12
1.6	Velocity matching	13
1.7	Key contributions	14
2.1	Parametric amplification in dispersion-engineered PPLN waveguides	35
2.2	Small-signal gain of the degenerate OPA	37
2.3	Measurements in the large-gain regime through optical parametric generation	38
2.4	Comparison of the gain and bandwidth of quadratic OPA in dispersion-engineered LN waveguides with other gain mechanisms in integrated photonics	41
2.5	Numerical simulation of small-signal optical parametric amplification	46
2.6	Numerical simulation of optical parametric generation	47
2.7	Dispersion engineering mappings	48
2.8	Comparison of the gain and 3-dB relative bandwidth of our quadratic OPA compared to other gain mechanisms in integrated photonics	50
3.1	Operating principle of the all-optical ReLU function using a nonlinear photonic waveguide	58
3.2	Images and modes of the PPLN nanophotonic waveguide	59
3.3	Measured and simulated output signal pulse energy versus input signal pulse energy	60
3.4	Measured variants of the ReLU function	61
3.5	Pump–probe ultrafast timing measurements of the ReLU dynamics	62
3.6	Simulated deep learning performance of the experimentally measured all-optical ReLU function for MNIST handwritten digits image classification	64
3.7	Comparison of energy and time per activation of this work compared to other approaches	65
3.8	Experimental Schematic for all-optical ReLU measurements	68
3.9	Measured spectrums of ω and 2ω	70
3.10	Number of signal photons as the input pump power is varied	71
3.11	Simulated ReLU-like nonlinear activation function with sub-femtojoule energies	72
3.12	Pretrained convolutional neural network architecture	73
3.13	Potential integrated photonic neural networks using the all-optical ultrafast ReLU function	75

4.1 Design and operating principle of the all-optical switch 81
4.2 Integrated nonlinear splitter and its linear optical characteristics in the all-optical switch 83
4.3 Ultra-low energy nonlinear optical transmission in the integrated nonlinear splitter 84
4.4 Femtosecond, femtojoule all-optical switching 87
4.5 Performance comparison of various on-chip all-optical switches operating at room temperature 90
4.6 Comparison of device design and operating principle between two all-optical switches 92
4.7 Nonlinear response of our phase-matched Nanophotonic PPLN switch 94
4.8 Nonlinear response of a phase-mismatched NDC switch 94
4.9 Nonlinear response of a phase-mismatched nanophotonic PPLN switch 95
4.10 Design of the adiabatic taper in the all-optical switch 96
4.11 Simulated coupling as a function of length of the adiabatic taper in the all-optical switch 96
4.12 3D simulation of the optical field propagating through the coupler for the all-optical switch 97
4.13 Autocorrelations of the input pulse for the all-optical switch 98
4.14 Deterministically finding the quasi-phase matching condition for the all-optical switch 100
4.15 Determining the input/output coupling loss of the all-optical switch . 101
4.16 Poling period and GVM variation as a function of waveguide geometry for the all-optical switch 102
4.17 Measured and simulated normalized OPG spectra as a function of temperature 103
4.18 Ultrafast nonlinear dynamics in the SHG region of the all-optical switch 104
4.19 Ultrafast nonlinear dynamics in the entire nonlinear splitter device . . 105
4.20 Measured output power spectral density output at the drop and the through ports as a function of the input pulse energy 106
4.21 Nonlinear optical transmission in the integrated nonlinear splitter . . 107
4.22 Performance comparison of various on-chip all-optical switches operating at room temperature with references 108
4.23 Schematic and simulations of a chip-scale integrated mode locked laser based on a TFLN all-optical switch and erbium doped LN waveguide 109
4.24 Design of an all-optical switch operating at 1550 nm 110
4.25 Schematic of an OTDM system 111
4.26 Schematic of a channel DEMUX using an all-optical switch 111
4.27 Illustration of AND and OR logic gates using the all-optical switch for optical channel demultiplexing 113
4.28 Schematic and simulations of the all-optical switch used as part of an integrated mode locked laser 114
5.1 Illustration of the generation of a squeezed vacuum and its all-optical measurement in nanophotonics 123

5.2 Generation and measurement of squeezed light in the LN nanophotonic chip . . . 126
5.3 Broadband squeezing measurements . . . 128
5.4 Experimental schematic for all-optical squeezing measurements . . . 130
5.5 Shot-noise calibration measurements . . . 132
5.6 Shot-noise level measurements at various values of pump energy . . . 133
5.7 Numerical simulations of the squeezer OPA . . . 135
5.8 Design and characterization of adiabatically tapered coupler . . . 136
5.9 Simulated coupling efficiencies, (A) for the signal, (B) for the pump field . . . 137
5.10 Generation and all-optical measurement of a squeezed vacuum state . 141
5.11 Required measurement amplifier gain for a given amount of squeezing 145
5.12 Squeezing degradation under photon loss . . . 146
5.13 Effective efficiency for various values of η_{OPA} and η_l . . . 148
5.14 Squeezing degradation with the photon loss . . . 148
5.15 Classical measurement of the Measurement OPA gain . . . 150
5.16 Performance comparison of measured squeezing levels and squeezing bandwidths on various nanophotonic platforms . . . 150
6.1 Principle and design of the multi-octave nanophotonic OPO . . . 156
6.2 OPO characterization . . . 158
6.3 Simulation results showing different operation regimes of the nanophotonic OPO . . . 159
6.4 Performance comparison of (a), integrated spectral broadening, and (b), frequency comb sync-pumped OPOs . . . 161
6.5 Key OPO design parameters as a function of waveguide geometry . . 164
6.6 Additional OPO parameters . . . 165
6.7 OPO coupler design . . . 166
6.8 Experimental Setup . . . 166
6.9 Extended Measurements to $\sim 20\times$ above threshold . . . 167
6.10 Absorption features of atmospheric molecules compared to the OPO spectra measured at 380 fJ of pump . . . 168
6.11 Simulated mode crossings compared to measured straight waveguide spectra . . . 169
6.12 OPO beatnote measurement . . . 170
6.13 OPO beatnote locked in the Temporal Self-Cleaning Regime . . . 171
6.14 SHG beatnote measurement . . . 172
6.15 Extended regimes of operation of the nanophotonic OPO and defining its resonance peaks . . . 174
6.16 OPO Characterization: $l = 2$, $\phi_{\mathrm{CEO}} = 0$ . . . 175
6.17 OPO Characterization: $l = 0$, $\phi_{\mathrm{CEO}} = 0$ . . . 176
6.18 OPO Characterization: $l = -2$, $\phi_{\mathrm{CEO}} = 0$ . . . 176
6.19 OPO Characterization: $l = 3$, $\phi_{\mathrm{CEO}} = 0$ . . . 177
6.20 OPO Characterization: $l = 1$, $\phi_{\mathrm{CEO}} = 0$ . . . 178
6.21 OPO Characterization: $l = -1$, $\phi_{\mathrm{CEO}} = 0$ . . . 178
6.22 OPO Characterization: $l = -3$, $\phi_{\mathrm{CEO}} = 0$ . . . 179

6.23 Further characterization of the coherence of regime (iii) for $l = -3$, $\phi_{\mathrm{CEO}} = 0$ . . . 179
6.24 OPO Characterization: Peak 2, $\phi_{\mathrm{CEO}} = \pi$ . . . 180
6.25 OPO Characterization: Peak 0, $\phi_{\mathrm{CEO}} = \pi$ . . . 181
6.26 OPO Characterization: Peak -2, $\phi_{\mathrm{CEO}} = \pi$ . . . 181
6.27 Intensity and phase evolution inside the crystal for the half-harmonic (top) and pump (bottom) of regime (iii) for $l = -3$, $\phi_{\mathrm{ceo}} = 0$ . . . 182
6.28 Temporal output of the two-octave combs at different detunings . . . 183
6.29 Three Octave Comb Characterization at $l = 3$, $\phi_{\mathrm{CEO}} = 0$ . . . 184
7.1 Time-multiplexed nanophotonic OPOs . . . 194
7.2 Measurement of independent oscillators . . . 195
7.3 Interference measurements for N = 40 . . . 197
7.4 Interference measurements for N = 70 . . . 198
7.5 Time-multiplexed architecture for programmable all-to-all coupled nonlinear resonators . . . 200
8.1 OPO Network Information Processor . . . 205
8.2 Short Pulse Synthesizer . . . 208
8.3 Intrapulse difference frequency generation unit . . . 209

LIST OF TABLES

Number *Page*
2.1 Comparison of on-chip amplifiers gain and bandwidth 49
5.1 State-of-the-art demonstrations in nanophotonics squeezing 151

NOMENCLATURE

ALE. Atomic Layer Etching.

BPM. Birefringent Phase Matching.

EOM. Electro-optic Modulator.

FH. First Harmonic.

GVD. Group Velocity Dispersion.

GVM. Group Velocity Mismatch.

OPA. Optical Parametric Amplification.

OPCPA. Optical Parametric Chirped Pulse Amplification.

OPO. Optical Parametric Oscillator.

PPLN. Periodically Poled Lithium Niobate.

QPM. Quasi-Phase Matching.

RNN. Recurrent Neural Network.

SCG. Supercontinuum Generation.

SH. Second Harmonic.

SHG. Second Harmonic Generation.

SHG. Second Harmonic Generation.

SPDC. Spontaneous Parametric Down Conversion.

TE. Transverse Electric.

TFLN. Thin-film Lithium Niobate.

TSC. Temporal Self-Cleaning.

Chapter 1

INTRODUCTION

1.1 Photonic Information Processing: When Nanophotonics Meets Strong Nonlinearity

Inside any smartphone or computer processor today, are billions of transistors that conduct the flow of electrons to process information. What if we replace those electrons with streams of light? What if instead of an electronic integrated circuit, we make a photonic integrated circuit that not only routes light but manipulates or prepares it to enable information processing? What advantages could such photonic information processors offer that electronic circuits cannot, and what new possibilities could they unlock beyond the capabilities of previous optical technologies? This dissertation is devoted to answering these questions by developing and exploring nanophotonic devices, circuits, and systems with strong nonlinearity for information processing.

Two key terms throughout this thesis are *nonlinearity* and *nanophotonic*. Nonlinearity enables complex operations where the outputs are not merely scaled and/or summed responses of the inputs. As Stainsław Ulam put it, "using a term like nonlinear science is like referring to the bulk of zoology as the study of non-elephant animals." The information-processing opportunities are immense. Nanophotonics involves tightly confining light within nanometer-scale waveguides, offering the immediate benefits of miniaturization and portability, and paving the way for scalability. Additionally, these waveguides provide unprecedented control over the dispersion of propagating light, which, as we will explore later, is a powerful design parameter.

In the world of electronics, transistors provide nonlinear manipulation of current. Their compact size and the unparalleled maturity of the silicon industry facilitate their dense integration into today's smartphones and computers. However, photonics lacks an equivalent platform that combines nonlinearity, nanometer-scale dimensions, and scalability. This dissertation takes a step toward achieving this trifecta in optics by developing a platform called nanophotonic PPLN (Periodically Poled Lithium Niobate). This platform combines strong nonlinearities with nanophotonic waveguides, enabling devices that outperform their electronic counterparts in terms of speed [1, 2]. It also supports information processing applications where the data is already in the optical domain. In terms of scalability, we have succeeded in extending these devices to the circuit and system levels, demonstrating that photonics can excel in certain information processing tasks [3, 4]. This transition from off-chip to on-chip optical information processors mirrors the shift in the 1960s when transistors replaced bulky vacuum tubes in electronics. It remains to be seen whether this nanophotonic PPLN platform will have a similar revolutionary impact.

It is here that I should clarify the two classes of optical information processors

that will be presented in this dissertation. The first encompasses computing applications, spanning from logic gates to specialized NP-hard problem solvers. For example, we have demonstrated all-optical activation functions for deep learning[1], and large-scale time-multiplexed OPOs for recurrent neural networks[5]. The second category focuses on optical sources that enable information to be generated and processed in optics. We have created versatile tools including multi-octave frequency combs [6, 7] and electrically pumped tunable continuous-wave sources [8]. Potential applications are astrocombs and breath analyzers. A common argument for optical information processing is that data, ranging from optical clocks to lidar, is often inherently optical. This second class aims to improve optical sources to facilitate optical information processing, whether in terms of bandwidth, required pulse energy, or even quantum enhanced.

The remaining sections of this introduction will delve into the intricacies of the nanophotonic PPLN platform. Section 1.2 will describe the developments in optics that led to nanophotonic PPLN. While this platform is often considered a recent trend, this section will describe how nanophotonic PPLN has evolved out of pursuits from multiple different fields of optics, and argue that as the convergence point of all these disciplines, it represents a significant milestone in optics. Rome was not built in a day, and neither was nanophotonic PPLN. Section 1.3 will provide a more in-depth exploration of nanophotonic PPLN and answer what it is, how it is fabricated, and what does it enable that was previously not possible in photonics? In Section 1.4, my main contributions to the platform of nanophotonic PPLN will be described, along with an overview of the remaining chapters of the thesis.

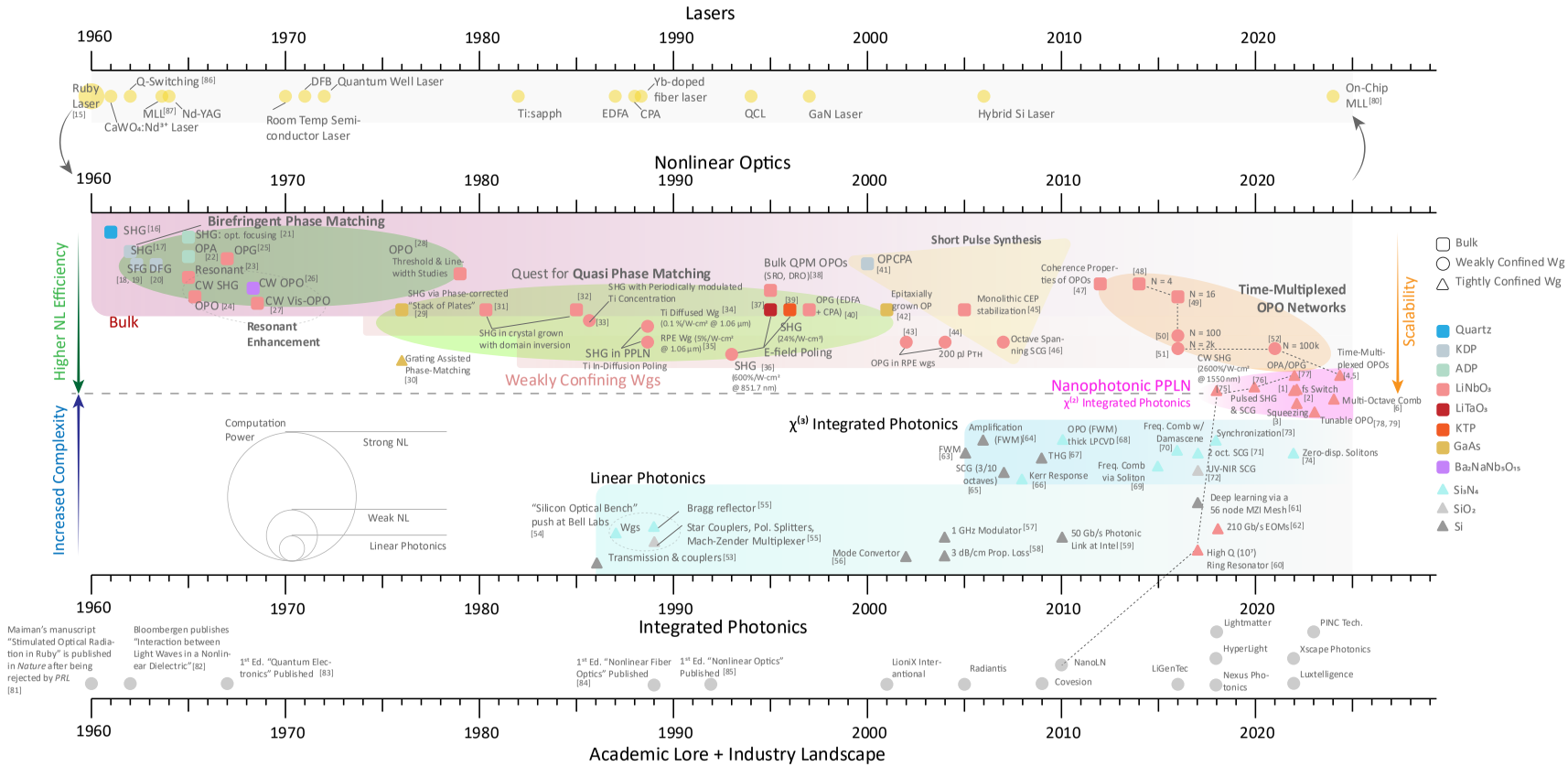

Figure 1.1: **Timeline of photonics leading up to Nanophotonic PPLN**. Note, for nonlinear optics emphasis was placed on parametric $\chi^{(2)}$ processes. Owing to limited space, many important events have been excluded. Some excellent review papers that cover events both in and tangential to this plot are referenced here. Early nonlinear optics: [9, 10]; LN Development [11]; Si photonics: [12, 13, 14].

1.2 Light-Matter Interactions Paving the Way to Nanophotonic PPLN

Nanophotonic PPLN is to optics what a Grand Prix winning F1 race car is to automobiles. It is a cutting edge material platform, the result of over six decades of continuous development — seven if you consider that LN was first synthesized in 1949. Just as the design of a modern race car is motivated by multiple factors such as drag, weight, and handling, nanophtonic PPLN is the result of streamlining how light interacts with matter. To fully appreciate just how advanced this platform is, this section will review the driving forces that led to nanophotonic PPLN through the lens of light-matter interactions.

Here will focus on three types of light-matter interactions: how matter generates intense light, how intense light interacts with matter, and how matter manipulates light — corresponding to the fields of lasers, nonlinear photonics, and integrated photonics, respectively. As illustrated in Fig. 1.1, goals and advancements within each of these fields have either led to or been influenced by the nanophotonic PPLN platform. In the case of nonlinear photonics, it was the need of ever higher nonlinear conversion efficiencies and the drive for scalability. For integrated photonics, it was the demand for all-optical complexity. Regarding lasers, not only do they serve as the optical sources driving nanophotonic PPLN devices, but new laser sources are now emerging based on this platform. In what follows, we will delve into these developments in greater detail.

1.2.1 Demand for Higher Nonlinear Efficiency

In nonlinear optics, there has always been an urgent need to enhance light-matter interactions, aiming for ever-higher nonlinear conversion efficiencies. This is illustrated in the second timeline from the top in Fig. 1.1. When light of sufficient intensity interacts with a dielectric medium, nonlinear electromagnetic phenomena occurs. Denoting the dipole moment per unit volume as $\mathbf{P}$, and the applied electric field as $\mathbf{E}$, this response is commonly expressed by the power series

$$\begin{aligned}\mathbf{P}(t) &= \epsilon_0 \left[\chi^{(1)}\mathbf{E}(t) + \chi^{(2)}\mathbf{E}^2(t) + \chi^{(3)}\mathbf{E}^3(t) + \cdots\right] \\ &\equiv \mathbf{P}^{(1)}(t) + \mathbf{P}^{(2)}(t) + \mathbf{P}^{(3)}(t) + \cdots\end{aligned} \tag{1.1}$$

where $\chi^{(n)}$ denotes the n^{th} order nonlinear optical susceptibility. Classically, this nonlinear susceptibility is viewed as the response of an electron driven by an electromagnetic field, $\mathbf{E}_A$, in an anharmonic potential well created by the interatomic field in the solid. Nonlinear optical behaviors that conserve both energy and momentum are called parametric processes. This dissertation largely concerns itself with $\chi^{(2)}$ parametric processes, the strongest order of nonlinearity.

For an electron to be driven beyond its quadratic minimum of the interatomic potential and demonstrate nonlinear behavior, a light source with sufficient power spectral brightness is required[1]. The first light source to reach this regime was Maiman's ruby laser in 1960 [15]. This is the starting point of the timeline in

[1] P_2/P_1 is $\sim E/E_A$. E_A is 10^8 V/cm. When focused, the early Ruby Lasers produced electric fields on the order of 10^5 V/cm [16]. More detailed treatments can be found in [10, 88, 82].

Fig. 1.1. A year later, Franken et al. had already demonstrated second harmonic generation (SHG), and the field of nonlinear optics was born [16]. However, the level of nonlinearity Franken observed was so weak, that the editor of *Physics Review Letters* mistook the faint spot on the image of the photographic plate that evidenced SHG as an undesirable smudge, and airbrushed it out. For the next six decades, the field of nonlinear optics would be in a constant pursuit for ways to increase the nonlinear efficiency to explore new nonlinear phenomena, unlock new regimes of operation, and find practical applications for this new field.

The normalized conversion efficiency for SHG, η_{SHG}, in a waveguide is defined as $P_{out}/(P_{in} \cdot L)^2$, and expressed as,

$$\eta_{SHG} = \left(\frac{2}{\epsilon_0 c^3}\right)\left(\omega^2\right)\left(\frac{d_{\text{eff}}^2}{n_1^2 n_2}\right)\left(\frac{A_{2\omega}}{A_\omega^2}\right)\text{sinc}^2\left(\frac{\Delta k L}{2}\right) \tag{1.2}$$

where ϵ_0 is the vacuum permittivity, c the speed of light in vacuum, ω the first harmonic (FH) frequency, d_{eff} the effective nonlinear coefficient, Δk the phase mismatch, L the length of the nonlinear medium, A the effective mode area, and n_1 and n_2 are the effective indices at the FH and SH, respectively [75, 76]. The equation for focused Gaussian beams in bulk is treated in detail by these other references [89, 21, 88], but retains many of the key characteristics of eq. 1.2 for the purpose of this discussion. This equation already suggests the many ways that SHG efficiency can be improved. The first term in eq. 1.2 is made up of fundamental constants. The second indicates that higher conversion efficiencies can be expected at shorter wavelengths, as long as deleterious effects such as photorefractive damage and pump-induced absorption[2] can be navigated. The third term is material-dependent and, for a given wavelength, can be used as a nonlinear optical figure of merit. The following term indicates that tighter mode confinement improves η_{SHG}, and the final phase-matching term shows that without proper consideration towards matching the phase velocities of the first and second harmonic frequencies, the SHG process can quickly become a zero-sum game. We will now delve deeper into how to enhance these various terms.

Material Development

The nonlinear figure of merit, represented by the third term in eq. 1.2, was among the earliest terms to be enhanced. In his original experiment, Franken focused a ruby laser on a quartz crystal. Compared to what is available to us today, Franken was using a poor nonlinear optical material in its bulk form with no efforts towards phase matching. It did not help that his laser source was a highly multimode millisecond laser with poor beam quality. It comes as no surprise that Franken reported a total power conversion efficiency of only "a fraction of a percent" of the few kW at his disposal [16]. Already by 1962 however, new nonlinear crystals were being explored. As cataloged in Fig. 1.1, quartz was soon replaced by KDP, ADP, and even

[2]Pump-induced absorption includes two-photon absorption [90], green-induced infrared absorption (GRIIRA) [91] and blue-light-induced infrared absorption (BLIIRA) [92].

lithium niobate. Systematic studies of the nonlinear figures of merit, transparency windows, and damage thresholds were conducted and tabulated [93, 90, 94, 95, 96]. A key breakthrough in developing new nonlinear materials occurred when Miller determined that the nonlinear susceptibility corresponds to the third power of the linear susceptibility by a factor now referred to as the Miller's delta [97]. It is also worth noting that $\chi^{(2)}$ is a third-rank tensor and as such is only present in mediums lacking inversion symmetry.

Phase matching

Efforts to match the phase velocities of the constituent waves, described by the final term in Eq. 1.2, have proven to be a challenge spanning decades. In 1962, Giordmaine demonstrated the concept of birefringent phase matching (BPM)[17], which became the primary modality for phase matching over the following two decades [98, 99]. This is indicated by the region shaded in green in Fig. 1.1. Birefringent materials can support two orthogonal polarization eigenmodes called the ordinary and extraordinary polarizations. The latter's phase velocity can be tuned by the angle of propagation and leads to angle phase matching, or "critically phase matched" BPM. When the phase-matching direction is perpendicular to the optical axis, "noncritically phase matched" BPM occurs. Such BPMing schemes vastly enhanced η_{SHG} compared to that of Franken and was the main mode for phase matching over the first two decades of nonlinear optics.

From the very early days of nonlinear optics however, it was recognized that there were other techniques to tune the relative phases of waves in a nonlinear optical measurement. Quasi-phase matching (QPM) gathered perhaps the most excitement. In QPM, the nonlinear susceptibility of the medium is periodically modulated such that at every coherence length interval the phase relation between the constituent waves are reset and continuous energy flow from the pump to signal wavelength is achieved. Compared to BPM, QPM allows for phase matching over the entire transparency window of a material, and as the input and output waves can share the same polarization, the diagonal terms of a material's nonlinear susceptibility are also accessible. These diagonal terms can often be larger than the off-diagonal terms, as is the case with the d_{33} term for lithium niobate. In principle, QPM also allows for very long nonlinear interaction lengths.

Experimentally achieving efficient Quasi-Phase Matching (QPM) spanned over two decades, as depicted in the light green shaded oval in Fig. 1.1. Early demonstrations of the concept date back to 1976 when lasers were passed through stacks of phase-corrected GaAs plates [29] — a material that was largely inaccessible to nonlinear optics beforehand as it lacked birefringence. In the early 1980s, this method evolved with the growth of specialized crystals featuring domain inversions in various nonlinear optic materials [31, 32]. Despite advancements, these approaches suffered from significant losses. It was not until 1986 that what some consider the first demonstrations of QPM in its modern form were realized [33]. The introduction of electric field poling in the early 1990s [36] further enhanced second harmonic efficiencies using QPM and rigorous tuning and tolerance studies were conducted

[100]. The technique was soon extended to bulk crystals and new methods of 3D structures have been explored [101]. In fact, the pursuit to find alternative ways to phase match continues to today, and some examples include [102, 103, 104].

Effective Mode Area

The last term to address in equation 1.2 is the effective mode area. In the development of QPM, we had already seen the first breakthrough towards decreasing A_{eff}. In 1974, the potential to decrease A_{eff} emerged with the discovery that Ti dopants could be indiffused into LN, creating a core region of higher refractive index to guide light [105]. Over a decade later, proton exchange techniques were introduced, yielding waveguides with lower losses [106]. These transitions are depicted in Figure 1.1, labeled as 'bulk' and 'Weakly Conifining Wgs.' Notably, ridge waveguides were initially considered impractically lossy, a perception that has evolved over time. This era of weakly confining waveguides led to effective areas of $\sim 50\ \mu\text{m}^2$ and second harmonic efficiencies on the order of 90 %/W-cm^2 at 1560 nm [107, 108]. For reference in bulk crystals driven by focused Gaussian beams A_{eff} is $\sim$ 100s-1000s of μm^2 and second harmonic efficiencies at 1550 nm are ~ 0.6 %/W-cm [90, 109]. Note that in the case of bulk materials, SHG efficiencies are often reported in terms of %/W-cm. This is because earlier findings revealed that using a confocally focused beam rather than a collimated one leads to higher overall power conversion. In essence, in bulk it is preferable to intentionally operate with a crystal length surpassing the Rayleigh range, thereby sacrificing the L^2 term to increase the P_{in}^2 term [21, 89][3]. Nanophotonic PPLN further reduces the A_{eff} term to approximately 1.6 μm^2, with measured η_{SHG} reaching as high as 2600 %/W-cm^2 [110].

1.2.2 Summary

We have hereby shown how nanophotonic PPLN is the result of optimizing every term in η_{SHG}, including those for material properties, phase matching, and effective mode area. In addition to reducing the waveguide dimensions to sub-wavelength scales, nanophotonic PPLN maintains QPM capabilities, thereby unlocking the d_{33} term of LN for nonlinear interactions. It is because of all of these advancements that nanophotonic PPLN can generate multi-octave frequency combs with three orders of magnitude less power compared to other integrated photonic platforms, the topic of Chapter 6.

Several additional techniques merit attention for enhancing overall power conversion efficiency and exploring new operational regimes. While not explicitly accounted for in Eq. 1.2, resonators significantly contribute to these goals. In the early stages of nonlinear optics, it was observed that total power conversion could be augmented by employing a resonant cavity, allowing for multiple passes of light through the nonlinear medium. This insight paved the way for innovations such as

[3]To get a sense for this improvement with some numbers, Bjorkholm demonstrated a 400-fold increase in second harmonic power from a 1 cm long ADP crystal using optimal focusing compared to a collimated beam [21].

the optical parametric oscillator (OPO) and resonant enhanced SHG [24, 23]. These early works are marked with the dashed line in Fig. 1.1 and denoted as 'Resonant Enhancement.' Furthermore, the utilization of femtosecond pulses and dispersion engineering for temporal confinement, in addition to the spatial confinement offered by nanophotonic waveguides, has not been discussed. This topic will be addressed in section 1.3.

1.2.3 New Lasers, New Nonlinear Optics

Thus far, our focus has been on enhancing the efficiency of light-matter interactions. However, another approach to accessing new regimes of operation is to generate more intense sources of light, namely by developing higher power lasers. In fact, nonlinear optics has played a pivotal role in the advancement of lasers [111], as evidenced by the interaction between the first and second topmost time axes in Fig. 1.1. Nonlinear-optic innovations such as Q-switching[86], mode-locking [87], and optical parametric chirped pulse amplification (OPCPA) [41] have enabled the production of higher intensity pump pulses with shorter pulse widths, allowing access to previously unreachable regimes due to insufficient peak power. These examples underscore the symbiotic relationship between laser technology and nonlinear optics. Since the inception of the ruby laser, the development of new lasers has often facilitated progress in nonlinear optics, and vice versa. Today, a new class of on-chip lasers have been developed on the thin-film lithium niobate (TFLN) platform [80, 112]. It will be interesting to see what new nonlinear optics they will enable.

1.2.4 Scaling Up Nonlinear Optics

Another impetus behind the development of the nanophotonic PPLN platform arises from the drive to explore large-scale nonlinear systems, as illustrated in the orange-shaded section of Fig. 1.1. This endeavor extends beyond mere volume manufacturing and component miniaturization; it aligns with a recent academic and industrial push to delve into large-scale time-multiplexed nonlinear systems in photonics. This initiative traces back to early experiments with optical Ising Machines utilizing free-space, bulk OPOs [113, 49]. However, tabletop time-multiplexing schemes proved challenging to scale, prompting a transition to fiber-based systems [50, 51]. Despite achieving impressive sizes of 100k time-multiplexed OPOs [52], these setups are constrained by their reliance on measurement feedback, a protocol predominantly executed in electronics. Such hybrid methodologies often compromise the inherent advantages of optical processing, prompting the exploration and advancement of all-optical systems. Recent investigations have also expanded beyond Ising problems to encompass other challenges such as the XY-problem [114] and artificial neural networks [5, 115].

Nanophtotonic PPLN is the perfect platform to study such all-optical systems. The tight spatial confinement of modes outlined earlier, not only enables compact device dimensions and enhances nonlinear interactions but also opens avenues for crafting extensive circuits cascading numerous components. With bending radii[4]

[4]The exact acceptable minimum radius is geometry, wavelength, and application dependent.

below 50 μm, it is possible to integrate fully programmable linear interferometers and detectors, all on a single chip. In contrast, weakly-guiding waveguides require millimeter-scale bending radii, which hinder the dense integration of components such as interferometers and resonators. Recent advances in TFLN, including high-speed electro-optic modulators (EOMs) [116] and integrated single-photon detectors [117], promise a path for scalable classical and quantum information processors. We will explore these possibilities in further detail in Chapters 7 and 8.

1.2.5 Integrated Photonics: Stronger Nonlinearity for Greater Functionality

A similar drive for nanophotonic PPLN also emerged from the integrated photonics community. Key demonstrations in this field are illustrated along the second-from-bottom timeline in Fig. 1.1. As indicated there, the field had gotten significant mileage out of solely linear components and had even demonstrated meshes of MZIs for optical deep learning applications [61]. For all-optical demonstrations however, an optical source of nonlinearity was required[5]. While some integrated photonic systems have been demonstrated using coupled $\chi^{(3)}$ resonators [73], these approaches often rely on high-Q cavities, imposing significant fabrication constraints. Nanophotonic PPLN offers considerably more gain without the need for high-Q cavities, making it well-suited for large-scale time-multiplexed all-optical networks. We have already seen early demonstrations of 70-node time-multiplexed OPOs on this platform [4].

1.2.6 Conclusion

To conclude, nanophotonic PPLN is the result of multiple needs in optics. The need for higher nonlinear efficiency, the need for more scalability, and the need for increased complexity in integrated photonics to name a few. Throughout this journey, lithium niobate has undergone numerous transformations, evolving into its current advanced form. Hopefully the earlier analogy of nanophotonic PPLN to an F1 race car now makes more sense. In fact, this comparison is particularly apt as the first year an F1 Grand Prix was held was 1950, the year after LN was first synthesized. While it might seem like a long time since Maiman's demonstration of the laser, it is worth noting that this period still falls within the span of a single professional career. In 1960, Professor Amnon Yariv had already completed his graduate studies and was working at Bell Labs. He joined Caltech's faculty in 1964 and continues to actively contribute to the field today [118]. In this context, nonlinear optics is still a relatively young discipline, and it is truly exciting to consider what can be achieved with this platform in the generations to come.

More information is provided in Fig. 1.3

[5]This is the opposite approach from measurement feedback, with the linear computation performed in optics and the nonlinear computation with electronics. While this does take advantage of the best of both worlds, opto-electronic conversions are expensive both in terms of energy and speed. If the number of electro-optic and opto-electronic conversions scales with the computation size, the advantages of such hybrid systems quickly disappear.

1.3 The Nuts & Bolts of Nanophotonic PPLN

Now that we have examined the pursuits in optics driving the demand for the nanophotonic PPLN platform, here we will explore the platform in detail. Specifically, we will review the key design opportunities it offers of mode-, QPM-, and dispersion-engineering as well as velocity matching with RF signals.

Lithium niobate refers to the thin layer of material on which we precisely etch a few-hundred-nanometers-tall ridges that guide light. In this unpoled state, the platform is called thin-film lithium niobate (TFLN). Periodic poling is the means by which we prepare certain segments of LN to interact light of targeted wavelengths in a nonlinear manner. By adding cladding, electrodes, and wirebonds we can add active components such as electro-optic modulators (EOMs) and heaters. The basic fabrication process flow is shown in Fig. 1.2.

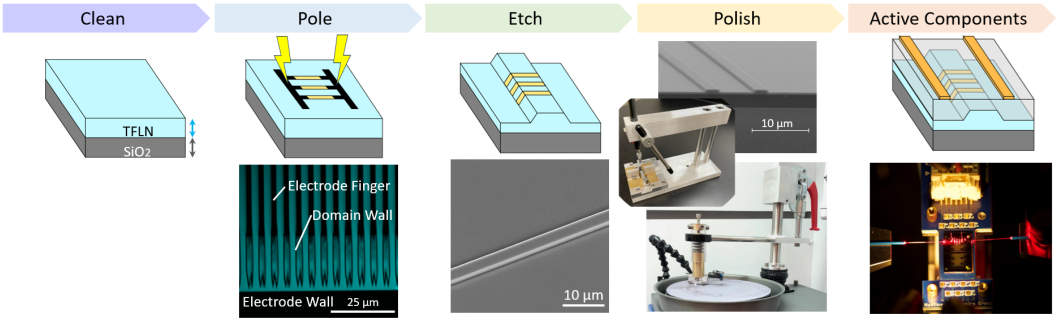

Figure 1.2: **Fabrication steps**. A more detailed description of the process can be found in [6].

Light propagates through these waveguides via the spatial modes supported by the structure. Figure 1.3a illustrates an example of the fundamental transverse electric (TE) mode in a typical structure. The modes that a waveguide can support depend on its geometry and injected wavelength. Practically, the most convenient parameter to adjust is the top width of the waveguide, as shown in the plots in Fig. 1.3b. With this mode landscape in mind, mode crossings and hybridizations can be utilized for mode conversion, coupler design, and diagnosing certain nonlinear optical processes. However, designing tapers that cross mode hybridizations requires careful consideration. The tight mode confinement provided by these waveguides allows for significantly tighter bending radii compared to weakly confining waveguides, enabling the creation of intricate structures. Figure 1.3c exemplifies this, and has been used to demonstrate nanophotonic PPLN optical parametric oscillators (OPOs) with on-chip resonators[6].

Periodic poling enables quasi-phase matching of distinct wavelengths, facilitating efficient wavelength conversions within this platform. As discussed in Section 1.2.1, E-field poling marked a significant milestone in the development of QPM. Although E-field poling becomes increasingly challenging as the poling period shortens, we have successfully extended this method to poling periods as short as 2 μm for 406 to 812 nm spontaneous parametric down conversion (SPDC), as illustrated in figure 1.4a [119]. In figure 1.4b, we QPM-engineered a poling period

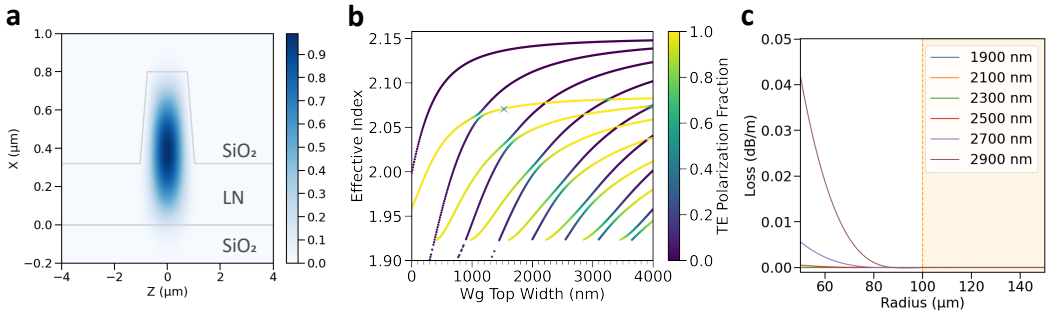

Figure 1.3: **Mode engineering**. **a** shows the fundamental TE mode of a typical waveguide structure. **b** shows that supported waveguide modes as the top width of the waveguide is swept. The geometry of the mode in **a** is marked by the blue cross. **c** shows the waveguide bending loss as a function of radius and wavelength.

defect that induced a phase shift, enabling switching between second harmonic generation (SHG) and optical parametric amplification (OPA). This results in a nanophotonic switch [2]. Additionally, we have utilized chirped poling periods to achieve broadband supercontinuum generation (SCG), producing a UV-visible comb [7].

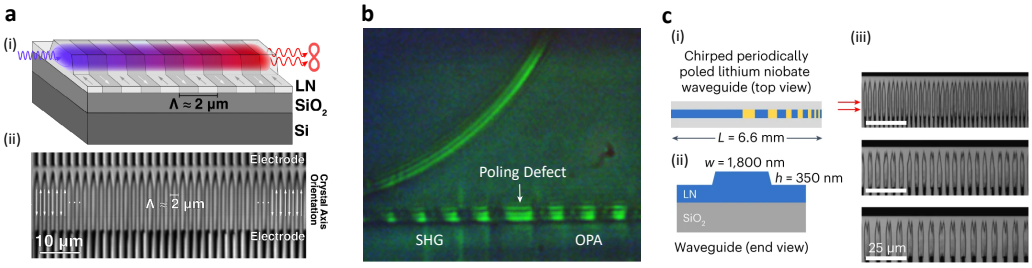

Figure 1.4: **QPM engineering**. **a** (i) illustration of a periodically poled nanophotonic PPLN waveguide for SPDC with a pump at 406 nm. (ii) a second harmonic microscope image of the poled region. The poling electrodes are the black fingers at the top and bottom of the figure, and the black regions in the middle are the domain walls between the periodically poled areas. **b** second harmonic microscope image of the poling defect engineered for an all-optical switch. **c** (i-ii) illustrations showing the concept design of chirped poling along with (iii) images of the poled region from the actual device. Figures taken or adapted from [119, 2, 7].

Nanophotonic PPLN waveguides provide tight mode confinement, allowing small changes in device geometry to significantly alter the effective indices for propagating light. This capability is essential for dispersion engineering, a feature predominantly reserved for nanophotonics. As illustrated in Fig 1.5a, adjusting the waveguide dimensions enables precise tuning of the group velocity mismatch (GVM) and group velocity dispersion (GVD) of the wavelengths involved. As shown in Fig. 1.5b (i) and (ii), this tuning is not possible for bulk LN. One particularly interesting

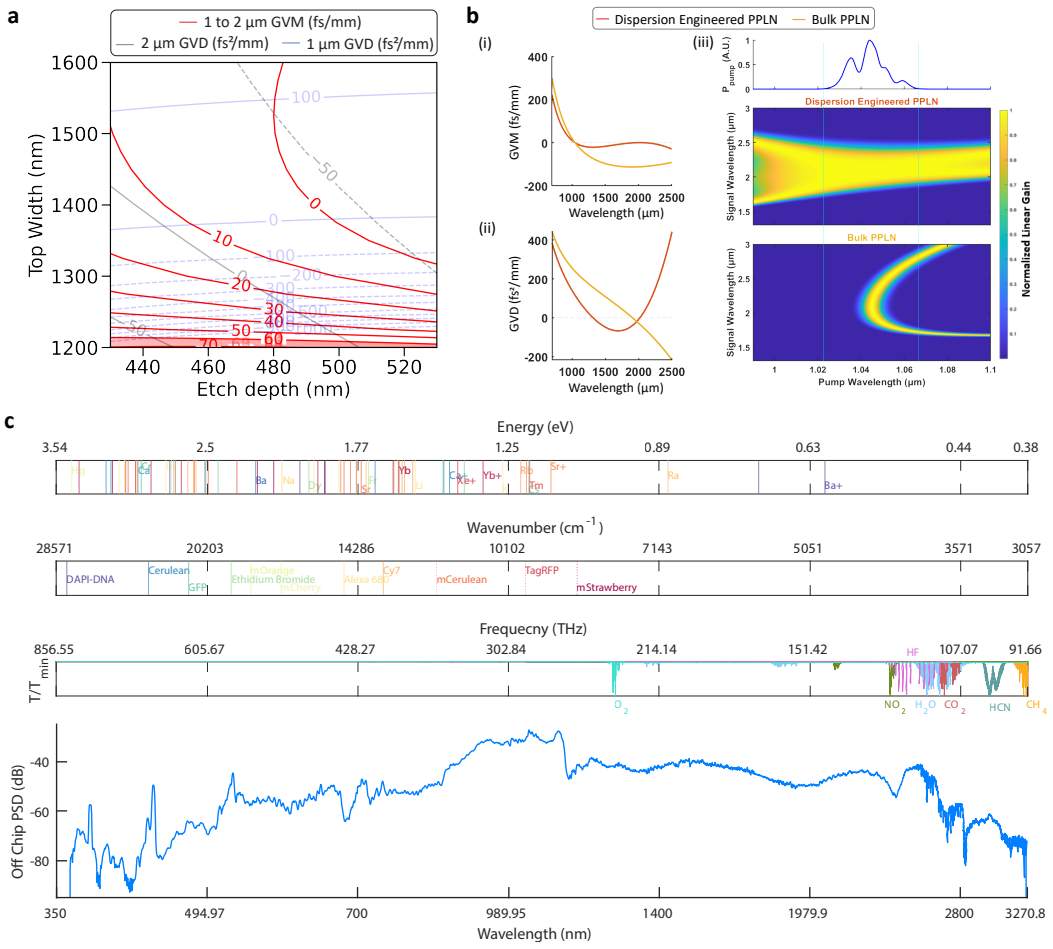

Figure 1.5: **Dispersion engineering**. **a** Dispersion landscape as a function of etch depth and top width for the design in Fig. 1.3. **b** (i) GVM and (ii) GVD comparison between dispersion engineered TFLN and bulk LN. Note that while the curve for TFLN can be tuned, the one for bulk is fixed. (iii) comparison of the gain bandwidth between a near-zero dispersion engineered PPLN and bulk PPLN. Adapted from [120]. **c** measured ultrabroad spectra out of the device in Chapter 6, compared against absorption lines of atoms, ions, and molecules.

region is the near-zero dispersion regime, where the GVM and GVD of the pump and signal are close to zero. This regime allows for ultrabroad, strong gain, with a gain bandwidth significantly broader than that of bulk materials. Figure 1.5b (iii) illustrates how a near-zero dispersion engineered nanophotonic PPLN waveguide can take full advantage of the bandwidth of fs pulses, compared to that in the bulk. We will explore this regime in greater detail in the following chapters. Figure 1.5c presents measured multi-octave spectra from a near-zero dispersion engineered waveguide. The broadband spectra and comb sources demonstrated throughout this dissertation will have significant potential for sensing and spectroscopy applications in physics, chemistry, and biology, as evidenced by the absorption lines of various

atoms, ions, and molecules.

Finally, velocity matching between the phase velocity of an RF wave and the group velocity of an optical wave enables efficient, high-speed electro-optic modulation. While using conventional weakly confining waveguides electro-optic modulators (EOMs) operating at up to 40 GHz with approximately 8 V half-wave voltage (V_π) are commercially available for C-band wavelengths, the tighter mode confinement of TFLN allows for advanced group velocity engineering. By combining TFLN with silica cladding, which has a lower dielectric constant compared to LN and thus increases the phase velocity of the RF wave, along with microstructured electrodes to reduce microwave losses, 50 GHz EOMs with a V_π of 1.3 V have been demonstrated [121, 62, 122]. Additionally, *Phase Sensitive Innovations* claims to have demonstrated electro-optic modulation in the 100-500 GHz range. Figure 1.6 showcases designs and actual images of RF EOMs fabricated in-house, which were operated at 10 GHz to demonstrate an all-optical mode-locked laser (MLL). These TFLN EOMs are ultra-compact, allowing for easy cascading into Mach-Zehnder interferometer (MZI) mesh structures or incorporation into periodically poled nonlinear circuits. This opens a path towards ultrafast, electronic programming of all-optical circuits using CMOS drivers, the applications of which will be explored in Chapter 7.

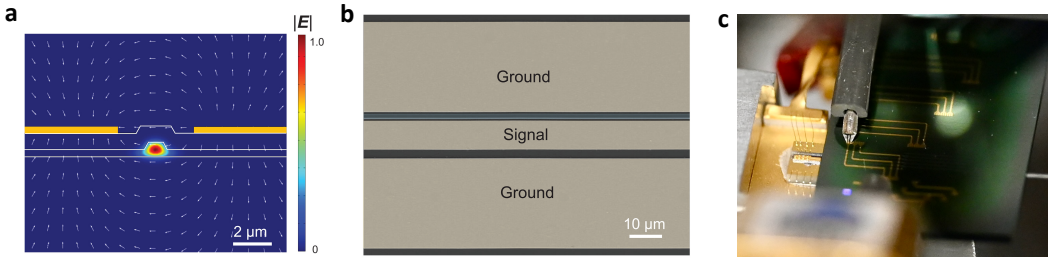

Figure 1.6: **Velocity matching**. **a** Simulated electric field distribution from an EOM on a device with silica cladding and **b** a false colored SEM of the fabricated electrodes. **c** shows the full device with RF probes being employed to provide the RF signal. Figures **a** and **b** were taken from [80].

1.4 Summary of Contributions & Thesis Overview

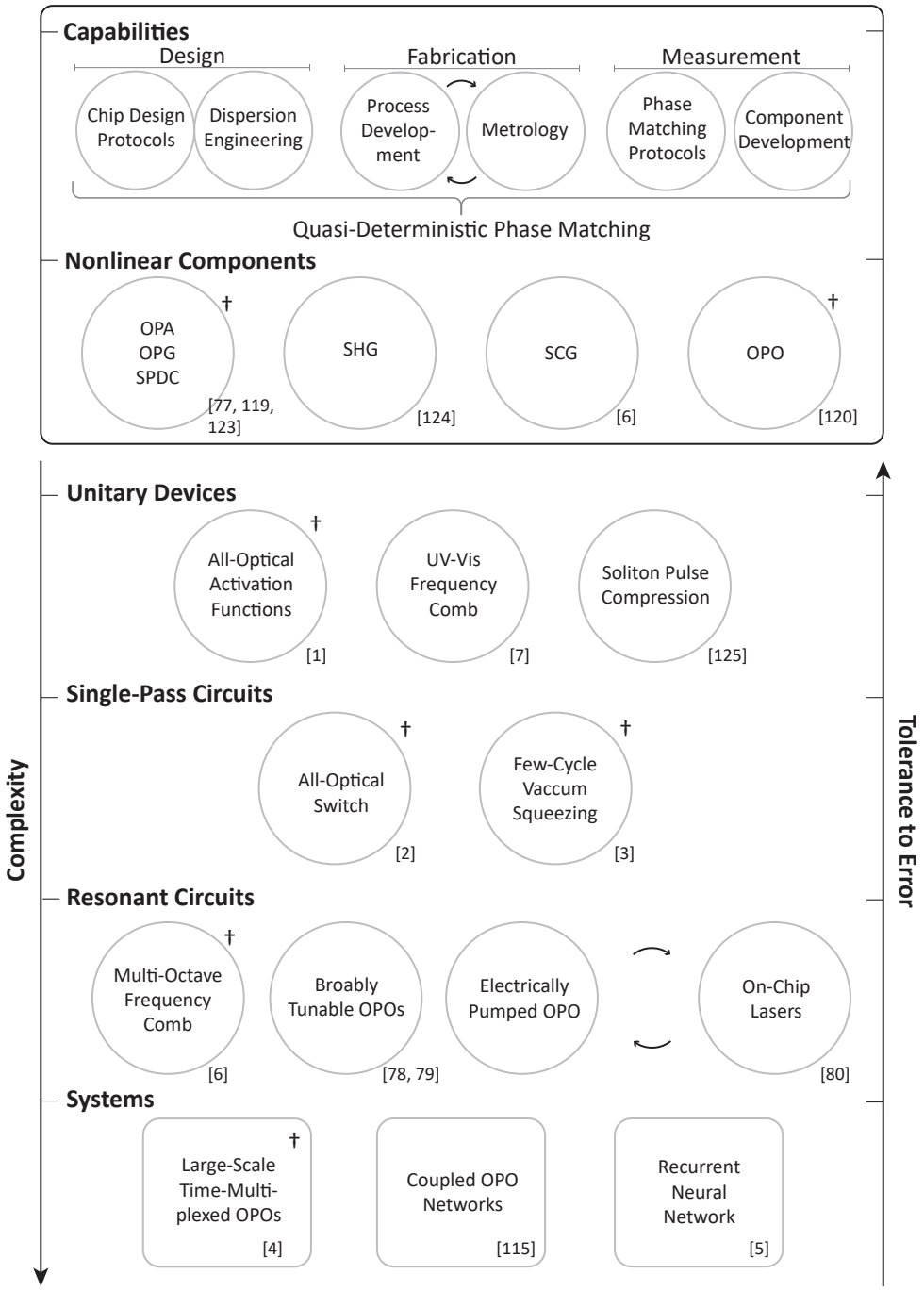

Figure 1.7: **Key contributions**. Projects that have resulted in a first co-author manuscript by the time of this dissertation are labeled with a †.

In the previous sections, the design concepts of nanophotonic PPLN were reviewed, and its role as a solution to many earlier pursuits in optics was described.

Here, my own contributions to the platform will be outlined, and an overview of the remaining chapters in this dissertation will be provided.

Starting with some context, as illustrated in the bottom time axis of Figure 1.1, TFLN wafers from NanoLN became commercially available in the early 2010s. Following the demonstration of high-Q ($\sim 10^5$) microdisks in 2014 [126], by 2017 it was demonstrated that low-loss nanophotonic waveguides can be fabricated on TFLN [60], and the stage was set for nonlinear optics research. The missing piece of E-field poling for QPM was soon developed, and in 2018 an ultra-high SHG efficiency of 2500 %/W-cm^2 was measured at 1550 nm in a poled nanophotonic PPLN waveguide[75]. Coinciding with the start of my graduate studies, a device from the same chip was injected with ~100 fs pulses at 2 μm, demonstrating how the combination of dispersion engineering with ultrashort pulses can unlock ultrabroad nonlinear interactions on this platform[76].

During my graduate studies, I added to this library of nonlinear photonic processes and in turn used these to demonstrate optical devices, circuits, and systems. This progression in complexity is summarized in Fig. 1.7. It is here that I should clarify that when I joined the Nonlinear Photonics Group at Caltech, we were just beginning to work with this platform. We still had no idea how to design, fabricate, or measure any of the ideas we had in mind. Once we had developed the basics, we were able to work our way slowly up the ladder in Fig. 1.7. Each new rung required a new round of development to allow us to meet the requirements for increasingly complex circuits with lower tolerance to error. In the following I will review this progression one at a time.

1.4.1 Capabilities

Before we could dive into practical demonstrations of nonlinear optics, we first had to develop all the building blocks to work with nanophotonic PPLN. Broadly speaking we needed to invent tools, recipes, and procedures to design, fabricate, and measure devices on this platform. My major contributions towards these efforts are highlighted in the top panel of Fig. 1.7. Even once we had developed our initial procedures, I found myself often returning to this design, fabricate, measure cycle to improve our quasi-phase-matching tolerances and later to develop new components such as ultra-broadband couplers, EOMs, and heaters.

My initial contributions to this platform began with measurements. During the Covid lockdown, with Alireza periodically checking in to make sure I had not blinded myself, I constructed my first free-space chip-coupling setup. These minimally dispersive, femtosecond pulse coupling setups, combined with our dispersion-engineered waveguides, enabled us to explore spatiotemporal confinement in nonlinear optics in a way that was previously very challenging. However, deterministically achieving phase matching with this setup proved to be a significant challenge. In our initial experiments, we often worked with chips containing hundreds of devices, each with slight design variations. My task was to identify which, if any, exhibited phase matching. Nonlinear effects were frequently obscured by noise from poor-quality poling, dreadful facet polishing, and sub-optimal coupling. Additionally,

without precise measurements of the waveguide dimensions, which often deviated significantly from our designs, we could not rely on our simulations to guide our efforts. In fact, we were not even sure what proper phase matching would look like. Over the years, I have developed numerous methods to find and tune phase matching.

My next major involvement focused on fabrication. One of our significant challenges was the inability to close the loop between simulation, fabrication, and measurement because we lacked precise knowledge of what we had fabricated. Key questions included: What is the etch profile? What is the thin film thickness, uniformity, and quality? What tools are best for accurately measuring these metrics? Gradually answering these questions has helped us bridge the gap between design and measurement. For example, in the context of QPM, I can now predict with reasonable certainty which device will be phase matched. Closing the loop has also been invaluable in developing new components such as pulley and adiabatic couplers.

I have also dedicated considerable time to developing and optimizing fabrication recipes. These include techniques and jigs for mechanical polishing, integrating active components, working with sapphire substrates, and most importantly, improving device tolerances to quasi-deterministically fabricate phase-matched devices with precise dispersion parameters. Along the way, I have explored new resists and initiated the investigation of adding chemistry to our typically mechanical waveguide etch, via atomic layer etching (ALE) [127].

The final challenge was to establish appropriate design protocols for our chips. For example, how many devices should be placed on a chip to allow for QPM, given our fabrication tolerances? What basic set of mode, loss, and dispersion simulations need to be run to settle on a device geometry? What design protocols should we follow to increase yield and avoid the limitations imposed by the various fabrication steps? A subset of these design protocols are shown in Figures 1.3 and 1.5. Additionally, a significant portion of my time was dedicated to simulating the dispersion characteristics of waveguides and documenting their landscape as a function of device geometry, wavelength, and substrate. These maps have empowered us to forecast intriguing regimes of operation, akin to our rendition of Mendeleev's periodic table. In the remaining chapters we will review the many new opportunities dispersion-engineering has allowed.

1.4.2 Nonlinear Components

Once we had a basic set of capabilities we immediately started developing nonlinear components. Some of these are cataloged in the second tier from the top of Fig. 1.7. For example, combining the power of the near-zero dispersion regime with fs pulses, we have been able to demonstrate multi-octave supercontinuum generation (SCG) extending from the UV-NIR starting with 1, 1.55, and 2μm sources, an example of which was shown in Fig. 1.5c. While most of our work thus far has been performed on a silica substrate, by developing the nanophotonic PPLN on sapphire substrate platform we soon hope to extend our SCG to the MIR.

We have also demonstrated SHG from each of these sources to efficiently generate a tunable UV source as short as 355 nm [124].

Arguably the most pivotal nonlinear building block was our demonstration of dispersion-engineered optical parametric amplification (OPA) [77]. This strong, broadband, and phase-sensitive gain element served as the cornerstone for many subsequent device and circuit-level demonstrations. Optical parametric generation (OPG) is a high gain OPA that is seeded by vacuum fluctuations. It splits (or "cuts" [88]) one pump photon into two photons. OPA and OPG will be extensively covered in Chapter 2.

To underscore the significance of OPA, it is crucial to address the recurring misconception that OPA is merely "the inverse of SHG." This misunderstanding has been a persistent challenge throughout the review process. In reality, the unique characteristics of OPA make it a vital component for circuit-level demonstrations. While SHG and OPA share similar phase matching conditions, the distinct behaviors of OPA have historically made it more challenging to observe in experiment. This is evidenced by the historical gap between the first experimental demonstrations of SHG and those of OPA/OPG in the early days of nonlinear optics (see Fig. 1.1).

The practical challenges of OPA/OPG can be attributed to two main factors. First, there is a stark difference in turn-on behavior. SHG exhibits a quadratic dependence on effective nonlinearity, length, and input power, whereas OPA/OPG shows an exponential dependence. For instance, the exponential turn-on behavior of OPG is akin to that of a diode, a characteristic absent in SHG. This means that suboptimal device characteristics and parasitic nonlinearities can be more detrimental (or even prohibitive) for OPA/OPG compared to SHG. Second, OPA/OPG's response to dispersion and phase mismatch differs markedly from SHG. Although the phase matching condition is similar for both processes, their phase matching behaviors and dispersion effects vary significantly. In SHG, the phase matching bandwidth is primarily dominated by the GVM between the fundamental and second harmonic waves. In contrast, for a degenerate OPA, the bandwidth is mainly influenced by the GVD of the signal, while GVM predominantly affects the gain magnitude. This means that a slight GVM in SHG can alter the spectral behavior (phase matching bandwidth), whereas in OPA, a slight GVM can drastically reduce the measurable gain. Consequently, dispersion engineering plays a more critical role in OPA. Similarly, OPG is highly sensitive to GVM, as a large GVM limits the exponential growth of spontaneously generated photons.

Another key attribute of OPA is its ability to provide both phase-sensitive and phase-insensitive gain. Degenerate OPA is inherently phase-sensitive, whereas non-degenerate OPA can operate in a phase-sensitive mode (when pump, signal, and idler are present) or a phase-insensitive mode (with only pump and signal at the input). These modes of operation enable important functionalities that are not achievable with SHG alone, as we shall see below.

1.4.3 Unitary Devices

With a comprehensive library of nonlinear building blocks at our disposal, we advanced to device-level demonstrations, as illustrated in the third tier from the top in Fig. 1.7. This phase was particularly exciting, as it allowed us to utilize nonlinear optics in ways that would captivate a broader audience. I am reminded of a conversation with Professor Mohammed Hassan, who was strongly opposed to developing ever faster optical sources merely for their own sake. His motivation for advancing ultrafast temporal resolution electron imaging tools (i.e., Attomicroscopy) was to record movies of quantum electron motion in action, "to see the quantum world." Similarly, our goal in developing the nanophotonic PPLN platform was not merely to push the limits of pulse energy and bandwidth in nonlinear optics, but to explore the broader potential of optical advantages for information processing.

For example, in single-pass configurations utilizing the properties of SHG and OPA, we have demonstrated femtojoule femtosecond all-optical activation functions [1]. While their immediate applications to deep learning will be thoroughly examined in Chapter 3, they exemplify how optics can deliver ultrafast nonlinearities. Since 2005, the clock rates of electronics have remained largely stagnant, hovering around 3-5 GHz. Even with overclocking and liquid nitrogen cooling, Intel's latest Core i9-14900KS has only managed to push this to 9.12 GHz. In contrast, optics can easily achieve clock rates exceeding 100 GHz. To fully harness these ultrafast speeds, an ultrafast all-optical activation function is essential, underscoring the importance of this device.

In terms of information processing enablers, we have leveraged single-pass nanophotonic PPLN devices to explore innovative optical sources. For example, using a QPM-engineered chirped poling design, we generated a UV-Vis frequency comb [7]. This same chip is being utilized to advance dual-comb spectroscopy in the UV, with pioneering efforts led by the Scott Diddams group [128]. Originally, the chip was intended for astrocomb applications but fell short due to input energy requirements. Moving forward, improving off-chip to on-chip coupling will be a crucial barrier to overcome.

Our precise engineering of specific non-zero dispersion parameters has enabled soliton-based schemes to achieve 2-3 times pulse compression, resulting in 30-40 fs pulses [125]. These ultrashort pulses not only open new avenues for fundamental research in extreme nonlinear optics but also hold significant value for advancing time-multiplexing techniques, which will be discussed in detail in Chapter 7.

1.4.4 Single-Pass Circuits

Advancing to the fourth tier from the top in Fig. 1.7, we encounter single-pass circuits. For the purposes of this dissertation, we define circuits as systems comprising two or more nanophotonic components. For instance, our all-optical switch consists of a poling defect sandwiched between SHG and OPA units, along with an additional coupler [2]. Similarly, our few-cycle vacuum squeezing circuit includes a squeezer unit and an amplifier unit with an intervening filter [3]. These circuits will be explored in detail in Chapters 4 and 5, respectively. The transition from in-

dividual devices to integrated circuits marked a significant milestone, representing the first step towards dense on-chip networks, a distinct advantage of nanophotonic PPLN over its bulkier predecessors.

To provide more context on our comparison with previous nonlinear platforms in quantum optics, let us delve into our squeezing experiment as an example. In this study, we generated and measured 4.9 dB of squeezing using nanophotonic PPLN waveguides. However, recent work by the Furusawa group achieved over 6.3 dB of squeezing using a large-mode area PPLN waveguide [129]. Their waveguide mode has a cross-sectional area of approximately 32.5 μm^2, much larger than our nanophotonic waveguides with a cross-sectional area of about 1.26 μm^2. Due to the tight spatial confinement in our nanophotonic devices, the nonlinear interaction is significantly stronger. For example, the normalized SHG efficiency reported by Kashiwazaki et al. [129] is approximately 60% W^{-1} cm^{-2} at 1.5 μm, while our estimated SHG efficiency is 1000% W^{-1} cm^{-2} at 2 μm. Consequently, large-mode waveguides typically require longer device lengths to achieve similar squeezing levels, resulting in larger device footprints and posing challenges for dense chip-scale integration. These longer interaction lengths also lead to higher propagation losses; for instance, Kashiwazaki et al. reported 16% loss for a 45 mm device. Such high losses are particularly detrimental in quantum photonics, especially for highly squeezed states required for fault-tolerant thresholds (e.g., ~10 dB squeezing with photon losses < 0.10). Conventional large-mode LN devices struggle to achieve such low losses. In contrast, our Squeezer OPA device is only 2.5 mm long. Notably, LN nanophotonics have demonstrated propagation losses as low as 2.7 dB/m [130], enabling generation of squeezing levels suitable for fault-tolerant thresholds in continuous-variable quantum information processing.

The tight spatial confinement of the modes in nanophotonics also provides the opportunity for fabricating large-scale quantum circuits with many components such as fully programmable linear interferometers and single-photon detectors within the same chip. This is enabled by tight bends in nanophotonics, which enables realization of substantially smaller linear components compared with large-mode integrated photonics. In large-mode waveguides, typically millimeter scale bending radii are required, limiting the dense fabrication of other components such as interferometers and resonators on one chip. On the other hand, similar to other nanophotonic platforms, LN nanophotonics can accommodate bending radii smaller than 50 μm, and thus realization of many components within the same chip, as exemplified by our small-scale nanophotonic circuit. Complementary recent advances in nanophotonic LN, such as high-speed electro-optic modulators [116] and integrated single-photon detectors [117], promise a path for scalable fault-tolerant ultrafast quantum information processors.

1.4.5 Resonant Circuits

By combining a resonator to these circuits with nonlinear elements, we have been able to explore cavity nonlinear dynamics at various time scales. These are shown in the second from the bottom tier in Fig. 1.7. For example, by combing fs pulses

with a near-zero dispersion engineered OPO, we have been able to demonstrate a multi-octave OPO that exploits a mechanism called Temporal Self-Cleaning (TSC) [6]. This will be treated in detail in Chapter 6. The mechanisms of broadly tunable laser sources using ps and ns pumping schemes have been explored in [79] and [78], respectively. In these schemes where a broad range of tuning is required, it has been found that operating off from zero dispersion is beneficial. Recently we have also started exploring CW pumped tunable OPOs [8].

It should be noted, however, that we are only beginning to uncover the possibilities offered by the rich dynamics of OPOs. For example, we have discovered that nanophotonic PPLN enables dispersion engineering beyond the second order, facilitating extreme on-chip pulse compression through the walk-off soliton mechanism [131]. Additionally, it provides a fertile ground for exploring various other soliton dynamics that were previously unattainable due to limitations in engineering the dispersion terms [132].

Finally, we have demonstrated a new class of lasers on this platform. As described in section 1.2.3, lasers and nonlinear optics share a symbiotic relationship. It will be interesting to see what information processing opportunities this new class of integrated sources [133, 134, 112, 80, 135] provide. For example, in the near future we can imagine using these sources to directly pump the single-pass and resonant devices in Fig. 1.7.

1.4.6 Systems

During a recent visit to Caltech, William Dally, Chief Scientist and Senior Vice President of Research at NVIDIA Corporation, made an insightful observation. He noted that while it is relatively straightforward to showcase individual devices that compute faster than their NVIDIA counterparts in isolation, the real challenge lies in developing systems capable of surpassing the performance of an entire NVIDIA GPU. This realization has served as a driving force behind our efforts to integrate our extensive library of devices and circuits into cohesive systems that retain a distinct optical advantage.

We have explored a number of pursuits for this during my dissertation, a few of which are shown in the bottom tier of Fig. 1.7. In Chapters 7 and 8, we will review our progress towards demonstrating large scale networks of time-multiplxed OPOs, and the computational advantages of these schemes. In fact we have recently demonstrated a recurrent neural network (RNN) based on an on-chip OPO [5] that operates with a 10 GHz clock rate. Here, the RNN solved a number of tasks including time-series prediction, nonlinear distortion equalization, and classification of noisy waveforms, all at a clock rate that would have been extremely challenging for electronics. We believe such demonstrations pave the way for large scale all-optical nonophotonic $\chi^{(2)}$ information processors.

For optical computing there are many dimensions to choose from to store and process information, such as space, frequency, and time. Why then, choose time-multiplexing for optical computing? One of the main reasons why many have opted for time-multiplexing is because it is uniquely suited to exploit the properties of

existing optical nonlinearities[113, 52]. Optical nonlinearities when combined with ultrafast pulses can operate in the fs regime with near-instantaneous refresh rates[1, 2], ideally suited for treating trains of pulses with GHz repetition rates. While it is difficult to make many identical copies of these nonlinearities or to make them treat multiple wavelengths equally, time-multiplexing has already demonstrated photonic networks with as much as 100k nodes using a single nonlinear element[52]. Time-multiplexed optical computers have the additional advantage that their inputs/outputs – be it optical communications or LiDAR – often already are in the form of a train of optical pulses. While time-multiplexed photonic computer architectures originally began as optical analogs of electronic computer architectures[136], recently there has been a large emphasis on designing architectures that are geared towards optics. Many non-von Neumann schemes have been explored/demonstrated, including complex optimization solvers (Ising Machines[113, 49], Hyperspin machines[137]) and artificial neural networks (deep learning[138], neuromorphic computers[51], reservoir computers[139], cellular automata[140]). Furthermore, with the recent advances made in integrated photonics, there are increasing opportunities to make time-multiplexed photonic systems that show significant advantages over electronics. A few notable components are 100 GHz electro-optic modulators[62], fs all-optical activation functions[1, 2], and on-chip synchronously pumped OPOs[79]. It will be interesting to see what complex circuits emerge as a result of these efforts.

References

[1] Gordon H.Y. Li†, **Ryoto Sekine**†, Rajveer Nehra†, Robert M. Gray†, Luis Ledezma, Qiushi Guo, and Alireza Marandi. "All-optical ultrafast ReLU function for energy-efficient nanophotonic deep learning". In: *Nanophotonics* 12.5 (2023), pp. 847–855. URL: https://doi.org/10.1515/nanoph-2022-0137.

[2] Qiushi Guo†, **Ryoto Sekine**†, Luis Ledezma†, Rajveer Nehra, Devin J. Dean, Arkadev Roy, Robert M. Gray, Saman Jahani, and Alireza Marandi. "Femtojoule femtosecond all-optical switching in lithium niobate nanophotonics". In: *Nature Photonics* 16.9 (Sept. 2022), pp. 625–631. URL: https://doi.org/10.1038/s41566-022-01044-5.

[3] Rajveer Nehra†, **Ryoto Sekine**†, Luis Ledezma, Qiushi Guo, Robert M. Gray, Arkadev Roy, and Alireza Marandi. "Few-cycle vacuum squeezing in nanophotonics". In: *Science* 377.6612 (2022), pp. 1333–1337. URL: https://www.science.org/doi/abs/10.1126/science.abo6213.

[4] Robert M. Gray†, **Ryoto Sekine**†, Luis Ledezma, Gordon H. Y. Li, Selina Zhou, Arkadev Roy, Midya Parto, and Alireza Marandi. "Large-scale time-multiplexed nanophotonic parametric oscillators". In: *arXiv* (2024). URL: https://arxiv.org/abs/2405.17355.

[5] Midya Parto, Gordon Li, **Ryoto Sekine**, Robert Gray, Luis Ledezma, James Williams, and Alireza Marandi. "An optical neural network based on nanophotonic optical parametric oscillators". In: *Conference on Lasers and Electro-Optics*. 2024, STu3P.7.

[6] **Ryoto Sekine**†, Robert M. Gray†, Luis Ledezma, Selina Zhou, Qiushi Guo, and Alireza Marandi. "Multi-octave frequency comb from an ultra-low-threshold nanophotonic parametric oscillator". In: *arXiv* (2023). URL: https://arxiv.org/abs/2309.04545.

[7] Tsung-Han Wu, Luis Ledezma, Connor Fredrick, Pooja Sekhar, **Ryoto Sekine**, Qiushi Guo, Ryan M. Briggs, Alireza Marandi, and Scott A.Diddams. "Visible-to-ultraviolet frequency comb generation in lithium niobate nanophotonic waveguides". In: *Nature Photonics* 18.3 (Mar. 2024), pp. 218–223. URL: https://doi.org/10.1038/s41566-023-01364-0.

[8] Luis Ledezma. "Towards Universal Integrated Laser Sources with Nonlinear Photonics". PhD thesis. California Institute of Technology, 2023.

[9] N. Bloembergen. "Nonlinear optics: past, present, and future". In: *IEEE Journal of Selected Topics in Quantum Electronics* 6.6 (2000), pp. 876–880.

[10] Martin M. Fejer. "Nonlinear Optical Frequency Conversion". In: *Physics Today* 47.5 (May 1994), pp. 25–32. URL: https://doi.org/10.1063/1.881430.

[11] Andreas Boes et al. "Lithium niobate photonics: Unlocking the electromagnetic spectrum". In: *Science* 379.6627 (2023), eabj4396. URL: https://www.science.org/doi/abs/10.1126/science.abj4396.

[12] S. Y. Siew et al. “Review of Silicon Photonics Technology and Platform Development”. In: *Journal of Lightwave Technology* 39.13 (2021), pp. 4374–4389.

[13] Lars Thylén and Lech Wosinski. “Integrated photonics in the 21st century”. In: *Photon. Res.* 2.2 (Apr. 2014), pp. 75–81. URL: https://opg.optica.org/prj/abstract.cfm?URI=prj-2-2-75.

[14] Chao Xiang, Warren Jin, and John E. Bowers. “Silicon nitride passive and active photonic integrated circuits: trends and prospects”. In: *Photon. Res.* 10.6 (June 2022), A82–A96. URL: https://opg.optica.org/prj/abstract.cfm?URI=prj-10-6-A82.

[15] T. H. Maiman. “Stimulated Optical Radiation in Ruby”. In: *Nature* 187.4736 (Aug. 1960), pp. 493–494. URL: https://doi.org/10.1038/187493a0.

[16] P. A. Franken et al. “Generation of Optical Harmonics”. In: *Phys. Rev. Lett.* 7 (4 Aug. 1961), pp. 118–119. URL: https://link.aps.org/doi/10.1103/PhysRevLett.7.118.

[17] J. A. Giordmaine. “Mixing of Light Beams in Crystals”. In: *Phys. Rev. Lett.* 8 (1 Jan. 1962), pp. 19–20. URL: https://link.aps.org/doi/10.1103/PhysRevLett.8.19.

[18] Robert C. Miller and Albert Savage. “Harmonic Generation and Mixing of $CaWO_4$: Nd^{3+} and Ruby Pulsed Laser Beams in Piezoelectric Crystals”. In: *Phys. Rev.* 128 (5 Dec. 1962), pp. 2175–2179. URL: https://link.aps.org/doi/10.1103/PhysRev.128.2175.

[19] A. W. Smith and N. Braslau. “Optical Mixing of Coherent and Incoherent Light [Letter to the Editor]”. In: *IBM Journal of Research and Development* 6.3 (1962), pp. 361–362.

[20] Archibald W. Smith and Norman Braslau. “Observation of an Optical Difference Frequency”. In: *Journal of Applied Physics* 34.7 (July 1963), pp. 2105–2106. URL: https://doi.org/10.1063/1.1729748.

[21] J. E. Bjorkholm. “Optical Second-Harmonic Generation Using a Focused Gaussian Laser Beam”. In: *Phys. Rev.* 142 (1 Feb. 1966), pp. 126–136. URL: https://link.aps.org/doi/10.1103/PhysRev.142.126.

[22] Charles C. Wang and George W. Racette. “Measurement of parametric gain accompanying optical difference frequency generation”. In: *Applied Physics Letters* 6.8 (Apr. 1965), pp. 169–171. URL: https://doi.org/10.1063/1.1754219.

[23] R. G. Smith, K. Nassau, and M. F. Galvin. “Efficient continuous optical second-harmonic generation”. In: *Applied Physics Letters* 7.10 (Nov. 1965), pp. 256–258. URL: https://doi.org/10.1063/1.1754246.

[24] J. A. Giordmaine and Robert C. Miller. “Tunable Coherent Parametric Oscillation in $LiNbO_3$ at Optical Frequencies”. In: *Phys. Rev. Lett.* 14 (24 June 1965), pp. 973–976. URL: https://link.aps.org/doi/10.1103/PhysRevLett.14.973.

[25] S. E. Harris, M. K. Oshman, and R. L. Byer. "Observation of Tunable Optical Parametric Fluorescence". In: *Phys. Rev. Lett.* 18 (18 May 1967), pp. 732–734. URL: https://link.aps.org/doi/10.1103/PhysRevLett.18.732.

[26] RG Smith et al. "Continuous optical parametric oscillation in Ba2NaNb5O15". In: *Applied Physics Letters* 12.9 (1968), pp. 308–310.

[27] R. L. Byer et al. "Visible CW paramteric oscillator". In: *Applied Physics Letters* 13.3 (Aug. 1968), pp. 109–111. URL: https://doi.org/10.1063/1.1652520.

[28] S. Brosnan and R. Byer. "Optical parametric oscillator threshold and linewidth studies". In: *IEEE Journal of Quantum Electronics* 15.6 (1979), pp. 415–431.

[29] D. E. Thompson, J. D. McMullen, and D. B. Anderson. "Second-harmonic generation in GaAs "stack of plates" using high-power CO2 laser radiation". In: *Applied Physics Letters* 29.2 (July 1976), pp. 113–115. URL: https://doi.org/10.1063/1.88989.

[30] J. P. van der Ziel et al. "Phase-matched second harmonic generation in a periodic GaAs waveguide". In: *Applied Physics Letters* 29.12 (Dec. 1976), pp. 775–777. URL: https://doi.org/10.1063/1.88945.

[31] Duan Feng et al. "Enhancement of second-harmonic generation in LiNbO3 crystals with periodic laminar ferroelectric domains". In: *Applied Physics Letters* 37.7 (Oct. 1980), pp. 607–609. URL: https://doi.org/10.1063/1.92035.

[32] A. Feisst and P. Koidl. "Current induced periodic ferroelectric domain structures in LiNbO3 applied for efficient nonlinear optical frequency mixing". In: *Applied Physics Letters* 47.11 (Dec. 1985), pp. 1125–1127. URL: https://doi.org/10.1063/1.96349.

[33] Bozena Jaskorzynska, Gunnar Arvidsson, and Fredrik Laurell. "Periodic Structures For Phase-Matching In Second Harmonic Generation In Titanium Lithium Niobate Wave Guides". In: *Integrated Optical Circuit Engineering III*. Ed. by Ralf Th. Kersten. Vol. 0651. International Society for Optics and Photonics. SPIE, 1986, pp. 221–228. URL: https://doi.org/10.1117/12.938154.

[34] J. Webjorn, F. Laurell, and G. Arvidsson. "Fabrication of periodically domain-inverted channel waveguides in lithium niobate for second harmonic generation". In: *Journal of Lightwave Technology* 7.10 (1989), pp. 1597–1600.

[35] R.L. Byer. "Second-harmonic generation of green light in periodically poled planar lithium niobate waveguide". English. In: *Electronics Letters* 25 (3 Feb. 1989), 174–175(1). URL: https://digital-library.theiet.org/content/journals/10.1049/el_19890127.

[36] M. Yamada et al. "First-order quasi-phase matched LiNbO3 waveguide periodically poled by applying an external field for efficient blue second-harmonic generation". In: *Applied Physics Letters* 62.5 (Feb. 1993), pp. 435–436. URL: https://doi.org/10.1063/1.108925.

[37] Shi-ning Zhu et al. “LiTaO3 crystal periodically poled by applying an external pulsed field”. In: *Journal of Applied Physics* 77.10 (May 1995), pp. 5481–5483. URL: https://doi.org/10.1063/1.359250.

[38] L. E. Myers et al. “Quasi-phase-matched optical parametric oscillators in bulk periodically poled LiNbO3”. In: *J. Opt. Soc. Am. B* 12.11 (Nov. 1995), pp. 2102–2116. URL: https://opg.optica.org/josab/abstract.cfm?URI=josab-12-11-2102.

[39] W. P. Risk and S. D. Lau. “Periodic electric field poling of KTiOPO4 using chemical patterning”. In: *Applied Physics Letters* 69.26 (Dec. 1996), pp. 3999–4001. URL: https://doi.org/10.1063/1.117850.

[40] A. Galvanauskas et al. “Fiber-laser-based femtosecond parametric generator in bulk periodically poled LiNbO3”. In: *Opt. Lett.* 22.2 (Jan. 1997), pp. 105–107. URL: https://opg.optica.org/ol/abstract.cfm?URI=ol-22-2-105.

[41] Ian N. Ross et al. “Generation of terawatt pulses by use of optical parametric chirped pulse amplification”. In: *Appl. Opt.* 39.15 (May 2000), pp. 2422–2427. URL: https://opg.optica.org/ao/abstract.cfm?URI=ao-39-15-2422.

[42] L. A. Eyres et al. “All-epitaxial fabrication of thick, orientation-patterned GaAs films for nonlinear optical frequency conversion”. In: *Applied Physics Letters* 79.7 (Aug. 2001), pp. 904–906. URL: https://doi.org/10.1063/1.1389326.

[43] Katia Gallo, Marc De Micheli, and Pascal Baldi. “Parametric fluorescence in periodically poled LiNbO3 buried waveguides”. In: *Applied Physics Letters* 80.24 (June 2002), pp. 4492–4494. URL: https://doi.org/10.1063/1.1486265.

[44] Xiuping Xie et al. “Picojoule threshold, picosecond optical parametric generation in reverse proton-exchanged lithium niobate waveguides”. In: *J. Opt. Soc. Am. B* 21.7 (July 2004), pp. 1397–1402. URL: https://opg.optica.org/josab/abstract.cfm?URI=josab-21-7-1397.

[45] Takao Fuji et al. “Monolithic carrier-envelope phase-stabilization scheme”. In: *Opt. Lett.* 30.3 (Feb. 2005), pp. 332–334. URL: https://opg.optica.org/ol/abstract.cfm?URI=ol-30-3-332.

[46] Carsten Langrock et al. “Generation of octave-spanning spectra inside reverse-proton-exchanged periodically poled lithium niobate waveguides”. In: *Opt. Lett.* 32.17 (Sept. 2007), pp. 2478–2480. URL: https://opg.optica.org/ol/abstract.cfm?URI=ol-32-17-2478.

[47] Alireza Marandi et al. “Coherence properties of a broadband femtosecond mid-IR optical parametric oscillator operating at degeneracy”. In: *Opt. Express* 20.7 (Mar. 2012), pp. 7255–7262. URL: https://opg.optica.org/oe/abstract.cfm?URI=oe-20-7-7255.

[48] Alireza Marandi et al. “Network of time-multiplexed optical parametric oscillators as a coherent Ising machine”. In: *Nature Photonics* 8.12 (Dec. 2014), pp. 937–942. URL: https://doi.org/10.1038/nphoton.2014.249.

[49] Kenta Takata et al. “A 16-bit Coherent Ising Machine for One-Dimensional Ring and Cubic Graph Problems”. In: *Scientific Reports* 6.1 (Sept. 2016), p. 34089. URL: https://doi.org/10.1038/srep34089.

[50] Peter L. McMahon et al. “A fully programmable 100-spin coherent Ising machine with all-to-all connections”. In: *Science* 354.6312 (2016), pp. 614–617. URL: https://www.science.org/doi/full/10.1126/science.aah5178 (visited on 02/14/2022).

[51] Takahiro Inagaki et al. “A coherent Ising machine for 2000-node optimization problems”. In: *Science* 354.6312 (2016), pp. 603–606. URL: https://www.science.org/doi/full/10.1126/science.aah4243 (visited on 02/14/2022).

[52] Toshimori Honjo et al. “100,000-spin coherent Ising machine”. In: *Science Advances* 7.40 (2021), eabh0952. URL: https://www.science.org/doi/abs/10.1126/sciadv.abh0952.

[53] R. Soref and J. Larenzo. “All-silicon active and passive guided-wave components for λ = 1.3 and 1.6 μm”. In: *IEEE Journal of Quantum Electronics* 22.6 (1986), pp. 873–879.

[54] C. H. Henry et al. “Low loss Si3N4–SiO2 optical waveguides on Si”. In: *Appl. Opt.* 26.13 (July 1987), pp. 2621–2624. URL: https://opg.optica.org/ao/abstract.cfm?URI=ao-26-13-2621.

[55] C.H. Henry, G.E. Blonder, and R.F. Kazarinov. “Glass waveguides on silicon for hybrid optical packaging”. In: *Journal of Lightwave Technology* 7.10 (1989), pp. 1530–1539.

[56] H. Morita. “Low loss mode size converter from 0.3 μm square Si wire waveguides to singlemode fibres”. English. In: *Electronics Letters* 38 (25 Dec. 2002), 1669–1670(1). URL: https://digital-library.theiet.org/content/journals/10.1049/el_20021185.

[57] Ansheng Liu et al. “A high-speed silicon optical modulator based on a metal–oxide–semiconductor capacitor”. In: *Nature* 427.6975 (Feb. 2004), pp. 615–618. URL: https://doi.org/10.1038/nature02310.

[58] Yurii A. Vlasov and Sharee J. McNab. “Losses in single-mode silicon-on-insulator strip waveguides and bends”. In: *Opt. Express* 12.8 (Apr. 2004), pp. 1622–1631. URL: https://opg.optica.org/oe/abstract.cfm?URI=oe-12-8-1622.

[59] Rachel Won. “Integrating silicon photonics”. In: *Nature Photonics* 4.8 (Aug. 2010), pp. 498–499. URL: https://doi.org/10.1038/nphoton.2010.189.

[60] Mian Zhang et al. “Monolithic ultra-high-Q lithium niobate microring resonator”. In: *Optica* 4.12 (Dec. 2017), pp. 1536–1537. URL: https://opg.optica.org/optica/abstract.cfm?URI=optica-4-12-1536.

[61] Yichen Shen et al. “Deep learning with coherent nanophotonic circuits”. In: *Nature Photonics* 11.7 (July 2017), pp. 441–446. URL: https://doi.org/10.1038/nphoton.2017.93.

[62] Cheng Wang et al. “Integrated lithium niobate electro-optic modulators operating at CMOS-compatible voltages”. In: *Nature* 562.7725 (Oct. 2018), pp. 101–104. URL: https://doi.org/10.1038/s41586-018-0551-y.

[63] Hiroshi Fukuda et al. “Four-wave mixing in silicon wire waveguides”. In: *Opt. Express* 13.12 (June 2005), pp. 4629–4637. URL: https://opg.optica.org/oe/abstract.cfm?URI=oe-13-12-4629.

[64] Mark A. Foster et al. “Broad-band optical parametric gain on a silicon photonic chip”. In: *Nature* 441.7096 (June 2006), pp. 960–963. URL: https://doi.org/10.1038/nature04932.

[65] I-Wei Hsieh et al. “Supercontinuum generation in silicon photonic wires”. In: *Opt. Express* 15.23 (Nov. 2007), pp. 15242–15249. URL: https://opg.optica.org/oe/abstract.cfm?URI=oe-15-23-15242.

[66] Kazuhiro Ikeda et al. “Thermal and Kerr nonlinear properties of plasma-deposited silicon nitride/silicon dioxide waveguides”. In: *Opt. Express* 16.17 (Aug. 2008), pp. 12987–12994. URL: https://opg.optica.org/oe/abstract.cfm?URI=oe-16-17-12987.

[67] B. Corcoran et al. “Green light emission in silicon through slow-light enhanced third-harmonic generation in photonic-crystal waveguides”. In: *Nature Photonics* 3.4 (Apr. 2009), pp. 206–210. URL: https://doi.org/10.1038/nphoton.2009.28.

[68] Jacob S. Levy et al. “CMOS-compatible multiple-wavelength oscillator for on-chip optical interconnects”. In: *Nature Photonics* 4.1 (Jan. 2010), pp. 37–40. URL: https://doi.org/10.1038/nphoton.2009.259.

[69] V. Brasch et al. “Photonic chip–based optical frequency comb using soliton Cherenkov radiation”. In: *Science* 351.6271 (2016), pp. 357–360. URL: https://www.science.org/doi/abs/10.1126/science.aad4811.

[70] Martin H. P. Pfeiffer et al. “Photonic Damascene process for integrated high-Q microresonator based nonlinear photonics”. In: *Optica* 3.1 (Jan. 2016), pp. 20–25. URL: https://opg.optica.org/optica/abstract.cfm?URI=optica-3-1-20.

[71] David R. Carlson et al. “Photonic-Chip Supercontinuum with Tailored Spectra for Counting Optical Frequencies”. In: *Phys. Rev. Appl.* 8 (1 July 2017), p. 014027. URL: https://link.aps.org/doi/10.1103/PhysRevApplied.8.014027.

[72] Dong Yoon Oh et al. “Coherent ultra-violet to near-infrared generation in silica ridge waveguides”. In: *Nature Communications* 8.1 (Jan. 2017), p. 13922. URL: https://doi.org/10.1038/ncomms13922.

[73] Jae K. Jang et al. “Synchronization of coupled optical microresonators”. In: *Nature Photonics* 12.11 (Nov. 2018), pp. 688–693. URL: https://doi.org/10.1038/s41566-018-0261-x.

[74] Miles H. Anderson et al. “Zero dispersion Kerr solitons in optical microresonators”. In: *Nature Communications* 13.1 (Aug. 2022), p. 4764. URL: https://doi.org/10.1038/s41467-022-31916-x.

[75] Cheng Wang et al. "Ultrahigh-efficiency wavelength conversion in nanophotonic periodically poled lithium niobate waveguides". In: *Optica* 5.11 (Nov. 2018), pp. 1438–1441. URL: https://www.osapublishing.org/optica/abstract.cfm?uri=optica-5-11-1438 (visited on 03/03/2019).

[76] Marc Jankowski et al. "Ultrabroadband nonlinear optics in nanophotonic periodically poled lithium niobate waveguides". In: *Optica* 7.1 (Jan. 2020), pp. 40–46. URL: https://www.osapublishing.org/optica/abstract.cfm?uri=optica-7-1-40 (visited on 01/18/2020).

[77] Luis Ledezma†, **Ryoto Sekine**†, Qiushi Guo†, Rajveer Nehra, Saman Jahani, and Alireza Marandi. "Intense optical parametric amplification in dispersion-engineered nanophotonic lithium niobate waveguides". In: *Optica* 9.3 (Mar. 2022), pp. 303–308. URL: https://opg.optica.org/optica/abstract.cfm?URI=optica-9-3-303.

[78] Luis Ledezma, Arkadev Roy, Luis Costa, **Ryoto Sekine**, Robert Gray, Qiushi Guo, Rajveer Nehra, Ryan M. Briggs, and Alireza Marandi. "Octave-spanning tunable infrared parametric oscillators in nanophotonics". In: *Science Advances* 9.30 (2023), eadf9711. URL: https://www.science.org/doi/abs/10.1126/sciadv.adf9711.

[79] Arkadev Roy†, Luis Ledezma†, Luis Costa, Robert Gray, **Ryoto Sekine**, Qiushi Guo, Mingchen Liu, Ryan M. Briggs, and Alireza Marandi. "Visible-to-mid-IR tunable frequency comb in nanophotonics". In: *Nature Communications* 14.1 (Oct. 2023), p. 6549. URL: https://doi.org/10.1038/s41467-023-42289-0.

[80] Qiushi Guo, Benjamin K. Gutierrez, **Ryoto Sekine**, Robert M. Gray, James A. Williams, Luis Ledezma, Luis Costa, Arkadev Roy, Selina Zhou, Mingchen Liu, and Alireza Marandi. "Ultrafast mode-locked laser in nanophotonic lithium niobate". In: *Science* 382.6671 (2023), pp. 708–713. URL: https://www.science.org/doi/abs/10.1126/science.adj5438.

[81] Charles H. Townes. "Theodore H. Maiman (1927–2007)". In: *Nature* 447.7145 (June 2007), pp. 654–654. URL: https://doi.org/10.1038/447654a.

[82] John A. Armstrong et al. "Interactions between light waves in a nonlinear dielectric". In: *Physical Review* 127 (1962), pp. 1918–1939. URL: https://api.semanticscholar.org/CorpusID:53491675.

[83] A. Yariv. *Quantum Electronics*. Wiley, 1967. URL: https://books.google.com/books?id=ZSBRAAAAMAAJ.

[84] Govind P. Agrawal. *Nonlinear fiber optics*. Academic Press, 1989.

[85] Robert W. Boyd. *Nonlinear Optics*. Academic Press, 1992.

[86] F. J. McClung and R. W. Hellwarth. "Giant Optical Pulsations from Ruby". In: *Journal of Applied Physics* 33.3 (Mar. 1962), pp. 828–829. URL: https://doi.org/10.1063/1.1777174.

[87] L. E. Hargrove, R. L. Fork, and M. A. Pollack. "Locking of He–Ne laser modes induced by synchronous intracavity modulation". In: *Applied Physics Letters* 5.1 (July 1964), pp. 4–5. URL: https://doi.org/10.1063/1.1754025.

[88] Robert L. Byer. "Parametric Oscillators and Nonlinear Materials". In: *Nonlinear Optics*. Ed. by Phillip G. Harper and Brian S. Wherrett. New York: Academic Press, 1975. Chap. 2, pp. 47–160.

[89] G. D. Boyd and D. A. Kleinman. "Parametric Interaction of Focused Gaussian Light Beams". In: *Journal of Applied Physics* 39.8 (July 1968), pp. 3597–3639. URL: https://doi.org/10.1063/1.1656831.

[90] Marc Jankowski, Jatadhari Mishra, and M M Fejer. "Dispersion-engineered $\chi^{(2)}$ nanophotonics: a flexible tool for nonclassical light". In: *Journal of Physics: Photonics* 3.4 (Sept. 2021), p. 042005. URL: https://dx.doi.org/10.1088/2515-7647/ac1729.

[91] Y. Furukawa et al. "Green-induced infrared absorption in MgO doped LiNbO3". In: *Applied Physics Letters* 78.14 (Apr. 2001), pp. 1970–1972. URL: https://doi.org/10.1063/1.1359137.

[92] H. Mabuchi, E. S. Poizik, and H. J. Kimble. "Blue-light-induced infrared absorption in KNbO3". In: *J. Opt. Soc. Am. B* 11.10 (Oct. 1994), pp. 2023–2029. URL: https://opg.optica.org/josab/abstract.cfm?URI=josab-11-10-2023.

[93] A.G. Astill. "Material figures of merit for non-linear optics". In: *Thin Solid Films* 204.1 (1991), pp. 1–17. URL: https://www.sciencedirect.com/science/article/pii/004060909190489K.

[94] Di Zhu et al. "Integrated photonics on thin-film lithium niobate". In: *Adv. Opt. Photon.* 13.2 (June 2021), pp. 242–352. URL: https://opg.optica.org/aop/abstract.cfm?URI=aop-13-2-242.

[95] Avik Dutt et al. "Nonlinear and quantum photonics using integrated optical materials". In: *Nature Reviews Materials* 9.5 (May 2024), pp. 321–346. URL: https://doi.org/10.1038/s41578-024-00668-z.

[96] Alexander L. Gaeta, Michal Lipson, and Tobias J. Kippenberg. "Photonic-chip-based frequency combs". In: *Nature Photonics* 13.3 (Mar. 2019), pp. 158–169. URL: https://doi.org/10.1038/s41566-019-0358-x.

[97] Robert C. Miller. "Optical second harmonic generation in piezoelectric crystals". In: *Applied Physics Letters* 5.1 (July 1964), pp. 17–19. URL: https://doi.org/10.1063/1.1754022.

[98] D. A. Kleinman. "Nonlinear Dielectric Polarization in Optical Media". In: *Phys. Rev.* 126 (6 June 1962), pp. 1977–1979. URL: https://link.aps.org/doi/10.1103/PhysRev.126.1977.

[99] P. D. Maker et al. "Effects of Dispersion and Focusing on the Production of Optical Harmonics". In: *Phys. Rev. Lett.* 8 (1 Jan. 1962), pp. 21–22. URL: https://link.aps.org/doi/10.1103/PhysRevLett.8.21.

[100] M.M. Fejer et al. "Quasi-phase-matched second harmonic generation: tuning and tolerances". In: *IEEE Journal of Quantum Electronics* 28.11 (1992), pp. 2631–2654.

[101] Xiaoyi Xu et al. "Femtosecond laser writing of lithium niobate ferroelectric nanodomains". In: *Nature* 609.7927 (Sept. 2022), pp. 496–501. URL: https://doi.org/10.1038/s41586-022-05042-z.

[102] Haoyang Du et al. “Highly efficient, modal phase-matched second harmonic generation in a double-layered thin film lithium niobate waveguide”. In: *Opt. Express* 31.6 (Mar. 2023), pp. 9713–9726. URL: https://opg.optica.org/oe/abstract.cfm?URI=oe-31-6-9713.

[103] Edgars Nitiss et al. “Optically reconfigurable quasi-phase-matching in silicon nitride microresonators”. In: *Nature Photonics* 16.2 (Feb. 2022), pp. 134–141. URL: https://doi.org/10.1038/s41566-021-00925-5.

[104] Xiyuan Lu et al. “Efficient photoinduced second-harmonic generation in silicon nitride photonics”. In: *Nature Photonics* 15.2 (Feb. 2021), pp. 131–136. URL: https://doi.org/10.1038/s41566-020-00708-4.

[105] R. V. Schmidt and I. P. Kaminow. “Metal-diffused optical waveguides in LiNbO3”. In: *Applied Physics Letters* 25.8 (Oct. 1974), pp. 458–460. URL: https://doi.org/10.1063/1.1655547.

[106] J. L. Jackel, C. E. Rice, and J. J. Veselka. “Proton exchange for high-index waveguides in LiNbO3”. In: *Applied Physics Letters* 41.7 (Oct. 1982), pp. 607–608. URL: https://doi.org/10.1063/1.93615.

[107] C. Langrock et al. “All-optical signal processing using /spl chi//sup (2)/ nonlinearities in guided-wave devices”. In: *Journal of Lightwave Technology* 24.7 (2006), pp. 2579–2592.

[108] Marc Jankowski et al. “Ultrabroadband nonlinear optics in nanophotonic periodically poled lithium niobate waveguides”. In: *Optica* 7.1 (Jan. 2020), pp. 40–46. URL: https://opg.optica.org/optica/abstract.cfm?URI=optica-7-1-40.

[109] Covesion. *Example uses of PPLN: Second Harmonic Generation*. Nov. 2020. URL: https://covesion.com/en/resource/example-uses-of-ppln/.

[110] Cheng Wang et al. “Ultrahigh-efficiency wavelength conversion in nanophotonic periodically poled lithium niobate waveguides”. In: *Optica* 5.11 (Nov. 2018), pp. 1438–1441. URL: https://opg.optica.org/optica/abstract.cfm?URI=optica-5-11-1438.

[111] Elsa Garmire. “Nonlinear optics in daily life”. In: *Opt. Express* 21.25 (Dec. 2013), pp. 30532–30544. URL: https://opg.optica.org/oe/abstract.cfm?URI=oe-21-25-30532.

[112] Mengjie Yu et al. “Integrated femtosecond pulse generator on thin-film lithium niobate”. In: *Nature* 612.7939 (Dec. 2022), pp. 252–258. URL: https://doi.org/10.1038/s41586-022-05345-1.

[113] Alireza Marandi et al. “Network of time-multiplexed optical parametric oscillators as a coherent Ising machine”. In: *Nature Photonics* 8.12 (2014), pp. 937–942. URL: https://www.nature.com/articles/nphoton.2014.249 (visited on 02/07/2022).

[114] Arkadev Roy. “Parametrically-driven nonlinear optical resonators and their networks for sensing and computing”. PhD thesis. California Institute of Technology, 2023.

[115] Gordon Li et al. *Time-multiplexed photonic computer*. US20240061316A1. 2023. URL: https://patents.google.com/patent/US20240061316A1/en.

[116] Cheng Wang et al. "Integrated lithium niobate electro-optic modulators operating at CMOS-compatible voltages". In: *Nature* 562.7725 (2018), pp. 101–104.

[117] Ayed Al Sayem et al. "Lithium-niobate-on-insulator waveguide-integrated superconducting nanowire single-photon detectors". In: *Applied Physics Letters* 116.15 (2020), p. 151102.

[118] Amnon Zalman Yariv. "On a class of bimodal oscillations powered by a steady, zero-frequency force—Implications to energy conversion and structural stability". In: *Applied Physical Sciences* 120.38 (Sept. 2023). URL: https://www.pnas.org/doi/full/10.1073/pnas.2311412120.

[119] Nathan A. Harper†, Emily Y. Hwang†, **Ryoto Sekine**, Luis Ledezma, Christian Perez, Alireza Marandi, and Scott K. Cushing. "Highly efficient visible and near-IR photon pair generation with thin-film lithium niobate". In: *Optica Quantum* 2.2 (Apr. 2024), pp. 103–109. URL: https://opg.optica.org/opticaq/abstract.cfm?URI=opticaq-2-2-103.

[120] **Ryoto Sekine**†, Robert Gray†, Luis Ledezma, Qiushi Guo, and Alireza Marandi. "Sync-pumped femtosecond OPO based on dispersion-engineered nanophotonic PPLN with 3-octave spectrum". In: *Conference on Lasers and Electro-Optics*. Optica Publishing Group, 2022, SM5K.2. URL: https://opg.optica.org/abstract.cfm?URI=CLEO_SI-2022-SM5K.2.

[121] Prashanta Kharel et al. "Breaking voltage–bandwidth limits in integrated lithium niobate modulators using micro-structured electrodes". In: *Optica* 8.3 (Mar. 2021), pp. 357–363. URL: https://opg.optica.org/optica/abstract.cfm?URI=optica-8-3-357.

[122] Mian Zhang et al. "Integrated lithium niobate electro-optic modulators: when performance meets scalability". In: *Optica* 8.5 (May 2021), pp. 652–667. URL: https://opg.optica.org/optica/abstract.cfm?URI=optica-8-5-652.

[123] James Williams et al. In: *Nanophotonics* (2024). URL: https://doi.org/10.1515/nanoph-2024-0054.

[124] Emily Hwang†, Nathan Harper†, **Ryoto Sekine**, Luis Ledezma, Alireza Marandi, and Scott Cushing. "Tunable and efficient ultraviolet generation with periodically poled lithium niobate". In: *Optics Letters* 48.15 (Aug. 2023), pp. 3917–3920. URL: https://opg.optica.org/ol/abstract.cfm?URI=ol-48-15-3917.

[125] Robert Gray, Thomas Zacharias, Rahul Chawlani, Luis Ledezma, **Ryoto Sekine**, James Williams, and Alireza Marandi. "Soliton pulse compression in lithium niobate nanophotonics". In: *Conference on Lasers and Electro-Optics*. 2024, SM3Q.6.

[126] Cheng Wang et al. "Integrated high quality factor lithium niobate microdisk resonators". In: *Opt. Express* 22.25 (Dec. 2014), pp. 30924–30933. URL:

https://opg.optica.org/oe/abstract.cfm?URI=oe-22-25-30924.

[127] Ivy I. Chen, Jennifer Solgaard, **Ryoto Sekine**, Azmain A. Hossain, Anthony Ardizzi, David S. Catherall, Alireza Marandi, James R. Renzas, Frank Greer, and Austin J. Minnich. "Directional atomic layer etching of MgO-doped lithium niobate using sequential exposures of H_2 and SF_6 plasma". In: *arXiv* (2023). URL: https://arxiv.org/abs/2310.10592.

[128] Carter Mashburn, Kristina Chang, Tsung-Han Wu, Luis Ledezma, **Ryoto Sekine**, Alireza Marandi, and Scott Diddams. "Towards UV-visible dual-comb spectroscopy with lithium niobate nanophotonic waveguides". In: *Conference on Lasers and Electro-Optics*. 2024, SW4F.3.

[129] Takahiro Kashiwazaki et al. "Continuous-wave 6-dB-squeezed light with 2.5-THz-bandwidth from single-mode PPLN waveguide". In: *APL Photonics* 5.3 (2020), p. 036104.

[130] Mian Zhang et al. "Monolithic ultra-high-Q lithium niobate microring resonator". In: *Optica* 4.12 (2017), pp. 1536–1537.

[131] Arkadev Roy et al. "Temporal walk-off induced dissipative quadratic solitons". In: *Nature Photonics* 16.2 (Feb. 2022), pp. 162–168. URL: https://doi.org/10.1038/s41566-021-00942-4.

[132] Nicolas Englebert, Robert Gray, **Ryoto Sekine**, Thomas Zacharias, Luis Ledezma, Selina Zhou, Carlos Mas Arabi, Simon-Pierre Gorza, François Leo, and Alireza Marandi. "Purely quadratic cavity solitons in a nanophotonic parametric oscillator". In: *Conference on Lasers and Electro-Optics*. 2024, STh3I.1.

[133] Scott A. Diddams, Kerry Vahala, and Thomas Udem. "Optical frequency combs: Coherently uniting the electromagnetic spectrum". In: *Science* 369.6501 (2020), eaay3676. URL: https://www.science.org/doi/abs/10.1126/science.aay3676.

[134] Lin Chang, Songtao Liu, and John E. Bowers. "Integrated optical frequency comb technologies". In: *Nature Photonics* 16.2 (Feb. 2022), pp. 95–108. URL: https://doi.org/10.1038/s41566-021-00945-1.

[135] Brian Stern et al. "Battery-operated integrated frequency comb generator". In: *Nature* 562.7727 (Oct. 2018), pp. 401–405. URL: https://doi.org/10.1038/s41586-018-0598-9.

[136] Harry F. Jordan and Vincent P. Heuring. "Time Multiplexed Optical Computers". In: *Proceedings of the 1991 ACM/IEEE Conference on Supercomputing*. Supercomputing '91. Albuquerque, New Mexico, USA: Association for Computing Machinery, 1991, pp. 370–378. URL: https://doi.org/10.1145/125826.126033.

[137] Marcello Calvanese Strinati and Claudio Conti. "Multidimensional hyperspin machine". In: *Nature Communications* 13.1 (Nov. 2022), p. 7248. URL: https://doi.org/10.1038/s41467-022-34847-9.

[138] Victor I Kopp and ON Alekseyev. "Optical neuron network based on ax (2) hologram recording". In: *Second International Conference on Optical Information Processing*. Vol. 2969. SPIE. 1996, pp. 104–107.

[139] Logan G Wright et al. “Deep physical neural networks trained with backpropagation”. In: *Nature* 601.7894 (2022), pp. 549–555.

[140] Gordon H. Y. Li et al. “Photonic elementary cellular automata for simulation of complex phenomena”. In: *Light: Science & Applications* 12.1 (May 2023), p. 132. URL: https://doi.org/10.1038/s41377-023-01180-9.

Chapter 2

INTENSE, BROADBAND, PHASE-SENSITIVE GAIN

Luis Ledezma[†], **Ryoto Sekine**[†], Qiushi Guo[†], Rajveer Nehra, Saman Jahani, and Alireza Marandi, "Intense optical parametric amplification in dispersion-engineered nanophotonic lithium niobate waveguides," *Optica*, 9, 303-308 (2022).
R.S. performed the measurements, assisted the fabrication development, and participated in writing of the manuscript.
[†] denotes equal contributions

2.1 Abstract

Strong amplification in integrated photonics is one of the most desired optical functionalities for computing, communications, sensing, and quantum information processing. Semiconductor gain and cubic nonlinearities, such as four-wave mixing and stimulated Raman and Brillouin scattering, have been among the most studied amplification mechanisms on chip. Alternatively, material platforms with strong quadratic nonlinearities promise numerous advantages with respect to gain and bandwidth, among which nanophotonic lithium niobate is one of the most promising candidates. Here, we combine quasi-phase matching with dispersion engineering in nanophotonic lithium niobate waveguides and achieve intense optical parametric amplification. We measure a broadband phase-sensitive on-chip amplification larger than 50 dB/cm in a 6-mm-long waveguide. We further confirm high gain operation in the degenerate and non-degenerate regimes by amplifying vacuum fluctuations to macroscopic levels, with on-chip gains exceeding 100 dB/cm over 600 nm of bandwidth around 2 μm. Our results unlock new possibilities for on-chip few-cycle nonlinear optics, mid-infrared photonics, and quantum photonics.

2.2 Introduction

Amplification is an important element of a wide range of optical systems, from computing [1] and sensing [2] to quantum information processing [3] and communications [4]. In integrated photonics, achieving intense amplification remains an important challenge. In silicon-based platforms, significant attention has been focused on cubic nonlinearities to realize amplification through four-wave mixing (FWM) [5, 6], stimulated Raman scattering (SRS) [7], and stimulated Brillouin scattering (SBS) [8]. Despite recent promising advances, the weak nature of these nonlinearities and the adverse effects of other competing nonlinearities hamper the amount of gain and bandwidths associated with these mechanisms. Another option providing gain on integrated platforms is the semiconductor optical amplifier (SOA). SOAs have evolved in the past decades as one of the leading optical gain mechanisms [9, 10], and heterogeneous integration of III-V SOAs with other platforms, especially silicon, has been one of the most active research directions in integrated photonics [10]. However, their limited bandwidth and integration challenges hin-

der their utilization in several applications, such as those that require accessing gain in multiple places on a chip. Furthermore, semiconductor gain is not phase-sensitive, limiting its use in quantum and communication applications that require noiseless amplification, e.g., processing of quantum microcombs [11] and few-cycle squeezed vacuum [12]. Hence, an integrated platform with a native gain mechanism that enables intense and phase-sensitive optical amplification of ultra-short pulses can address several of the current challenges in photonics.

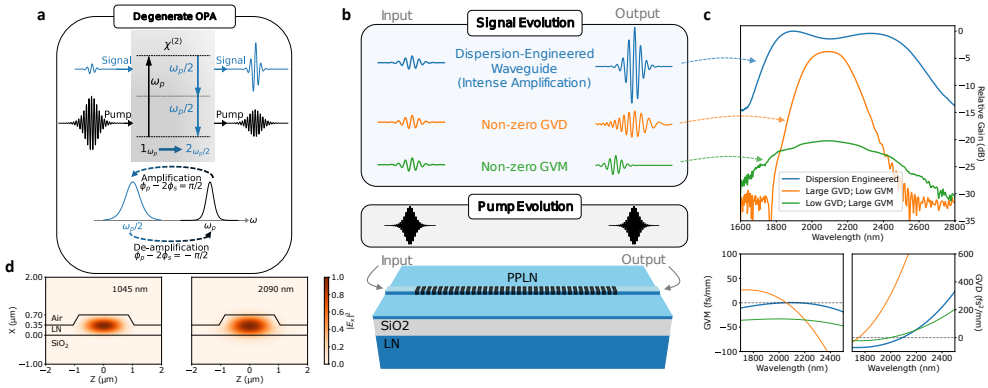

Figure 2.1: **Parametric amplification in dispersion-engineered PPLN waveguides. a**, In degenerate optical parametric amplification through three-wave mixing in a $\chi^{(2)}$ medium, energy is transferred from the pump at ω_p to signal at $\omega_p/2$, providing amplification for the signal. When the relative phase between pump and signal changes by π, the flow of energy reverses, resulting in deamplification of the signal. **b**, In a PPLN waveguide, group velocity dispersion (GVD) leads to pulse temporal spreading with a decrease in peak power and gain, while group velocity mismatch (GVM) causes temporal walk-off between the pump and signal pulses reducing their interaction. Hence engineering the waveguides for low GVD and GVM is necessary to maximize the OPA performance. **c**, Simulated relative gain spectrum for the three dispersion cases shown in **b** in a 6-mm-long waveguide with 75-fs pump pulses, along with the simulated GVM (with respect to the pump at 1045 nm) and GVD. The dispersion-engineered lithium niobate waveguide (blue trace) exhibits low GVM between the pump at 1045 nm and the signal around 2090 nm, and low GVD for both wavelengths, and it has a top width of 1,700 nm, an etch depth of 350 nm and total thin-film thickness of 700 nm. The orange trace represents a waveguide with low GVM but large GVD (900-nm top width, 680-nm thickness, 420-nm etch depth), while the green trace is for a waveguide with low GVD but large GVM (3-μm top width, 750-nm thickness, 150-nm etch depth). **d**, Electric field profiles of the fundamental quasi-TE modes for the dispersion-engineered waveguide at the pump and signal wavelengths.

Quadratic nonlinearities provide an alternative path for achieving strong optical amplification through three-wave mixing [13, 14]. Such processes have been extensively used in bulk optical systems leading to amplification at wavelengths

where other gain mechanisms are not easily available [15, 16]. Recently, integrated photonic platforms with strong quadratic nonlinearities have attracted significant attention since they can provide a range of functionalities unavailable in other platforms [17, 18, 19, 20]. Examples of these processes include second harmonic and supercontinuum generation [21, 22], electro-optic modulation [23, 24], quadratic parametric oscillators [25, 26], and bright sources of entangled photons [27]. Despite the recent significant progress, realization of intense optical amplification in quadratically nonlinear integrated photonics has remained elusive.

In integrated photonics, strong quadratic nonlinear interactions have been enabled by tight spatial confinement of the waveguide modes and the possibility to provide momentum conservation through modal [28] or quasi-phase matching [21, 22]. Further enhancement has also been achieved by utilization of appropriate resonators [25, 26], however, resonant dynamics associated with the cavity lifetime are typically not appropriate for amplification in many applications as they limit the gain bandwidth.

In this work, we present an integrated, high-gain, broadband, traveling-wave, optical parametric amplifier based on quadratic nonlinearities. We show phase-sensitive amplification by operating the amplifier at degeneracy. The large parametric gain of our device is enough to amplify quantum fluctuations to macroscopic levels, therefore allowing the amplifier to function as an optical parametric generator of infrared radiation. Our design strategy is based on quasi-phase matching combined with spatio-temporal confinement of pulses in dispersion-engineered lithium niobate waveguides; a combination that is not easily available on other nonlinear photonic platforms.

2.3 Device Design and Fabrication

We focus on optical parametric amplification (OPA) at degeneracy through three-wave mixing in a $\chi^{(2)}$ waveguide (Fig. 2.1a). As shown in Fig. 2.1b, for efficient short-pulse OPA, negligible group velocity dispersion (GVD) at the signal and pump wavelengths (ω_s and ω_p) are required to preserve the temporal confinement of these pulses and hence their high peak intensities along the waveguide. Additionally, in quadratic parametric processes, the group velocity mismatch (GVM) between the pump and signal frequencies needs to be minimized so that both pulses travel together along the waveguide, maximizing their parametric interaction. The effects of GVD and GVM on the OPA gain spectrum are shown in Fig. 2.1c for a 6-mm-long waveguide for three different waveguide geometries. These numerical simulations confirm the importance of dispersion engineering for maximizing the gain and bandwidth of OPA around degeneracy.

We design our waveguides for degenerate OPA of signal wavelengths around 2 μm, with a pump centered at 1045 nm. The GVD and GVM we obtain is marked as "dispersion-engineered" in Fig. 2.1c, where we also show the corresponding curves for non-zero GVD and non-zero GVM cases. For a 35-fs-long signal pulse, the optimized waveguide has a dispersion length of more than 30 mm at 2090 nm, and a walk-off length between the pump (1045 nm) and the signal (2090 nm) of

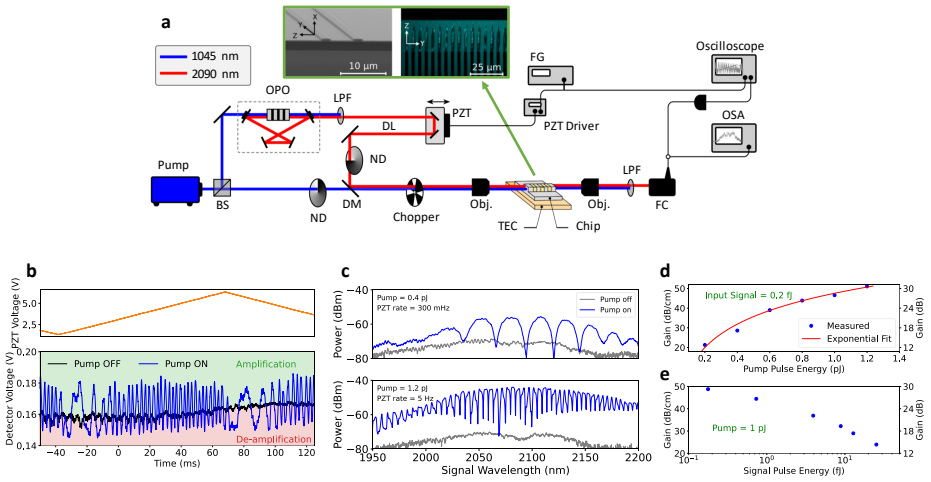

Figure 2.2: **Small-signal gain of the degenerate OPA. a**, Short-pulse OPA measurement setup; we use ~75-fs pump pulses and ~35-fs signal pulses (generated from a free-space OPO) to characterize the OPA in a dispersion-engineered PPLN waveguide. The insets show an SEM image of the chip facets after polishing and a second-harmonic microscope image of the periodic poling before waveguide fabrication. BS: beam splitter, OPO: optical parametric oscillator, LPF: long pass filter, DL: optical delay line, PZT: piezoelectric transducer, ND: variable neutral density filter, DM: dichroic mirror, Obj.: reflective objective, TEC: thermoelectric cooling stage, FC: fiber coupler, OSA: optical spectrum analyzer. **b**, Top: triangular voltage driving the PZT in the delay line. Bottom: measured detector output with and without the pump. Ripples demonstrate phase-sensitive amplification of the entire signal pulse. **c**, Measured signal spectrum with and without the pump. Scanning the signal phase while acquiring the spectrum produces ripples due to the phase-sensitive nature of the amplification. **d**, Measured gain versus pump pulse energy along with the expected exponential behavior. Input signal pulse energy in the waveguide is fixed at 0.2 fJ. **e**, Measured gain versus input signal pulse energy for 1 pJ pump pulse energy showing evidence of gain saturation over the entire range of signal energies measured.

almost 100 mm. In comparison, other cases in Fig. 2.1c correspond to a waveguide with non-zero GVD, which has a dispersion length of 2 mm at 2090 nm, and a non-zero GVM waveguide with a 1 mm walk-off length. Beyond temporal confinement, nanophotonic waveguides also enable sub-wavelenth spatial confinement. Fig. 2.1d shows the profiles of the fundamental quasi-TE modes of the waveguide for the pump and signal wavelengths. The similarity of both field distributions produces a large modal overlap and a strong nonlinear interaction (see Section 2.6.1) leading to intense amplification.

With this dispersion-engineered waveguide, where pump and signal pulses co-propagate at the same group velocity with negligible linear distortion, one can approximate the parametric process with a continuous wave model [22] (see also

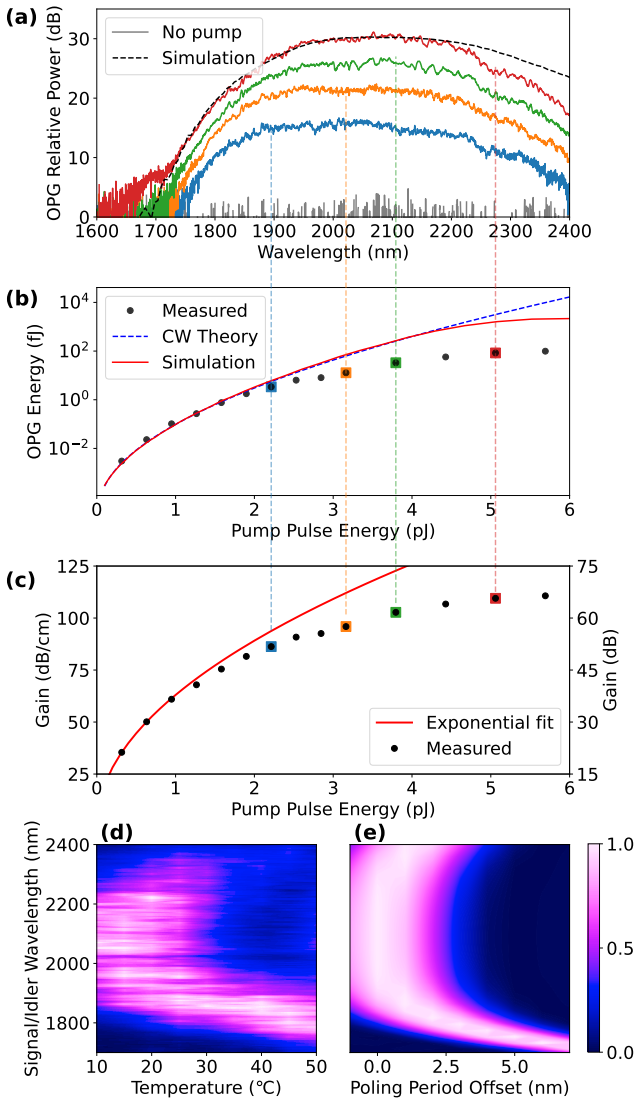

Figure 2.3: **Measurements in the large-gain regime through optical parametric generation.** **a**, OPG spectra for different pump energies. Dashed line is average of 100 numerical simulations using a semi-classical quantum noise seed in a nonlinear envelope model (see Section 2.6.4). The OPG power is referenced to the noise floor of the analyzer. **b**, OPG pulse energy versus pump pulse energy in the waveguide for a 6-mm-long device. **c**, Extracted gain versus pump pulse energy showing values exceeding 100 dB/cm. **d**, Measured normalized OPG spectra in linear units as a function of chip temperature. **e**, Simulated normalized gain in linear units as a function of signal/idler wavelength and quasi-phase matching poling period offset from nominal (see Section 2.6.1).

Section 2.6.3). At degeneracy, the pump frequency is twice the signal frequency, leading to phase-sensitive amplification. A signal with the correct phase with respect to the pump (Fig. 2.1a) is amplified by a factor of $\exp(2gL)$ in a device of

length L. The gain parameter is $g = \sqrt{\eta P_{\text{pump}} - (\Delta k/2)^2}$, where P_{pump} is the pump power, η is the nonlinear efficiency, and Δk is the phase mismatch after quasi-phase matching ($\Delta k = \beta_p - 2\beta_s - 2\pi/\Lambda$), with a constant poling period Λ. When the relative phase between signal and pump is changed by π, the device transitions from a degenerate OPA to a second harmonic generator with energy flowing from the signal to the pump (Fig. 2.1a), resulting in de-amplification of the signal by a factor of $\exp(-2gL)$.

To fabricate the device, we use a commercial wafer (NANOLN), with a 700-nm-thick X-cut MgO-doped LN thin-film on 2-μm-thick SiO_2. We start with periodic poling of the chip followed by waveguide patterning and dry etching with Ar^+ plasma. Insets of Fig. 2.2a show a scanning electron microscope (SEM) image of a pair of waveguides near the chip facet, and a second-harmonic microscope image of the periodic poling before waveguide etching. Additional fabrication details are included in Section 2.6.5.

2.4 Results and Discussion

2.4.1 Optical Parametric Amplification

We measured the small-signal gain of a 6-mm-long dispersion-engineered periodically poled lithium niobate (PPLN) waveguide with the setup shown in Fig. 2.2a. The chip temperature was set to 15 °C using a thermoelectric cooling stage (TEC) to optimize the phase matching condition. The OPA pump pulses are ~75-fs-long, from a mode-locked fiber laser centered at 1045 nm. The signal pulses are ~35-fs-long centered at 2090 nm generated from a table-top degenerate optical parametric oscillator [29]. The pump and signal pulses are coupled into the same PPLN waveguide using a reflective objective. The phase difference between pump and signal is scanned by a piezoelectric transducer (PZT) in a delay arm, and the transmitted signal is measured with a 2 μm detector followed by an oscilloscope (Fig. 2.2b). The ripples show the entire pulse being amplified and de-amplified as the phase of the signal is scanned. We also measured the spectra with an optical spectrum analyzer (OSA) for the two cases of pump on and pump off (Fig. 2.2c), with an acquisition time for the OSA being much longer than the periodicity of the phase scan. The ripples in the spectrum with the pump on again confirm the phase-sensitive amplification of the broadband signal.

We also scan the pump power and record the maximum gain in the measured spectra. Figure 2.2d shows this gain along with the expected exponential response exhibiting a maximum parametric gain of ~30 dB (~50 dB/cm) on the chip for a pump pulse energy of just 1.2 pJ in the waveguide. The agreement with the theoretical estimate suggests that the low-pump-depletion approximation is still valid and larger gain values are available by a further increase in pump energy (Section 2.6.3).

Figure 2.2e shows the behavior of gain vs input signal energy for a pump pulse energy of 1 pJ. The decrease in gain over the entire measured range indicates that the gain is already saturating even for input signal energies as low as 0.2 fJ, which is the lowest energy that we could accurately measure in our setup. This suggest that the amplifier can provide larger levels of gain for signal energies in the aJ range. We

explore this possibility in the next section.

2.4.2 Optical Parametric Generation

To measure the largest possible bandwidth and unsaturated gain in our dispersion-engineered PPLN waveguides, we removed the input signal (leaving only vacuum fluctuations present near the 2 μm signal wavelength). When the gain of an OPA is large, spontaneously generated signal photons can grow to macroscopic levels in a process known as parametric superfluorescence or optical parametric generation (OPG), with an expected number of photons at the output given by [30] $\langle n \rangle = \sinh^2(gL) \approx 0.25 \exp(2gL)$. For a fixed device length, the rate of growth of OPG pulse energy versus pump pulse energy can be used to extract the OPA gain as follows. The number of OPG photons is $\langle n \rangle = \sinh^2(gL)$, which for parametric gains larger than ~10 dB can be approximated well by $0.25 \exp(2gL)$. The OPG energy is proportional to $\langle n \rangle$, so we have $E_{\mathrm{OPG}} = a \exp(2gL) = a \exp\left(b\sqrt{E_{\mathrm{pump}}}\right)$, where a is the overall detection efficiency (including output coupling losses) and b is a constant that depends on factors such as the input coupling losses, pump peak-to-average power ratio, waveguide length, and waveguide nonlinear efficiency. We have also assumed that $g \approx \sqrt{\eta P_{\mathrm{pump}}} \propto \sqrt{E_{\mathrm{pump}}}$ within the gain-bandwidth. The measured OPG energy can be fitted to an exponential versus $\sqrt{E_{\mathrm{pump}}}$ to extract a and b. This leads to an estimated OPA gain for degenerate operation given by $G_s = \exp(2gL) = E_{\mathrm{OPG}}/a$ (see Section 2.6.4 for a comparison between this simplified model and full short-pulse simulations). This method of characterization has the additional advantage of not requiring a coherent input signal, hence the output pulses reveal the full gain bandwidth of the amplifier. Removing the input signal also maximizes the dynamic range of operation of the OPA, eliminating gain saturation effects for a large range of pump levels up to the OPG threshold. For larger pump energies, it is possible to operate the OPG in the saturated regime where high efficiency broadband downconversion can be followed by spectral broadening [31].

We characterized our 6-mm-long waveguide through an OPG measurement using the setup from Fig. 2.2a without the input signal path to the chip (more details in Section 2.6.7). Figure 2.3a shows several measured output spectra for different pump pulse energies along with a simulated spectra from a wideband nonlinear envelope equation solver seeded with semi-classical quantum noise (see Sections 2.6.2 and 2.6.4). The total measured gain bandwidth (at 10 dB below the peak) exceeds 600 nm. The output OPG pulse energy as a function of the pump pulse energy in the waveguide is displayed in Fig. 2.3b. The exponential growth of the signal as a function of pump pulse energy is used to accurately extract the parametric gain as described above.

The extracted gain is shown in Fig. 2.3c, exceeding 66 dB on the chip for the 6-mm-long waveguide (110 dB/cm) with less than 6 pJ of estimated pump pulse energy in the waveguide. The departure from the exponential trend at higher pump powers happens before the 10% pump depletion level (see Section 2.6.4) and it is likely the result of other nonlinear effects that become relevant at high gain regimes,

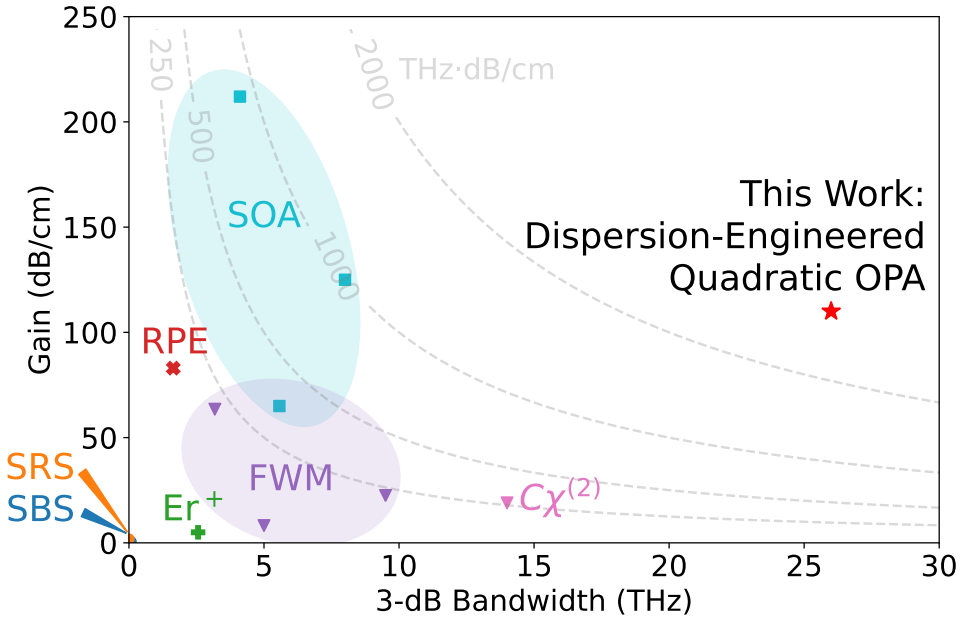

Figure 2.4: **Comparison of the gain and bandwidth of quadratic OPA in dispersion-engineered LN waveguides with other gain mechanisms in integrated photonics.** The methodology used to generate this comparison along with the numerical values and references are included in Section 2.6.8 and Table 2.1. RPE: reverse-proton-exchanged PPLN waveguide; SBS: stimulated Brillouin scattering; SRS: stimulated Raman scattering; Er^{+}: Erbium doped LN waveguide; FWM: four-wave mixing; SOA: semicondutor optical amplifier; $C\chi^{(2)}$: Cascaded three-wave mixing.

including loss through parasitic green generation and scattering. Further studies are necessary to identify and inhibit such processes, but it is important to note that these issues do not limit the use of the amplifier since gain levels beyond 50 dB are reached before entering this region.

Figure 2.3d shows the measured OPG spectrum as a function of the chip temperature. This measurement is compared with the theoretical OPA gain as a function of poling period shown in Fig. 2.3e (see Section 2.6.1), confirming the transition from broadband degenerate to narrowband non-degenerate regime, which happens above 30 °C in the experiment. Achieving OPG in the non-degenerate regime confirms having a phase-insensitive parametric gain with similar magnitude (~100 dB/cm), which can be a useful on-chip resource for quantum and classical photonics [32, 33].

2.5 Conclusion

We have demonstrated an on-chip optical parametric amplifier, with gain levels exceeding 30 dB for weak input femtosecond pulses, and 60 dB for vacuum

fluctuations, over more than 600 nm of bandwidth around 2 μm, using a waveguide that is only 6-mm-long. Furthermore, we have shown that we can operate the amplifier near degeneracy to obtain phase-sensitive amplification. Our results represent a paradigm shift for on-chip optical amplifiers, as shown in Fig. 2.4. This extraordinary performance of quadratic OPA is achieved by combination of dispersion engineering and quasi-phase matching leading to strong nonlinear interactions owing to spatio-temporal confinement of the pump and signal pulses.

The magnitude of the OPA gain we obtain exceeds the reported gain by cubic nonlinearities and is comparable to what can be achieved with SOAs. The OPA bandwidth is significantly broader than other mechanisms. Currently, the maximum measured gain per unit length is limited by the maximum pump pulse energy that we can safely couple into the waveguide, since the input coupling loss is ~25 dB. (see Section 2.6.7) Improving the coupling loss by more than 10 dB seems feasible by developing integrated spot converters [34]. Such improvement can lead to a gain of more than 150 dB/cm putting the on-chip OPA in direct competition with the largest single-mode SOA gains reported. Further enhancement can be achieved by improving the poling duty cycle, depth, and fidelity [35]. Parametric sweeps confirm that our dispersion engineering is not too sensitive to fabrication variations in waveguide width and etch depth (see Section 2.6.6). Studying the noise behavior of the OPA will be the subject of future work. Combined with other linear and nonlinear functionalities available on thin-film LN, the presented intense OPA can open unprecedented opportunities in integrated photonics, for instance for quantum information processing, mid-infrared sources, optical computing, femtosecond frequency combs and laser ranging.

2.6 Supplementary Information

In this supplementary document, we include background theory on CW parametric amplification in waveguides as well as details on the nonlinear single envelope simulations for OPA and OPG. We also include additional fabrication and characterization details and a companion table for Fig. 2.4 of the main text.

2.6.1 CW Parametric amplification theory

We briefly review here the CW theory of degenerate parametric amplification, in which a strong pump field at frequency ω_p interacts with a signal field at frequency $\omega_s = \omega_p/2$. In the limit of no loss, the coupled wave equations are

$$\frac{\partial A_p}{\partial z} = -i\kappa A_s^2 e^{i\Delta k z}, \tag{2.1}$$

$$\frac{\partial A_s}{\partial z} = -i\kappa A_s^* A_p e^{-i\Delta k z}, \tag{2.2}$$

where A_p and A_s are the pump and signal complex envelopes, normalized such that $|A_i|^2$ is the power carried by the pulses, $\Delta k = \beta_p - 2\beta_s - 2\pi/\Lambda$ is the phase mismatch, and κ is the nonlinear coupling coefficient, which is related to the second

harmonic normalized efficiency η by

$$\eta = \kappa^2 = \frac{2\omega_s^2 d_{\text{eff}}^2}{n_{\omega_s}^2 n_{\omega_p} \epsilon_0 c^3 A_{\text{eff}}}. \tag{2.3}$$

Here, $d_{\text{eff}} = (2/\pi) d_{33}$ for periodic quasi-phase matching with 50% duty cycle, $d_{33} \approx 20.5$ pm/V for a pump centered at 1045 nm, and A_{eff} is the effective area of the nonlinear interaction, given by [22],

$$A_{\text{eff}} = \frac{\left(\int \left(\mathbf{e}_{\omega_s} \times \mathbf{h}_{\omega_s}^* \right) \cdot \mathbf{dS} \right)^2 \int \left(\mathbf{e}_{\omega_p} \times \mathbf{h}_{\omega_p}^* \right) \cdot \mathbf{dS}}{\left| \int \sum_{i,j,k} \bar{d}_{ijk} e_{i,\omega_p}^* e_{j,\omega_s} e_{k,\omega_s} dx dy \right|^2}, \tag{2.4}$$

where $\mathbf{e}_\mu$ are dimensionless transverse mode profiles scaled such that the peak value of $\left(\mathbf{e}_\mu \times \mathbf{h}_\mu^* \right) \cdot \mathbf{z}$ is unity, and $\bar{d}_{ijk}$ is the $\chi^{(2)}$ tensor normalized with respect to d_{33}. Note that a large overlap integral (denominator of A_{eff}) leads to a small effective area and a stronger nonlinear interaction (large η).

Assuming no pump depletion, the signal equation of motion reduces to

$$\frac{\partial A_s}{\partial z} = -i\kappa A_p A_s^* e^{-i\Delta k z} = \gamma A_s^* e^{-i\Delta k z}, \tag{2.5}$$

where $\gamma \equiv -i\kappa A_p$ can be made real by an appropriate definition of the pump absolute phase. This equation can be solved by separating the signal into its real and imaginary parts (i.e., its quadratures), $A_s = A_1 + iA_2$, yielding for the real part:

$$A_1(z) = A_1(0) \left[\cosh(gz) + \frac{\gamma}{g} \sinh(gz) \right] \exp(i\Delta k z/2) + A_2(0) \frac{\Delta k}{2g} \sinh(gz) \exp(i\Delta k z/2), \tag{2.6}$$

where we have introduced the parametric gain parameter $g = \sqrt{|\gamma|^2 - (\Delta k/2)^2} = \sqrt{\eta P_p - (\Delta k/2)^2}$.

In the large gain regime, $\eta P_p \gg (\Delta k/2)^2$, $\gamma/g \approx 1$ and $\Delta k/2g \approx 0$, so the power of the real quadrature grows as

$$|A_1(z)|^2 = G|A_1(0)|^2 = |A_1(0)|^2 \exp(2gz) \approx |A_1(0)|^2 \exp\left(2\sqrt{\eta P_p} z \right), \tag{2.7}$$

with a power gain $G \approx \exp\left(2\sqrt{\eta P_p} z \right)$.

For the case of non-degenerate operation, if only the pump and the signal are present at the input, then an idler will be generated with the right phase to produce signal amplification. In that case the amplification is not phase-sensitive and the gain is given by:

$$G = \frac{\gamma^2}{g^2} \sinh^2(gz), \tag{2.8}$$

where g and γ are the same as in the degenerate case, but the phase mismatch is $\Delta k = \beta_p - \beta_s - \beta_i - 2\pi/\Lambda$. This gain expression was used to generate Fig. 2.3e on the main paper.

2.6.2 Single envelope simulation

We used a method similar to that described in [36] to simulate quadratic interactions over a large bandwidth using a single envelope in the frequency domain. We write a spectral component of the electric field propagating in the z-direction on a single waveguide mode as:

$$\mathbf{E}(x, y, \omega) = A(z, \Omega)\mathbf{e}(x, y, \omega)e^{-i(\beta_0 - \omega_0/v_{\text{ref}})z}, \tag{2.9}$$

where ω and $\Omega = \omega - \omega_0$ are the optical and envelope angular frequencies, ω_0 is the simulation center frequency, β_0 is the waveguide propagation constant at ω_0, v_{ref} is the simulation reference frame velocity, x, y are the transversal waveguide coordinates, $\mathbf{e}(x, y, \omega)$ is the mode transversal field distribution, and $A(z, \omega)$ is the complex amplitude of the field that evolves during propagation. Note that $A(z, \omega)$ is a rapidly-varying envelope, i.e., it includes the phase factor $e^{-i\beta(\omega)z}$ acquired during linear propagation. Furthermore, $A(z, \omega)$ is an analytic signal, i.e., it only contains positive frequencies ($A(z, \omega < 0) = 0$).

We obtained an equation of motion for $A(z, \Omega)$ by ignoring counter-propagating terms (which are usually phase mismatched), and assuming a constant nonlinear coefficient and mode overlap integral, both of which are weak functions of frequency away from any material resonances. No limitations are placed upon the maximum spectral bandwidth of the simulation. The resulting propagation equation is,

$$\frac{\partial A}{\partial z} = -i\left[\beta(\omega) - \beta_0 - \frac{\Omega}{v_{\text{ref}}} - i\frac{\alpha}{2}\right]A - \frac{i\omega\epsilon_0 X_0}{8}d(z) \\ \mathcal{F}_\Omega\left\{a^2(z,t)e^{j\phi(z,t)} + 2a(z,t)a^*(z,t)e^{-j\phi(z,t)}\right\}, \tag{2.10}$$

where $d(z) = \pm 1$ is the sign of the quadratic nonlinear coefficient that is modulated in quasi-phase matching, $a(z, t)$ is the time domain representation of $A(z, \Omega)$, $\phi(z, t) = \omega_0 t - (\beta_0 - \omega_0/v_{\text{ref}})z$, $\mathcal{F}_\Omega$ is the Fourier transform in the Ω variable. The effective nonlinear coefficient X_0 is defined as:

$$X_0 = \sum_{ijk} \chi^{(2)}_{ijk} \int e^*_i(\omega_1)e_j(\omega_2)e_k(\omega_1 - \omega_2)\,\mathrm{d}S\,, \tag{2.11}$$

where $\chi^{(2)}_{ijk}$ is the quadratic nonlinear susceptibility tensor, j, k, l are Cartesian components of the corresponding vectors, and ω_1 and ω_2 are two suitable chosen frequencies, e.g., the signal and pump frequencies in our case.

The time domain terms inside the Fourier transform of Eq. (6.3) represent the processes of sum frequency generation $\left(\propto a(t)^2\right)$ and difference frequency generation ($\propto a(t)a(t)^*$), which combined can predict all classical second order interactions, such as second harmonic generation and parametric amplification. Since $A(z)$ is fast varying, carrier dynamics can be resolved. In particular, phase mismatch is automatically included and the term $d(z)$ can be used to accurately simulate different quasi-phase matching gratings. This also means that the spatial domain needs to

be sampled finely enough to resolve these dynamics. We solve the evolution equation (6.3) with the split-step Fourier technique using the fourth-order Runge-Kutta method for the nonlinear step.

We used a combination of commercial software (Lumerical Inc.) and custom built effective-index routines to solve for the waveguide modes and generate the dispersion characteristics shown in Fig. 2.1c,d of the main text.

2.6.3 Small-Signal OPA Simulation

We simulated optical parametric amplification for the dispersion-engineered 2.5-mm-long waveguide described in the main text, including quasi-phase matching through a periodic modulation of $d(z)$. As the input, we used a 100-fs-long pump pulse centered at 1045 nm, and a 35-fs-long signal pulse centered at 2090 nm, both with a hyperbolic secant profile. The output power spectral density (PSD) for three pump power levels, with a fixed input signal level, are shown in Fig. 2.5a. For the largest pump pulse energy shown, significant spectral broadening is observed at both, the pump and signal wavelengths, revealing a strong non-linear regime similar to [22]. Figure 2.5b shows the gain as a function of the pump energy for three different input signal levels as well as the CW theory and measured data. Pump depletion and spectral broadening effects make the gain deviate from the theoretical CW prediction at large pump and signal power levels (to calculate the gain, the output signal energy is integrated from 1,600 nm to 3,000 nm). At low pump power levels, the pulsed gain curve follows the CW theory as expected for dispersion-engineered waveguides according to the argument provided in the main paper. Note that a low signal level is necessary in order to extract the maximum gain from a strong pump. It is for this reason that to characterize the maximum gain of our waveguides we performed measurements on the OPG regime, with no input signal except for vacuum fluctuations.

2.6.4 OPG simulation

In the main text we argue that operating the amplifier in the OPG regime (with a strong pump and no input signal) provides a practical way of extracting the gain of the amplifier avoiding saturation effects and also revealing its full gain-bandwidth. In this section we support these claims with semi-classical simulations of parametric generation.

Seeding the OPA with an input noise having an energy of half-a-photon per frequency mode, and a uniformly distributed random phase, has been known to provide the same average signal output power as the quantum mechanical solution [37]. This is equivalent to neglecting thermal excitations and modeling the remaining vacuum fluctuations as complex Gaussian random variables with zero mean and a half-a-photon variance [38]. Fig. 2.6a shows the simulated average output power (integrated from 1,600 nm to 3,000 nm) for the 6-mm-long dispersion-engineered waveguide, along with the expected curve from the CW theory and our measured data. The simulation deviates from the theory at pump energies larger than 4 pJ due to efficient parametric generation (OPG) producing pump depletion (also shown in

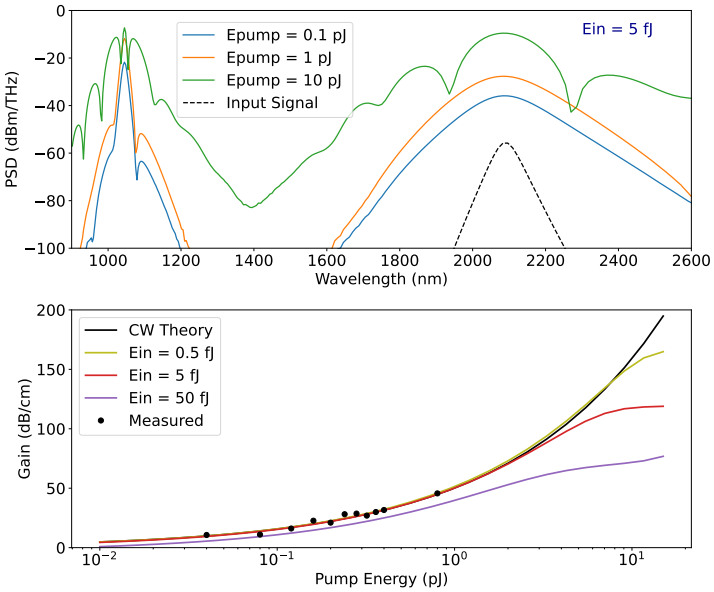

Figure 2.5: **Numerical simulation of small-signal optical parametric amplification. a**, Power spectral density at the output of a 2.5-mm-long, dispersion-engineered waveguide showing low distortion parametric amplification for pump energies of 0.1 pJ and 1 pJ, and spectral broadening for a pump energy of 10 pJ. The 100-fs-long pump is centered at 1045 nm and the 35-fs-long signal is centered at 2090 nm. The input signal energy is fixed at 5 fJ. **b**, Simulated gain as a function of pump power for three different input signal levels along with the prediction from the CW theory and the measured values (from main paper Fig. 2.2c). It is evident that the CW theory is valid for this dispersion-engineered waveguide before gain saturation and spectral broadening effects start dominating at high pump power levels. The maximum measured gain was limited by input coupling losses, and improving the input coupling by 10 dB leads to small-signal gains exceeding 150 dB/cm, putting the on-chip OPA in direct competition with the largest single mode SOA gains reported.

Fig. 2.6a). The simulations results shown in Fig. 2.6a are the ensemble average of 100 simulations, each simulation producing a different result due to the stochastic nature of the input signal. This is illustrated in Fig. 2.6b., where the output spectra OPG for a pump energy of 3 pJ is shown for the first 20 simulations along with the average of 100 simulations.

2.6.5 Device Fabrication

We used a commercial wafer (NANOLN), with a 700-nm-thick X-cut MgO-doped LN thin-film on 2-μm-thick SiO_2. The fabrication process begins with periodically poling the chip. The poling electrodes (15 nm Cr/55 nm Au) were patterned using e-beam lithography, e-beam evaporation and metal lift-off. Then ~300 V pulses were applied across the electrodes to produce periodic domain inversion over a 6-mm length with a period of ~5 μm. We visually inspected the

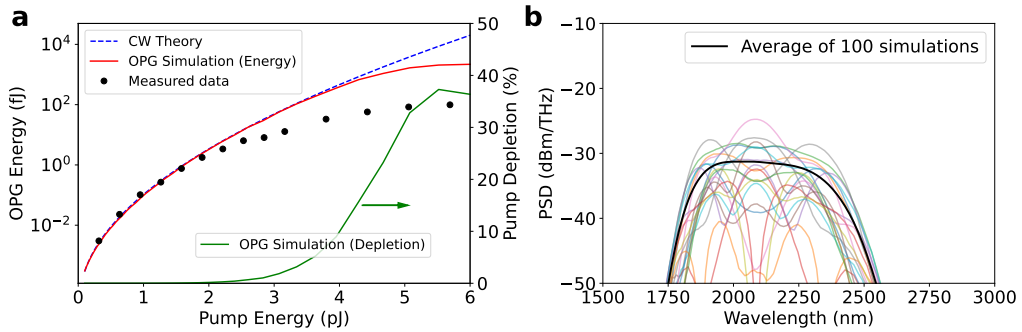

Figure 2.6: **Numerical simulation of optical parametric generation. a**, Simulated OPG energy as a function of pump energy along with the CW theory and measured data. The pump is a 100-fs-long hyperbolic secant pulse center at 1045 nm. The results are the average of 100 simulations. In each simulation, the input signal is a realization of a complex Gaussian random variable with zero mean and half-a-photon variance. The simulation results deviate from the CW theory for pump energy levels above ~4 pJ beyond which efficient parametric generation occurs and the no-pump-depletion approximation is no longer valid. The simulated pump depletion level ($P_{\mathrm{OPG}}/P_{\mathrm{pump}}$) is shown on the right hand axis. **b**, Output power spectral density for 20 OPG simulations illustrating its stochastic nature, as well as the average for 100 simulations.

poling quality using second harmonic microscopy (an example image is shown in an inset of Fig. 2.2a. The metal electrodes were removed by chemical etching. The waveguides were patterned by e-beam lithography using hydrogen silsesquioxane (HSQ) as the e-beam resist. The pattern was transferred to the LN layer by dry etching with Ar^+ plasma. Finally, the waveguide facets were polished to reduce the coupling losses.

2.6.6 Dispersion Engineering Maps

After selecting a thin-film thickness of 700 nm, the width and etch depth of the waveguide can be varied to create maps of GVD at 2 μm and GVM between the 1 μm pump and 2 μm signal. We can also factor-in the waveguide length and pulse width by the following procedure. The GVM between the signal and pump defines a walk-off length given by $L_{\mathrm{gvm}} = \tau/\mathrm{GVM}$, where τ is the pulse width. If the waveguide width is L_{wg}, then we want to minimize the ratio $L_{\mathrm{wg}}/L_{\mathrm{gvm}}$. A map of this ratio, for $L_{\mathrm{wg}} = 6$ mm and $\tau = 35$ fs, is shown in Fig. S3a, along with the corresponding contour levels at 0.5 (where the waveguide is half the walk-off length).

Similarly, a dispersion length can be defined as $L_{\mathrm{gvd}} = \tau^2/\mathrm{GVD}$, and the metric would be the ratio $L_{\mathrm{wg}}/L_{\mathrm{gvd}}$. The corresponding map is shown in Fig. 2.7b, along with the contour level at 0.25 (where the waveguide is only a quarter of the dispersion length). For both contours in Fig. 2.7b, the black dot corresponds to our waveguide geometry.

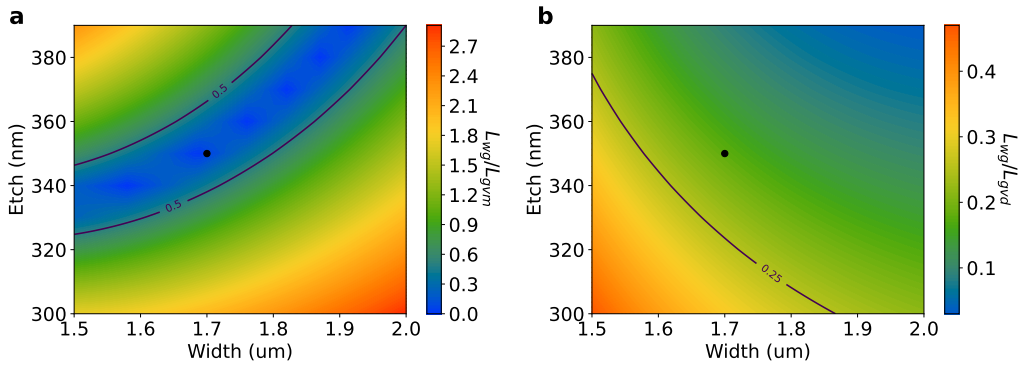

Figure 2.7: **Dispersion engineering mappings.** **a**, Waveguide length to walk-off length ratio. **b**, Waveguide length to dispersion length ratio. Both maps are for a 700-nm thick film, 6-mm long waveguide, and 35-fs pulse width. The black dot indicates our waveguide design.

2.6.7 Waveguide Characterization

For the OPA measurements we use the setup shown in Fig. 2.2a with both, 1 μm and 2 μm pulses, coupled into the waveguide. The 1 μm source (the pump) was a 1 W Yb mode-locked laser that produces nearly transform-limited 75-fs-long pulses at a 250 MHz repetition rate (Menlo Systems Orange). Part of the pump was sent directly to the chip, while the rest was fed into a near-synchronously pumped degenerate OPO [39] to produce 2 μm pulses. The 1 μm and 2 μm pulses were combined at a dichroic mirror, and coupled into the waveguides using a reflective objective (Newport 50102-02). The two pulses were temporally overlapped by adjusting the optical delay line, and their relative phase was scanned by the piezoelectric transducer on the delay line. The chip was placed on a thermoelectric cooling stage (TEC), and the temperature was finely tuned to adjust the quasi-phase matching condition. The output of the chip was collected with another reflective objective and the remaining pump power was filtered. A 2 μm detector followed by an oscilloscope was used to monitor the entire signal power without and without the pump beam (Fig. 2.2b). We used an optical spectrum analyzer (OSA) covering 1200 - 2400 nm (Yokogawa AQ6375B) with a 2 nm resolution bandwidth (Fig. 2.2c) to characterize the spectral gain distribution.

For the OPG measurements of Fig. 2.3 of the main text, only the 1 μm path was used. The output of a 10-W Yb mode-locked laser (Menlo Systems Orange High Power 10) with 100-fs pulse length was passed through an optical chopper to reduce thermally induced damage. The average input power was swept using a variable ND filter and the output was recorded using the same OSA.

The input/output coupling losses were estimated based on a combination of linear and non-linear measurements as follows. Comparing the optical power before and after the chip gives the total loss $L_t = L_i + L_{wg} + L_o$, where L_i is the input coupling loss, L_{wg} is the waveguide loss, and L_o is the output coupling loss. We estimated the waveguide loss, L_{wg}, to be much less than 1 dB based on Q-factor

Table 2.1: Comparison of on-chip amplifiers gain and bandwidth

Type	Length	Gain		Signal	3-dB Bandwidth (Signal + Idler)		Reference
		Absolute	Normalized	Wavelength	Absolute	Relative	
$\chi^{(2)}$	6 mm	62 dB	104 dB/cm	2090 nm	380 nm (26 THz)	18.2 %	This Work
$\chi^{(2)}$	12 mm	100 dB	83 dB/cm	2700 nm	10 nm (1.64 THz)	0.4 %	[40]
SOA	1.2 mm	25.5 dB	213 dB/cm	1575 nm	34 nm (4.11 THz)	2.2 %	[41]
SOA	2 mm	13 dB	65 dB/cm	2010 nm	75 nm (5.6 THz)	3.7 %	[42]
SOA	2 mm	25 dB	125 dB/cm	1550 nm	69 nm (8.1 THz)	4.5 %	[10]
FWM $\chi^{(3)}$	4 mm	25.4 dB	63.5 dB/cm	2170 nm	50 nm (3.18 THz)	2.3 %	[5]
FWM $\chi^{(3)}$	2 cm	45 dB	22.5 dB/cm	2170 nm	150 nm (9.5 THz)	6.9 %	[43]
FWM $\chi^{(3)}$	1.7 cm	13.9 dB	8.2 dB/cm	1550 nm	40 nm (5 THz)	2.7 %	[44]
SBS	2.9 cm	5.2 dB	1.8 dB/cm	1550 nm	< 50 MHz	$\ll$ 0.1 %	[8]
SRS	4.6 cm	2.3dB dB	0.5 dB/cm	1545 nm	80 GHz	< 0.1 %	[45]
Er^{+} doped	3.6 cm	18 dB	5 dB/cm	1530 nm	20 nm (2.56 THz)	1.3 %	[46]
C$\chi^{(2)}$	2 cm	38.3 dB	19.2 dB/cm	1550 nm	+14 THz	7.2 %	[47]

measurements in other chips using the same fabrication process. Since the total loss L_t is ~29 dB (at 2 μm) we neglect the waveguide loss in what follows.

As explained in Section 2.4.2 of the main article, the OPG data can be used to estimate the gain $G_s = \exp(2gL)$ without any knowledge of the input/output coefficients. This is because this gain depends only on the rate of growth of the OPG power, and not on its absolute value. We also know that the expected number of photons generated during OPG is given by $\langle n \rangle = \sinh^2(gL) \approx 0.25 \exp(2gL) = 0.25 G_s$. Thus, by estimating G_s, we are also estimating the average number of photons generated, from which the OPG power in the waveguide follows immediately: $P_{\mathrm{OPG}} = \hbar\omega \langle n \rangle f_{rep}$. Comparing this expected power with the measured power gives us a total output collection efficiency of 5.85 dB at 2 μm. This corresponds to 26 % output coupling efficiency, which compares well with output coupling losses in similar waveguides estimated by other methods [31].

Subtracting this output coupling loss from the total throughput loss gives us an input coupling loss at 2 μm of ~23 dB, which is considerably larger than the output coupling loss. This is expected since only the power coupled to the fundamental TE mode is considered at the input, while most of the radiated modes are expected to be collected by the objective at the output. At 1 μm, we assume that the output coupling loss is also 5.85 dB, since we use a low-dispersion metallic collective objective. The measured throughput loss at 1 μm is ~31 dB, so the input coupling loss was estimated to be ~25 dB. Note that the input coupling loss at 1 μm is expected to be larger than that at 2 μm due to the corresponding mode sizes.

2.6.8 On-chip amplifier state of the art comparison

Detailed bandwidth and gain numbers used to generate Fig. 2.4 from the main text and Fig. 2.7 are available in Table 2.1 along with the corresponding references. Previous works include only on-chip traveling-wave amplifiers. We have striven to include the best and most recent results, but not all publications report enough data to extract 3 dB bandwidth values and could not be added to the comparison. To

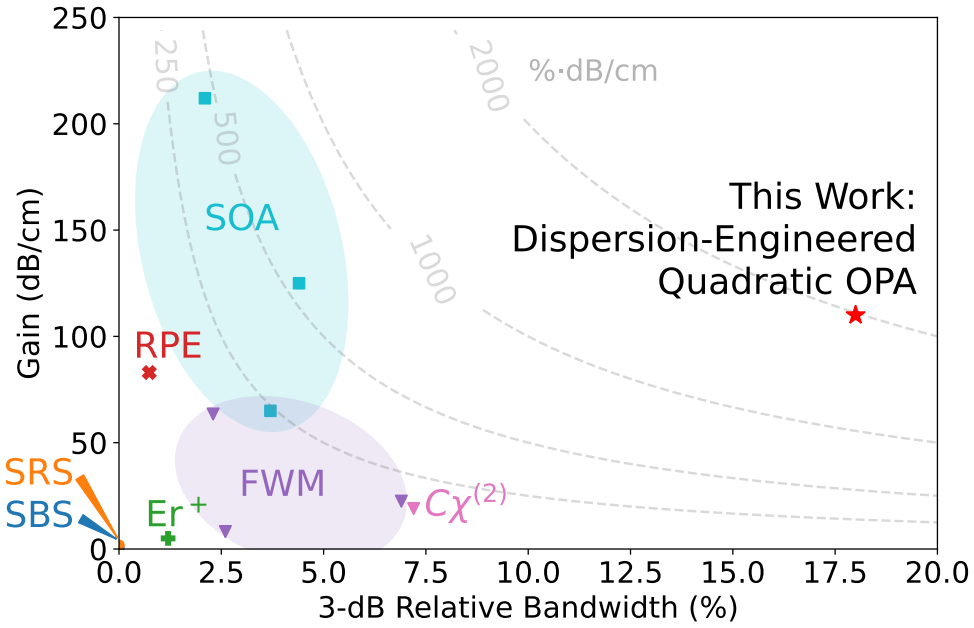

Figure 2.8: **Comparison of the gain and bandwidth of quadratic OPA in dispersion-engineered LN waveguides with other gain mechanisms in integrated photonics.** This is an alternative representation of the data in Fig. 2.4 of the main text using relative bandwidth as the horizontal axis.

estimate the bandwidth of the FWM cases we have added together the signal and idler bandwidths.

References

[1] Bhavin J. Shastri et al. "Photonics for artificial intelligence and neuromorphic computing". In: *Nature Photonics* 15.2 (Feb. 2021), pp. 102–114. URL: https://www.nature.com/articles/s41566-020-00754-y (visited on 01/30/2021).

[2] Johann Riemensberger et al. "Massively parallel coherent laser ranging using a soliton microcomb". In: *Nature* 581.7807 (May 2020), pp. 164–170. URL: https://www.nature.com/articles/s41586-020-2239-3 (visited on 01/30/2021).

[3] Yaakov Shaked et al. "Lifting the bandwidth limit of optical homodyne measurement with broadband parametric amplification". In: *Nature Communications* 9.1 (Feb. 2018), p. 609. URL: https://www.nature.com/articles/s41467-018-03083-5 (visited on 01/24/2021).

[4] Z. Tong et al. "Towards ultrasensitive optical links enabled by low-noise phase-sensitive amplifiers". In: *Nature Photonics* 5.7 (July 2011), pp. 430–436. URL: http://www.nature.com/articles/nphoton.2011.79 (visited on 03/26/2021).

[5] Xiaoping Liu et al. "Mid-infrared optical parametric amplifier using silicon nanophotonic waveguides". In: *Nature Photonics* 4.8 (Aug. 2010), pp. 557–560. URL: https://www.nature.com/articles/nphoton.2010.119 (visited on 01/22/2021).

[6] K. J. A. Ooi et al. "Pushing the limits of CMOS optical parametric amplifiers with USRN:Si 7 N 3 above the two-photon absorption edge". In: *Nature Communications* 8.1 (Jan. 2017), p. 13878. URL: https://www.nature.com/articles/ncomms13878 (visited on 01/22/2021).

[7] Haisheng Rong et al. "Low-threshold continuous-wave Raman silicon laser". In: *Nature Photonics* 1.4 (Apr. 2007), pp. 232–237. URL: https://www.nature.com/articles/nphoton.2007.29 (visited on 01/24/2021).

[8] Eric A. Kittlaus, Heedeuk Shin, and Peter T. Rakich. "Large Brillouin amplification in silicon". In: *Nature Photonics* 10.7 (July 2016), pp. 463–467. URL: https://www.nature.com/articles/nphoton.2016.112 (visited on 01/23/2021).

[9] Bahawal Haq et al. "Micro-Transfer-Printed III-V-on-Silicon C-Band Semiconductor Optical Amplifiers". In: *Laser & Photonics Reviews* 14.7 (2020), p. 1900364. URL: https://onlinelibrary.wiley.com/doi/abs/10.1002/lpor.201900364 (visited on 01/25/2021).

[10] M. L. Davenport et al. "Heterogeneous Silicon/III–V Semiconductor Optical Amplifiers". In: *IEEE Journal of Selected Topics in Quantum Electronics* 22.6 (Nov. 2016), pp. 78–88.

[11] Zijiao Yang et al. "A Squeezed Quantum Microcomb on a Chip". In: *Nature Communications* 12.1 (Aug. 2021), p. 4781.

[12] Rajveer Nehra et al. "Few-Cycle Vacuum Squeezing in Nanophotonics". In: *arXiv:2201.06768 [quant-ph]* (Jan. 2022).

[13] Malcolm H. Dunn and Majid Ebrahimzadeh. “Parametric Generation of Tunable Light from Continuous-Wave to Femtosecond Pulses”. In: *Science* 286.5444 (Nov. 1999), pp. 1513–1517. URL: https://science.sciencemag.org/content/286/5444/1513 (visited on 07/09/2020).

[14] Yu-Chieh Lin, Yasuo Nabekawa, and Katsumi Midorikawa. “Optical parametric amplification of sub-cycle shortwave infrared pulses”. In: *Nature Communications* 11.1 (July 2020), p. 3413. URL: https://www.nature.com/articles/s41467-020-17247-9 (visited on 03/15/2021).

[15] Giulio Cerullo and Sandro De Silvestri. “Ultrafast optical parametric amplifiers”. In: *Review of Scientific Instruments* 74.1 (Jan. 2003), pp. 1–18. URL: https://aip.scitation.org/doi/10.1063/1.1523642 (visited on 01/23/2021).

[16] Shu-Wei Huang et al. “High-energy pulse synthesis with sub-cycle waveform control for strong-field physics”. In: *Nature Photonics* 5.8 (Aug. 2011), pp. 475–479. URL: https://www.nature.com/articles/nphoton.2011.140 (visited on 03/15/2021).

[17] Eric J. Stanton et al. “Efficient second harmonic generation in nanophotonic GaAs-on-insulator waveguides”. In: *Optics Express* 28.7 (Mar. 2020), pp. 9521–9532. URL: https://www.osapublishing.org/oe/abstract.cfm?uri=oe-28-7-9521 (visited on 03/27/2021).

[18] Daniil M. Lukin et al. “4H-silicon-carbide-on-insulator for integrated quantum and nonlinear photonics”. In: *Nature Photonics* 14.5 (May 2020), pp. 330–334. URL: https://www.nature.com/articles/s41566-019-0556-6 (visited on 03/15/2021).

[19] Dalziel J. Wilson et al. “Integrated gallium phosphide nonlinear photonics”. In: *Nature Photonics* 14.1 (Jan. 2020), pp. 57–62. URL: https://www.nature.com/articles/s41566-019-0537-9 (visited on 03/15/2021).

[20] Alexander W. Bruch et al. “Pockels soliton microcomb”. In: *Nature Photonics* 15.1 (Jan. 2021), pp. 21–27. URL: https://www.nature.com/articles/s41566-020-00704-8 (visited on 03/15/2021).

[21] Cheng Wang et al. “Ultrahigh-efficiency wavelength conversion in nanophotonic periodically poled lithium niobate waveguides”. In: *Optica* 5.11 (Nov. 2018), pp. 1438–1441. URL: https://www.osapublishing.org/optica/abstract.cfm?uri=optica-5-11-1438 (visited on 03/03/2019).

[22] Marc Jankowski et al. “Ultrabroadband nonlinear optics in nanophotonic periodically poled lithium niobate waveguides”. In: *Optica* 7.1 (Jan. 2020), pp. 40–46. URL: https://www.osapublishing.org/optica/abstract.cfm?uri=optica-7-1-40 (visited on 01/18/2020).

[23] Mian Zhang et al. “Broadband electro-optic frequency comb generation in a lithium niobate microring resonator”. In: *Nature* 568.7752 (Apr. 2019), pp. 373–377. URL: https://www.nature.com/articles/s41586-019-1008-7 (visited on 01/30/2021).

[24] Cheng Wang et al. “Integrated lithium niobate electro-optic modulators operating at CMOS-compatible voltages”. In: *Nature* 562.7725 (Oct. 2018),

p. 101. URL: https://www.nature.com/articles/s41586-018-0551-y (visited on 02/20/2019).

[25] Timothy P. McKenna et al. "Ultra-low-power second-order nonlinear optics on a chip". In: *arXiv:2102.05617 [physics, physics:quant-ph]* (Feb. 2021). URL: http://arxiv.org/abs/2102.05617 (visited on 03/08/2021).

[26] Juanjuan Lu et al. "Ultralow-threshold thin-film lithium niobate optical parametric oscillator". In: *arXiv:2101.04735 [physics]* (Jan. 2021). URL: http://arxiv.org/abs/2101.04735 (visited on 03/08/2021).

[27] Jie Zhao et al. "High Quality Entangled Photon Pair Generation in Periodically Poled Thin-Film Lithium Niobate Waveguides". In: *Physical Review Letters* 124.16 (Apr. 2020), p. 163603. URL: https://link.aps.org/doi/10.1103/PhysRevLett.124.163603 (visited on 10/19/2020).

[28] Rui Luo et al. "Highly tunable efficient second-harmonic generation in a lithium niobate nanophotonic waveguide". In: *Optica* 5.8 (Aug. 2018), pp. 1006–1011. URL: https://www.osapublishing.org/optica/abstract.cfm?uri=optica-5-8-1006 (visited on 02/23/2019).

[29] Alireza Marandi et al. "Cascaded half-harmonic generation of femtosecond frequency combs in the mid-infrared". In: *Optica* 3.3 (Mar. 2016), pp. 324–327. URL: https://www.osapublishing.org/optica/abstract.cfm?uri=optica-3-3-324 (visited on 01/16/2021).

[30] W. H. Louisell, A. Yariv, and A. E. Siegman. "Quantum Fluctuations and Noise in Parametric Processes. I." In: *Physical Review* 124.6 (Dec. 1961), pp. 1646–1654. URL: https://link.aps.org/doi/10.1103/PhysRev.124.1646 (visited on 06/25/2019).

[31] Marc Jankowski et al. "Efficient Octave-Spanning Parametric Down-Conversion at the Picojoule Level". In: *arXiv:2104.07928 [physics]* (Apr. 2021). arXiv: 2104.07928. URL: http://arxiv.org/abs/2104.07928 (visited on 04/20/2021).

[32] Z. Y. Ou et al. "Realization of the Einstein-Podolsky-Rosen paradox for continuous variables". In: *Physical Review Letters* 68.25 (June 1992), pp. 3663–3666. URL: https://link.aps.org/doi/10.1103/PhysRevLett.68.3663 (visited on 04/14/2021).

[33] J. Hansryd et al. "Fiber-based optical parametric amplifiers and their applications". In: *IEEE Journal of Selected Topics in Quantum Electronics* 8.3 (May 2002), pp. 506–520.

[34] Ni Yao et al. "Efficient light coupling between an ultra-low loss lithium niobate waveguide and an adiabatically tapered single mode optical fiber". In: *Optics Express* 28.8 (Apr. 2020), pp. 12416–12423. URL: https://www.osapublishing.org/oe/abstract.cfm?uri=oe-28-8-12416 (visited on 04/20/2020).

[35] M. Rüsing, J. Zhao, and S. Mookherjea. "Second harmonic microscopy of poled x-cut thin film lithium niobate: Understanding the contrast mechanism". In: *Journal of Applied Physics* 126.11 (Sept. 2019), p. 114105. URL: https://aip.scitation.org/doi/abs/10.1063/1.5113727 (visited on 03/30/2021).

[36] C. R. Phillips et al. “Supercontinuum generation in quasi-phasematched waveguides”. In: *Optics Express* 19.20 (Sept. 2011), pp. 18754–18773. URL: https://www.osapublishing.org/oe/abstract.cfm?uri=oe-19-20-18754 (visited on 02/18/2019).

[37] D. A. Kleinman. “Theory of Optical Parametric Noise”. In: *Physical Review* 174.3 (Oct. 1968), pp. 1027–1041. URL: https://link.aps.org/doi/10.1103/PhysRev.174.1027 (visited on 07/16/2020).

[38] Gunnar Arisholm. “Quantum noise initiation and macroscopic fluctuations in optical parametric oscillators”. In: *Journal of the Optical Society of America B* 16.1 (Jan. 1999), p. 117. URL: https://www.osapublishing.org/abstract.cfm?URI=josab-16-1-117 (visited on 02/14/2019).

[39] Marc Jankowski et al. “Temporal Simultons in Optical Parametric Oscillators”. In: *Phys. Rev. Lett.* 120 (5 Feb. 2018), p. 053904. URL: https://link.aps.org/doi/10.1103/PhysRevLett.120.053904.

[40] Xiuping Xie et al. “Picojoule threshold, picosecond optical parametric generation in reverse proton-exchanged lithium niobate waveguides”. In: *JOSA B* 21.7 (July 2004), pp. 1397–1402. URL: https://www.osapublishing.org/josab/abstract.cfm?uri=josab-21-7-1397 (visited on 10/21/2020).

[41] Kasper Van Gasse, Ruijun Wang, and Gunther Roelkens. “27 dB gain III–V-on-silicon semiconductor optical amplifier with > 17 dBm output power”. In: *Optics Express* 27.1 (Jan. 2019), pp. 293–302. URL: https://www.osapublishing.org/oe/abstract.cfm?uri=oe-27-1-293 (visited on 01/25/2021).

[42] Nicolas Volet et al. “Semiconductor optical amplifiers at 2.0-μm wavelength on silicon”. In: *Laser & Photonics Reviews* 11.2 (2017), p. 1600165. URL: https://onlinelibrary.wiley.com/doi/abs/10.1002/lpor.201600165 (visited on 03/18/2021).

[43] Bart Kuyken et al. “50 dB parametric on-chip gain in silicon photonic wires”. In: *Optics Letters* 36.22 (Nov. 2011), pp. 4401–4403. URL: https://www.osapublishing.org/ol/abstract.cfm?uri=ol-36-22-4401 (visited on 01/23/2021).

[44] Mark A. Foster et al. “Broad-band optical parametric gain on a silicon photonic chip”. In: *Nature* 441.7096 (June 2006), pp. 960–963. URL: https://www.nature.com/articles/nature04932 (visited on 01/22/2021).

[45] Vanessa Sih et al. “Raman amplification of 40 Gb/s data in low-loss silicon waveguides”. In: *Optics Express* 15.2 (Jan. 2007), pp. 357–362. URL: https://www.osapublishing.org/oe/abstract.cfm?uri=oe-15-2-357 (visited on 04/13/2021).

[46] Junxia Zhou et al. “On-chip integrated waveguide amplifiers on Erbium-doped thin film lithium niobate on insulator”. In: *arXiv:2101.00783 [physics]* (Jan. 2021). URL: http://arxiv.org/abs/2101.00783 (visited on 04/08/2021).

[47] Yong Meng Sua, Jia-Yang Chen, and Yu-Ping Huang. “Ultra-wideband and high-gain parametric amplification in telecom wavelengths with an optimally mode-matched PPLN waveguide”. In: *Optics Letters* 43.12 (June 2018). Publisher: Optical Society of America, pp. 2965–2968. URL: https://www.osapublishing.org/ol/abstract.cfm?uri=ol-43-12-2965 (visited on 06/07/2021).

Chapter 3

ALL-OPTICAL ULTRAFAST RELU FUNCTION FOR ENERGY-EFFICIENT NANOPHOTONIC DEEP LEARNING

Gordon H.Y. Li†, **Ryoto Sekine**†, Rajveer Nehra†, Robert M. Gray†, Luis Ledezma, Qiushi Guo, and Alireza Marandi, "All-optical ultrafast ReLU function for energy-efficient nanophotonic deep learning," *Nanophotonics*, 12, 847-855 (2022).
R.S. fabricated and phase-matched the device, and developed a new facet-polishing procedure.
† denotes equal contributions

3.1 Abstract

In recent years, the computational demands of deep learning applications have necessitated the introduction of energy-efficient hardware accelerators. Optical neural networks are a promising option; however, thus far they have been largely limited by the lack of energy-efficient nonlinear optical functions. Here, we experimentally demonstrate an all-optical Rectified Linear Unit (ReLU), which is the most widely used nonlinear activation function for deep learning, using a periodically-poled thin-film lithium niobate nanophotonic waveguide and achieve ultra-low energies in the regime of femtojoules per activation with near-instantaneous operation. Our results provide a clear and practical path towards truly all-optical, energy-efficient nanophotonic deep learning.

3.2 Introduction

Over the past decade, deep learning has revolutionized many important applications including computer vision, speech recognition, and natural language processing [1]. However, the explosive growth of modern deep learning models has quickly outpaced improvements in conventional von Neumann computing architectures and ushered in the use of dedicated hardware accelerators. The quest for ever-faster and more energy-efficient hardware for deep learning began with exploiting the graphics processing unit (GPU), then application-specific integrated circuits such as Google's tensor processing unit (TPU), and more recently the development of non-von Neumann analog architectures [2, 3]. Naturally, photonics has attracted attention as a promising candidate due to its potential for massive parallelism and ultrafast operation [4]. Indeed, optical neural networks (ONNs) have been experimentally demonstrated in a variety of platforms including free-space optics [5, 6, 7, 8, 9, 10, 11], optical fiber [12, 13, 14, 15, 16, 17], and photonic integrated circuits [18, 19, 20, 21, 22].

In general, deep neural networks require two major types of computations: (1) linear operations in the form of matrix multiplications and convolutions, which represent the synaptic connections of the network, and (2) nonlinear activation functions,

which represent the neuron activations. ONNs excel at performing energy-efficient linear operations in the optical domain, which forms the bulk of computations for deep learning. However, a major remaining roadblock is achieving scalable energy-efficient nonlinear activation functions, which comprises a smaller but essential part of the deep learning workload. Thus, the majority of ONN implementations still opt to utilize digital electronics to perform the nonlinear activation functions. In doing so, the optoelectronic and analog-to-digital conversion typically imposes significant speed and energy limitations. On the other hand, the demonstrated all-optical approaches based on various processes [17, 13, 19, 7, 23, 24, 25] are still too energy-intensive and/or slow compared to electronics. This is because photon–photon interactions are typically weak and require either high light intensities or high-Q resonant cavities, both of which are undesirable for scalable computing purposes. An all-optical, ultrafast, and energy-efficient nonlinear activation function is yet to be demonstrated to unlock the full capabilities of ONNs. Such a function should also be compact, highly scalable, and compatible with existing deep learning models.

In this work, we propose and experimentally demonstrate the first photonic device, to the best of our knowledge, that satisfies all the aforementioned criteria for an all-optical nonlinear activation function. It implements the Rectified Linear Unit (ReLU) function, defined as $\mathrm{ReLU}(x) = \max(0, x)$, which is one of the most widely used nonlinear activation functions for deep learning. The widespread adoption of the ReLU function was essential in sparking the deep learning revolution due to its favorable properties for backpropagation training and simple implementation in digital electronics [1]. However, its optical implementation has remained challenging and posed a major hurdle for the real-world applicability of ONNs.

3.3 Methods

3.3.1 Principle of operation

The operating principle of our device is illustrated in Fig. 3.1. We encode the signal information into the coherent optical field of pulses centered at frequency 2ω, with positive values represented by $\phi_{2\omega} = +\pi/2$ phase states, and negative values represented by $\phi_{2\omega} = -\pi/2$ phase states. By co-propagating the signal pulses with bias pulses centered at frequency ω, with fixed input power and phase at $\phi_\omega = +\pi/2$, we can induce different nonlinear optical effects for the two possible $\phi_{2\omega}$ signal phases depending on the value of the phase relationship $2\phi_\omega - \phi_{2\omega}$. For the positive signal values with phase $\phi_{2\omega} = +\pi/2$, the phase relationship yields $2\phi_\omega - \phi_{2\omega} = +\pi/2$. This induces second harmonic generation (SHG), which is a $\chi^{(2)}$ nonlinear optical process that converts two photons of frequency ω into a photon of frequency 2ω, hence depleting ω and amplifying 2ω. Conversely, for the negative signal values with phase $\phi_{2\omega} = -\pi/2$, the phase relationship yields $2\phi_\omega - \phi_{2\omega} = 3\pi/2 \rightarrow -\pi/2$. This induces degenerate optical parametric amplification (DOPA), which is the inverse process of SHG that converts a photon of frequency 2ω into two photons of frequency ω, hence depleting 2ω and amplifying ω. By judiciously choosing the length and bias power, we can achieve the desired shape of the ReLU

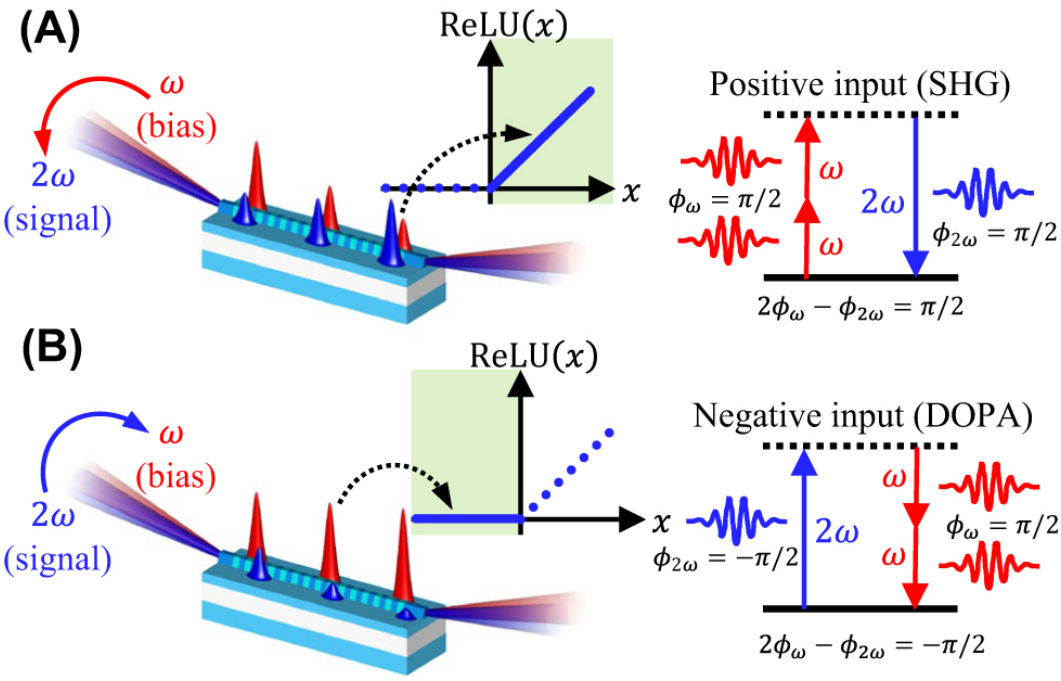

Figure 3.1: Operating principle of the all-optical ReLU function using a nonlinear photonic waveguide. (A) For positive inputs with phase of $\phi_{2\omega} = +\pi/2$, the phase relationship between the signal and bias is $2\phi_\omega - \phi_{2\omega} = \pi/2$, which causes SHG that depletes ω and amplifies 2ω. (B) For negative inputs, $\phi_{2\omega} = -\pi/2$, the phase relationship $2\phi_\omega - \phi_{2\omega} = 3\pi/2 \rightarrow -\pi/2$ causes DOPA that amplifies ω and depletes 2ω.

function. We emphasize that our approach utilizes coherent parametric processes which allows us to implement both positive and negative values (i.e. the information is encoded in the field amplitude), unlike previous optical [7, 13, 17, 19, 23, 24, 25] and optoelectronic methods [11, 14, 15, 16, 21, 26, 27, 28, 29] based on incoherent absorption processes that can only implement positive values (i.e. the information is encoded in the optical power).

3.3.2 Device design

To implement the $\chi^{(2)}$-based ReLU function, we use a periodically poled thin-film lithium niobate (PPLN) nanophotonic waveguide that exploits the strong and instantaneous $\chi^{(2)}$ optical nonlinearity of lithium niobate and tight spatial confinement of the waveguide modes to enhance the nonlinearity [30]. Additionally, careful qausi-phase matching and dispersion engineering enables ultra-broadband and low-energy interactions over mm-long propagation lengths, further enhancing the nonlinear optical processes using femtosecond laser pulses [31, 32, 33]. Images of the device are shown in Fig. 3.2. The PPLN nanophotonic waveguide is $L = 2.5$ mm long and was fabricated on a 700 nm thick X-cut MgO-doped lithium niobate thin-film on 2-μm-thick SiO_2 with lithium niobate substrate by dry etching

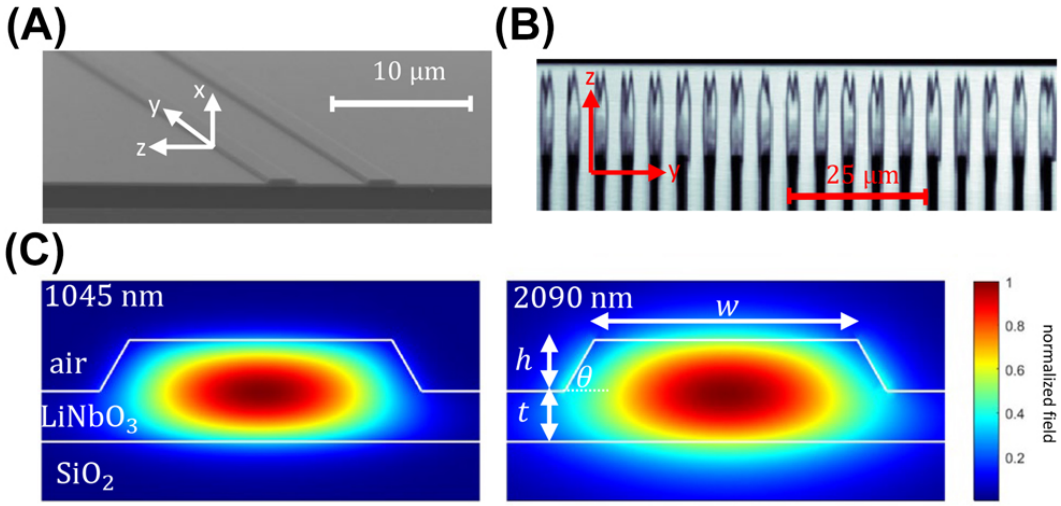

Figure 3.2: Images of the PPLN nanophotonic waveguide. (A) Scanning electron microscope image of the ridge waveguide. (B) Two-photon absorption microscope image of the PPLN ferroelectric domains with poling period of 5 μm. (C) Simulated electric field distributions of the fundamental TE modes at 1045 nm (2ω) and 2090 nm (ω).

with Ar^+ plasma, achieving smooth ridge side-walls with slant angle of $\theta \approx 60°$ as shown in Fig. 3.2(A). The waveguide was electrically poled with a period of 5.17 μm, as shown in Fig. 3.2(B), to ensure efficient SHG and DOPA. Dispersion engineering of the fundamental TE mode of the ridge waveguide, shown in Fig. 3.2(C), allows for negligible group velocity mismatch and group velocity dispersion of ω and 2ω pulses centered at 1045 nm and 2090 nm, respectively. This enforces good temporal overlap of the pulses over the entire PPLN propagation length. The ideal parameters found from simulation were a ridge top width of $w = 1700$ nm and etch-depth of $h = 350$ nm. See [33] for further details about fabrication and dispersion engineering of PPLN nanophotonic waveguides.

3.4 Results

3.4.1 Femtojoule ReLU function

The measured response of the all-optical ReLU is shown in Fig. 3.3.The nonlinear function given by the PPLN was measured using a free-space chip characterization setup. The source at 1045 nm (signal) was a Yb:fiber mode-locked laser producing 75-fs long pulses at a 250-MHz repetition rate (Menlo Systems Orange). The same laser pumped a homemade degenerate optical parametric oscillator to generate the pulses at 2090 nm (bias). The 2ω and ω pulses were coupled into and out of the PPLN using reflective objectives focused on the waveguide facets. Finally, the relative phase of the 2ω signal and ω bias was set using a delay arm, and the power varied using a tunable attenuator. See Supplementary Section 3.7.1 for further details about the experimental setup.

Our experimental results show good agreement with the ideal ReLU function

($R^2 = 0.9895$), and demonstrates energy-efficient signal pulse energies in the regime of femtojoules per activation. Note that the important feature of the function is its nonlinear shape, since scaling/shifting the horizontal/vertical directions can be accomplished with linear optical transformations. In theory, the ideal ReLU function requires an arbitrarily long PPLN and low bias pulse energy. However, in practice we must choose the bias pulse energy so as to best approximate the ReLU function given our fixed device length. Thus, there are small discrepancies around $E_{2\omega}(0) = 0$, since neither the SHG nor DOPA processes sufficiently saturate at the ultra-low energies. The maximum cutoff pulse energy is determined by the onset of supercontinuum generation from strong back-conversion processes, which undesirably degrades the pulse shape. To verify that the expected device response matches our physical picture of the operating principle, we also performed nonlinear pulse propagation simulations of the PPLN nanophotonic waveguide. See Supplementary Section 3.7.3 for more details about the simulation methods.

Remarkably, we show that the PPLN nanophotonic waveguide can also approximate other commonly used variants of the ReLU function, simply by tuning the

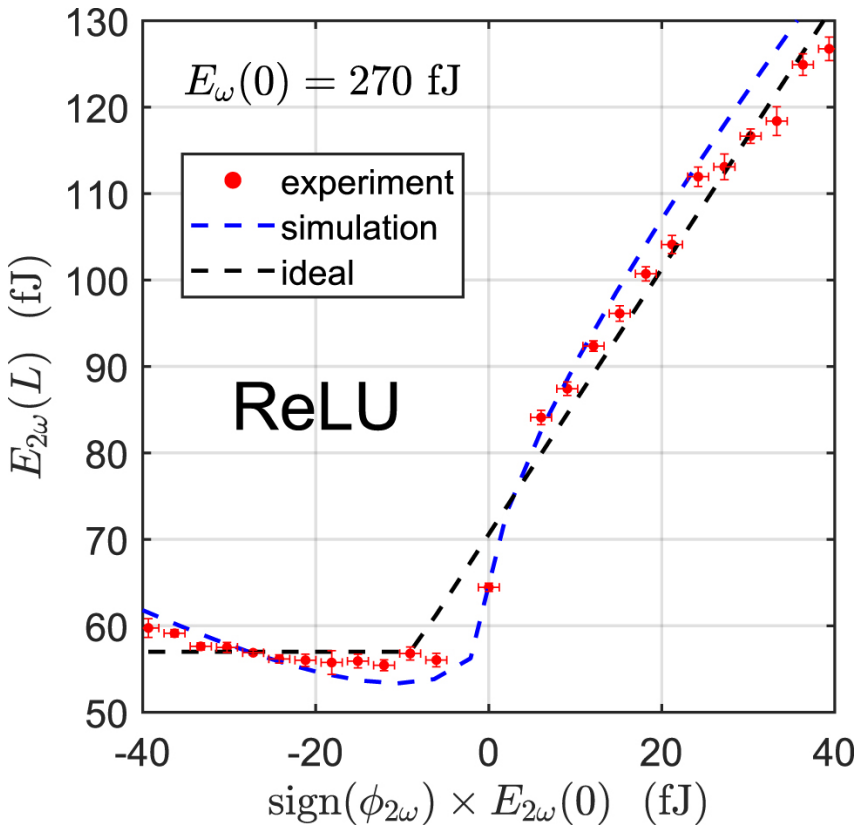

Figure 3.3: Output signal pulse energy versus input signal pulse energy for both negative and positive inputs. There is good agreement between the ideal ReLU function (dashed black line), simulation (dashed blue line) and experimental results (red circles) for a bias pulse energy of $E_\omega(0) = 270$ fJ, and signal pulse energies of femtojoules per activation.

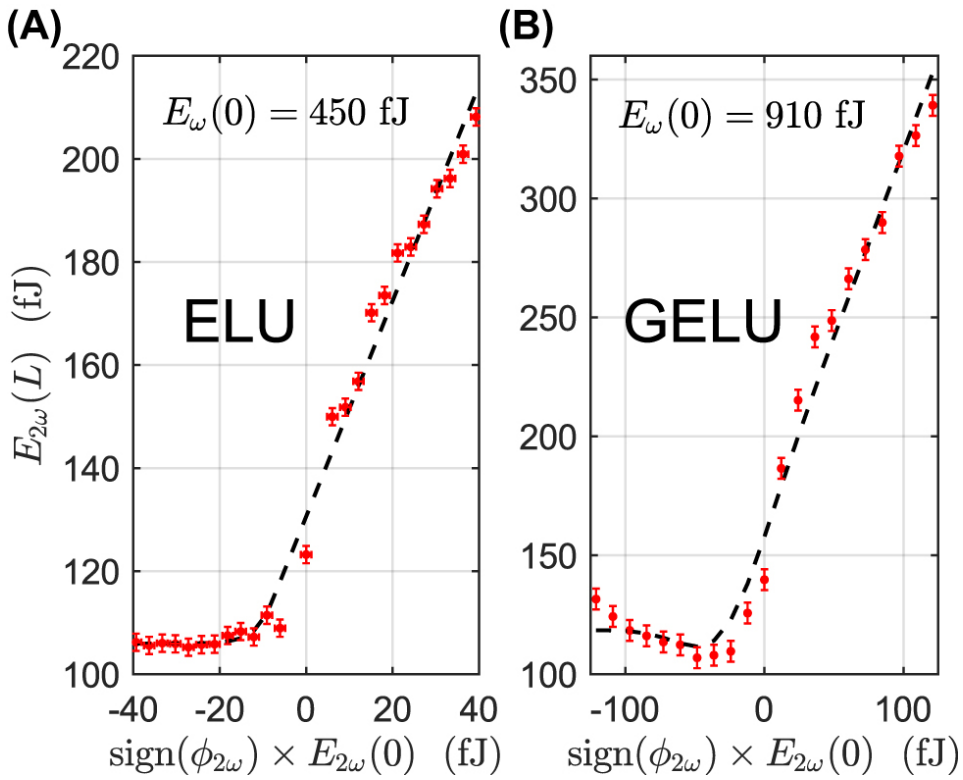

Figure 3.4: Other variants of the ReLU function can be approximated by tuning the bias pulse energy. For example, the (a) ELU function using bias pulse energy of $E_\omega(0) = 450$ fJ and (b) GELU function using bias pulse energy of $E_\omega(0) = 910$ fJ. Ideal function curves are shown by the dashed black lines, and experimental results with red circles.

bias pulse energy. For example, the Exponential Linear Unit (ELU) defined as $\mathrm{ELU}(x) = x$ if $x > 0$ and $\mathrm{ELU}(x) = \exp\{(x)\} - 1$ if $x < 0$, which has been shown to outperform the ReLU function in certain cases [34], is achieved using a bias pulse energy of $E_\omega(0) = 450$ fJ as shown in Fig. 3.4(A). In addition, we also implement the Gaussian Error Linear Unit (GELU) defined as $\mathrm{GELU}(x) = x\Phi(x)$ where $\Phi(x)$ is the Gaussian cumulative distribution using a bias pulse energy of $E_\omega(0) = 910$ fJ as shown in Fig. 3.4(B). The GELU function is used extensively in Transformer networks for natural language processing, which are regularly amongst the largest deep learning models [35]. Thus, our all-optical PPLN nanophotonic waveguide implementation gains greater real-world applicability by being compatible with a wide range of existing deep learning models, especially the largest models where energy efficiency is paramount. Indeed, compatibility has been problematic in previous implementations of optical [7, 17, 23, 24, 25] and optoelectronic [11, 14, 15, 26, 29] nonlinear activation functions, which do not reflect the most commonly used functions in digital electronic neural networks. By alleviating this problem, we expand the potential functionality of ONNs by avoiding the need to train new specialized models.

3.4.2 Ultrafast time response

Ideally, the time per activation should be near-instantaneous due to the ultrafast $\chi^{(2)}$ nonlinearity in lithium niobate. However, in practice, the response time is limited by the finite phase-matching bandwidth as well as non-zero group velocity mismatch, group velocity dispersion, and higher-order dispersion terms. To determine the response time of the device, we used the pump–probe technique commonly used to characterize all-optical switches [32, 36, 37] (see Supplementary Section 3.7.4 for more details). In this case, the pump pulse is the ω pulse and the probe pulse is the 2ω pulse. We measured the ultrafast ReLU dynamics by varying the time delay between the ω and 2ω pulses at a fixed pulse energy. Fig. 3.5 shows the intensity envelope of the pump–probe signal as the time delay is varied as well as the autocorrelation of the input ω pulse.

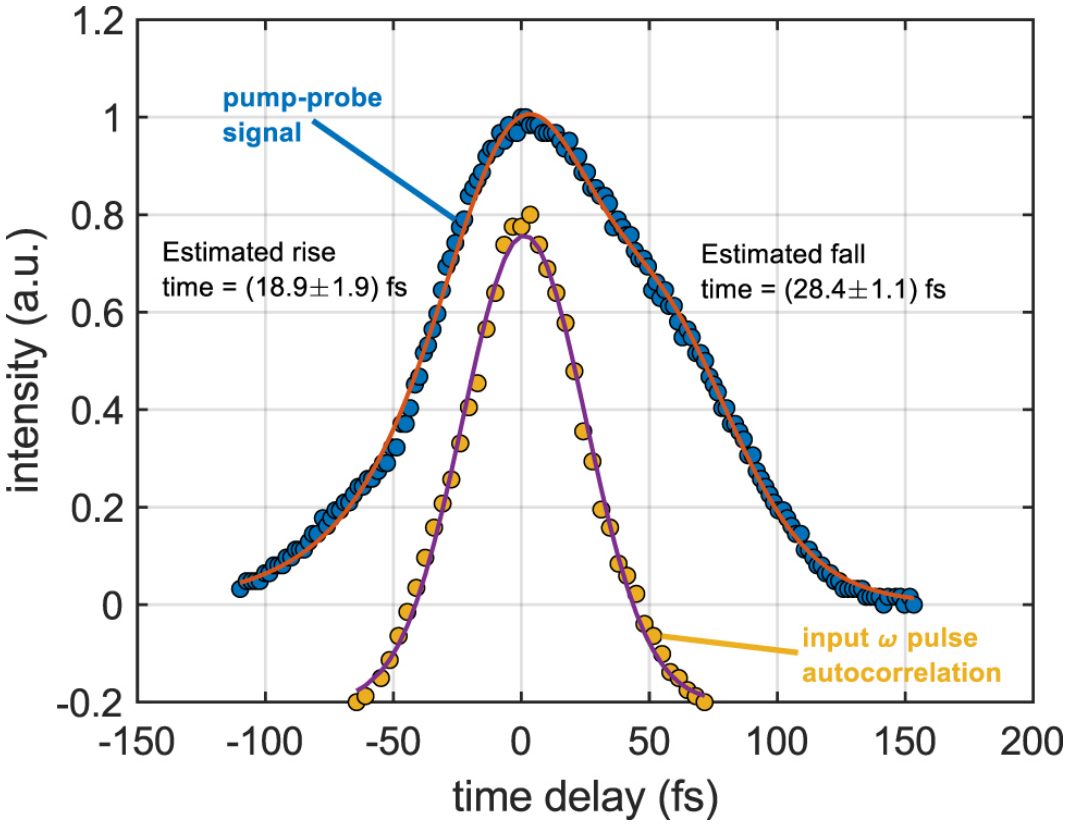

Figure 3.5: Pump–probe ultrafast timing measurements of the ReLU dynamics. The autocorrelation (yellow circles shifted vertically for clarity) of the input ω pulse is well-explained by a Gaussian profile (purple line) with FWHM of (56.4 ± 1.5) fs. The pump–probe signal obtained at a fixed pulse energy (blue circles) is fit (orange line) by convolving the input autocorrelation with exponential growth and decay for positive and negative time delays, respectively. The best fit yields a rise time of (18.9 ± 1.9) fs and a fall time of (28.4 ± 1.1) fs.

3.4.3 Simulated Deep Learning Performance

One distinct advantage of our approach is that, unlike previous all-optical [19] and optoelectronic [21] nonlinear activation functions, it can faithfully reproduce the ideal ReLU function, which uses both positive and negative values. Therefore, we can leverage the large number of existing pretrained deep learning models that use the ReLU function (or its variants) for nonlinear activations. Although ONNs have been demonstrated that accurately reproduce linear operations such as matrix multiplication and convolution, the use of atypical nonlinear activation functions in the optical domain has required the training of new custom deep learning models [38, 39]. To improve upon this, we simulated the performance of the all-optical ReLU function when used as part of a pretrained convolutional neural network (CNN) for the prototypical task of MNIST handwritten digits image classification [40]. The MNIST dataset contains 28×28 pixels gray-scale images of handwritten digits with 50,000 training samples and 10,000 test samples. We used a standard CNN architecture (see Supplementary Section 3.7.5 for full details) containing convolutional layers and ideal ReLU layers followed by a fully-connected layer and softmax classification output. The pretrained CNN achieved an ideal test accuracy of 99.13%. Next, the ideal ReLU layers were replaced with custom layers representing the experimentally measured ReLU response (after proper shifting/scaling) without changing any of the other layers. This caused a slight drop in test accuracy to 98.8% due to the slight deviations between the experimentally measured and ideal ReLU functions. To remedy this, the CNN was then fine-tuned by training for only 2 epochs (the CNN sees each sample once per epoch) to regain the ideal pretrained model accuracy of 99.13% as shown in Fig. 3.6. Fine-tuning is necessary for any analog hardware implementation due to unavoidable fabrication errors, noise and other nonidealities encountered [41]. Note that this method requires far less time compared to previous proposals for training new custom ONN models, which required >25 training epochs [38, 39]. Therefore, our all-optical ReLU provides the missing link to allow ONNs to take advantage of existing pretrained models. We note that the softmax classification layer is yet to be faithfully implemented in an ONN which accounts for a small portion of the computation compared to the convolutions, matrix multiplications and ReLU nonlinear activations.

3.5 Discussion

3.5.1 Comparison of energy and time per activation

In this section, we compare the PPLN nanophotonic waveguide to other optical [13, 17, 19, 23], optoelectronic [11, 14, 15, 16, 21, 26, 27, 28, 29], analog electronic [42, 43, 44], and digital electronic [45] nonlinear activation functions to demonstrate the state-of-the-art performance of our device. In this case, the appropriate figure of merit is the energy-time product, which properly accounts for both the energy consumed and time taken per activation. To quantify the energy per activation, we follow the convention in [39], as being the energy needed to generate a 50% change in the power transmission with respect to the transmission with null input. In this case, our device has an energy per activation of ~16 fJ. The bias pulse energy is not

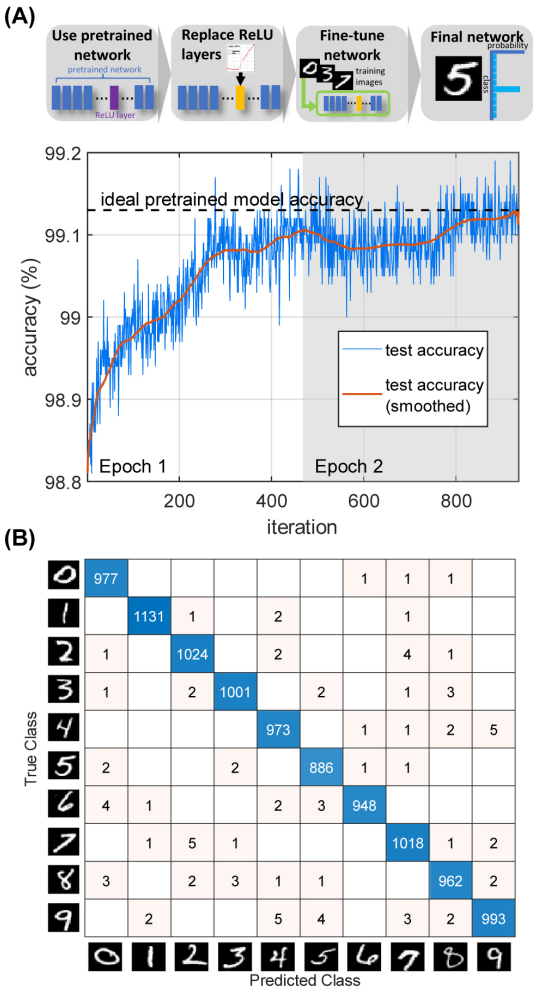

Figure 3.6: Simulated deep learning performance of the experimentally measured all-optical ReLU function for MNIST handwritten digits image classification. (A) A pretrained CNN was used where the ideal ReLU layers are replaced with custom layers representing the experimentally measured ReLU response (after shifting/scaling) then fine-tuned by training for 2 epochs (batch size of 128) to improve the test accuracy (blue line) back to the ideal pretrained model accuracy (dashed black line). (B) Confusion matrix on the MNIST task for the final network, which achieved 99.13% test accuracy.

included since it is not destroyed and can, at least theoretically, be reused for many signal pulses. This is because the bias pulse is not dissipated as heat, unlike the case often encountered for absorption-based processes. Assuming perfect phase-matching and that positive/negative values occur equally likely, then the bias pulse should be amplified/deamplified equally likely by the processes of DOPA/SHG, respectively. The time per activation is given by the signal pulse width of ~75 fs, owing to the near-instantaneous $\chi^{(2)}$ nonlinearity of lithium niobate as explained in Section 3.3.2. Therefore, we achieve an energy-time product of 1.2×10^{-27} J s.

The energy and time per activation of our device is compared to other experimental demonstrations in Fig. 3.7.

We attempted to consider device-level metrics wherever possible to provide a fair comparison, however, we acknowledge that this was not always possible for nonlinear activations as part of complete networks since fan-out and cascadability constraints impose additional energy and time costs. Despite this, the outstanding metrics of our device represents a significant breakthrough for optical nonlinear activation functions. For state-of-the-art digital electronics, such as the NVIDIA A100 Tensor Core GPU [46] based on 7-nm process node [47], we generously assume that the ReLU function consumes ~1 fJ per activation, and occurs in a single 1 GHz clock cycle. We see that, although our device still has an order of magnitude greater energy per activation, the time per activation is four orders of magnitude faster. Hence, we achieve an energy-time product that is three orders of magnitude better than state-of-the-art digital electronics. Our numerical simulations (Supplementary Section 3.7.3) predict that the PPLN nanophotonic waveguide can realistically achieve a ReLU-like response with sub-femtojoule energy per activation.

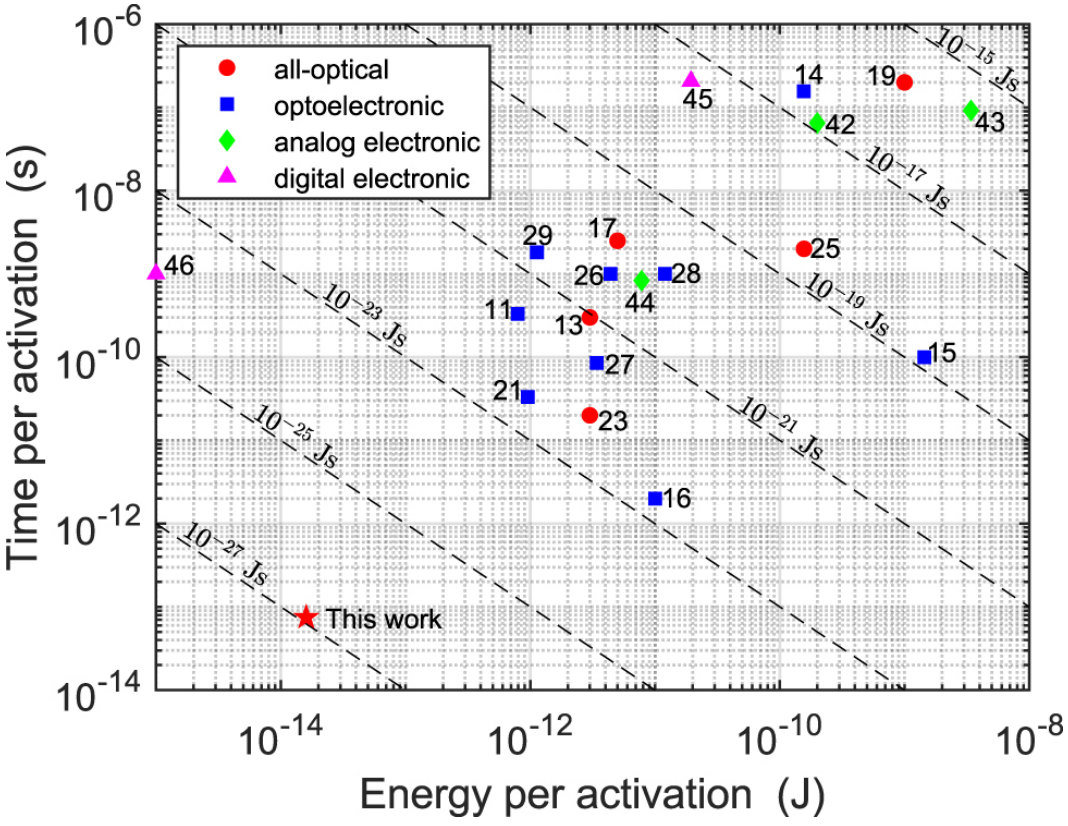

Figure 3.7: Comparison of energy and time per activation of this work (red star) to previous all-optical (red circle), optoelectronic (blue square), analog electronic (green diamond), and digital electronic (magenta triangle) nonlinear activation functions. The numeric labels show reference numbers and dashed black lines show the energy-time product contours.

This would even surpass the energy efficiency of state-of-the-art digital electronics. We attribute the discrepancy between our experimental results and the theoretically predicted limits for the energy scale to the imperfect phase-matching and fabrication error of our device. It is worth mentioning how these device-level metrics potentially translate to those of complete neural networks. In this case, additional system-level energy costs such as laser wall-plug efficiency and transport losses can significantly increase the effective activation energy. However, we note that the same is also true in digital electronics such as GPUs where electrical data movement energy costs can exceed the actual switching energy by several orders of magnitude [48].

3.5.2 Potential network architectures

So far, we have demonstrated how PPLN nanophotonic waveguides can implement all-optical, ultrafast, energy-efficient nonlinear activation functions, which forms only one building block of a full neuron. In this section, we briefly discuss how our device can be integrated into a complete ONN architecture. Interestingly, DOPA and SHG are theoretically noiseless amplification/deamplification processes. Therefore, the all-optical ReLU function should not contribute additional noise to a photonic neural network. In principle, the all-optical ReLU is compatible with most existing ONN architectures that can accurately implement linear operations such as matrix multiplication and convolutions. However, in practice, the speed bottleneck will likely be the encoding of information into the required coherent optical amplitudes. In this case, PPLN nanophotonic waveguides can be monolithically integrated with high-speed electro-optic modulators in thin-film lithium niobate, demonstrated to achieve bandwidths beyond 100 GHz [49]. Furthermore, the light sources can also be integrated on-chip using thin-film lithium niobate optical parametric oscillators [50]. Therefore, all the fundamental building blocks needed for a complete ONN in thin-film lithium niobate already exist. Given the rapid increases in scalability of thin-film lithium niobate photonics, we are confident that a complete ONN can be demonstrated in the near-future. One potential approach is to use Mach–Zehnder interferometer meshes [18] or photonic tensor cores with waveguide cross-bar arrays [20] to implement the linear matrix multiplications, then cascaded into PPLN nanophotonic waveguides to perform nonlinear activations. Another promising method is to use a time-multiplexed architecture similar to ones demonstrated for coherent Ising machines [51] or photonic reservoir computers [14, 15]. See Supplementary Section 3.7.6 for more detailed descriptions and schematics of potential integrated lithium niobate nanophotonic neural networks for deep learning.

A valid concern is harnessing the full capabilities of the all-optical ReLU function. It is challenging to fully exploit the ultrafast time response of the nonlinear optical processes since current interfacing electronics is currently limited to GHz bandwidths [48]. However, this should not automatically preclude the use of ultrafast nonlinear optics for optical computing. For example, coherent Ising machines [51] and optical signal processing [52], which require optical input and optical output, are prime candidates for near-term applications. In the future, all-optical computing hardware using such parametric ultrafast nonlinear activation functions

may operate with THz clock rates. Crucially, the all-optical ReLU is cascadable since DOPA/SHG are inherently energy-conserving, i.e. the output is sufficiently energetic to serve as the input trigger for at least one other neuron. If multiple outputs are desired, i.e. fan-out, then intermediate amplification is needed, which can be provided by the same type of PPLNs demonstrated. Therefore, in principle, the bottleneck of optoelectronic conversion and analog-to-digital conversion can be bypassed.

3.6 Conclusion

In conclusion, we have demonstrated an all-optical ultrafast ReLU function using a PPLN nanophotonic waveguide. It has an energy per activation of ~16 fJ and time per activation of ~75 fs, thus achieving a state-of-the-art energy-time product of 1.2×10^{-27} J s. Furthermore, we demonstrated how the same device can be used to implement other common variants of the ReLU function, and showed how it can exploit existing pretrained deep learning models to greatly reduce training time. Given the simplicity of our device, and the rapid improvements in scalability of thin-film lithium niobate photonics, we envisage that it will be able to replace periphery digital electronic circuits for calculating nonlinear activations in ONNs. Therefore, we have presented a clear and practical path towards truly all-optical, energy-efficient photonic deep learning.

3.7 Supplementar Information

3.7.1 Experimental setup

The experimental setup for the optical ReLU measurements is depicted in Fig. 3.8. The pump laser is a mode-locked Yb-fiber laser which provides 70 fs pulses at 1045 nm with up to 1 W average power at a 250 MHz repetition rate (Menlo Systems Orange A). The laser output is then split into two paths. The first path is sent to a synchronously pumped degenerate optical parametric (SPDOPO) oscillator based on periodically-poled lithium niobate (PPLN) which is used to efficiently generate pulses at 2090 nm[53]. The OPO is locked using a "dither and lock" scheme, facilitated by the Lock-In + PID application for Red Pitaya [54, 55]. A variable ND filter is added to the output of the OPO to control the 2090 nm power sent to the device. The second 1045 nm path is sent to a delay stage. Course adjustment of the delay is done through manual tuning of the stage position and micrometer arm while fine adjustment is performed using a piezoelectric actuator. This delay enables temporal overlap of the two paths, and fine adjustment is used to change the relative phase of the fundamental and second harmonic for the OPA process. Like the other path, a variable ND filter is also placed along this path for adjusting the 1045 nm power. The two paths are recombined at a dichroic mirror with high transmission at 1045 nm and high reflectivity at 2090 nm before going to the device.

Focusing to and coupling from the device is done using a reflective objective (Newport 50102-02). Temperature tuning of the device for fine adjustment of the quasi-phase matching condition is done using a thermoelectric cooling stage (TEC).

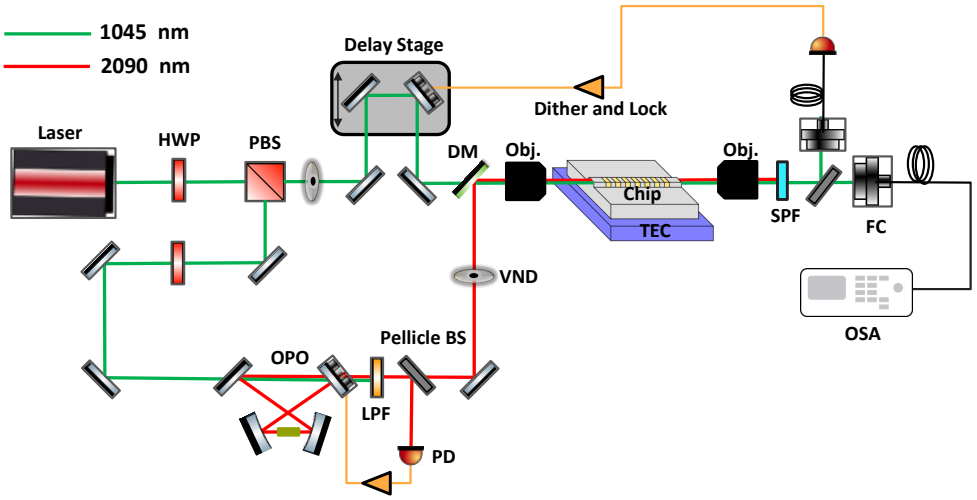

Figure 3.8: Experimental Schematic for all-optical ReLU measurements. The pump laser at 1045 nm is first split into two paths. One beam is used to pump our SPDOPO above threshold generating signal at centered at 2090 nm. The other beam is guided to a delay stage and further overlaps with the 2090 nm OPO signal at a dichroic mirror. Both beams are then coupled in and out from the chip using high NA reflective objectives. Next, the waveguide output is filtered with a short pass filter for filtering out the 2090 nm followed by splitting 1045 nm into two paths. Both of the 1045 nm beams are coupled into multimode fibers; one beam is measured by the OSA while the other beam is used to lock the delay stage. PBS: Polarizing beamsplitter, HWP: Half-wave plate, DM: Dichroic mirror, Obj.: Reflective objective, VND: Variable neutral-density filter, LPF: Long-pass filter, SPF: Short-pass filter, FC: Fiber Coupler, OSA: Optical spectrum analyzer, PD: Photodetector, OPO: Optical parametric oscillator.

The output of the chip is short-pass filtered around 1700 nm to remove all remaining signal at 2090 nm and then split into two paths. The signal on one path is measured with a detector and used for feedback to the delay stage. A "dither and lock" scheme, similar to that used for the OPO, is employed here to lock the relative phases of the two inputs to switch between amplification and deamplification in the OPA process [54, 55]. The second path is coupled to fiber and sent to an optical spectrum analyzer (OSA) for measuring the output power and spectrum (Yokogawa AQ6370D).

3.7.2 Device fabrication and characterization

For our devices, a wafer with 700 nm of X-cut MgO-doped LN on top of 2 μm of SiO_2 was used. 15 nm of Cr underneath 55 nm of Au were then e-beam evaporated and patterned via e-beam lithography to form poling electrodes. 300V pulses

were used to pole the chip, and the quality was confirmed using second harmonic microscopy. Waveguides were subsequently patterned on the chip using hydrogen silsesquioxane (HSQ) as the e-beam resist and 15 nm of Ti as an adhesion layer. They were dry etched with Ar^+ plasma in an inductively-coupled plasma reactive-ion etcher (ICP-RIE), and the remaining resists and side-wall re-deposition were removed using Buffered oxide etchant (BOE) and RCA-1. Finally, the waveguide facets were mechanically polished.

In Fig. 3.9, we display the measured spectrums of 2ω, ω and their non-linear interaction in the waveguide. (a) and (b) show the input spectrums of 2ω and ω, respectively and (c) shows the evolution of 2ω pulse as the phase difference is modulated. We can see that for the positive signal values corresponding to the phase relationship $2\phi_\omega - \phi_{2\omega} = \pi/2$, the 2ω signal grows due to SHG process while depleting the ω pulse. On the other hand, for the phase relationship $2\phi_\omega - \phi_{2\omega} = -\pi/2$, the ω pulse grows due to optical parametric amplification, thereby depleting the 2ω as evident from the dip in the spectrum.

We now estimate the input and output coupling efficiencies of our device. A detailed discussion is provided in previous work on optical parametric generation (OPG) and amplification (OPA) [33, 56]; here we outline the main steps. For a degenerate OPG process in the high parametric gain regime, the generated average photon-number in an ideal case is given by

$$\langle N \rangle \approx \frac{1}{4} e^{2L\sqrt{\eta P}}, \tag{3.1}$$

where P, L and η are pump power, interaction length, and non-linear interaction efficiency. In the presence of experimental imperfections such as off-chip coupling, coupling to optical fibers, and detection inefficiencies, the average photon-number is given as

$$\langle N \rangle \approx \frac{\eta_1}{4} e^{2L\sqrt{\eta_2 P}}, \tag{3.2}$$

where all optical losses on the OPG signal are combined in η_1 parameter and η_2 quantifies the non-linear interaction strength and the input coupling efficiency of our second harmonic signal. From our measured data for OPG power, we determine the average photon number for various values of the second harmonic pump. By fitting the data, we can extract the η_1 and η_2 parameters. In Fig. 3.10, the measured average number of photons are displayed with respect to the input pump power. From the fit, we extract $\eta_1 \approx 0.20$, i.e., the estimated output coupling loss is about 7 dB, which shows a good agreement with our previous paper [33, 56]. Given the total coupling loss measured at low power, we then determine the input coupling loss as the difference between total and output coupling losses. We note that coupling losses < 1 dB per facet have been reported for thin-film lithium niobate photonics [57], which is promising for large-scale circuits.

3.7.3 Simulation method

We numerically solved an analytical nonlinear envelope equation (NEE) in the frequency domain using a split-step Fourier technique to simulate the pulse propaga-

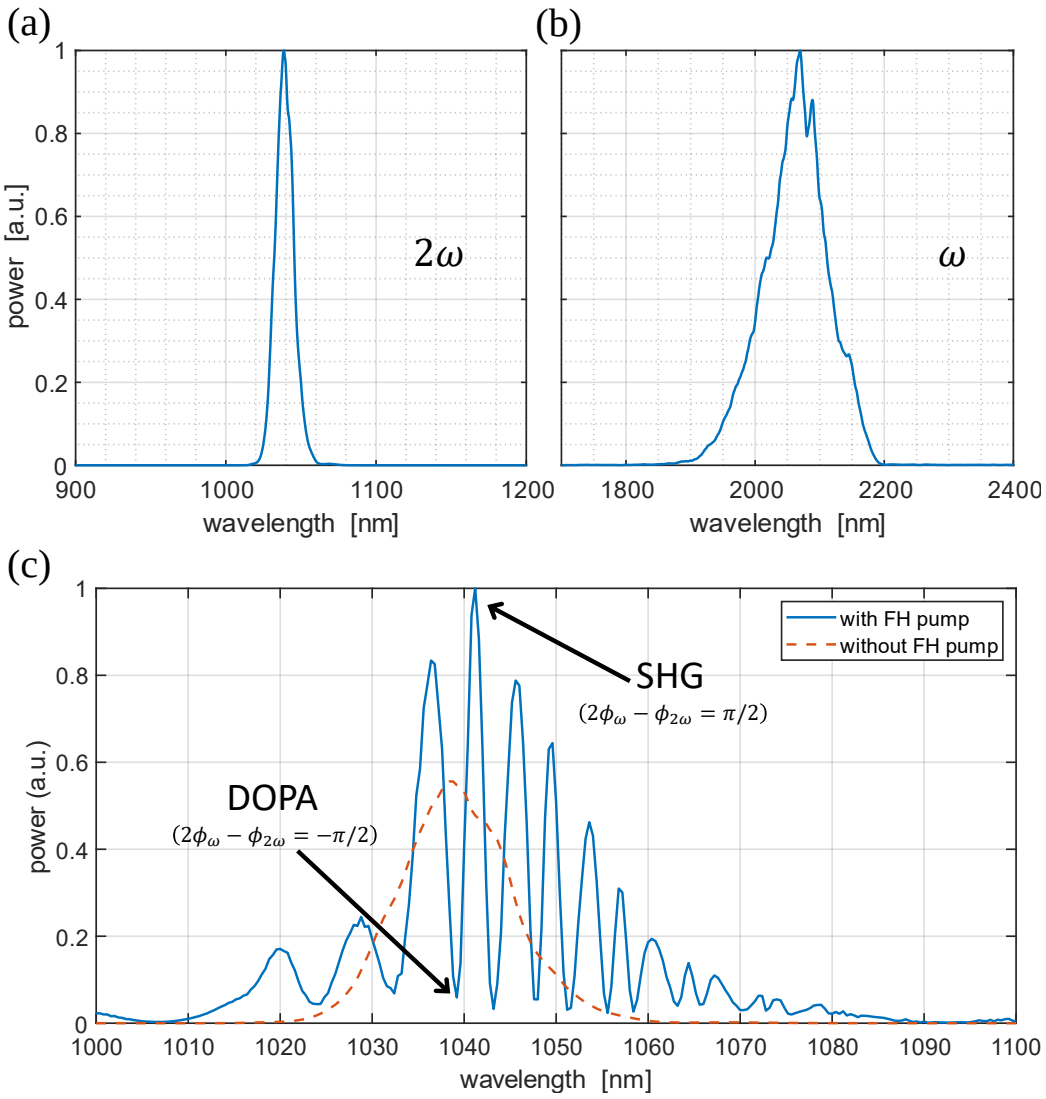

Figure 3.9: Measured spectrums of ω and 2ω. In (a) and (b) correspond to the waveguide input 2ω and ω, respectively. (c) shows the evolution of the waveguide output 2ω as the phase difference between 2ω and ω is modulated.

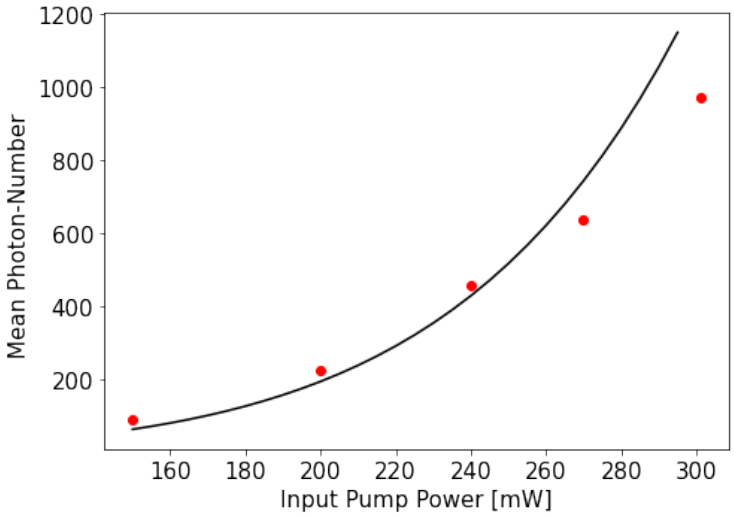

Figure 3.10: Number of signal photons as the input pump power is varied. The red points are experimentally measured data for several values of pump power and the black curve shows the exponential fit used for estimating the output coupling efficiency, i.e., the η_1 parameter in Eq. 5.47.

tion and nonlinear dynamics in the waveguide. The nonlinear step was implemented using fourth-order Runge-Kutta method. We obtained the NEE by ignoring counter-propagating modes, which are usually phase mismatched, and assuming a constant nonlinear coefficient across the entire simulation bandwidth. The fundamental and second harmonic pulses were assumed to have a transform-limited, hyperbolic-secant profile. The NEE is given by:

$$\frac{\partial A}{\partial z} = -i\left[\beta(\omega) - \beta_0 - \frac{\Omega}{v_{ref}} - i\frac{\alpha}{2}\right]A - \frac{i\omega\varepsilon_0 X_0}{8}d(z) \\ \mathcal{F}_\Omega\left\{a^2(z,t)e^{j\phi(z,t)} + 2a(z,t)a^*(z,t)e^{-j\phi(z,t)}\right\}, \quad (3.3)$$

where $A(z,\omega)$ is the complex amplitude of the field during propagation, $a(z,t)$ is the time domain representation of $A(z,\Omega)$, $\phi(z,t) = \omega_0 t - (\beta_0 - \omega_0/v_{ref})z$, β_0 is the waveguide propagation constant at frequency ω_0, $\Omega = \omega - \omega_0$ is the envelope frequency, ω is the optical frequency, α is the attenuation constant, $d(z) = \pm 1$ is the instantaneous sign of the nonlinear coefficient due to quasi-phase matching, $\mathcal{F}_\Omega$ is the Fourier transform in Ω, and X_0 is the effective nonlinear coefficient.

To simulate the ReLU response of our experimental device, shown in Fig. 3.3 in the main text, we assumed $\alpha \approx 0.1$ dB/cm and used the following waveguide geometry obtained from atomic force microscope measurements: waveguide top width of 1768 nm, ridge height (etch depth) of 377 nm, and a total lithium niobate thin-film thickness (before etching) of 713 nm. We use the effective nonlinear coefficient as a fitting parameter to match the experimental data and inferred a value of $X_0 \approx 0.36 \times 10^{-12}$ V^2, which is about $\sim 1/3$ of its ideal value.

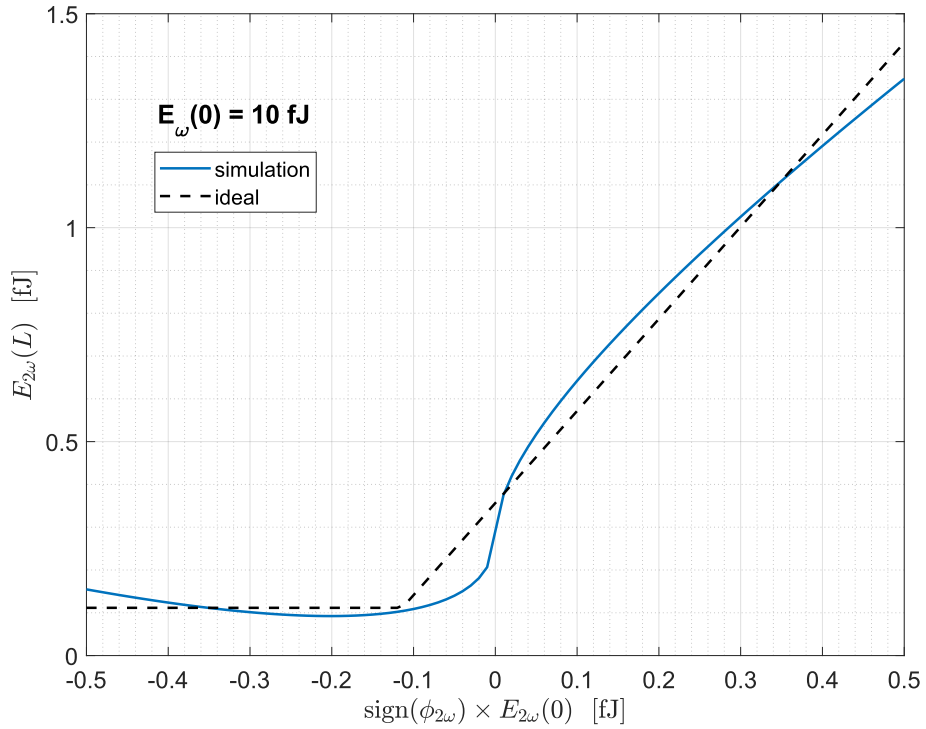

Figure 3.11: Simulated ReLU-like nonlinear activation function with sub-femtojoule energies achieved using bias pulse energy of $E_\omega(0) = 10$ fJ and ideal PPLN parameters.

Given the fabrication error and imperfect phase-matching of our device, we could only experimentally achieve an energy of $\sim$ 16 fJ per activation. However, Fig. 3.11 shows the simulated ideal performance of a PPLN with length $L = 2.5$ mm, ridge top width of $w = 1700$ nm, etch-depth of $h = 350$ nm, and bias pulse energy of $E_\omega(0) = 10$ fJ. We see that it can achieve a ReLU-like function with sub-femtojoule energy per activation.

3.7.4 Fitting of pump-probe signal

The input autocorrelation was fit using a Gaussian profile:

$$G(t) = \frac{1}{\sigma\sqrt{2\pi}} e^{\frac{-t^2}{2\sigma^2}}, \tag{3.4}$$

where σ is related to the FWHM by $FWHM = 2\sigma\sqrt{2\ln 2}$. The exponential function with characteristic decay time of $\tau = 1/\lambda$ is defined as:

$$F(t) = e^{-\lambda t}. \tag{3.5}$$

The convolution between $G(t)$ and $F(t)$ is defined as:

$$I(t') = F(t) * G(t) = \frac{1}{\sigma\sqrt{2\pi}} \int_0^\infty e^{-\lambda t} e^{-\frac{(t'-t)^2}{2\sigma^2}} \, dt \, . \tag{3.6}$$

We fit the pump-probe signal with exponential growth and decay functions for positive and negative time delays, respectively, convolved with the input autocorrelation by using the analytical formula for Eq. 3.6:

$$I(t') = \frac{1}{2} e^{-\lambda\left(t'-\sigma^2\lambda/2\right)} \left[1 + \operatorname{erf}\left(\frac{t'-\sigma^2\lambda}{\sqrt{2}\sigma}\right)\right] , \tag{3.7}$$

where $\operatorname{erf}(x) = \frac{2}{\sqrt{\pi}} \int_0^x e^{-z^2} \, dz$ is the error function.

3.7.5 Convolutional neural network architecture

The pretrained convolutional neural network (CNN) architecture is shown in Fig. 3.12. The CNN was trained on the MNIST handwritten digits image classification [58] using stochastic gradient descent with momentum (SGDM) with initial learn rate of 0.01 and batch size of 128. For fine-tuning after the ideal ReLU layers were replaced with custom layers representing the experimentally measured ReLU response, the initial learn rate was decreased to 0.001.

	Name	Type	Activations	Learnables
1	imageinput 28×28×1 images with 'zerocenter' normalization	Image Input	28×28×1	-
2	conv_1 8 3×3×1 convolutions with stride [1 1] and padding 'same'	Convolution	28×28×8	Weights 3×3×1×8 Bias 1×1×8
3	batchnorm_1 Batch normalization with 8 channels	Batch Normalization	28×28×8	Offset 1×1×8 Scale 1×1×8
4	relu_1 ReLU	ReLU	28×28×8	-
5	maxpool_1 2×2 max pooling with stride [2 2] and padding [0 0 0 0]	Max Pooling	14×14×8	-
6	conv_2 16 3×3×8 convolutions with stride [1 1] and padding 'same'	Convolution	14×14×16	Weights 3×3×8×16 Bias 1×1×16
7	batchnorm_2 Batch normalization with 16 channels	Batch Normalization	14×14×16	Offset 1×1×16 Scale 1×1×16
8	relu_2 ReLU	ReLU	14×14×16	-
9	maxpool_2 2×2 max pooling with stride [2 2] and padding [0 0 0 0]	Max Pooling	7×7×16	-
10	conv_3 32 3×3×16 convolutions with stride [1 1] and padding 'same'	Convolution	7×7×32	Weights 3×3×16×32 Bias 1×1×32
11	batchnorm_3 Batch normalization with 32 channels	Batch Normalization	7×7×32	Offset 1×1×32 Scale 1×1×32
12	relu_3 ReLU	ReLU	7×7×32	-
13	fc 10 fully connected layer	Fully Connected	1×1×10	Weights 10×1568 Bias 10×1
14	softmax softmax	Softmax	1×1×10	-
15	classoutput crossentropyex with '0' and 9 other classes	Classification Output	-	-

Figure 3.12: Pretrained convolutional neural network architecture.

3.7.6 Potential integrated photonic neural networks

A promising approach to integrating the all-optical ultrafast ReLU into a complete ONN is to monolithically integrate it with high-speed electro-optic modulators in thin-film lithium niobate nanophotonic circuits. Fig. 3.13 shows two examples of how this can be accomplished. One method, shown in Fig. 3.13(a), uses a spatially-multiplexed approach. It consists of a mesh of Mach-Zehnder inteferometers, akin to those demonstrated in silicon photonics [18], to perform linear operations, directly followed by an array of PPLNs to perform the ReLU activations. Therefore, in this approach, each neuron represents a separate PPLN and the entire neural network layer is computed in a constant time step. Subsequent layers are identical in structure and can be directly cascaded following the array of PPLNs. The bias pulse can be directly fed to each PPLN using out-of-plane couplers as shown in Fig. 3.13(a), or by using in-plane photonic crossbar switches. The bias and signal pulses can be decoupled using wavelength-division multiplexing (WDM) filters either on-chip or off-chip.

The second method, shown in Fig. 3.13(b), uses a time-multiplexed approach based on a single photonic neuron folded in time with feedback-modulated delay loops [59]. In this architecture, each delay loop at each time step represents a different synaptic connection in the neural network layer. By properly updating the feedback modulators at each time step, the required linear operations can be achieved. Therefore, only one PPLN performing ReLU activations is needed to represent all neurons, but the number of delay loops and time steps to compute each neural network layer equals the number of synapses for each neuron. This architecture may be advantageous in that it relaxes the experimental constraints for fabricating and controlling a large number of PPLNs like in the spatially-multiplexed method.

Given the relatively long (~mm) length of the PPLN, but ultrafast response time, it is desirable to employ a time-multiplexed approach for scalability. Furthermore, although we show the use of free-space coupling here, this can be eliminated through the monolithic integration of thin-film lithium niobate lasers [60], and integrated detectors [61]. This is substantially more complicated than any previously demonstrated thin-film lithium niobate photonic circuit [33, 62, 63, 32], but rapid improvements in fabrication quality/tolerance in thin-film lithium niobate photonics promise a path toward a monolithically integrated photonic neural network in the near future.

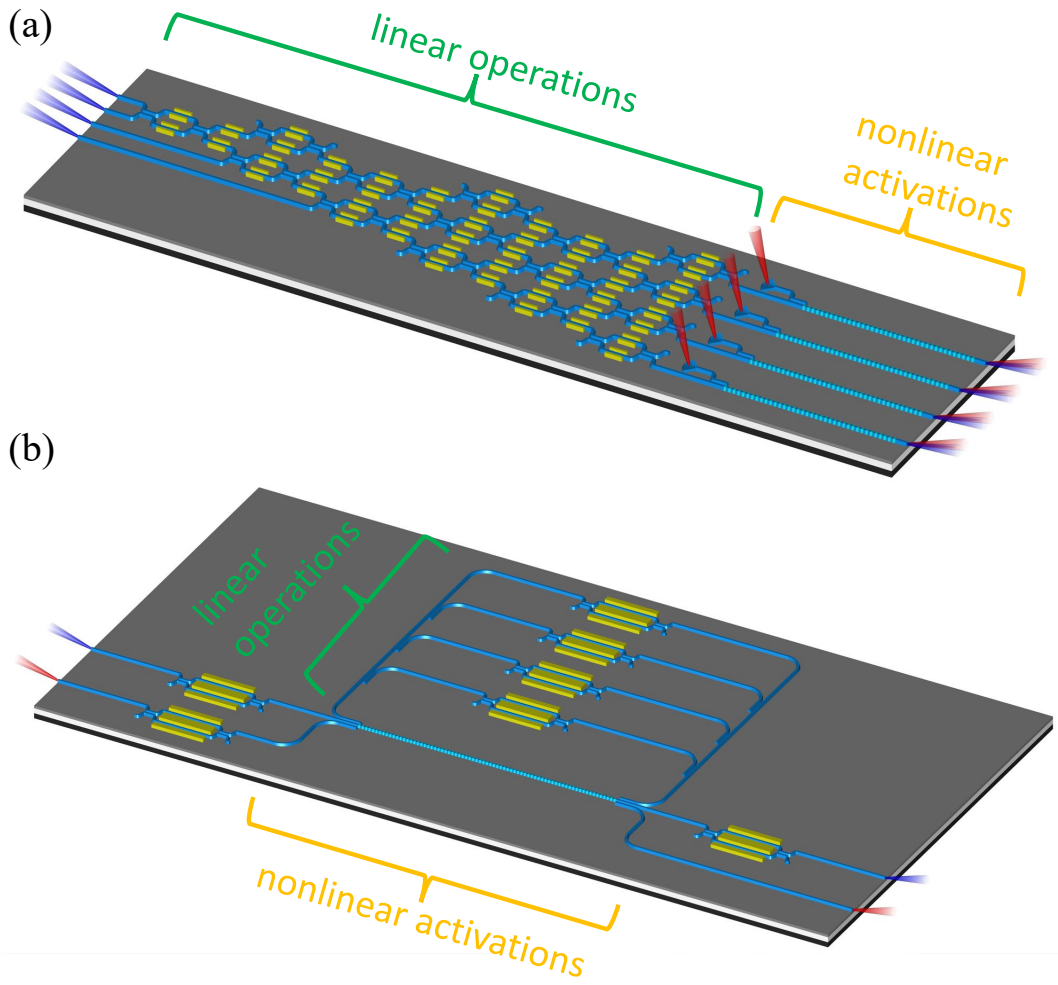

Figure 3.13: Potential integrated photonic neural networks using the all-optical ultrafast ReLU function. (a) Spatially-multiplexed design based on a mesh of Mach-Zehnder interferometers performing linear operations, directly cascaded into an array of PPLNs performing the ReLU activations. (b) Time-multiplexed design based on feedback-modulated delay loops performing linear operations and the PPLN performing ReLU activations, acting as the single photonic neuron folded in time.

References

[1] Ian Goodfellow, Yoshua Bengio, and Aaron Courville. *Deep learning*. MIT press, 2016.

[2] Vivienne Sze et al. "Efficient processing of deep neural networks: A tutorial and survey". In: *Proceedings of the IEEE* 105.12 (2017), pp. 2295–2329.

[3] Yann LeCun. "Deep learning hardware: past, present, and future". In: *2019 IEEE International Solid-State Circuits Conference-(ISSCC)*. IEEE. 2019, pp. 12–19.

[4] Gordon Wetzstein et al. "Inference in artificial intelligence with deep optics and photonics". In: *Nature* 588.7836 (2020), pp. 39–47.

[5] Xing Lin et al. "All-optical machine learning using diffractive deep neural networks". In: *Science* 361.6406 (2018), pp. 1004–1008. URL: https://www.science.org/doi/abs/10.1126/science.aat8084.

[6] Tiankuang Zhou et al. "Large-scale neuromorphic optoelectronic computing with a reconfigurable diffractive processing unit". In: *Nature Photonics* 15.5 (2021), pp. 367–373.

[7] Ying Zuo et al. "All-optical neural network with nonlinear activation functions". In: *Optica* 6.9 (2019), pp. 1132–1137.

[8] Tianyu Wang et al. "An optical neural network using less than 1 photon per multiplication". In: *arXiv preprint arXiv:2104.13467* (2021).

[9] Ziyu Gu, Yesheng Gao, and Xingzhao Liu. "Optronic convolutional neural networks of multi-layers with different functions executed in optics for image classification". In: *Optics Express* 29.4 (2021), pp. 5877–5889.

[10] Mario Miscuglio et al. "Massively parallel amplitude-only Fourier neural network". In: *Optica* 7.12 (2020), pp. 1812–1819.

[11] Xavier Porte et al. "A complete, parallel and autonomous photonic neural network in a semiconductor multimode laser". In: *Journal of Physics: Photonics* 3.2 (2021), p. 024017.

[12] Xingyuan Xu et al. "11 TOPS photonic convolutional accelerator for optical neural networks". In: *Nature* 589.7840 (2021), pp. 44–51.

[13] George Mourgias-Alexandris et al. "An all-optical neuron with sigmoid activation function". In: *Optics Express* 27.7 (2019), pp. 9620–9630.

[14] François Duport et al. "All-optical reservoir computing". In: *Optics express* 20.20 (2012), pp. 22783–22795.

[15] François Duport et al. "Fully analogue photonic reservoir computer". In: *Scientific Reports* 6.1 (2016), pp. 1–12.

[16] Bhavin J Shastri et al. "Spike processing with a graphene excitable laser". In: *Scientific Reports* 6.1 (2016), pp. 1–12.

[17] Antoine Dejonckheere et al. "All-optical reservoir computer based on saturation of absorption". In: *Optics Express* 22.9 (2014), pp. 10868–10881.

[18] Yichen Shen et al. "Deep learning with coherent nanophotonic circuits". In: *Nature Photonics* 11.7 (2017), pp. 441–446.

[19] Johannes Feldmann et al. “All-optical spiking neurosynaptic networks with self-learning capabilities”. In: *Nature* 569.7755 (2019), pp. 208–214.

[20] Johannes Feldmann et al. “Parallel convolutional processing using an integrated photonic tensor core”. In: *Nature* 589.7840 (2021), pp. 52–58.

[21] Farshid Ashtiani, Alexander J Geers, and Firooz Aflatouni. “Single-chip photonic deep neural network for instantaneous image classification”. In: *arXiv preprint arXiv:2106.11747* (2021).

[22] Shaofu Xu et al. “Optical coherent dot-product chip for sophisticated deep learning regression”. In: *arXiv preprint arXiv:2105.12122* (2021).

[23] Bin Shi, Nicola Calabretta, and Ripalta Stabile. “InP photonic integrated multi-layer neural networks: Architecture and performance analysis”. In: *APL Photonics* 7.1 (Jan. 2022), p. 010801. URL: https://doi.org/10.1063/5.0066350.

[24] Mario Miscuglio et al. “All-optical nonlinear activation function for photonic neural networks”. In: *Opt. Mater. Express* 8.12 (Dec. 2018), pp. 3851–3863. URL: https://opg.optica.org/ome/abstract.cfm?URI=ome-8-12-3851.

[25] Aashu Jha, Chaoran Huang, and Paul R. Prucnal. “Reconfigurable all-optical nonlinear activation functions for neuromorphic photonics”. In: *Opt. Lett.* 45.17 (Sept. 2020), pp. 4819–4822. URL: https://opg.optica.org/ol/abstract.cfm?URI=ol-45-17-4819.

[26] Alexander N. Tait et al. “Neuromorphic photonic networks using silicon photonic weight banks”. In: *Scientific Reports* 7.1 (Aug. 2017), p. 7430. URL: https://doi.org/10.1038/s41598-017-07754-z.

[27] Jasna Crnjanski et al. “Adaptive sigmoid-like and PReLU activation functions for all-optical perceptron”. In: *Optics Letters* 46.9 (2021), pp. 2003–2006.

[28] Rubab Amin et al. “ITO-based electro-absorption modulator for photonic neural activation function”. In: *APL Materials* 7.8 (2019), p. 081112.

[29] Charis Mesaritakis et al. “Artificial neuron based on integrated semiconductor quantum dot mode-locked lasers”. In: *Scientific Reports* 6.1 (2016), pp. 1–10.

[30] Cheng Wang et al. “Ultrahigh-efficiency wavelength conversion in nanophotonic periodically poled lithium niobate waveguides”. In: *Optica* 5.11 (2018), pp. 1438–1441.

[31] Marc Jankowski et al. “Ultrabroadband nonlinear optics in nanophotonic periodically poled lithium niobate waveguides”. In: *Optica* 7.1 (2020), pp. 40–46.

[32] Qiushi Guo et al. “Femtojoule femtosecond all-optical switching in lithium niobate nanophotonics”. In: *Nature Photonics* 16.9 (Sept. 2022), pp. 625–631. URL: https://doi.org/10.1038/s41566-022-01044-5.

[33] Luis Ledezma et al. “Intense optical parametric amplification in dispersion-engineered nanophotonic lithium niobate waveguides”. In: *Optica* 9.3 (Mar. 2022), pp. 303–308. URL: https://opg.optica.org/optica/abstract.cfm?URI=optica-9-3-303.

[34] Djork-Arné Clevert, Thomas Unterthiner, and Sepp Hochreiter. "Fast and accurate deep network learning by exponential linear units (elus)". In: *arXiv preprint arXiv:1511.07289* (2015).

[35] Tom B Brown et al. "Language models are few-shot learners". In: *arXiv preprint arXiv:2005.14165* (2020).

[36] Masaaki Ono et al. "Ultrafast and energy-efficient all-optical switching with graphene-loaded deep-subwavelength plasmonic waveguides". In: *Nature Photonics* 14.1 (Jan. 2020), pp. 37–43. URL: https://doi.org/10.1038/s41566-019-0547-7.

[37] Gustavo Grinblat et al. "Ultrafast sub–30-fs all-optical switching based on gallium phosphide". In: *Science Advances* 5.6 (2019), eaaw3262. URL: https://www.science.org/doi/abs/10.1126/sciadv.aaw3262.

[38] Xianxin Guo et al. "Backpropagation through nonlinear units for the all-optical training of neural networks". In: *Photon. Res.* 9.3 (Mar. 2021), B71–B80. URL: https://opg.optica.org/prj/abstract.cfm?URI=prj-9-3-B71.

[39] Ian AD Williamson et al. "Reprogrammable electro-optic nonlinear activation functions for optical neural networks". In: *IEEE Journal of Selected Topics in Quantum Electronics* 26.1 (2019), pp. 1–12.

[40] Li Deng. "The MNIST Database of Handwritten Digit Images for Machine Learning Research [Best of the Web]". In: *IEEE Signal Processing Magazine* 29.6 (2012), pp. 141–142.

[41] Saumil Bandyopadhyay, Ryan Hamerly, and Dirk Englund. "Hardware error correction for programmable photonics". In: *Optica* 8.10 (Oct. 2021), pp. 1247–1255. URL: https://opg.optica.org/optica/abstract.cfm?URI=optica-8-10-1247.

[42] Sangheon Oh et al. "Energy-efficient Mott activation neuron for full-hardware implementation of neural networks". In: *Nature Nanotechnology* 16.6 (2021), pp. 680–687.

[43] Olga Krestinskaya, Khaled Nabil Salama, and Alex Pappachen James. "Learning in memristive neural network architectures using analog backpropagation circuits". In: *IEEE Transactions on Circuits and Systems I: Regular Papers* 66.2 (2018), pp. 719–732.

[44] Yucong Huang et al. "Analog Circuit Implementation of Neurons with Multiply-Accumulate and ReLU Functions". In: *Proceedings of the 2020 on Great Lakes Symposium on VLSI*. 2020, pp. 493–498.

[45] Massimo Giordano et al. "Analog-to-digital conversion with reconfigurable function mapping for neural networks activation function acceleration". In: *IEEE Journal on Emerging and Selected Topics in Circuits and Systems* 9.2 (2019), pp. 367–376.

[46] Jack Choquette et al. "Nvidia a100 tensor core gpu: Performance and innovation". In: *IEEE Micro* 41.2 (2021), pp. 29–35.

[47] Qing Xie et al. "Performance comparisons between 7-nm FinFET and conventional bulk CMOS standard cell libraries". In: *IEEE Transactions on Circuits and Systems II: Express Briefs* 62.8 (2015), pp. 761–765.

[48] Chris Cole. "Optical and electrical programmable computing energy use comparison". In: *Opt. Express* 29.9 (Apr. 2021), pp. 13153–13170. URL: https://opg.optica.org/oe/abstract.cfm?URI=oe-29-9-13153.

[49] Mian Zhang et al. "Integrated lithium niobate electro-optic modulators: when performance meets scalability". In: *Optica* 8.5 (2021), pp. 652–667.

[50] Juanjuan Lu et al. "Ultralow-threshold thin-film lithium niobate optical parametric oscillator". In: *Optica* 8.4 (Apr. 2021), pp. 539–544. URL: https://opg.optica.org/optica/abstract.cfm?URI=optica-8-4-539.

[51] Yoshihisa Yamamoto et al. "Coherent Ising machines—optical neural networks operating at the quantum limit". In: *npj Quantum Information* 3.1 (Dec. 2017), p. 49. URL: https://doi.org/10.1038/s41534-017-0048-9.

[52] Stefan Wabnitz and Benjamin Eggleton. *All-Optical Signal Processing: Data Communication and Storage Applications*. Vol. 194. Jan. 2015.

[53] Marc Jankowski et al. "Temporal Simultons in Optical Parametric Oscillators". In: *Phys. Rev. Lett.* 120 (5 Feb. 2018), p. 053904. URL: https://link.aps.org/doi/10.1103/PhysRevLett.120.053904.

[54] Alireza Marandi et al. "Coherence properties of a broadband femtosecond mid-IR optical parametric oscillator operating at degeneracy". In: *Opt. Express* 20 (2012), pp. 7255–7262.

[55] Marcelo Alejandro Luda et al. "Compact embedded device for lock-in measurements and experiment active control". In: *Review of Scientific Instruments* 90 (2019), p. 023106.

[56] Luis Ledezma et al. "100 dB/cm broadband optical parametric amplification in dispersion engineered nanophotonic lithium niobate waveguides". In: *CLEO: Science and Innovations*. Optical Society of America. 2021, SF1C–7.

[57] Changran Hu et al. "High-efficient coupler for thin-film lithium niobate waveguide devices". In: *Optics Express* 29.4 (2021), pp. 5397–5406.

[58] Li Deng. "The mnist database of handwritten digit images for machine learning research". In: *IEEE Signal Processing Magazine* 29.6 (2012), pp. 141–142.

[59] Florian Stelzer et al. "Deep neural networks using a single neuron: folded-in-time architecture using feedback-modulated delay loops". In: *Nature communications* 12.1 (2021), pp. 1–10.

[60] Xiangmin Liu et al. "Tunable single-mode laser on thin film lithium niobate". In: *Optics Letters* 46.21 (2021), pp. 5505–5508.

[61] Ayed Al Sayem et al. "Lithium-niobate-on-insulator waveguide-integrated superconducting nanowire single-photon detectors". In: *Applied Physics Letters* 116.15 (2020), p. 151102.

[62] Luis Ledezma et al. "Widely-tunable optical parametric oscillator in lithium niobate nanophotonics". In: *arXiv preprint arXiv:2203.11482* (2022).

[63] Rajveer Nehra et al. "Few-cycle vacuum squeezing in nanophotonics". In: *arXiv preprint arXiv:2201.06768* (2022).

Chapter 4

FEMTOJOULE, FEMTOSECOND ALL-OPTICAL SWITCH

Qiushi Guo[†], **Ryoto Sekine**[†], Luis Ledezma[†], Rajveer Nehra, Devin Dean, Arkadev Roy, Robert M. Gray, Saman Jahani, and Alireza Marandi, "Femtojoule, femtosecond all-optical switching in integrated lithium niobate photonics", *Nature Photonics*, 16, 625-631 (2022).
R.S. developed the measurement techniques, assisted the fabrication development, and participated in writing of the manuscript.
[†] denotes equal contributions

4.1 Abstract

Optical nonlinear functions are crucial for various applications in integrated photonics, including all-optical information processing[1], photonic neural networks[2, 3] and on-chip ultrafast light sources[4, 5]. However, the weak native nonlinearity of most nanophotonic platforms has imposed barriers for such functions by necessitating large driving energies, high-Q cavities or integration with other materials with stronger nonlinearity. Here we effectively utilize the strong and instantaneous quadratic nonlinearity of lithium niobate nanowaveguides for the realization of cavity-free all-optical switching. By simultaneous engineering of the dispersion and quasi-phase matching, we design and demonstrate a nonlinear splitter that can achieve ultralow switching energies down to 80 fJ, featuring a fastest switching time of ~46 fs and a lowest energy–time product of 3.7×10^{-27}J·sin integrated photonics. Our results can enable on-chip ultrafast and energy-efficient all-optical information processing, computing systems and light sources.

4.2 Introduction

Photons are known to be excellent information carriers. Yet, the quest for all-optical information processing – a technology that can potentially eliminate the limitations on the bandwidth and energy consumption of electronic and opto-electronic systems – is generally deemed to be challenging because optical nonlinearities are usually weak. All-optical switching using cubic ($\chi^{(3)}$) nonlinearities[6, 7] and saturable absorption[8, 9, 10] in semiconductor materials typically requires pulse energies on the order of picojoules or beyond. Such energy requirements hinder their widespread utilization for any applications, as they necessitate bulky and power-hungry light sources. To lower the energy requirement of all-optical switching, one approach consists of enhancing the optical nonlinearity in optical cavities. However, this enhancement is accompanied by a cavity photon lifetime, which unavoidably increases the switching times and typically leads to low bandwidths of up to tens of gigahertz[1, 11, 12, 13, 14, 15, 16]. Therefore, all-optical switching in solid-state photonic platforms faces a performance trade-off between the energy per bit and the switching time[17], making the energy-time product an apt figure of merit[18]. A

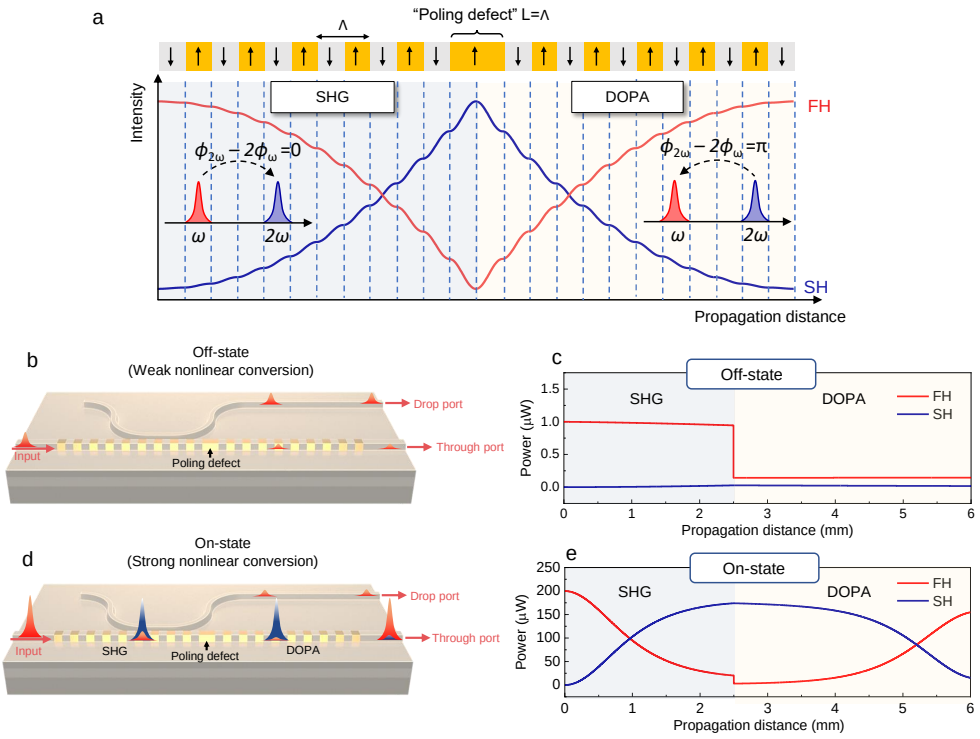

Figure 4.1: **Device design and operating principle.** **a**, Illustration of the QPM engineering in periodically poled lithium niobate (PPLN) waveguide. The poling defect (a longer ferroelectric domain with a length $L = \Lambda$) shifts the phase difference between the FH and SH by π. As a result, the poling defect switches the SHG to DOPA in the second half of the PPLN waveguide. The insets illustrate the phase relation and the direction of energy transfer between the FH and the SH. **b**, Schematic of the integrated nonlinear splitter device and its operation in the off state when the input FH pulse energy is low. **c**, Simulated evolution of the FH and SH optical power along the main waveguide for the off-state, in which the transmittance of the FH is low (15%). **d**, Schematic of the integrated nonlinear splitter device and its operation in the on state when the input pulse energy is high. **e**, Simulated evolution of the FH and SH optical power along the main waveguide for the on state, in which the transmittance of the FH is high (85%). The simulations in **c** and **e** assume an input pulse of 46 fs at 2,090 nm and device parameters of a 2.5-mm-long SHG region, a 3.5-mm-long DOPA region and 85% outcoupling of the FH by the directional coupler.

promising path towards a better energy–time product is the utilization of stronger and instantaneous nonlinearities, such as the quadratic nonlinearity ($\chi^{(2)}$).

Compared to the $\chi^{(3)}$ nonlinearity, $\chi^{(2)}$ nonlinearity in non-centrosymmetric materials requires lower light intensities by many orders of magnitude. When the phase-matching condition is achieved and in the absence of substantial dispersion, nonlinear optical interactions can grow substantially as a function of propagation length, thus circumventing the need for resonant enhancement and compromising

switching speed. Recently, thin-film lithium niobate (TFLN) has emerged as a promising integrated photonic platform. TFLN-based nanophotonic waveguides exhibit strong $\chi^{(2)}$ nonlinearity and a high normalized nonlinear frequency conversion efficiency in the continuous wave (c.w.) regime (>1000%/W-cm^2)[19, 20, 21, 22] that is not easily attainable in bulk material platforms, thanks to the strong spatial confinement of the waveguide modes as well as quasi-phase matching (QPM). Additionally, the tight spatial confinement of the waveguide modes allows dispersion engineering[23, 24, 25], which enables temporal confinement of interacting waves over long interaction lengths, leading to further enhancement of the nonlinear processes using ultrashort pulses.

4.3 Results

Here we achieve cavity-free all-optical switching in an integrated LN nonlinear splitter, which cascades two distinct phase-matched $\chi^{(2)}$ nonlinear processes: second-harmonic generation (SHG) and degenerate optical parametric amplification (DOPA). Simultaneously, dispersion engineering of our device allows spatiotemporal confinement of the pulses over the length of the device, leading to ultralow-energy (femtojoule) and ultrafast (femtosecond) all-optical switching with a high extinction ratio. It is worth noting that the design and operating principle of our device are fundamentally different from the all-optical switches based on nonlinear directional couplers in micro-waveguides[26]. In those devices, the switching originates from the perturbation of the evanescent coupling due to phase-mismatched $\chi^{(2)}$ nonlinearity and self-phase modulation of the input pulses[27, 28], whereas in our device the switching mechanism arises from the phase-matched wavelength conversions and the spectral selectivity of the linear directional coupler, leading to a record-level performance (Supplementary Section 4.6.1 provides a detailed comparison).

The main element of our all-optical switch is a QPM-engineered LN nanophotonic waveguide. Figure 4.1a illustrates the concept of this QPM engineering. A uniform periodically poled LN waveguide (with periodicity Λ) is perturbed by a 'poling defect', that is, an isolated ferroelectric domain of length $L = \Lambda$ in the middle of the waveguide. Although the poling period is designed for phase-matched SHG, the poling defect locally changes the phase relationship between the first-harmonic (FH) and the second-harmonic (SH) waves by $\Delta\phi = \phi_{2\omega} - 2\phi_{\omega} = \pi$ (ref. [29]). Because the direction of power flow between the FH and the SH is dependent on the relative phase between them, the π phase shift due to the poling defect switches the nonlinear process from SHG to DOPA, in which the generated SH serves as the pump to amplify the FH.

In addition to the QPM-engineered main waveguide, our all-optical switch is composed of a neighbouring linear directional coupler, as sketched in Fig. 4.1b and d. The linear directional coupler evanescently couples out most (85%) of the FH, while leaving most of SH freely propagating in the main waveguide. This whole device exhibits a strongly intensity-dependent splitting ratio. When the input FH intensity is low (in the off state shown in Fig. 4.1b), most of the input FH does not

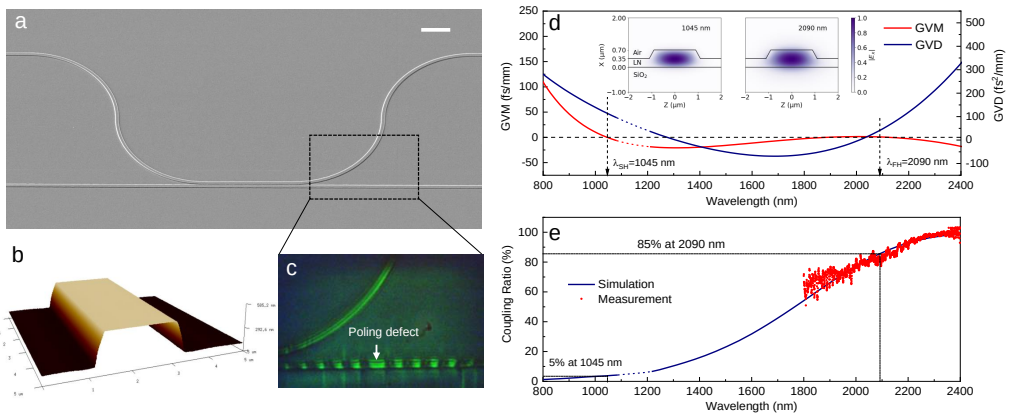

Figure 4.2: **Integrated nonlinear splitter and its linear optical characteristics.** **a**, SEM image of the fabricated nonlinear splitter. Scale bar, 20 μm. The device has a 2.5-mm-long SHG region and a 3.5-mm-long DOPA region. The directional coupler has a coupling length of 70 μm and a gap of 650 nm between the waveguide top surfaces. **b**, 2D AFM scan on LN waveguide. **c**, SH microscope image showing the inverted domains and the poling defect along the waveguides. **d**, Simulated GVM (red) between the FH and SH and GVD (blue) for the quasi-transverse electric (quasi-TE) modes of the dispersion-engineered LN waveguide. The optimized waveguide has a top width of 1,650 nm, an etching depth of 350 nm and a total thin-film thickness of 700 nm. The waveguide exhibits low (0.4 fs mm^{-1}) GVM between the pump at 1,045 nm and the signal around 2,090 nm, and low GVD for both wavelengths. Inset: electric field distributions of the fundamental quasi-TE modes for the dispersion-engineered waveguide at 1,045 nm and 2,090 nm. The black dashed line in the main plot denotes zero GVM. Black dashed arrows mark the FH and SH wavelengths. **e**, Measured (red symbols) and simulated (blue solid curve) outcoupling ratio of the directional coupler as a function of the wavelength. In **d** and **e**, the dotted lines correspond to the regime where mode crossing between the fundamental TE mode and the second-order transverse magnetic mode occurs, which is distant enough from the SH central wavelength and is not expected to affect the device operation.

convert to SH, and hence is directed by the linear coupler to the drop port. This is illustrated by the simulated power evolution of both the FH and the SH in the main waveguide in Fig. 4.1c. In this off state, the transmittance of the FH in the main waveguide (through port) is low. However, when the input FH intensity is high (or in the on state as shown in Fig. 4.1d, e), due to the efficient SHG at the beginning of the waveguide, most of the FH can convert to the SH, which remains in the main waveguide after passing through the coupler, and negligible FH is directed to the drop port. In the second half of the main waveguide, the poling defect switches the SHG process to DOPA, through which most of the SH converts back to the FH. As shown in Fig. 4.1e, in the on state, the device favours transmission of the

FH to the through port, because most of the input pulse energy can be 'stored' in (that is, converted to) the SH, which is unaffected by the linear coupler. Because the FH transmission strongly depends on the input pulse energy of the FH, the intensity-dependent nonlinear splitter functions as an all-optical switch.

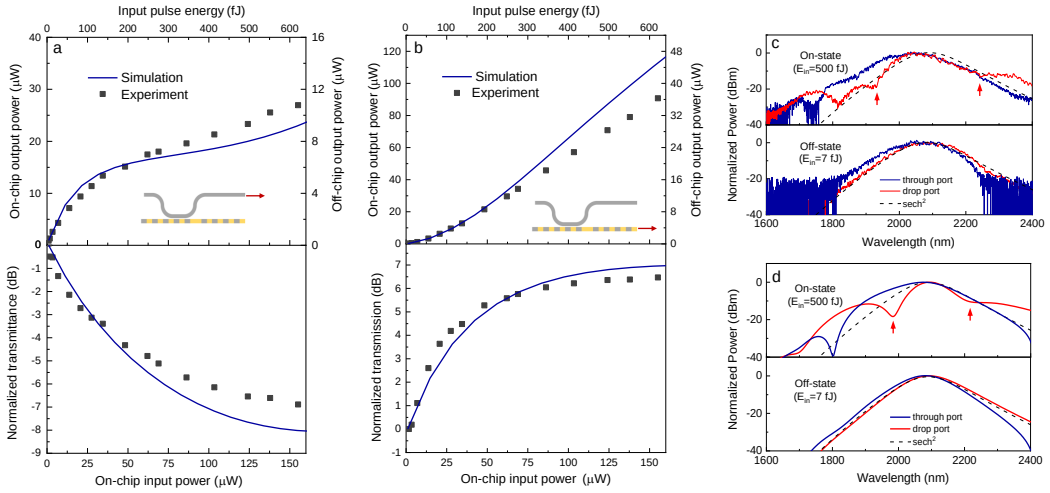

Figure 4.3: **Ultra-low energy nonlinear optical transmission in the integrated nonlinear splitter. a**, Top: output pulse energy of the 2,090-nm FH from the drop port as a function of on-chip input average power/pulse energy. Bottom: normalized transmittance ($10\log\left(T/T_{P_{\text{in}}\to 0}\right)$) of the FH from the drop port. **b**, Top: output pulse energy of the FH from the through port as a function of input average power/pulse energy. Bottom: normalized transmittance ($10\log\left(T/T_{P_{\text{in}}\to 0}\right)$) of the FH from the through port. In both **a** and **b**, the blue solid lines are simulation results. Black symbols are the measured data. The insets illustrate the ports at which we collected the data. **c**, Measured output FH spectra at the through port (blue) and the drop port (red) in the on state (top) and the off state (bottom). The input FH pulse energy is 500 fJ for the on state and 7 fJ for the off state. In the on state, the dip in the spectrum of the drop port, which does not persist in the through port or in the off state, is further strong experimental evidence for the interplay of SHG and DOPA in the switching mechanism. **d**, Simulated output FH spectra at the through port (blue) and the drop port (red) in the on state (top) and the off state (bottom), corresponding to the measurements in **c**. In both **c** and **d**, the spectral dips are labelled by red arrows.

We fabricated the nonlinear splitter on a 700-nm-thick X-cut MgO-doped LN thin film on a 2-μm-thick SiO_2 layer on top of a LN substrate (NANOLN). Details about the periodic poling, the waveguide patterning and etching are provided in the Methods. As shown in the scanning electron microscope (SEM) image in Fig. 4.2a and the atomic force microscope (AFM) image in Fig. 4.2b, the Ar-based dry etching process yields smooth waveguide sidewalls (with surface roughness of ~1 nm) and a sidewall angle of ~60°. The top width of the main waveguide and the etching depth are measured to be 1,650 nm and 350 nm, respectively, with an error

of ±5 nm. In Supplementary Section 4.6.7, we discuss how the variation of the waveguide top width, etching depth and the thin-film thickness affect the nominal poling period and the device performance consistency. The inverted ferroelectric domains and the poling defect along the main waveguide are shown in the SH image in Fig. 4.2c. Based on the simulation shown in Fig. 4.1e, the device is designed to have a 2.5-mm-long SHG region and a 3.5-mm-long DOPA region. Such a design can ensure that both the SHG and DOPA process are efficient enough, which in turn leads to low switching energy and high switching contrast in the on state.

To achieve ultralow-energy and ultrafast operation, we engineer the dispersion of the LN ridge waveguide and minimize both the group velocity dispersion (GVD) and the group velocity mismatch (GVM) between the FH and the SH[24]. Negligible GVD at the FH and SH wavelengths preserves the temporal confinement of these pulses and hence their high peak intensities along the waveguide, thereby ensuring efficient short-pulse and low-energy SHG and DOPA. Additionally, negligible GVM between the FH and SH waves guarantees that both FH and SH pulses travel together along the waveguide. As shown in Fig. 4.2d, in the dispersion-engineered waveguide, the fundamental quasi-transverse electric (TE) modes at the FH (2,090 nm) and SH (1,045 nm) have a very low GVM of 0.4 fs mm^{-1}. In addition, the GVD for both the FH and SH waves are as low as 40 fs^2mm^{-1} and 114 fs^2mm^{-1}, respectively. For a 46-fs-long input pulse at 2,090 nm, the optimized waveguide has a dispersion length of more than 50 mm. The walk-off length (pulse length divided by GVM), representing the propagation distance after which the pump and SH pulses acquire a temporal separation equal to their pulse width, is 115 mm. Remarkably, Fig. 4.2d also shows that, around 2,090 nm, there exists a large wavelength window within which the GVM is close to zero. Therefore, choosing the operating wavelength to be around 2,090 nm can ensure reliably achieving low GVM in the presence of fabrication imperfections.

To ensure that the coupling ratio of the directional coupler is resilient to fabrication errors, we adopt an adiabatic design in which the main waveguide is uniform with a fixed width, while the coupler waveguide width is adiabatically tapered[30]. The detailed geometry of the directional coupler is discussed in Supplementary Section 4.6.2. Figure 4.2e shows the wavelength-dependent coupling ratio, which is the ratio between the output power at the drop port and the input power. Owing to the large mode area difference between the fundamental TE modes at 2,090 nm and 1,045 nm, the 70-μm-long directional coupler exhibits a large coupling ratio of over 85% for wavelengths beyond 2,090 nm and a small coupling ratio of less than 5% for wavelengths below 1,045 nm. The measured (red symbols) results around 2,090 nm agree well with the simulation results (blue solid curve). We did not perform the coupling ratio measurement around 1,045 nm because the external input light can be coupled to higher-order spatial modes around 1,045 nm, which strongly affects the accuracy of the measurements.

We characterized the nonlinear optical behaviour of the device using 46-fs-long pulses at 2,090 nm from a synchronously pumped degenerate optical parametric oscillator (OPO) with a repetition frequency of 250 MHz. The characterization of the 2,090-nm pulses is elaborated in Supplementary Section 4.6.3. By measuring

the nonlinear splitter devices with different poling periods, we found that 5.11 μm is the optimal poling period for realizing QPM, which is in good agreement with the theoretical period of 5.08 μm. The experimental details of optimizing the QPM condition are discussed in the Methods and Supplementary Section 4.6.5. At the optimum QPM condition, we measured the output power of the FH both at the through port and the drop port. The detailed calibration of the input/output coupling loss of our waveguide is discussed in Supplementary Section 4.6.6.

As shown in Fig. 4.3a, the normalized transmittance from the input to the drop port, defined as $10\log\left(T/T_{P_{\text{in}}\to 0}\right)$, shows a clear reduction (~7 dB) when the on-chip input FH pulse energy increases from 0 to 600 fJ. This behaviour is well captured by the simulation (blue solid line). Such a reduction in the transmittance is a result of the strong depletion of FH waves during the SHG process, because the directional coupler only couples out the FH in the first half of the main waveguide. The time-domain nonlinear dynamics of the SHG process is elaborated in Supplementary Section VIII. Because the energy is conserved during the frequency conversion process, based on the measured 7 dB (80 %) depletion of the FH shown in Fig. 4.3a and assuming that the propagation loss of the FH is far less than its depletion, we estimated that an input FH pulse energy of 600 fJ in the waveguide converts to a SH pulse energy of 480 fJ.

The normalized transmittance of the FH from the input port to the through port increases by more than 5 dB as the input pulse energy increases, as shown in Fig. 3b. This behaviour is opposite that of the transmittance to the drop port, which confirms that the poling defect indeed switches the SHG to the DOPA process in the second half of the main waveguide, thereby converting the generated SH back into the FH. The experimental result agrees well with the simulation (blue solid line), despite showing a slightly lower peak transmittance, which can be ascribed to the slightly lower SHG efficiency in the first half of the device or the imperfect phase shift imposed by the poling defect. Based on the results shown in Fig. 4.3a,b, we can deduce that the largest parametric gain in the DOPA region is more than 12 dB at an input FH pulse energy of 600 fJ, which translates to a gain per unit length of 34 dB/cm given that the DOPA region is 3.5 mm long. Notably, this result is consistent with our recent parametric gain measurement on a similar QPM LN waveguide, which exhibits a gain per unit length of 35 dB/cm when pumped with ~500-fJ, 1,045-nm pulses[24]. Moreover, the measured output FH power from the main waveguide agrees well with the simulation.

The interplay of SHG and DOPA in the all-optical switching mechanism is also evident from the output spectra. In Fig. 4.3c we compare the measured output FH spectra at the drop port and the through port. Ultrashort pulses from mode-locked lasers often have a temporal/spectral shape that can be described with a squared hyperbolic secant (sech^2) function. When the device is subjected to 500 fJ of input pulse energy (in the on state), the output spectrum at the drop port (red) deviates from the initial sech^2 spectral shape, showing spectral dips around 1,920 nm and 2,250 nm, which indicate a strong depletion of the FH. However, the output spectrum at the through port (blue) does not show such dips at high input pulse energies and has a spectral shape similar to the sech^2 function, which indicates the recovery of

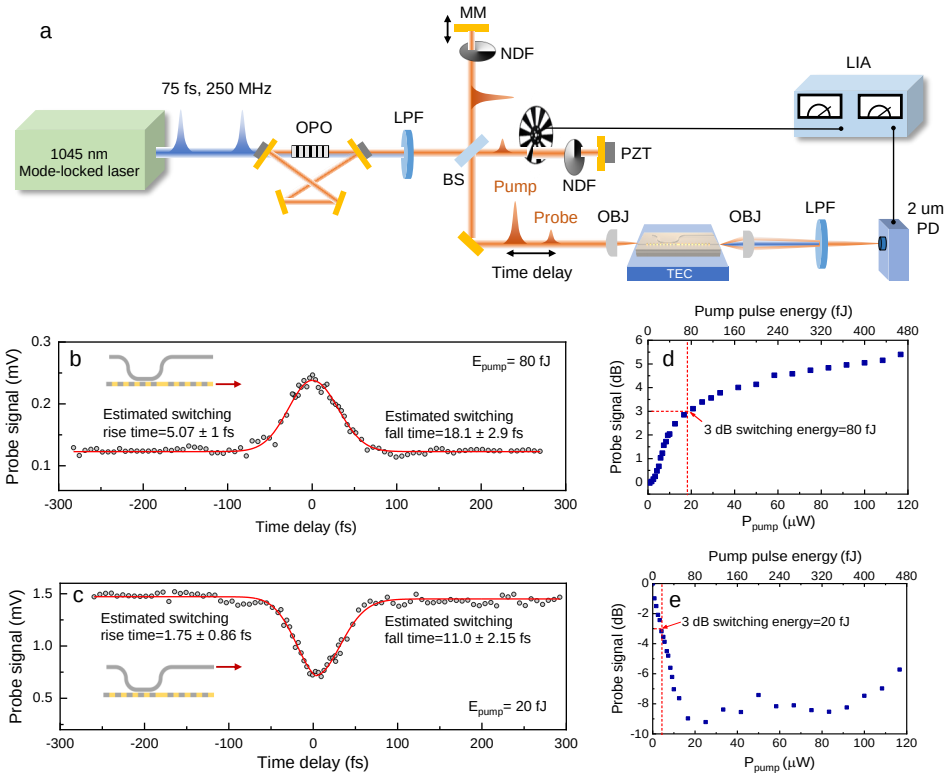

Figure 4.4: **Femtosecond, femtojoule all-optical switching.** **a**, Experimental set-up for the femtosecond all-optical switching measurement. Approximately 46-fs pulses at 2,090 nm generated from a free-space OPO are used to characterize the device. Pump and probe fields with relative time delay $\Delta\tau$ are injected into the waveguide via the objective lens. Probe transmission depends on whether the two pulses excite the device simultaneously or at different times. LPF, long-pass filter; MM, motorized mirror; PZT, piezoelectric transducer; NDF, neutral density filter; BS, beamsplitter; OBJ, objective lens; LIA, lock-in amplifier; PD, photodetector. **b**, Measured dynamics of the on state at the through port. The input pump pulse energy (E_{pump}) is 80 fJ. **c**, Measured dynamics of the on state at the drop port. E_{pump} is 20 fJ. The insets illustrate the ports at which we collected the data. **d**, Relative probe signal power at the through port as a function of pump pulse power (energy). **e**, Relative probe signal power at the drop port as a function of pump pulse power (energy). The 3-dB switching energies at the through port and the drop port are 80 fJ and 20 fJ, respectively.

the FH power. When the device is in the off state (Fig. 4.3c, bottom panel), the output spectra measured at the through port and the drop port both have sech^2 shapes because of the weak nonlinear conversion in the off state. Similar behaviours can also be seen in the simulated output spectra for the on state (Fig. 4.3d, top panel) and the off state (Fig. 4.3d, bottom panel). In Supplementary Section 4.6.8 we provide a detailed analysis of the nonlinear dynamics that explains the origin of the

spectral dips. We also explain how the spectral dips are indicative of the power flow direction. The slight difference between the simulated and the experimental spectra can be attributed to a slight difference of pulse shapes after the depletion in the temporal domain due to complexities such as the chirp of the input pulses, the group delay dispersion accumulated along the waveguide propagation, or the non-zero GVM between the FH and SH. It is worth noting that when the input pulse energy exceeds 600 fJ, the input FH exhibits substantial spectral broadening during the SHG[23], and the phase relation between the FH and SH changes. This leads to a lower parametric gain of the DOPA (details are presented in Supplementary Section 4.6.8).

We further characterize the all-optical switching dynamics and the switching energy of the nonlinear splitter device using a degenerate pump–probe technique, similar to the measurement technique used in ref.[18]. As shown in Fig. 4.4a, a beam containing ~46-fs-long pulses centred at 2,090 nm generated from a table-top degenerate OPO[31] is split into two beams by a beamsplitter in a Michelson interferometer. One beam with a weak optical fluence (3 fJ, 770 nW on-chip average power) is used as the probe beam, and another beam with a high/tunable optical fluence and adjustable time delay (controlled by a motorized delay stage) is used as the pump beam. In the measurement, we couple the output of the Michelson interferometer, which contains both pump and probe beams, to our chip, and switch the transmission of the probe signal by controlling the power of the pump pulse. Additionally, we employ the lock-in modulation and demodulation scheme at 80 Hz to acquire the output probe signal only, rather than acquiring both the pump and probe signals. To suppress the interference between the pump and probe beams, we use a piezoelectric transducer in the optical path of the probe and modulate the phase of the probe pulses at 350 Hz, which is much faster than the integration time (1 s) of the lock-in amplifier.

The dynamics of the on state for the probe signal is measured at the through port and the drop port as plotted in Fig. 4.4b,c, respectively. At the through port, we observe that the probe pulse is clearly appearing when the pump pulse temporally overlaps with it, whereas at the drop port the probe pulse is eliminated. To extract the rise and fall times of the switching mechanism, we fitted the data with exponential growth and decay functions for relative time delays $\Delta\tau < 0$ fs and $\Delta\tau > 0$ fs, respectively, convolved with the autocorrelation of the input pulse, which was approximated by a Gaussian profile with a full-width at half-maximum of 65.2 fs (Supplementary Section 4.6.3 provides details). For the measurement at the through port (Fig. 4.4b), the best fit yields a switching rise time of 5.1±1 fs and a fall time of 18.1±2.9 fs. The measurement at the drop port shows a switching rise time of 1.75±0.86 fs and a fall time of 11.0±2.15 fs.

Although, in our current experiment, the switching time is limited by the exit pulse length of 46 fs, our results in Fig. 4.4b indicate that the intrinsic switching time (or response speed) of our device is ~18 fs. This means that if the input pulses have fall times shorter than 18 fs, the switch will not operate efficiently and will distort the pulses at the output. Despite the instantaneous quadratic nonlinearity, the entire all-optical switch still has a finite response time due to the non-zero GVM, GVD

and the finite QPM bandwidth, making switching for shorter pulses challenging. We have confirmed with numerical simulations that the asymmetry in the switching dynamics shown in Fig. 4.4b,c could be caused by the interplay of several dispersion mechanisms, such as GVM and GVD.

The measured ultrafast switching also indicates that the slow dynamics commonly observed in LN and other materials, such as the photorefractive effect[32] and photothermal effect[33] are absent, primarily due to the low photon energies of the input FH and the generated SH, the ultralow input pulse energy and the non-resonant nature of the switch. We have also ruled out the intensity-dependent index change (Kerr effect) of the LN waveguide as the possible mechanism for the switching and nonlinear transmission characteristics[34], given the fact that no switching behaviour and power-dependent transmission were observed on a similar device without poling in the main waveguide.

Figure 4.4d, e shows the extinction ratio between the on and off states of the switch for both output ports at $\Delta\tau = 0$. We estimated a switching pump energy of 80 fJ (20 fJ) for the through port (the drop port) at the 3-dB contrast level. Within 500 fJ of input pulse energy, we obtain a switching contrast of over 5 dB in the through port and a switching contrast of over 8 dB in the drop port. Such a high switching contrast is difficult to realize using the saturable absorption in semiconductors[10] and low-dimensional materials[35, 36, 37] without coupling them to optical cavities, because it, in general, requires very high optical fluence to excite a substantial portion of electrons from the valence band to the conduction band. It is worth noting that the extinction ratio of our device can be further enlarged to be more than 10 dB at low energy by engineering the coupling ratio of the directional coupler (see Supplementary Section 4.6.10 for details).

4.4 Discussion

In summary, we have demonstrated on-chip all-optical switching based on the strong instantaneous nonlinear response of an LN nano-waveguide, with simultaneous dispersion and QPM engineering. In Fig. 4.5 we compare our device with existing on-chip all-optical switches in terms of the intrinsic switching time and the switching energy. Our device features a fastest switching time of ~46 fs, corresponding to the largest operational bandwidth of 9.6 THz, as well as an ultralow 3-dB switching energy of 80 fJ. Moreover, our device shows the state-of-the-art switching energy–time product of 3.7×10^{-27} J s. Our nonlinear splitter also enables the simultaneous realization of switch-on and switch-off operations as well as a large extinction ratio of over 5 dB when subjected to less than 500 fJ of input pulse energy. Moreover, although our current device is designed for operation at 2,090 nm, the same concept can be applied to telecommunication wavelengths such as 1,550 nm. In Supplementary Section 4.6.11, we describe the waveguide design and dispersion engineering for 1,550 nm. Operating the device at a shorter wavelength can also reduce the required lengths for the poling regions due to a larger effective nonlinearity[38].

We envision that the femtojoule switching energy and the terahertz bandwidth

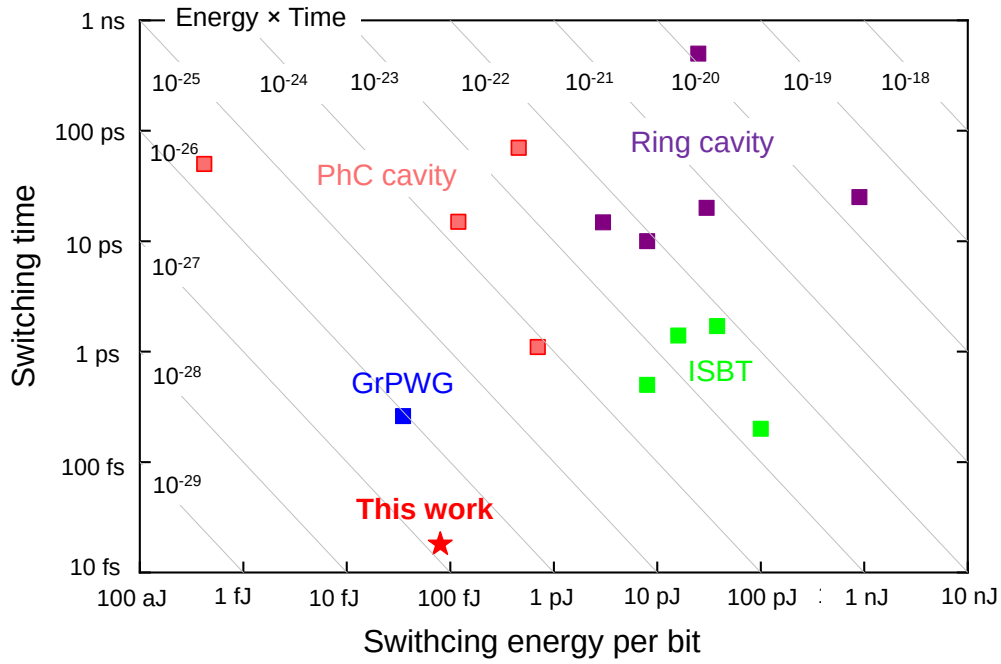

Figure 4.5: **Performance comparison of various on-chip all-optical switches operating at room temperature.** The data points show the intrinsic switching time and switching energy per bit for switches based on a photonic-crystal (PhC) cavity, ring cavity, inter-subband transition (ISBT) and graphene loaded plasmonic waveguide (GrPWG). Our device features a state-of-the-art on-chip switching time of ~46 fs and a low switching energy–time product of 3.7×10^{-27} J s. The references in this plot are included in Supplementary Section 4.6.9.

of our all-optical switch can enable new opportunities for terabit per second (Tbps) all-optical information processing in optical time-division multiplexing (OTDM) systems for communication and computing. In Supplementary Section 4.6.12 we describe the potential applications of our switch for energy-efficient Tbps channel demultiplexing and channel insertion, which are challenging tasks for conventional all-optical switches with more than picosecond switching times. In addition, our switch can also directly interface with the recently developed LN-based on-chip pulsed light sources, such as Kerr soliton microcombs[39, 40, 41] and electro-optical combs[42] for on-chip ultrafast information processing[43]. As another important application, our device can serve as an energy-efficient and ultrafast mode-locking element for developing chip-scale mode-locked lasers on TFLN that can generate ~100-fs ultrashort pulses (Supplementary Section 4.6.12). The ultrahigh speed, low-energy operation and the larger modulation depth of our device are essential for ultrashort pulse generation, self-starting mode-locking and long-term stability of the generated laser pulses.

4.5 Methods

4.5.1 Device fabrication

We fabricated the nonlinear splitter devices on a 700-nm-thick X-cut MgO-doped LN thin film on 2-μm-thick SiO_2 on top of a LN substrate (NANOLN). We first patterned the poling electrodes (15-nm Cr/55-nm Au) with varied electrode finger periodicities using electron-beam lithography. The electrodes were then formed by electron-beam evaporation and metal liftoff. We performed the ferroelectric domain inversion (periodic poling) by applying several 380-V, 5-ms-long pulses at room temperature with the sample submerged in oil. We visually inspected the poling quality using a SH microscope. Next, we removed the electrodes by wet chemical etching, and patterned the waveguides using electron-beam lithography. The pattern was transferred to the LN layer by Ar^+ plasma etching. Finally, the waveguide facets were polished to enable good light-coupling efficiencies.

4.5.2 Optical measurements

For the linear and nonlinear optical measurements, we employed a free-space light-coupling set-up, as shown in Fig. 4.4a. The 1,045-nm source is a 1-W Yb mode-locked laser that produces nearly transform-limited 75-fs-long pulses at a 250-MHz repetition rate (Menlo Systems Orange). The output 1,045-nm beam was fed into a near-synchronously pumped degenerate OPO [44] to produce ~46-fs-long pulses centred at 2,090 nm. Detailed characterization of the 2,090-nm pulses is discussed in the Supplementary Section 4.6.3. The output 2,090-nm beam was split into two beams by a beamsplitter in a Michelson interferometer. The two beams were then recombined and coupled into the nonlinear splitter chip by a reflective objective (Newport 50102-02). The average off-chip input power was calibrated by a thermal power meter (Thorlabs PM16-401). The input/output coupling losses at 2,090 nm were estimated to be 21.6 dB/4 dB. For the power-dependent transmittance measurements in Fig. 4.3, only one output beam from the Michelson interferometer was used. The chip was placed on a thermoelectric cooling stage. To adjust the QPM condition, temperature tuning was used (Supplementary Section 4.6.5). For the results in Fig. 4.3a, b, the output power was measured by an optical spectrum analyser covering 1,200–2,400 nm (Yokogawa AQ6375B) with a 2-nm-resolution bandwidth. For the result in Fig. 4.4b–e, the output power was measured by an IR 2-μm photoreceiver (Newport 2034).

4.5.3 Numerical simulations

We used commercial software (Lumerical) to solve for the waveguide modes as well as to obtain the dispersion characteristics shown in Fig. 4.2c. In the simulation, the anisotropic index of the LN was modelled by the Sellmeier equations[45]. For the nonlinear optical simulation, we solved an analytical nonlinear envelope equation in the frequency domain using a split-step Fourier technique to simulate the pulse propagation and nonlinear dynamics in the waveguide[46]. The nonlinear step was solved with a fourth-order Runge–Kutta method. Details regarding the single-envelope simulation are provided in Supplementary Section 4.6.4.

4.6 Supplementary Information

4.6.1 Comparison with nonlinear directional coupler presented in Ref.[26]

Here, we want to emphasize that both the design and operating principle of our all-optical switch are fundamentally different from those reported by Schiek et al. [26]. We also explain why our device operating principle leads to significant improvement in the device performance compared this work.

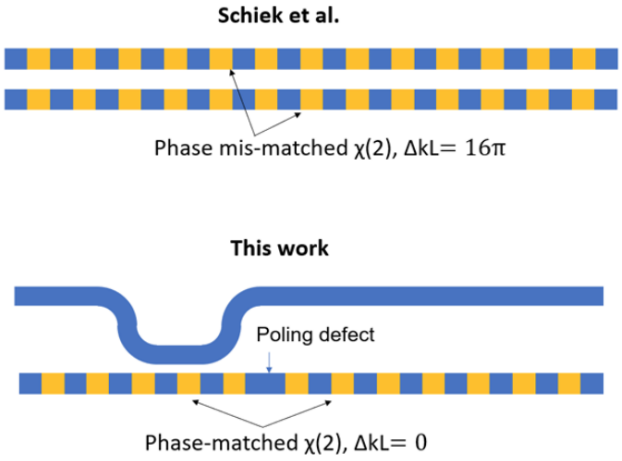

Figure 4.6: Comparison of device design and operating principle.

As shown in Fig. 4.6, the nonlinear directional coupler (NDC) device presented by R. Schiek et al. has two neighboring PPLN waveguide with a very long coupling region. Because the coupling region is long, the input FH can be coupled back and forth between the two neighboring waveguides. Both of the PPLN waveguides operate in large phase-mismatched ($\Delta k \sim 16\pi$) second harmonic generation (or effective $\chi^{(3)}$) regime. ($\Delta k = 1.8\pi \times (219 - T/°C)$) and the device is operating at 210 °C (see page 2 of Ref.[26]). The phase-mismatched SHG produces an effective $\chi^{(3)}$ nonlinearity and self-phase modulation on the input FH pulse. The intensity-dependent self-phase modulation of the FH further perturbs the evanescent coupling ratio of the FH pulse, thus leading to the switching behavior.

In sharp contrast, in our device as shown in Fig. 4.6, we employed phase-matched SHG and DOPA processes separated by the "poling defect" in the waveguide. In the first section of our device, energy flows monotonically from the input pulse towards its second harmonic, while on the second section of our device, energy flows monotonically from the second harmonic towards the fundamental. Therefore, there is no self-phase modulation of the FH pulse in our device. The wavelength selective directional coupler still operates as a linear splitter over its length (i.e. we do not perturb its operation due to the propagation of the modes). Instead, the switching behavior of our device is enabled by the phase-matched frequency conversion and frequency dependent output coupling. Here, we explain why our device operating principle leads to significantly better performance.

Power efficiency: the fundamental difference in operating principle described above leads to dramatic performance difference between our device and the NDC by Schiek et al. Compared to phase-matched $\chi^{(2)}$ processes presented in our work, the all-optical switch based phase-mismatched $\chi^{(3)}$ nonlinearities requires much higher input power. We want to emphasize that even if we implement the NLDC approach in nanophotonic LN platform with the same device length and waveguide geometry as our case, the device performance will still be much inferior to our device.

To ensure a fair comparison, we compare the peak power requirements if both designs are implemented on the same nanophotonic PPLN platform and operate at 2090 nm. The NDC demonstrated by Schiek et al. requires more than 50 W of peak power in 50-mm-long diffused waveguides at 1550 nm. In previous work, Schiek et al. report a normalized nonlinear efficiency (η) of 60%/W/cm^2 for their waveguides at 1550 nm [26], which is typical of those large-mode waveguides. To estimate the required power of their design in our PPLN platform and at our wavelength, we first consider the wavelength difference. Since η scales as ω^4 [38], at 2090 nm η will be reduced to 18%/W/cm^2 for the Ti-diffused waveguides, while our nanophotonic platform provides $\eta \sim$ 1100%/W/cm^2 at these wavelengths[19]. Therefore, implementing such a NDC in LN nanophotonic platform would benefit from a 61-fold larger normalized nonlinear efficiency at the same wavelength.

Second, we consider the length difference. The NDC mechanism is based on self-phase-modulation due to phasemismatched $\chi^{(2)}$ nonlinearities. In the limit of large phase mismatch, with the same amount of ΔkL, the phase shift scales linearly with normalized nonlinear efficiency and power, and quadratically with the device length, i.e. $\Phi_{SPM} \propto \eta P L^2$ (Equation 6 in Ref.[27]). By implementing NDC on our nanophotonic PPLN platform with the same length as our device (~6 mm), L^2 is smaller by a factor of 69. Therefore, to realize the same amount of phase shift with the same amount of ΔkL, the NDC design demonstrated by Schiek et al. still requires a peak power level of above 56 W if it is implemented in our nanophotonic PPLN platform. In our device, however, we have experimentally demonstrated all-optical switching with only ~1.5 W of peak power (80 fJ of 46 fs pulse) in a 6-mm-long waveguide. This illustrates that just the operating principle of our device leads to more than an order of magnitude improvement in the power requirement compared to the NDCs design. The fundamental reason behind this is that the phasematched interactions are more efficient than the phase-mismatched interactions employed in NDCs.

Bandwidth: Another important disadvantage of using phase-mismatched $\chi^{(2)}$ nonlinearity is the attainable bandwidths. As highlighted in Page 3 of Ref.[26]: "... the wavelength dependence of the phase-mismatch yields different effective nonlinearities for the different spectral components which introduce a kind of nonlinear dispersion." In other words, to enable large bandwidths (and femtosecond switching), the nonlinear effect should have a flat response over the entire pulse bandwidth. In our work, we achieve this through dispersion engineering and operating in the phase-matched case with low group velocity mismatch between the pump and the second harmonic. As shown in Fig. 4.7, we can achieve a flat phase-matching spectrum over the pump bandwidth even for a 46-fs input pulses and hence all-optical

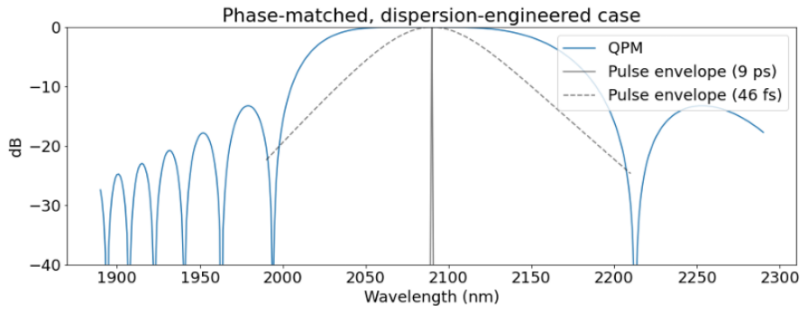

Figure 4.7: Comparison of input pulse envelop (grey) and the nonlinear response (blue) for phase-matched $\chi^{(2)}$ process in dispersion-engineered LN waveguides (the operation principle of our design).

switching with minimal distortion.

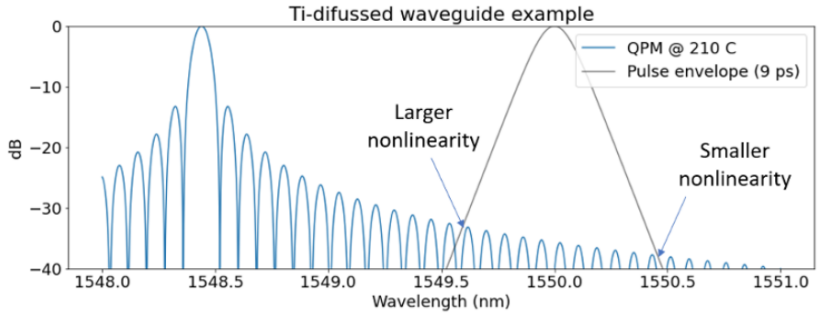

Figure 4.8: Comparison of input pulse envelop (grey) and the nonlinear response (blue) for phase-mismatched $\chi^{(2)}$ process leading to effective $\chi^{(3)}$ (the operation principle of NDC).

On the other hand, Fig. 4.8 shows the phase matching plot for the Ti-diffused waveguide device described in Ref.[26], which operates far from phase matching in order to obtain self-phase modulation of the input pulses. Even though the pulse is 9-ps long and the entire pulse bandwidth is far from the phase matching peak, there is still considerable dispersion, with different parts of the pulse spectrum experiencing different effective $\chi^{(3)}$ values. This leads to the pulse distortions and asymmetries described in Ref.[26] even for 9-ps pulses.

These fundamental spectral dependencies in phase-mismatched effective $\chi^{(3)}$ processes indicate that it may not be even possible to achieve distortion-free all-optical switching with femtosecond pulses using the NDC design. By using the same mismatch ($\Delta kL = 16\pi$) as Ref.[26], we compare in Fig. 4.9 the cases of a 9-ps pulse and a 46-fs pulse in dispersion-engineered nanophotonic waveguides. In this scenario, the pulse spectrum is closer to the phase matching peak, so the effective $\chi^{(3)}$ function is even more dispersive than the previously reported experiment (indicating that even a 9-ps pulse would undergo more severe distortions for an NDC implemented in our nanophotonic platform compared to the old platform). This

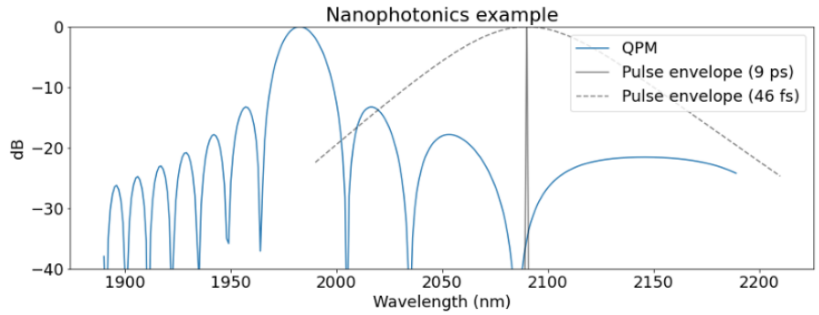

Figure 4.9: Comparison of input pulse envelop (grey) and the nonlinear response (blue) for phase-mismatched $\chi^{(2)}$ process in dispersion engineered nanophotonic LN waveguides.

results in even more distortion for 46-fs pulses, as expected. The simple solution is to operate even farther away from phase-matching, which will decrease the effective $\chi^{(3)}$ coefficient. Therefore, even in the presence of dispersion engineering, it is not clear (and likely impossible) how to achieve femtosecond, femtojoule performance with the NDC design implemented in state-of-the-art nonlinear photonic platforms.

4.6.2 Design of the adiabatically tapered directional coupler

During the device fabrication process, the waveguide width, height, and coupling gap can vary. As a result, the effective index n_{eff} of the waveguide, as well as the coupling strength between the waveguides, will change. The coupling efficiency of the conventional directional coupler, which has neighboring waveguides of identical size, usually suffers from poor tolerance to fabrication errors and can hardly be used as broadband component[30]. Here we adopt an adiabatically tapered directional coupler design[30], which ensures broadband operation and good tolerance to fabrication errors. Figure 4.10 shows the design of the directional coupler, which is composed of a tapered top waveguide (linearly tapered from W_1 to W_2 and a non-tapered bottom waveguide with a width of W_0. The dimensions, including W_1, W_2, W_0, the coupling length L and the coupling gap are labeled in the figure. The gap is fixed throughout the tapered region. Note that the etched LN waveguide has $\sim 60^\circ$ slant angle, the geometry shown in Figure 4.10 corresponds to the top surface of the etched ridge waveguide. For an adiabatic coupler shown in Figure 4.10, the power coupling efficiency ζ can be estimated by the Landau-Zener formula[30, 47]:

$$\zeta = 1 - \exp\left(\frac{-2\pi g^2}{\partial n_{\text{eff}}/\partial z}\frac{2\pi}{\lambda}\right) \tag{4.1}$$

where the coupling strength g equals to the half of the n_{eff} index difference between the even mode and the odd mode at the center of coupler, the $\partial n_{\text{eff}}/\partial z$ is the changing rate of the n_{eff} when varying the waveguide width along the propagation direction z, and λ is the wavelength. For very small g, light can hardly be coupled to neighboring waveguide since $\zeta \approx 0$, while for large g the coupling efficiency $\zeta \approx 1$.

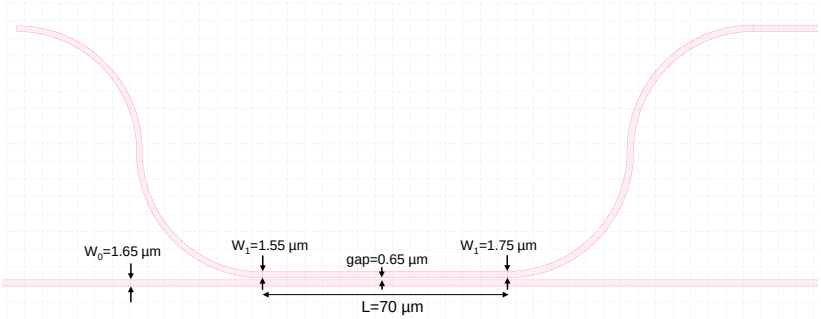

Figure 4.10: Design of the adiabatically tapered directional coupler. The directional coupler is composed two neighboring waveguides. The top width of the top waveguide is linearly tapered from $W_1 = 1.55\ \mu$m to $W_2 = 1.75\ \mu$m, whereas the bottom waveguide is not tapered, with a constant top width of $W_0 = 1.65\ \mu$m. The coupling length L is 70 μm.

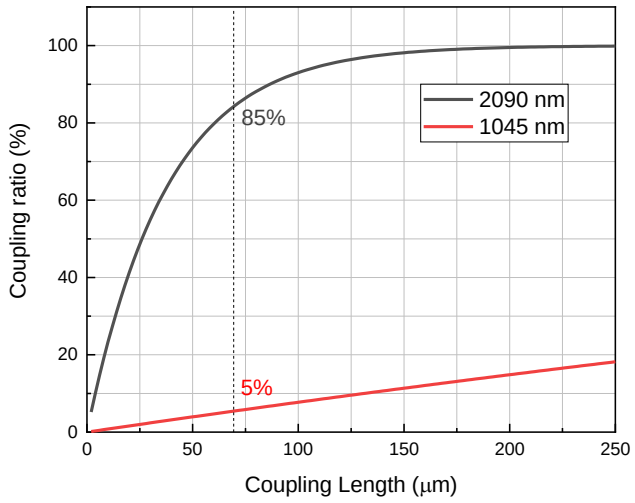

Figure 4.11: Coupling efficiency as a function of coupling length for 2090 nm and 1045 nm light. When the coupling length is is 70 μm, the coupling efficiency for 2090 nm and 1045 nm are 85 % and 5 %, respectively.

Based on Eq. 4.1, in Fig. 4.11 we plot the coupling efficiency ζ of the adiabatically tapered directional coupler with the design parameters shown in Fig. 4.10. When the coupling length is 70 μm, the coupling efficiency for the fundamental TE mode at 2090 nm and the fundamental TE mode at 1045 nm are 85 % and 5 %, respectively. By performing a frequency dependent analysis (Fig. 4.2c in the main text), we have verified that the coupler is broadband around 2090 nm, and has a low coupling ratio for light at 1000 nm. Fig. 4.12 shows a 3-D FDTD (Lumerical) simulation of the wave propagation for the fundamental TE mode at 2090 nm and

1045 nm. Due to the large difference in the mode sizes, the fundamental TE mode at 2090 nm can be efficiently coupled from the bottom waveguide to the top waveguide, while the fundamental TE mode at 1045 nm mostly remains in the bottom waveguide.

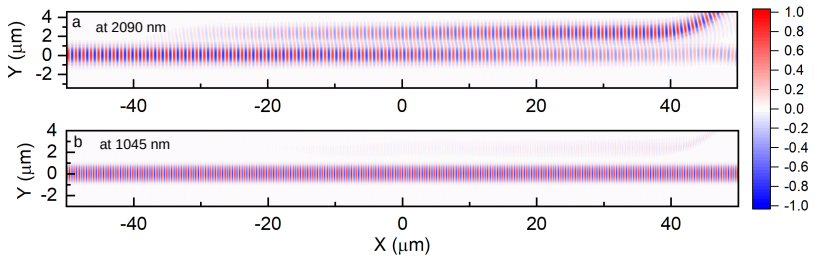

Figure 4.12: Simulated light field propagation for **a** λ = 2090 nm and **b** λ = 1045 nm. Fundamental TE mode at 2090 nm can be efficiently coupled from the bottom waveguide to the top waveguide, while the fundamental TE mode at 1045 nm mostly remains in the bottom waveguide.

4.6.3 Characterization of input pulses

The quantitatively analysis of our switching device including the nonlinear dynamics, the input/output coupling loss, the switching time and energy necessitates an accurate measurement of the input pulses. In Fig. 4.13a, we plot the measured spectrum of input pulses (red solid line). By comparing it with the spectra of 30-fs, 35-fs and 40-fs pulses centered at 2.09 μm, we found that the 35-fs pulse has the best agreement with our experimental spectrum. We also performed the interferometric autocorrelation measurement of the input pulses, as shown in Fig. 4.13b. The Gaussian fitting of the peaks of the autocorrelation has a FWHM of 65.2 fs, indicating that the actual pulse length is close to 46.2 fs. The slightly longer pulse length obtained from the autocorrelation measurement indicates that the input pulse is chirped, presumably due to the dispersive elements in our setup such as the pellicle, the long-pass filter and the neutral density (ND) filter. The relation between temporal profile of the pulse before ($a(t)$) and after ($a''(t)$) the dispersive element is given by[48]

$$a''(t) \approx \left(1 + j\frac{\beta_2 L}{2}\frac{d^2}{dt^2}\right) a(t) \tag{4.2}$$

where L is length of the dispersive medium and β_2 is the group velocity dispersion (GVD) of the dispersive medium. Based on the results in Fig. S1a and b, we can estimate a total group dispersion delay (GDD) of $\beta_2 L = \pm 362$ fs^2. We determine the sign of GDD in section 4.6.5.

4.6.4 Single envelope simulation

We used a method similar to that described in [49] to simulate quadratic interactions over a large bandwidth using a single envelope in the frequency domain. We

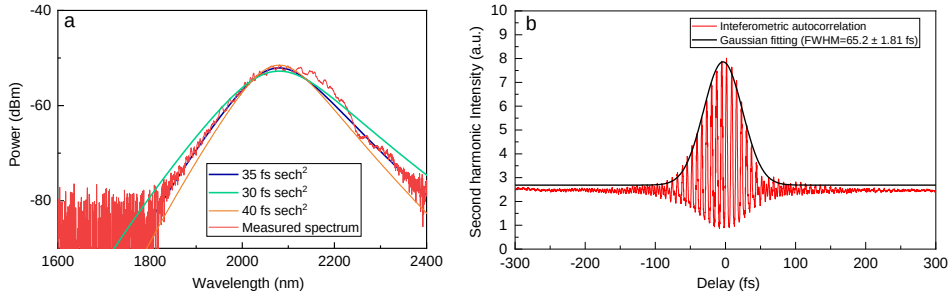

Figure 4.13: **a**, Measured spectrum of input 2.09 μm pulses (red) compared with the spectra of 30- (green), 35- (blue) and 40-fs (orange) pulses. **b**, autocorrelation of the input pulses. The Gaussian fit (black) of the envelop of the interferometric autocorrelation has a FWHM of 65.2 fs.

write a spectral component of the electric field propagating in the z-direction on a single waveguide mode as:

$$\mathbf{E}(x, y, \omega) = A(z, \Omega)\mathbf{e}(x, y, \omega)e^{-i(\beta_0 - \omega_0/v_{\text{ref}})z}, \tag{4.3}$$

where ω and $\Omega = \omega - \omega_0$ are the optical and envelope angular frequencies, ω_0 is the simulation center frequency, β_0 is the waveguide propagation constant at ω_0, v_{ref} is the simulation reference frame velocity, x, y are the transversal waveguide coordinates, $\mathbf{e}(x, y, \omega)$ is the mode transversal field distribution, and $A(z, \omega)$ is the complex amplitude of the field that evolves during propagation. Note that $A(z, \omega)$ is a rapidly-varying envelope, i.e. it includes the phase factor $e^{-i\beta(\omega)z}$ acquired during linear propagation. Furthermore, $A(z, \omega)$ is an analytic signal, i.e., it only contains positive frequencies ($A(z, \omega < 0) = 0$).

We obtained an equation of motion for $A(z, \Omega)$ by ignoring counter-propagating terms (which are usually phase mismatched), and assuming a constant nonlinear coefficient and mode overlap integral, both of which are weak functions of frequency away from any material resonances. No limitations are placed upon the maximum spectral bandwidth of the simulation. The resulting propagation equation is,

$$\frac{\partial A}{\partial z} = -i\left[\beta(\omega) - \beta_0 - \frac{\Omega}{v_{\text{ref}}} - i\frac{\alpha}{2}\right]A - \frac{i\omega\epsilon_0 X_0}{8}d(z) \\ \mathcal{F}_\Omega\left\{a^2(z,t)e^{j\phi(z,t)} + 2a(z,t)a^*(z,t)e^{-j\phi(z,t)}\right\}, \tag{4.4}$$

where $d(z) = \pm 1$ is the sign of the quadratic nonlinear coefficient that is modulated in quasi-phase matching, $a(z, t)$ is the time domain representation of $A(z, \Omega)$, $\phi(z, t) = \omega_0 t - (\beta_0 - \omega_0/v_{\text{ref}})z$, $\mathcal{F}_\Omega$ is the Fourier transform in the Ω variable. The effective nonlinear coefficient X_0 is defined as:

$$X_0 = \sum_{ijk} \chi^{(2)}_{ijk} \int e^*_i(\omega_1)e_j(\omega_2)e_k(\omega_1 - \omega_2)\,\mathrm{d}S\,, \tag{4.5}$$

where $\chi^{(2)}_{ijk}$ is the quadratic nonlinear susceptibility tensor, j, k, l are Cartesian components of the corresponding vectors, and ω_1 and ω_2 are two suitable chosen frequencies, e.g., the signal and pump frequencies in our case.

The time domain terms inside the Fourier transform of Eq. (6.3) represent the processes of sum frequency generation $\left(\propto a(t)^2\right)$ and difference frequency generation $(\propto a(t)a(t)^*)$, which combined can predict all classical second order interactions, such as second harmonic generation and parametric amplification. Since $A(z)$ is fast varying, carrier dynamics can be resolved. In particular, phase mismatch is automatically included and the term $d(z)$ can be used to accurately simulate different quasi-phase matching gratings. This also means that the spatial domain needs to be sampled finely enough to resolve these dynamics. We solve the evolution equation (6.3) with the split-step Fourier technique using the fourth-order Runge-Kutta method for the nonlinear step.

4.6.5 Deterministically finding the quasi-phase-matching condition

In this section, we introduce the experimental methods that we used to deterministically find the quasi-phase-matching condition. Although we can determine the required poling period for a particular LN waveguide cross-sectional geometry by performing the numerical simulations, the fabrication errors in terms of the waveguide width, height, and the variation of the thin film thickness can shift the nominal poling period. To account for the fabrication errors, we fabricated 20 nonlinear splitter devices on the same chip including 20 poling periods ranging from 4.97 μm to 5.17 μm. The shift between consecutive poling periods is 10 nm. By monitoring the second harmonic generation of all the devices at the output coupler ports, we found that a period of 5.11 μm is closest to quasi-phase-matching.

In addition, we used a thermoelectric cooler (TEC) underneath the chip to change the temperature of the device and coated thin organic materials, thereby fine-tuning the refractive index and the nominal poling period of the LN waveguides[50]. Based on our earlier experiments[24], we found that 1 °C temperature increase of LN nanophotonic waveguide can offset the nominal poling period by $\sim$ 0.2 nm. Therefore, one can account for the 10-nm poling period interval by applying $\sim$ 50 °C temperature change to our device. Since the output coupler evanescently couples out $\sim$ 85% of FH power right after the SHG process, by monitoring the FH power out of the outcoupler, we can have a knowledge on the efficiency of the SHG process and the amount of phase mismatch, which are essential for determining the optimal operating temperature of the device.

Fig. 4.14a shows the simulated output FH power at the drop port as a function of input FH power. When the phase mismatch is zero (Δpp=0 nm, black), the output FH power exhibits a strong saturation as input FH power increases, since the SHG process depletes the FH power strongly. Also, the output FH power is low since most of the FH is converted to the SH, which is not strongly coupled out. When the input power is higher (e.g. beyond 30 mW), the saturation becomes less pronounced due to the back-conversion from the SH to FH, which will be discussed in the following sections. When the phase mismatch increases, the output-input becomes steadily

closer to a linear relation since less FH will be depleted. Experimentally, using the 5.11-μm poling period device, we observed a similar trend, as shown in Fig. 4.14b. When the device temperature is either too high (> 70 °C) or too low (< 50 °C), the output-input curves exhibit insignificant saturation of FH and higher output FH power. By comparing the experimental curves with the simulation, we found that the optimal temperature range for achieving phase-matching is 60-65°C.

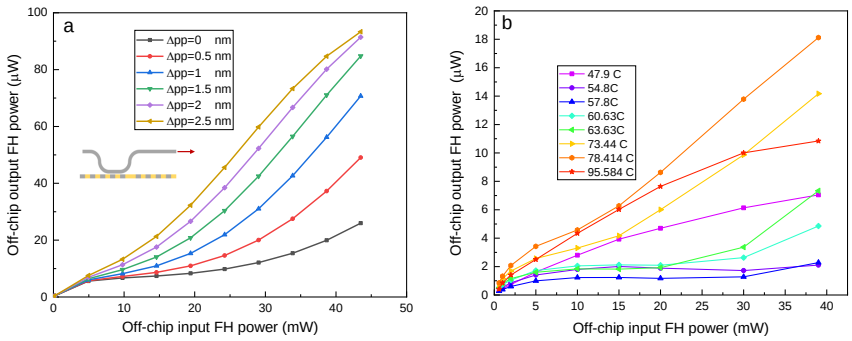

Figure 4.14: **Deterministically finding the quasi-phase matching condition a**, simulated output FH power at the drop port as a function input FH power and the phase mismatch. Δpp denotes the offset to the nominal poling period (pp). **b**, measured output FH power at the output coupler as function of input FH power and temperature.

4.6.6 Calibration of the input/output coupling loss

Quantifying the input/output coupling loss during our LN nonlinear splitter measurement is critical for determining the on-chip input pulse energy and evaluating the device efficiency as an all-optical switch. Although we can accurately measure the total loss (throughput), it is still difficult to disentangle the losses imposed by the input coupling, the waveguide propagation and the output coupling. In our earlier optical parametric amplification (OPA) measurements[24] of a similar LN nanophotonic waveguide on the same free-space light coupling setup we used in this work, we have extrapolated that the input coupling loss is ~ 25 dB and the output coupling loss is ~ 5.8 dB. In our free-space coupling scheme, the input coupling has much lower efficiency compared to the output because we need to couple a free space beam to the single fundamental TE mode in the LN waveguide, whereas on the output side nearly all the outcoupled light can be collected by a large objective and then be readout by the detector. Here, we determine the input/outcoupling loss in our measurements by comparing the simulated phase-matched SHG process with the measurement results.

In Fig. 4.15, the black symbols show the measured output FH power at the the drop port as a function of input FH power. The power values are measured off the chip. The total loss we experimentally measured is 26.6 dB. Assuming there is

$\sim$ 1 dB waveguide propagation loss, the total coupling loss is $\sim$ 25.6 dB. In Fig. 4.15a, we also plot the simulated results with different combinations of input/output coupling losses. The simulation assumes 46.2 fs of chirped 2.09 μm input FH pulses with a GDD of 362 fs^2, according to the analysis in section 4.6.2. It can be seen from Fig. 4.15a that the simulation with 21.6 dB input coupling loss and 4 dB output coupling loss has the best agreement with the experimental results (green solid line). Moreover, it is clear from Fig. 4.15b that only the positive GDD can lead to good agreement with the experimental results.

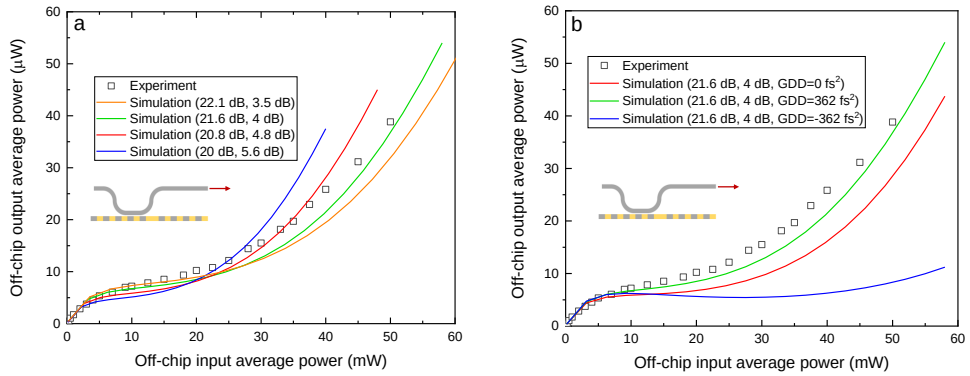

Figure 4.15: **Determining the input/output coupling loss. a**. Measured (black symbols) and simulated (solid lines) output FH power at the the drop port as a function of input FH power. The simulation assumes different combinations of input/output coupling losses, while the total coupling loss is fixed at 25.6 dB. **b**. Measured (black symbols) and simulated (solid lines) output FH power at the drop port. The simulation results assuming a GDD of input pulse of 362 fs^2, 0 ^{2} and -362 fs^2 are shown in green, red and blue. All simulations assume 21.6 dB/4 dB input/output coupling losses.

4.6.7 Device fabrication variation and device operating wavelength tuning

By optimizing the voltage, electric pulse duration and shape, the yield for successful and uniform periodic poling is higher than 90 %. Such a poling condition can work for poling period ranging from 2.5 μm to 6 μm. We defined our poling pattern through electron-beam lithography, and it has negligible error in poling periods.

The nominal poling period for quasi-phase-matching critically depends on the geometry (waveguide width, etching depth, thin-film LN thickness, and sidewall angle). Fig. 4.16 below shows our simulation of the nominal poling period as a function of etching depth and top width of the LN waveguide. In summary, the nominal poling period is shifted by 0.7 nm if the top width is shifted by 1 nm; the nominal poling period is shifted by 1.2 nm if the etching depth is shifted by 1 nm; the nominal poling period is shifted by 5 nm if the thin film is shifted by 1 nm.

We found the phase-matching condition is most sensitive to variation of the total thin-film thickness.

Our e-beam patterning process of HSQ resist can result in a fabrication error of 5-10 nm in terms of waveguide widths. During the dry etching, we carefully monitor the remaining LN thickness by using the white light interferometer (Filmetrics). We can well control the etching depth, with an error within 5 nm. The sidewall angle of approximately 60° is set by the physics of the dry etching process, so it does not vary considerably from chip to chip. Usually, for the neighboring devices fabricated on the same chip, their performance is very similar, and their slight difference can be compensated by temperature tuning. However, when they are far apart on the chip, their performance can be quite different. This is because of the variation of the total thin-film LN thickness on the chip.

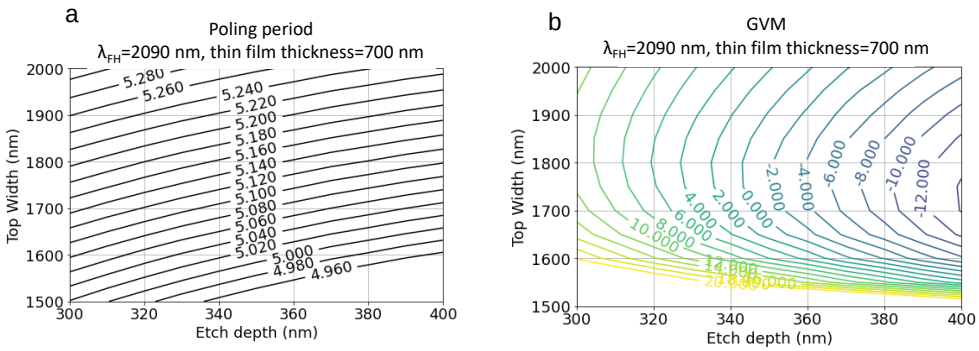

Figure 4.16: **a**. Dependence of nominal poling period on the etching depth and the top width of the waveguide. **b**. Dependence of GVM on the etching depth and the top width of the waveguide.

By globally tuning the device temperature using a TEC, the variation of waveguide width, and etching depth and their effects on the nominal poling period can be compensated. We have experimentally explored such temperature tunability using another device, which is a straight periodically poled lithium niobate waveguide with a similar geometry [24]. As shown in Fig. 4.17 below, by comparing the experimental result and the simulation, we found that tuning the device temperature from 10 °C to 55 °C is equivalent to shifting the nominal poling period (or the operating wavelength) of the device by 8 nm. The figure also shows that while the temperature is important for achieving phase-matched processes, the operation is not very sensitive to temperature and a change of chip temperature in the order of tens of degrees would not prohibit operation.

We believe that with the advancement of thin-film LN manufacturing, the device consistency over the chip will be greatly improved. Also, implementing on-chip electro-thermal heaters [51] will greatly help reduce the device variation and increase the operating wavelength tuning range.

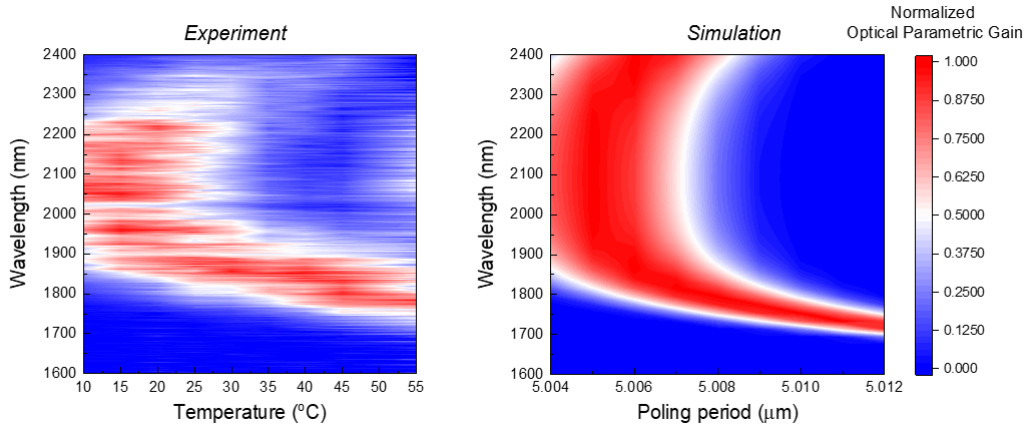

Figure 4.17: **a** Measured normalized optical parametric gain spectra in linear units as a function of chip temperature. **b** Simulated normalized optical parametric gain in linear units as a function of signal/idler wavelength and quasi-phase-matching poling period offset from nominal.

4.6.8 Nonlinear dynamics

In this section, we discuss the ultrafast and the strong nonlinear dynamics of the FH and SH pulses in our device. The nonlinear dynamics in the time domain can help us understand the spectral features we experimentally observed, as well as the operating regime for all-optical switching. We also show that when the input pulse energy is below 600 fJ, the temporal shape of the FH pulse is minimally perturbed at the through output in both on- and off- states.

A. Nonlinear dynamics in the SHG region

We first discuss the nonlinear dynamics in the first 2.5-mm-long SHG region. Figure 4.18 left panels show the simulated "snapshots" of the FH (red) and SH (blue) pulses right after the SHG process (before the poling defect) under various input pulse energies (4 fJ to 2 pJ). The right panel show the corresponding spectra. Due to the very small GVM (-0.41 fs/mm), it can be seen that the FH and SH pulses are still temporally overlapped after the 2.5-mm-long SHG process, showing negligible temporal walk-off. As shown in Fig. 4.18 a and b, during the conversion process, the FH pulse is slightly broadened since the higher intensity part of the FH pulse has higher SHG conversion efficiency, and the wings of the FH pulse has a lower conversion efficiency.

Further increasing the input FH pulse energy results in stronger depletion of the FH pulse. The strong depletion can even lead to a temporal dip in the FH pulse, as shown in Fig. 4.18 c. The corresponding spectrum, which is the Fourier transform of the pulses in the time domain, also shows the spectral dips around the center wavelength (2090 nm) of the FH pulse.

In the presence of a temporal dip, the output FH pulse can be regarded as

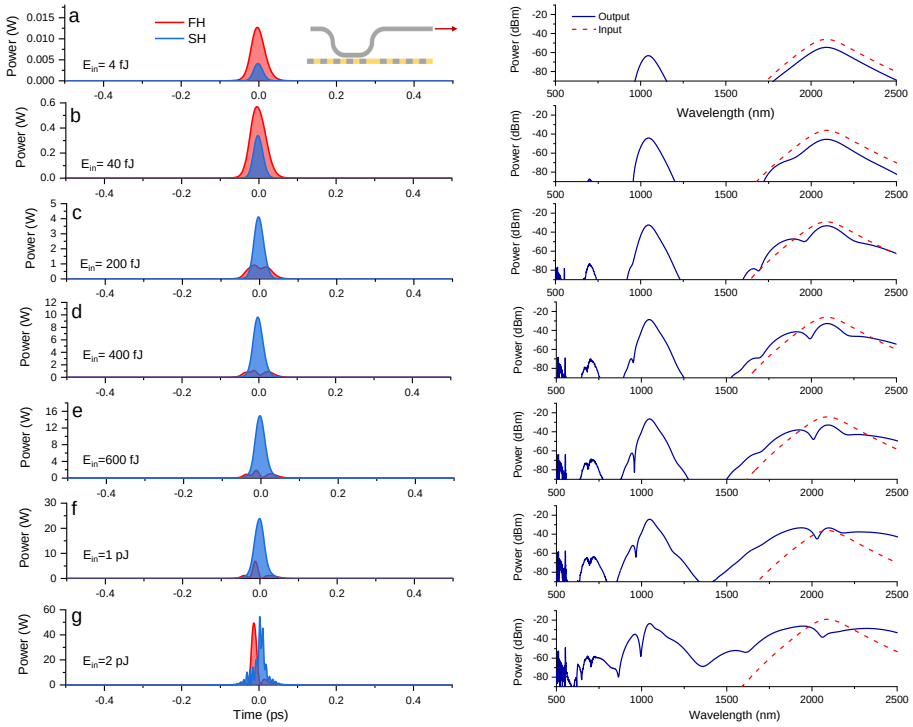

Figure 4.18: **Ultrafast nonlinear dynamics in the SHG region. a-g** Left: simulated time-domain output of the fundamental (FH) and the second harmonic (SH) under various input pulse energies. The FH and SH pulses are represented by the red and the blue pulses. Right: simulated output spectra under various input pulse energies (blue solid lines). The dashed lines are the spectra of input pulses. The spectral features around 700 nm and 522 nm correspond to the sum frequency generation (SFG) between FH and SH and the forth harmonic of the FH.

being split into two neighboring pulses, which are shorter than the input FH pulse. Therefore, some spectral broadening can be seen (Fig. 4.18 c). By further increasing the input FH energy, the higher intensity part of the two neighboring FH pulses can still transfer energy to the SH, thus leading to the generation of additional temporal dips and further broadening of the spectrum (Fig. 4.18 d-g).

B. Nonlinear dynamics in the entire device

Figure 4.19 illustrates the ultrafast nonlinear dynamics in the entire device. By comparing it with Fig. 4.7 it is evident that after the poling defect and the 3.5-mm DOPA section, the depleted FH pulses (red pulses) recovers in power, without showing obvious temporal dips. Such power recovery is more pronounced when the input pulse energy is higher since both the SHG and DOPA processes become stronger, as revealed by Fig. 4.19 a-e. It can be seen that the recovery of the FH power also eliminates the spectral dips around 2.09 μm. In addition, during the DOPA process, the FH extracts the power from the SH. As a result, the SH pulse

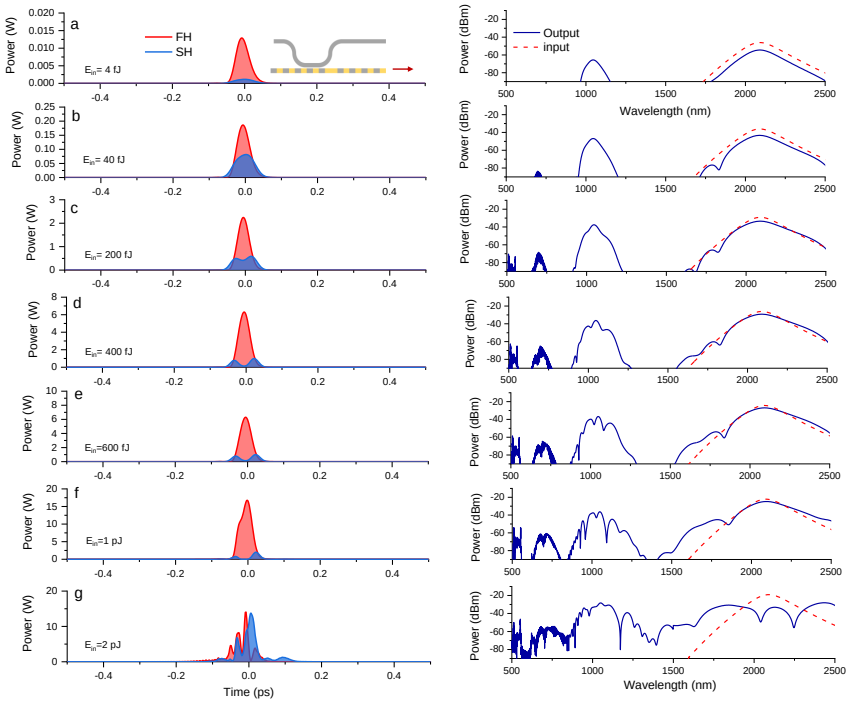

Figure 4.19: **Ultrafast nonlinear dynamics in the entire nonlinear splitter device. a-g** Left: simulated time-domain output of the fundamental (FH) and the second harmonic (SH) under various input pulse energies. The FH and SH pulses are represented by the red and the blue pulses. Right: simulated output spectra under various input pulse energies (blue solid lines). The dashed lines are the spectra of the input pulses. In the simulation, the device has a 2.5-mm-long SHG region, a 3.5-mm-long DOPA region, 85% (5%) of outcoupling of the FH (SH) in the directional coupler. We also assume the propagation loss of FH and SH are both 1 dB/cm.

(blue) can be depleted. When the DOPA process is strong enough, temporal dips can occur on the SH pulse, as shown in Fig. 4.19 c-f. This results in the spectral dips and the spectral broadening around 1045 nm. Therefore, compared to the results shown in section A, it is evident that the occurrence of temporal and spectral dips is indicative of the power flow direction between the FH and the SH.

Figure 4.20 shows the spectra that we experimentally collected both at drop port and the through port. When the input pulse energy is less than 600 fJ, at the drop port (Fig. 4.20a), spectral dips (labeled by the white arrows) can be found around 2.09 μm, whereas the no clear spectral dips can be found around 1.045 μm. This indicates the power is flowing from the FH to the SH. At the through port, spectral dips (labeled by the white arrows) can be found around the 1.045 μm and no spectral dips can be found around 2.09 μm, which means that the power is flowing from the SH to the FH. However, when the input pulse energy exceeds 600 fJ, the power flow directions discussed above are no longer valid, as spectral dips and significant

spectral broadening emerges around 1.045 μm in Fig. 4.20a. This behavior is a result of the power flowing back from the SH to the FH in the 2.5-mm-long SHG region, which will be elaborated in the following section.

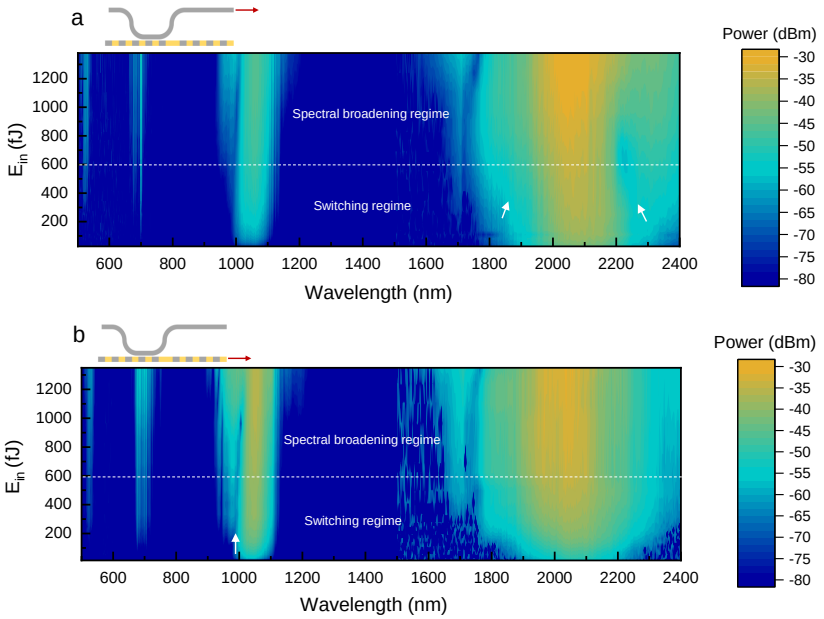

Figure 4.20: Measured output power spectral density output at the drop port (a) and the through port (b) as a function of the input pulse energy (E_{in}). The spectral dips are labeled by the white arrows. The dashed white line separates the all-optical switching regime and the spectral broadening regime. Note that in (a) the power of the SH spectrum is much lower than the power of the FH spectrum due to much lower out-coupling ratio (~5%).

C. Operating regime for the all-optical switching

In the main text, we discussed the nonlinear transmittance at low input FH pulse energies (0-600 fJ). Here in Fig. 4.21 a and b. we plot the measured power dependent transmittance when the input pulse energy is varied from 0 to 1400 fJ (black symbols). The blue solid lines are the simulated results, showing good agreement with the experimental results. In the simulation, we assumes 35 fs input pulses with chirp at 2.09 μm. The device has a 2.5-mm-long SHG region, a 3.5-mm-long DOPA region, 85% (5%) of outcoupling of the FH (SH) in the directional coupler. We also assume the propagation loss of the FH and the SH are both 1 dB/cm.

The regime that the nonlinear splitter can function as an all-optical switch is highlighted by the yellow color. When the input FH pulse energy exceeds 600 fJ, the strong depletion of FH during the SHG process leads to the splitting of FH pulse and therefore significant spectral broadening, as shown in section A. Meanwhile,

the phase difference between the FH and the SH is altered. As a result, in the SHG region, the SH energy can even flow back into the FH, which is evident by the increased FH transmission at higher input pulse energy shown in Fig. 4.21a. The change of the phase difference between the FH and SH during the SHG process can also lower the parametric gain of the DOPA. This explains why the transmittance of the FH at the through port is no longer increasing, as shown in Fig. 4.21b. Fig. 4.21 c shows the simulated power evolution of the FH and the SH along the entire device. Clearly, when the input pulse energy is high (e.g. 1200 fJ), significant back-conversion can happen in the SHG region.

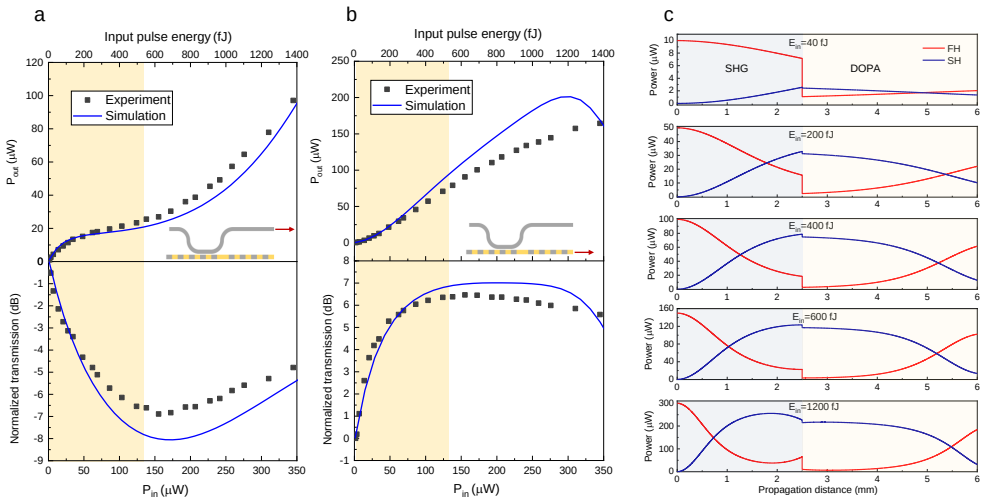

Figure 4.21: **Nonlinear optical transmission in the integrated nonlinear splitter a**, Upper panel: average output power of 2.09 μm FH from the drop port as a function of on-chip input average power/pulse energy. Lower panel: normalized transmittance of the FH at the drop port. **b**, Upper panel: average output power of FH from the through port as a function of input average power/pulse energy. Lower panel: normalized transmittance of the FH from the through port. In both **a** and **b**, the blue solid lines are the simulation results. The black symbols are the measurement results. The regions highlighted in yellow are the all-optical switching regimes. **c**, Simulated evolution of the FH and the SH optical power along the main waveguide at various input pulse energies.

4.6.9 Performance comparison of on-chip all-optical switches

Figure 4.22 summarizes the switching time and energy per bit of various all-optical switching devices. The references are labeled in the figure. To make a fair comparison, here we mainly focus on comparing on-chip all-optical switches operating at room temperature.

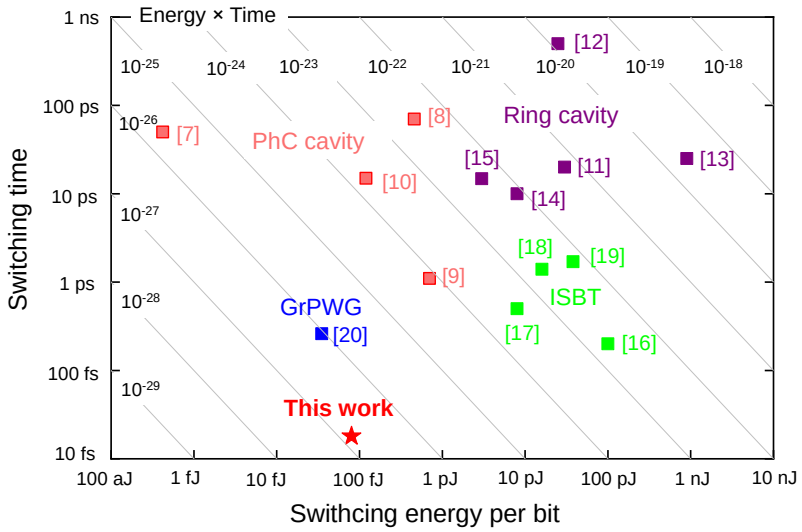

Figure 4.22: Performance comparison of various on-chip all-optical switches operating at room temperature. The data points dictate the switching time and switching energy per bit for switches based on photonic crystal (PhC) cavity[1, 12, 13, 52], ring cavity[53, 11, 54, 14, 55], inter-subband transition (ISBT)[8, 56, 57, 58], and graphene loaded plasmonic waveguide (GrPWG)[18]. Our device features the record-low switching energy-time product of 1.4×10^{-27} J·s, representing around an order of magnitude improvement over the previous all-optical switch based on graphene-loaded plasmonic waveguides.

4.6.10 Toward higher switching contrast

In the device presented in this work, the maximum switching contrast is limited by the coupling ratio of the directional coupler, which is 85 % at 2090 nm. This gives rise to 15% of remaining FH transmission in the "off-state". Therefore, the maximum switching contrast can be achieved in the current device is 8 dB (100% divided by 15%).

However, the switching contrast can be enlarged to be more than 10 dB at low energy by engineering the coupling ratio of the directional coupler. Fig. 4.23 illustrates the design. As shown in Fig. 4.23a, the switch is still of 6-mm-length, containing a 1.4 mm SHG region and 4.6 mm DOPA region. Moreover, the directional coupler is designed to have 99.5% output coupling at 2.09 μm and 15% output coupling at 1.045 μm (according on Fig. 4.11). The numerical simulation results of this design are shown in Fig. 10 b and c. Using 46.2 fs pulses at 2.09 μm as input, the switching contrast is more than 20 dB within 600 fJ energy. The energy required for achieving 10 dB switching is 136 fJ. To further lower the 10 dB switching energy, one can consider operating the device at a shorter wavelength [38] or prolonging the SHG and DOPA regions.

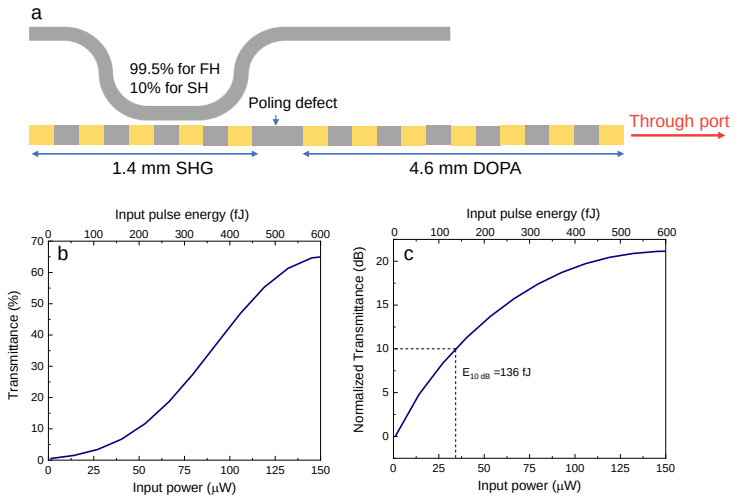

Figure 4.23: **a**. Schematic of chip-scale integrated mode locked lasers based on TFLN all-optical switch and erbium doped LN waveguide. **b**. Evolution of the pulse in the time domain for 300 roundtrips simulated by a split-step Fourier method. The mode-locking is self-starting from the amplified spontaneous emission (ASE) noise. The simulation assumes a modest small signal gain of 7 dB in the erbium doped LN waveguide region and a net normal group velocity dispersion (GVD) of 150 fs^2/mm in LN waveguide and a group velocity mismatch (GVM) of 10 fs/mm in the periodically poled LN region. **c**. In the steady-state, the integrated mode locked laser can emit 107 fs ultrashort pulses at 1550 nm.

4.6.11 Dispersion engineering at telecommunication wavelengths

In the main text, the design and operation our device at 2.09 μm are mostly motivated by the current practical considerations regarding nanophotonic LN platform. These practical considerations include the ease of dispersion engineering, avoiding other potential parasitic nonlinear processes such as photorefractive effect, and having a very low material loss for LN. However, in principle, the same device concept can be achieved at other wavelengths, for example telecommunication wavelength around 1550 nm.

In Fig. 4.24, we show a carefully designed waveguide geometry for 1550 nm, in which the GVD and GVM can also be close to zero. Our numerical simulations suggest that the switch, which still contains a 2.5-mm-long SHG region and a 3.5-mm-long DOPA region and 85 % output coupling of the FH, can operate with pulses as short as 50 fs, and a 3 dB switching energy as low as 18.8 fJ. It is worth noting that at 1550 nm, the 3 dB switching energy can be much lower than that at 2090 nm (~80 fJ). This is because at a shorter wavelength, the effective nonlinearity of LN waveguide becomes much larger due to better field confinement and the wavelength dependence of LN's nonlinear coefficient[38].

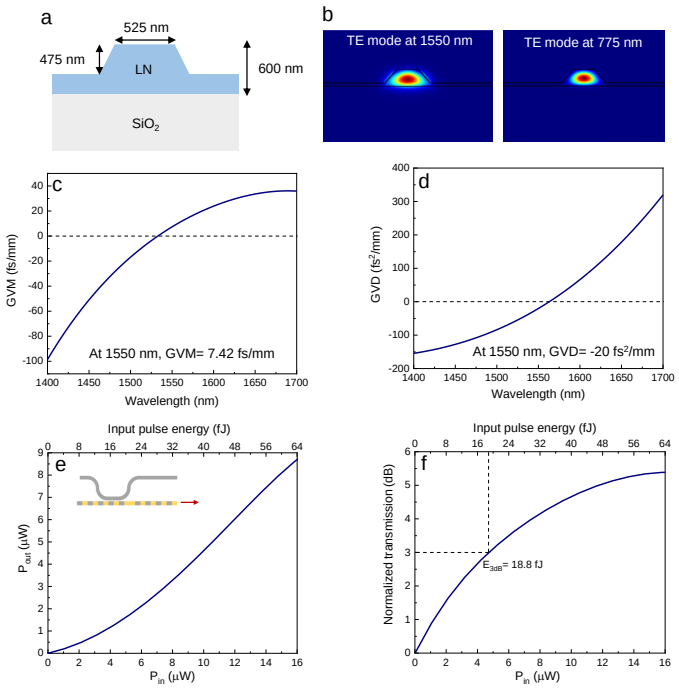

Figure 4.24: **a**. Dispersion engineered waveguide geometry at 1550 nm. **b**. Electric field distributions of the fundamental quasi-TE modes for the dispersion-engineered waveguide at 1550 nm and 775 nm. **c**. Simulated group velocity mismatch (GVM) between the quasi-TE modes of the dispersion-engineered LN waveguide at 1550 nm and 775 nm. At 1550 nm, the GVM is 7.4 fs/mm. **d**. Simulated group velocity dispersion (GVD) for the quasi-TE mode of the dispersion-engineered LN waveguide. At 1550 and 775 nm, the GVD is -20 fs^2/mm and 246.8 fs^2/mm, respectively. **e**. Simulated average output power of 1550 nm FH from the through port as a function of input average power/pulse energy. **f**. Normalized transmittance of 1550 nm FH at the through port. The required pulse energy for 3 dB transmission modulation is 18.8 fJ. For simulations shown in **e** and **f**, the input 1550 nm pulse length is 50 fs.

4.6.12 Applications of femotosecond, femotojoule all-optical switch

A. Terabit/s (Tbps) information processing

One of the most promising architectures that can benefit from our all-optical switch is optical time-division multiplexing (OTDM)[59, 60]. While generating high data rate (>100 Gbps or Tbps) optical signals has been feasible using electronic and opto-electronic components, for instance for telecommunication, processing such optical signals with Tbps rates has remained challenging. The all-optical switch demonstrated in this work can be the missing piece in enabling all-optical signal processing in time-multiplexed systems, not only for communication applications but also for optical computing platforms. Here we briefly show how such time-multiplexing is achieved in current experiments with fast data rates. We also

briefly discuss the shortcomings of previously demonstrated all-optical switches to process such optical signals. We also emphasize that with the recent advances in nanophotonic lithium niobate, such a multiplexing (and demultiplexing) architecture can be realized on a single chip, with compatibility with digital computers. Our all-optical switch enables an unprecedented and practical path to perform all-optical signal processing with THz clock rates, which has been beyond the reach of electronic, optoelectronic, and optical systems so far.

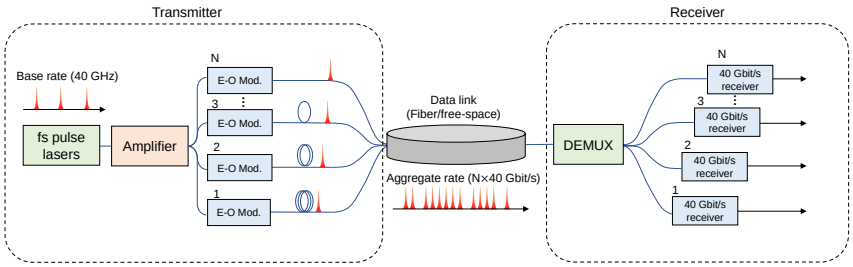

Figure 4.25: Schematic of an OTDM system. The transmitter is based on optical delay lines to generate aggregated Tbps optical signals using GHz electrooptic (E-O) modulators from Gbps electronic signals. The receiver part can demultiplex the aggregated Tbps signal into Gbps signal, which can be detected by Gbps optical receivers. E-O Mod.: electro-optic modulator, DEMUX: demultiplexing.

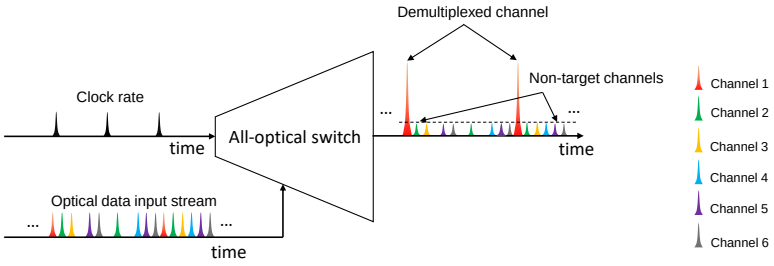

Figure 4.26: Schematic of a channel DEMUX using an all-optical switch. Different signal channels (at the same wavelength) are represented by different colors of pulses. The DEMUX uses a control pulse train at the base bit rate to "pick up" the target channel. The demultiplexed channel can then be read out by Gbps optical receivers.

As shown in Fig. 4.25, with optical delay lines, OTDM time-multiplexes ultrashort optical pulse trains at a base bit rate (e.g. 40 Gbps) to form a composite bit stream with a much higher bit rate of $N\times40$ Gbps, where N is the number of channels. Realizing Tbps OTDM transmitter on thin-film lithium niobate platform is highly promising, given the recent advancements made on high repetition rate femtosecond pulse generation in thin-film lithium niobate platform, as well as

electro-optic modulators. However, such a high bit rate poses significant challenges for signal processing using conventional optoelectronic devices. One prime example is demultiplexing (DEMUX) in the receiver part. It is known that optical receivers (photodetectors) can only resolve the Gbps data rate. Therefore, the OTDM system requires all-optical switches to "pick up" individual Gbps channels from an aggregated Tbps data stream, as illustrated in Fig. 4.26.

To enable Tbps DEMUX or information processing, a switch must have a switching time shorter than 1 ps. However, realizing Tbps information processing is impossible with conventional all-optical switches and integrated all-optical switches with optical resonator structures, although they can be more compact. This is because of the following reasons:

- **Long switching time imposed by high-Q resonators**. A resonator with a very modest Q factor of 10,000 has a photon lifetime of 11 ps. As summarized in Fig. 4.5 in our main text, existing all-optical switches with cavity structures (i.e. Photonic crystal (PhC) cavities and ring cavities) all have a switching time longer than 10 ps. Therefore, an all-optical switch with picosecond switching time is not fast enough to achieve Tbps data rate information processing. Also, an all-optical switch with 10s of picosecond switching time does not offer a significant speed advantage over conventional electro-optic modulators.

- **Speed limitations of carrier-based switches**. While there are impressive demonstrations of all-optical switches with the help of carriers in semiconductors, it is worth noting that in many of such switches, the slow carrier dynamics imposes a limit on switching speed. Hence, our use of instantaneous parametric nonlinearity is an important ingredient in achieving a switch with potentially 10s of THz of speed.

- **Importance of low-energy operation** With such a high bit rate, it is important to note that operation in the fJ is critical for a switch. For instance, a 10-Tbps switch at 100 fJ switching energy corresponds to requiring 1 W of average power.

As application examples, the all-optical switch presented in this work can enable fJ energy/bit and Tbps DEMUX and channel insertion, which are illustrated in Fig. 4.27. At the through port, the device can demultiplex the channel by serving as an AND logic gate. Here we assume both the clock and the Tbps signal have 40 fJ/bit energy. Without the clock pulse train, the pulse energy measured at the through port is 40 fJ$\times$15% $\times$ 1.4 = 8.45 fJ, where 1.4 corresponds to 1.5 dB transmission enhancement according to the results shown in Fig. 4.3b in the main text. When the pulses in the clock and signal are temporally overlapped, according to our measurement result shown in Fig. a, the resulting pulse energy measured at the through port is 80 fJ$\times$15% $\times$ 2.34 = 28 fJ. To further increase the contrast between the targeted channels and the non-targeted channels, one can employ a design with higher switching contrast, which is shown in Supplementary Information section 4.6.10.

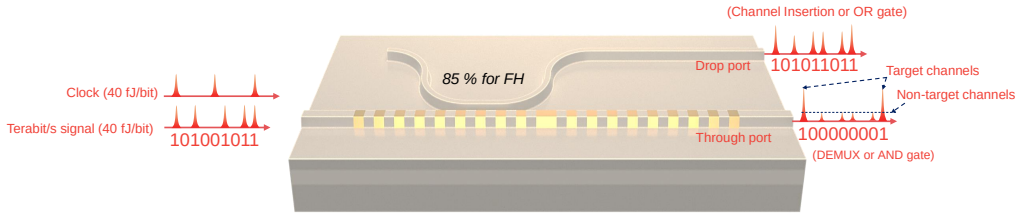

Figure 4.27: Illustration of optical channel demultiplexing (AND logic gate) at the through port and new channel insertion (OR logic gate) at the drop port using the all-optical switch demonstrated in this work.

At the drop port, the device can be used for channel insertion by serving as an OR logic gate. This allows the insertion of channels without significantly disturbing other existing channels. Here we still assume both the clock and the Tbps signal have 40 fJ/bit energy. Without the clock pulse train, the pulse energy measured at the drop port is 40 fJ×15% × 0.74 = 25 fJ, where 0.74 corresponds to -1.5 dB transmission reduction. When the pulses and in the clock and signal are temporally overlapped, according to our measurement result shown in Fig. 4.3a in the main text, the resulting pulse energy measured at the through port is 80 fJ×15% × 0.53 = 36 fJ, where 0.53 corresponds to -2.7 dB transmission reduction.

B. On-chip generation of ultrashort light pulses

As another important application, the all-optical switch demonstrated in this work can serve as an energy-efficient and ultrafast artificial saturable absorber for developing chip-scale mode-locked lasers on thin-film lithium niobate (TFLN). Recently, significant advancement has been made on integrating laser gain medium on TFLN [61], including semiconductor gain medium and solid-state gain medium including Er and Yb ions [62, 63, 64, 65, 63]. However, for making integrated femtosecond lasers, realizing an ultrafast and energy-efficient mode-locking element is still elusive.

Since our device shows a very superlinear P_{out} versus P_{in} relation that occurs at a low input pulse energy (Fig. 4.3b in the main text), it can function as an ultrafast and energy-efficient artificial saturable absorber for mode-locking, i.e. by offering higher transmission to higher intensity pulses, and offering lower transmission to lower intensity pulses.

In the figure below, we illustrate an example of how we can utilize our all-optical switch in developing chip-scale mode-locked lasers. The laser cavity is composed of a gain region made of a long LN waveguide doped by solid-state gain medium including such as Er or Yb ions, two on-chip wavelength-division multiplexers (980/1550 WDMs), and an all-optical switch device. By pumping the erbium-

doped LN waveguide by a 980 nm diode, amplified spontaneous emission (ASE) signal at 1550 nm will be generated. The WDM guides the 1550 nm ASE signal to the laser cavity and the residual 980 nm pump out of the chip. The all-optical switch will serve as an energy-efficient and ultrafast saturable absorber which favors the resonance of high-intensity short pulses, while rejects low intensity long-pulse or CW operation. Therefore, after many roundtrips, the effective saturable absorption of our switch in the cavity can lead to steady-state ultrashort pulse mode-locking.

Fig 4.28 b and c show the numerical simulation of laser mode-locking by split-step Fourier method (SSFM). The erbium doped gain medium was modeled using a method described in Ref.[66]. The simulation assumes a modest small-signal gain of 7 dB in the erbium-doped LN waveguide region, a cavity free spectral range (FSR) of 10 GHz, a normal group velocity dispersion (GVD) of 150 fs^2/mm in LN waveguide and a group velocity mismatch (GVM) of 10 fs/mm in the periodically poled LN region, and a 0.2-mm-long length of SHG region and a 0.2-mm-long length of DOPA region. We seeded the gain region with random noise as the initial condition in order to emulate the mode locking process. As shown in Fig. b, the mode-locking can be self-starting from the amplified spontaneous emission (ASE) noise. In the steady state, the laser can emit ~100 fs ultrashort pulses at 1550 nm (Fig. 4.28 b).

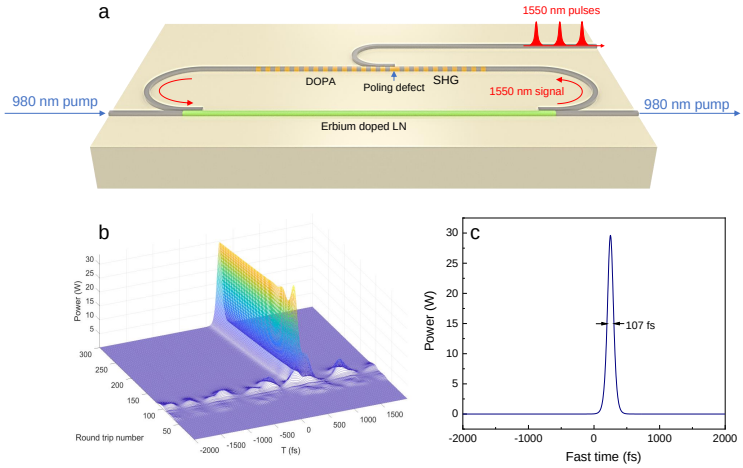

Figure 4.28: **a**. Schematic of chip-scale integrated mode locked lasers based on TFLN all-optical switch and erbium doped LN waveguide. **b**. Evolution of the pulse in the time domain for 300 roundtrips simulated by a split-step Fourier method. The mode-locking is self-starting from the amplified spontaneous emission (ASE) noise. The simulation assumes a modest small signal gain of 7 dB in the erbium doped LN waveguide region and a net normal group velocity dispersion (GVD) of 150 fs^2/mm in LN waveguide and a group velocity mismatch (GVM) of 10 fs/mm in the periodically poled LN region. **c**. In the steady-state, the integrated mode locked laser can emit 107 fs ultrashort pulses at 1550 nm.

The energy and speed of our all-optical switch offer a promising path for making

high efficiency high rep-rate ultra-short pulse on-chip sources. The low energy operation and the larger modulation depth of our device are essential for low lasing thresholds, self-starting mode-locking, and long-term stability of the generated laser pulses. The high speed of our device makes it possible to generate ultrashort pulses 100 fs, which is challenging to achieve using semiconductor saturable absorbers typically with picosecond relaxation time. Unlike the passive pulse generation mechanisms (such as Kerr frequency combs) such a mode-locked laser can enable the generation of ultrashort pulses with high peak powers, which can be essential for future nonlinear photonic devices and circuits.

References

[1] Kengo Nozaki et al. “Sub-femtojoule all-optical switching using a photonic-crystal nanocavity”. In: *Nature Photonics* 4.7 (2010), pp. 477–483.

[2] Gordon Wetzstein et al. “Inference in artificial intelligence with deep optics and photonics”. In: *Nature* 588.7836 (Dec. 2020), pp. 39–47. URL: https://doi.org/10.1038/s41586-020-2973-6.

[3] Farshid Ashtiani, Alexander J. Geers, and Firooz Aflatouni. “An on-chip photonic deep neural network for image classification”. In: *Nature* 606.7914 (June 2022), pp. 501–506. URL: https://doi.org/10.1038/s41586-022-04714-0.

[4] Katia Shtyrkova et al. “Integrated CMOS-compatible Q-switched mode-locked lasers at 1900nm with an on-chip artificial saturable absorber”. In: *Opt. Express* 27.3 (Feb. 2019), pp. 3542–3556. URL: https://opg.optica.org/oe/abstract.cfm?URI=oe-27-3-3542.

[5] Neetesh Singh, Erich Ippen, and Franz X. Kärtner. “Towards CW mode-locked laser on chip – a large mode area and NLI for stretched pulse mode locking”. In: *Opt. Express* 28.15 (July 2020), pp. 22562–22579. URL: https://opg.optica.org/oe/abstract.cfm?URI=oe-28-15-22562.

[6] Gustavo Grinblat et al. “Ultrafast sub-30-fs all-optical switching based on gallium phosphide”. In: *Science Advances* 5.6 (2019), eaaw3262.

[7] Yuanmu Yang et al. “Femtosecond optical polarization switching using a cadmium oxide-based perfect absorber”. In: *Nature Photonics* 11.6 (2017), p. 390.

[8] Norio Iizuka, Kei Kaneko, and Nobuo Suzuki. “All-optical switch utilizing intersubband transition in GaN quantum wells”. In: *IEEE Journal of Quantum Electronics* 42 (2006), pp. 765–771.

[9] R Takahashi, Y Kawamura, and H Iwamura. “Ultrafast 1.55 μm all-optical switching using low-temperature-grown multiple quantum wells”. In: *Applied Physics Letters* 68.2 (1996), pp. 153–155.

[10] GJ Spühler et al. “Semiconductor saturable absorber mirror structures with low saturation fluence”. In: *Applied Physics B* 81.1 (2005), pp. 27–32.

[11] Vilson R Almeida et al. “All-optical switching on a silicon chip”. In: *Optics Letters* 29.24 (2004), pp. 2867–2869.

[12] Takasumi Tanabe et al. “Fast all-optical switching using ion-implanted silicon photonic crystal nanocavities”. In: *Applied Physics Letters* 90.3 (2007), p. 031115.

[13] Xiaoyong Hu et al. “Picosecond and low-power all-optical switching based on an organic photonic-bandgap microcavity”. In: *Nature Photonics* 2.3 (2008), pp. 185–189.

[14] Alejandro Martínez et al. “Ultrafast all-optical switching in a silicon-nanocrystal-based silicon slot waveguide at telecom wavelengths”. In: *Nano Letters* 10.4 (2010), pp. 1506–1511.

[15] Mehmet Fatih Yanik et al. “All-optical transistor action with bistable switching in a photonic crystal cross-waveguide geometry”. In: *Optics Letters* 28.24 (2003), pp. 2506–2508.

[16] Zhen Chai et al. “Ultrafast all-optical switching”. In: *Advanced Optical Materials* 5.7 (2017), p. 1600665.

[17] Mohammad Taghinejad and Wenshan Cai. “All-optical control of light in micro-and nanophotonics”. In: *ACS Photonics* 6.5 (2019), pp. 1082–1093.

[18] Masaaki Ono et al. “Ultrafast and energy-efficient all-optical switching with graphene-loaded deep-subwavelength plasmonic waveguides”. In: *Nature Photonics* 14 (2020), pp. 37–43.

[19] Cheng Wang et al. “Ultrahigh-efficiency wavelength conversion in nanophotonic periodically poled lithium niobate waveguides”. In: *Optica* 5.11 (2018), pp. 1438–1441.

[20] Jie Zhao et al. “Shallow-etched thin-film lithium niobate waveguides for highly-efficient second-harmonic generation”. In: *Optics Express* 28.13 (2020), pp. 19669–19682.

[21] Jia-Yang Chen et al. “Ultra-efficient frequency conversion in quasi-phase-matched lithium niobate microrings”. In: *Optica* 6.9 (2019), pp. 1244–1245.

[22] Ashutosh Rao et al. “Actively-monitored periodic-poling in thin-film lithium niobate photonic waveguides with ultrahigh nonlinear conversion efficiency of 4600% W^{-1} cm^{-2}”. In: *Optics Express* 27 (2019), pp. 25920–25930.

[23] Marc Jankowski et al. “Ultrabroadband nonlinear optics in nanophotonic periodically poled lithium niobate waveguides”. In: *Optica* 7.1 (Jan. 2020), pp. 40–46. URL: https://www.osapublishing.org/optica/abstract.cfm?uri=optica-7-1-40 (visited on 01/18/2020).

[24] Luis Ledezma et al. “Intense optical parametric amplification in dispersion-engineered nanophotonic lithium niobate waveguides”. In: *Optica* 9.3 (Mar. 2022), pp. 303–308. URL: https://opg.optica.org/optica/abstract.cfm?URI=optica-9-3-303.

[25] Marc Jankowski et al. “Quasi-static optical parametric amplification”. In: *Optica* 9.3 (Mar. 2022), pp. 273–279. URL: https://opg.optica.org/optica/abstract.cfm?URI=optica-9-3-273.

[26] R Schiek, AS Solntsev, and DN Neshev. “Temporal dynamics of all-optical switching in quadratic nonlinear directional couplers”. In: *Applied Physics Letters* 100.11 (2012), p. 111117.

[27] R. DeSalvo et al. “Self-focusing and self-defocusing by cascaded second-order effects in KTP”. In: *Opt. Lett.* 17.1 (Jan. 1992), pp. 28–30. URL: https://opg.optica.org/ol/abstract.cfm?URI=ol-17-1-28.

[28] Roland Schiek. “All-optical switching in the directional coupler caused by nonlinear refraction due to cascaded second-order nonlinearity”. In: *Optical and Quantum Electronics* 26.4 (Apr. 1994), pp. 415–431. URL: https://doi.org/10.1007/BF00304246.

[29] Katia Gallo et al. “All-optical diode in a periodically poled lithium niobate waveguide”. In: *Applied Physics Letters* 79 (2001), pp. 314–316.

[30] Xiang Guo, Chang-Ling Zou, and Hong X Tang. “70 dB long-pass filter on a nanophotonic chip”. In: *Optics express* 24.18 (2016), pp. 21167–21176.

[31] Alireza Marandi et al. “Cascaded half-harmonic generation of femtosecond frequency combs in the mid-infrared”. In: *Optica* 3.3 (2016), pp. 324–327.

[32] Haowei Jiang et al. “Fast response of photorefraction in lithium niobate microresonators”. In: *Optics Letters* 42.17 (2017), pp. 3267–3270.

[33] Judson D Ryckman et al. “Photothermal optical modulation of ultra-compact hybrid Si-VO 2 ring resonators”. In: *Optics Express* 20.12 (2012), pp. 13215–13225.

[34] N Finlayson et al. “Picosecond switching induced by saturable absorption in a nonlinear directional coupler”. In: *Applied Physics Letters* 53.13 (1988), pp. 1144–1146.

[35] Wei Li et al. “Ultrafast all-optical graphene modulator”. In: *Nano Letters* 14.2 (2014), pp. 955–959.

[36] Qiaoliang Bao et al. “Atomic-layer graphene as a saturable absorber for ultrafast pulsed lasers”. In: *Advanced Functional Materials* 19.19 (2009), pp. 3077–3083.

[37] Sze Y Set et al. “Laser mode locking using a saturable absorber incorporating carbon nanotubes”. In: *Journal of Lightwave Technology* 22.1 (2004), p. 51.

[38] Marc Jankowski, Jatadhari Mishra, and Martin M Fejer. “Dispersion-engineered $\chi^{(2)}$ nanophotonics: a flexible tool for nonclassical light”. In: *Journal of Physics: Photonics* (2021).

[39] Yang He et al. “Self-starting bi-chromatic $LiNbO_3$ soliton microcomb”. In: *Optica* 6.9 (2019), pp. 1138–1144.

[40] Zheng Gong et al. “Near-octave lithium niobate soliton microcomb”. In: *Optica* 7.10 (2020), pp. 1275–1278.

[41] Zheng Gong et al. “Soliton microcomb generation at 2 μm in z-cut lithium niobate microring resonators”. In: *Optics Letters* 44.12 (2019), pp. 3182–3185.

[42] Mian Zhang et al. “Broadband electro-optic frequency comb generation in a lithium niobate microring resonator”. In: *Nature* 568.7752 (2019), pp. 373–377.

[43] Wim Bogaerts et al. “Programmable photonic circuits”. In: *Nature* 586.7828 (2020), pp. 207–216.

[44] Marc Jankowski et al. “Temporal Simultons in Optical Parametric Oscillators”. In: *Phys. Rev. Lett.* 120 (5 Feb. 2018), p. 053904. URL: https://link.aps.org/doi/10.1103/PhysRevLett.120.053904.

[45] David E Zelmon, David L Small, and Dieter Jundt. “Infrared corrected Sellmeier coefficients for congruently grown lithium niobate and 5 mol.% magnesium oxide–doped lithium niobate”. In: *JOSA B* 14.12 (1997), pp. 3319–3322.

[46] C. R. Phillips et al. “Supercontinuum generation in quasi-phasematched waveguides”. In: *Optics Express* 19.20 (Sept. 2011), pp. 18754–18773. URL: https://www.osapublishing.org/oe/abstract.cfm?uri=oe-19-20-18754 (visited on 02/18/2019).

[47] Curt Wittig. “The Landau- Zener Formula”. In: *The Journal of Physical Chemistry B* 109.17 (2005), pp. 8428–8430.
[48] Andrew Weiner. *Ultrafast optics*. Vol. 72. John Wiley & Sons, 2011.
[49] CR Phillips et al. “Supercontinuum generation in quasi-phasematched waveguides”. In: *Optics Express* 19.20 (2011), pp. 18754–18773.
[50] Dieter H Jundt. “Temperature-dependent Sellmeier equation for the index of refraction, n e, in congruent lithium niobate”. In: *Optics letters* 22.20 (1997), pp. 1553–1555.
[51] Fuwan Gan et al. “Maximizing the thermo-optic tuning range of silicon photonic structures”. In: *2007 Photonics in Switching*. IEEE. 2007, pp. 67–68.
[52] Chad Husko et al. “Ultrafast all-optical modulation in GaAs photonic crystal cavities”. In: *Applied Physics Letters* 94.2 (2009), p. 021111.
[53] Tarek A Ibrahim et al. “All-optical switching in a laterally coupled microring resonator by carrier injection”. In: *IEEE Photonics Technology Letters* 15.1 (2003), pp. 36–38.
[54] Michael Waldow et al. “25ps all-optical switching in oxygen implanted silicon-on-insulator microring resonator”. In: *Optics Express* 16.11 (2008), pp. 7693–7702.
[55] Jason S Pelc et al. “Picosecond all-optical switching in hydrogenated amorphous silicon microring resonators”. In: *Optics express* 22.4 (2014), pp. 3797–3810.
[56] GW Cong et al. “Low-saturation-energy-driven ultrafast all-optical switching operation in (CdS/ZnSe)/BeTe intersubband transition”. In: *Optics express* 15.19 (2007), pp. 12123–12130.
[57] Takasi Simoyama et al. “Absorption dynamics in all-optical switch based on intersubband transition in InGaAs–AlAs–AlAsSb coupled quantum wells”. In: *IEEE Photonics Technology Letters* 19.8 (2007), pp. 604–606.
[58] Yan Li et al. “Ultrafast all-optical switching with low saturation energy via intersubband transitions in GaN/AlN quantum-well waveguides”. In: *Optics express* 15.26 (2007), pp. 17922–17927.
[59] Dave M Spirit, Andrew D Ellis, and Pete E Barnsley. “Optical time division multiplexing: Systems and networks”. In: *IEEE Communications Magazine* 32.12 (1994), pp. 56–62.
[60] TD Vo et al. “Photonic chip based transmitter optimization and receiver demultiplexing of a 1.28 Tbit/s OTDM signal”. In: *Optics express* 18.16 (2010), pp. 17252–17261.
[61] Camiel Op de Beeck et al. “III/V-on-lithium niobate amplifiers and lasers”. In: *Optica* 8.10 (2021), pp. 1288–1289.
[62] Qiang Luo et al. “On-chip ytterbium-doped lithium niobate microdisk lasers with high conversion efficiency”. In: *Optics Letters* 47.4 (2022), pp. 854–857.
[63] Yuan Zhou et al. “On-chip microdisk laser on Yb 3+-doped thin-film lithium niobate”. In: *Optics Letters* 46.22 (2021), pp. 5651–5654.

[64] Zhaoxi Chen et al. “Efficient erbium-doped thin-film lithium niobate waveguide amplifiers”. In: *Optics Letters* 46.5 (2021), pp. 1161–1164.

[65] Minglu Cai et al. “Erbium-doped lithium niobate thin film waveguide amplifier with 16 dB internal net gain”. In: *IEEE Journal of Selected Topics in Quantum Electronics* 28.3 (2021), pp. 1–8.

[66] Nam Quoc Ngo et al. *Ultra-fast fiber lasers: principles and applications with MATLAB® models*. CRC Press, 2018.

Chapter 5

FEW-CYCLE VACUUM SQUEEZING IN A NANOPHOTONIC CIRCUIT

Rajveer Nehra†, **Ryoto Sekine**†, Luis Ledezma, Qiushi Guo, Robert M. Gray, Arkadev Roy and Alireza Marandi, "Few-cycle vacuum squeezing in nanophotonics," *Science*, 377, 1333-37 (2022).
R.S. fabricated the device, contributed to the optical characterization, and participated in the writing of the manuscript.
† denotes equal contributions

5.1 Abstract

One of the most fundamental quantum states of light is the squeezed vacuum, in which noise in one of the quadratures is less than the standard quantum noise limit. In nanophotonics, it remains challenging to generate, manipulate, and measure such a quantum state with the performance required for a wide range of scalable quantum information systems. Here, we report the development of a lithium niobate–based nanophotonic platform to demonstrate the generation and all-optical measurement of squeezed states on the same chip. The generated squeezed states span more than 25 terahertz of bandwidth supporting just a few optical cycles. The measured 4.9 decibels of squeezing surpass the requirements for a wide range of quantum information systems, demonstrating a practical path toward scalable ultrafast quantum nanophotonics.

5.2 Introduction

Quantum information processing offers great promise for computation, secure communication, metrology, and sensing. Many physical platforms such as nuclear spins, superconducting circuits, photonics, trapped ions, quantum dots, and neutral atoms have widely been explored in the pursuit to build quantum information processors [1]. Among these, photonics stands out because of its potential for scalability, room-temperature logical operations, and ease of encoding quantum information in both discrete and continuous variables [2].

In continuous-variable (CV) quantum photonics, information is encoded in continuous amplitude and phase values of the quantized electromagnetic field. The single-mode and multimode squeezed states are widely used for various applications, including quantum-enhanced interferometry such as in the Laser Interferometer Gravitational-Wave Observatory [3], microscopy [4], and quantum teleportation [5]. Moreover, highly entangled CV quantum states, that is, cluster states [6, 7, 8], serve as a universal resource for one-way quantum computation.

Typically, such high-quality CV states are generated from a single- or two-mode squeezed vacuum produced using quadratic ($\chi^{(2)}$) parametric processes either in

bulk crystals or waveguides with large (~10-100 μm^2) mode areas [8, 9, 10, 6, 7]. Although such experiments using bulky discrete components have been successful in demonstrating small- and medium-scale quantum circuits, it is desirable to achieve CV quantum states with comparable qualities in nanophotonics to enable large-scale integrated quantum circuits.

In nanophotonics, silicon nitride (SiN) and silica platforms have been used for many quantum photonic experiments, such as entangled photon-pair generation, squeezing, error correction, and small-scale Gaussian boson sampling [11, 12, 13]. However, their inherently weak cubic ($\chi^{(3)}$) nonlinearity typically necessitates using high–quality factor resonators, which imposes limitations on accessible squeezing levels and bandwidths. Despite advances, the measured squeezing levels have so far remained around 2 dB in nanophotonics (see supplementary materials, section 5.5.8).

On the other hand, the measurements in CV quantum systems have typically relied on balanced homodyne detection using highly efficient and low-noise photodetectors, which are limited to bandwidths in the mega- to gigahertz range [14]. Moreover, in nanophotonics, the loss associated with transferring the microscopic quantum states from a tightly confined mode to a photodetector has imposed barriers in the measurement capabilities of such states [15, 16, 17]. A potential solution for these measurement challenges lies in all-optical measurement schemes based on a noiseless phase-sensitive amplifier with sufficiently large gain [18, 19, 20, 21] that can eliminate the bandwidth limitations of homodyne detection and the sensitivity to detection losses. However, achieving such large gains (>30 dB) over broad optical bandwidths is challenging in nanophotonics with cubic nonlinearity [22]. Such an all-optical measurement allows one to exploit the entire optical bandwidth of quantum fields and thereby paves a practical path toward ultrafast all-optical CV quantum information processors using time- and frequency-multiplexed schemes [6, 7, 8].

Recently, lithium niobate (LN) nanophotonics has opened promising avenues in optical communication, sensing, and computation owing to its extraordinary optical, electrical, and acoustic properties [23]. A combination of subwavelength confinement of the optical mode, strong $\chi^{(2)}$ nonlinearity, high-fidelity quasi-phase-matching by periodic poling, and dispersion engineering for longer interaction lengths has enabled devices outperforming the traditional LN devices [24, 25, 26].

5.3 Results

In this work, we used a nanophotonic circuit in LN to experimentally demonstrate the generation and all-optical measurement of an ultra-short-pulse squeezed vacuum as the building block of scalable CV quantum nanophotonics. Our circuit combines two dispersion-engineered phase-sensitive optical parametric amplifiers (OPAs) [24], (Fig. 5.1). The first OPA generates a microscopic squeezed vacuum, which is then amplified with a high-gain OPA to macroscopic levels within the same nanophotonic chip. The resulting macroscopic field carries information about the microscopic squeezed state, which can be measured with a high tolerance to loss.

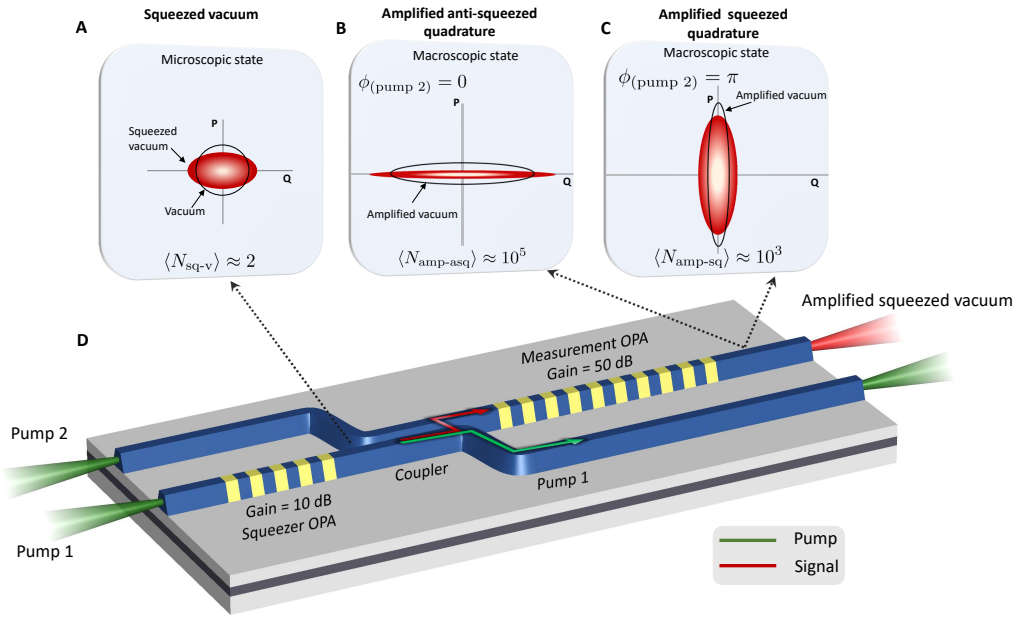

Figure 5.1: **Illustration of the generation of a squeezed vacuum and its all-optical measurement in nanophotonics.** Phase-space distributions (filled ellipses) of (A) phase-quadrature squeezed vacuum, and its amplification in the (B) anti-squeezed and (C) squeezed quadratures. The black circle in (A) represents the microscopic vacuum state, and black ellipses in (B) and (C) correspond to the macroscopic vacuum state amplified in Q and P quadratures, respectively. (D) Sketch of our nanophotonic device consisting of the squeezer OPA, tapered adiabatic coupler, and measurement OPA. When pumped, the squeezer OPA generates a squeezed vacuum state, which is selectively coupled into an adjacent waveguide. It is subsequently amplified by the measurement OPA to macroscopic power levels. The measurement OPA amplifies the quadrature under measurement to sufficiently above the vacuum noise, thereby making the measurement insensitive to losses due to off-chip coupling and imperfect detection. For (A), (B), and (C), we consider 10 dB of squeezing with mean photon number $\langle N_{\text{sq-v}} \rangle \approx 2$, and a 50 dB phase-sensitive gain in the measurement OPA, thereby amplifying the few-photon squeezed state to a macroscopic power level.

The phase-space distributions for the vacuum (black circle) and the phase-quadrature squeezed vacuum (filled ellipse) are shown in Fig. 5.1. The measurement OPA selects a certain quadrature of the microscopic squeezed field and amplifies it to macroscopic levels, in principle without adding any noise. In Fig. 5.1B and C, the phase-space distributions (filled ellipses) corresponding to amplified anti-squeezed and amplified squeezed quadratures are shown for two particular pump phases of the measurement OPA, $\phi_{\text{Pump 2}}$. We set $\phi_{\text{Pump 1}} = 0$ and use it as the phase reference for pump 2.

In the case of Fig. 5.1B with $\phi_{\text{Pump 2}} = 0$, the anti-squeezed quadrature (Q) is amplified while the orthogonal phase quadrature (P) is deamplified such that the output field is dominated entirely by the Q quadrature, and the P quadrature can be considered negligible. In such a high-gain amplification regime, the total average photon number (power) of the output field is $\langle \hat{N}_+ \rangle \propto \langle \hat{Q}^2_{\text{asq-amp}} \rangle \approx O(10^5)$, where $\langle \hat{N}_+ \rangle$ and $\langle \hat{Q}_{\text{asq-amp}} \rangle$ denote the photon number and quadrature operators, respectively, for the amplified anti-squeezed quadrature. Likewise, by changing the pump phase of the measurement OPA to $\phi_{\text{Pump 2}} = \pi$, the original squeezed quadrature is amplified to achieve $\langle \hat{N}_- \rangle \propto \langle \hat{P}^2_{\text{sq-amp}} \rangle \approx O(10^3)$, where $\langle \hat{N}_- \rangle$ and $\langle \hat{P}_{\text{sq-amp}} \rangle$ represent the photon number and quadrature operators, respectively, for the amplified squeezed quadrature (Fig. 5.1C). As a result, the macroscopic output of the measurement OPA provides a direct all-optical measurement for the quadrature variances of the microscopic squeezed state. Likewise, we determine the quadrature variances of the microscopic vacuum state by measuring the average photon number of the macroscopic amplified vacuum state when the squeezer OPA pump 1 is blocked. The phase-space distributions of the amplified vacuum are represented as the black ellipses in Fig. 5.1B and C corresponding to $\phi_{\text{Pump 2}} = 0$ and $\phi_{\text{Pump 2}} = \pi$, respectively. The anti-squeezing (S_+) and squeezing (S_-) can then be determined as $S_\pm[\text{dB}] = 10\log_{10}[\langle \hat{N}_\pm \rangle / \langle \hat{N}_{\text{v}} \rangle]$, where $\langle \hat{N}_{\text{v}} \rangle \propto \langle \hat{Q}^2_{\text{v-amp}} \rangle$ denote the average photon number of the vacuum state amplified in the amplitude and phase quadratures, respectively (Fig. 5.1B and C).

In the ideal case, the squeezing (anti-squeezing) can be determined as

$$S_\pm[\text{dB}] = 10\log_{10}\left[\frac{\sinh^2(r_2 \pm r_1)}{\sinh^2 r_2}\right], \tag{5.1}$$

where r_1 and r_2 are the gain parameters for the squeezer and measurement OPAs, respectively. Sufficient gain (> 33 dB for ~ 11 dB of squeezer OPA gain; supplementary materials, section 5.5.5) in the measurement OPA allows a direct measurement of the phase-squeezed vacuum generated in the squeezer OPA. Crucially, the high-gain measurement OPA makes our measurement tolerant to off-chip coupling losses and photodetection inefficiencies as high as ~ 7 dB (supplementary materials, section 5.5.4).

In experiments, the squeezer (low-gain) and measurement (high-gain) OPAs of our circuit are periodically poled with lengths of 2.5 and 5.0 mm, respectively. The output of the squeezer OPA (microscopic squeezed vacuum) is coupled to the

measurement OPA through a directional coupler. To make our directional coupler broadband and less susceptible to fabrication imperfections, we used an adiabatic design where both of the waveguides are tapered, while keeping the gap constant throughout the coupler length. The coupler directs the squeezed vacuum to the adjacent waveguide toward the measurement OPA and keeps the residual pump of the squeezer OPA in the original waveguide (Fig. 5.1D). The fabricated adiabatic coupler causes ~30% loss for the squeezed vacuum and leaks ~20% of the squeezer pump to the measurement OPA. Our numerical simulations suggest that the coupling performance of the adiabatic coupler can be improved to > 98% for the squeezed signal and < 5% for the squeezer pump with proper calibration of fabrication steps, which will lead to better measurement qualities (supplementary materials, section 5.5.4).

In our simplified experimental setup (Fig. 5.2A) the squeezer and measurement OPAs are pumped by a mode-locked laser (Menlo Systems Orange A) generating ~75-fs-long nearly transform-limited pulses at a 250-MHz repetition rate. The relative phase between pump 1 (squeezer OPA) and pump 2 (measurement OPA) pulses is modulated by a piezoelectric transducer (PZT) on the pump 2 arm. At the output of the nanophotonic chip, the amplified squeezed signal and measurement OPA pump are first separated using a dichroic mirror and then are detected by two different optical spectrum analyzers (OSAs; see supplementary materials, section 5.5.1). In Fig. 5.2A, we show (i) a false-colored scanning electron microscope (SEM) image of our nanophotonic circuit, (ii) a zoomed-in SEM image of the coupler region, and (iii) a false-colored second harmonic microscope image of the periodically poled region before etching the waveguides.

Figure 5.2B shows an example measurement of our squeezed state. The green trace shows the output signal of the measurement OPA using an OSA in a zero-span mode at 2090 nm while keeping both pump 1 and pump 2 on and modulating the PZT by a 1-Hz ramp signal. To accurately measure the squeezing, we need to eliminate the effect of residual interference of the two pumps at the output of the measurement. We achieve this by determining the maximum and minimum of this residual interference and then calibrating our amplified shot-noise levels by subsequently varying the power of pump 2 to these maximum and minimum pump powers while blocking pump 1. These two levels of pump 2 result in a "shot-noise maximum" and "shot-noise minimum," as shown in Fig. 5.2B, while the "original shot-noise" corresponds to the pump 2 level during the squeezing measurement. Hence, in the squeezing measurement, the shaded area below (above) the shot-noise minimum (shot-noise maximum) corresponds to squeezing (anti-squeezing) at the input of the high-gain OPA. We measured a squeezing and anti-squeezing level of 4.2 ±0.2 dB and 9.7 ± 0.1 dB, respectively, with 0.8 pJ of squeezer OPA pump energy. A detailed discussion on our shot-noise calibration measurements can be found in section 5.5.2 of the supplementary materials.

We further characterize the dependence of squeezing at 2090 nm on the pump power while keeping pump 2 constant and performing the shot-noise calibration for each power level as shown in Fig. 5.2C. As we increase the pump power in the squeezer OPA, the level of measured squeezing increases at first. However, above

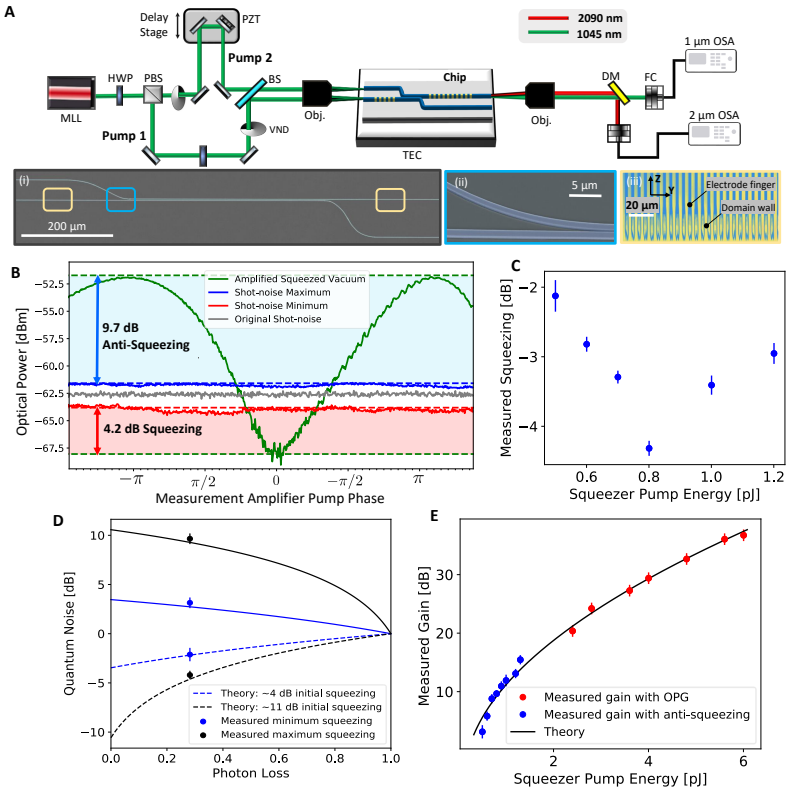

Figure 5.2: **Generation and measurement of squeezed light in the LN nanophotonic chip.** (**A**) Experimental setup. A mode-locked laser (MLL) is used to pump the squeezer (pump 1) and measurement (pump 2) OPAs. At the output of the nanophotonic chip, the amplified squeezed signal (red) and residual pump 2 (green) are separated using a dichroic mirror (DM) and measured by two different OSAs. Bottom row shows the following: (i) a false-colored SEM image of our nanophotonic circuit, (ii) a zoomed-in SEM image of the coupler region, and (iii) a false-colored second harmonic microscope image of the periodically poled region before etching the waveguides. (**B**) Squeezing measurement by an OSA in the zero-span mode at 2090 nm. (**C**) The squeezing measured at 2090 nm for several values of pump 1 while keeping pump 2 constant. (**D**) Loss analysis of the squeezing measurements. The solid (dashed) curves show the degradation of anti-squeezing (squeezing) as the photon loss increases, and the solid data points correspond to measured values of minimum and maximum squeezing. (**E**) The squeezer gain dependence on the energy of pump 1. Blue points are measured from anti-squeezing, and red points are directly obtained from optical parametric generation (OPG) measurements. Error bars are obtained from the statistics of the measurements. PBS, polarized beam splitter; BS, beam splitter; HWP, half-wave plate; Obj., reflective objective; VND, variable neutral-density filter; FC, fiber coupler; TEC, thermoelectric cooler.

0.8 pJ of pump pulse energy, we observe that further increasing the squeezer pump decreases the level of measured squeezing. The degradation of measured squeezing at high pump powers may be due to the existence of a small phase noise and relative chirp between pump 1 and pump 2, which can mix the loss-degraded squeezed quadrature with the relatively large anti-squeezed quadrature [27]. Additionally, parasitic nonlinear effects such as the photorefractive effect and nonlinear absorption mechanisms in the waveguide can also account for the degradation of squeezing at higher pump powers.

Figure 5.2D shows how squeezing levels degrade in the presence of photon loss $(1-\eta)$. Analytically, $S_{\pm}^{\eta}[\mathrm{dB}] = 10\log[(1-\eta)+\eta e^{\pm 2r_1}]$, where $(1-\eta)$ determines the loss experienced by the microscopic squeezed signal and r_1 is the squeezing parameter characterizing nonlinear interaction strength (supplementary materials, section 5.5.5). The solid dots in Fig. 5.2Care the experimental data points for the minimum and maximum amount of measured squeezing at 2090 nm. From these measurements, we estimate the total loss $L = 1-\eta \approx 0.3$ experienced by the microscopic squeezed signal before being fully amplified by the measurement OPA. The estimated total loss is mostly dominated by the coupling efficiency of the adiabatic coupler, which we measured using an auxiliary signal centered at 2090 nm (supplementary materials, section 5.5.4). From the squeezing and anti-squeezing measurements in Fig. 5.2D, our inferred squeezing after correcting for losses is 10.48 ± 0.87 dB with the pump energy of <1 pJ. This paves the way for fault-tolerant CV quantum processors in LN nanophotonics, as 10.5 dB of squeezing is sufficient for many architectures, including recent proposals with Gottesman-Kitaev-Preskill qubit encodings [28].

Figure 5.2E depicts the gain in the squeezer OPA as a function of pump 1 pulse energy. The gain for lower pump energies (<2.4 pJ) is determined from the anti-squeezing measurements, whereas for higher pump energies (>2.4 pJ), we obtain the gain from a direct measurement of average photon number (supplementary materials, section 5.5.4). When there is no input seed into the measurement OPA, the average number of photons in the high parametric gain regime ($\langle \hat{N} \rangle \sim G/4$) allows us to estimate the gain. The solid curve is the fit that includes the overall detection efficiency (including off-chip coupling losses and imperfect detection after the measurement OPA) and the nonlinear strength as fitting parameters. From the fit, we extract the overall detection efficiency of $\eta_{\text{overall}}^{\text{off-chip}} \sim 0.20$ (supplementary materials, section 5.5.5). This level of linear loss puts an upper limit of <1 dB to the measurable squeezing for a standard balanced homodyne detection. This is not a limiting factor for our all-optical squeezing measurements, because of the noiseless amplification by the measurement OPA. Note that such lossy measurements are even more detrimental for highly squeezed states, as they are extremely sensitive to losses. This can be seen in Fig. 5.2D, where ~11 of initial squeezing degrades by ~10 dB in the presence of the detection losses of $L_{\text{overall}}^{\text{off-chip}} = 1-\eta_{\text{overall}}^{\text{off-chip}} = 0.80$. However, our all-optical measurement is not affected by $L_{\text{overall}}^{\text{off-chip}}$ losses owing to the amplification by the measurement OPA and allows us to measure the squeezing levels as high as 4.9 dB. Thus, our current measured squeezing is mostly limited

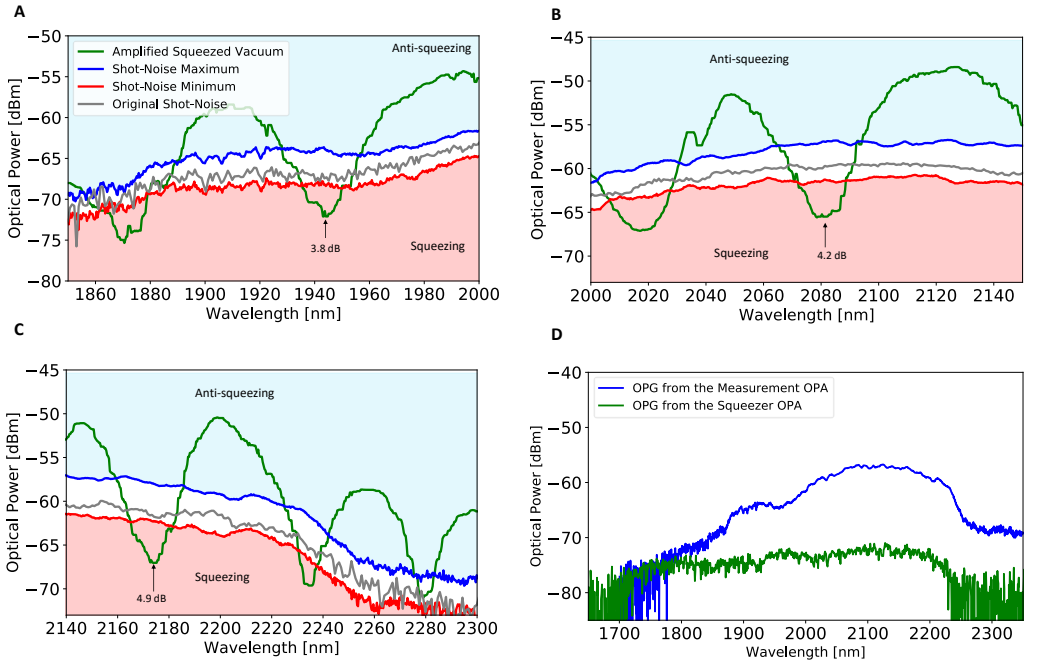

Figure 5.3: **Broadband squeezing measurements**. (**A** to **C**) Three measurements over different selected bandwidths of the OSA when the PZT is modulated with a 300 mHz ramp signal. The shot noise traces (blue, gray, and red) were acquired with pump 1 blocked. (**D**) Optical parametric generation from the squeezer OPA (green) and measurement amplifier OPA (blue). Both traces are acquired at ~6 pJ of pulse energy.

by the coupling loss associated with the on-chip adiabatic coupler, which can reach with near unity coupling efficiencies through better calibration of fabrication steps, as suggested by our numerical simulations (supplementary materials, section 5.5.4).

Figures 5.3A, to C shows the measured squeezing over a broad bandwidth. The amplified shot-noise is calibrated, using the same method as discussed earlier, over the entire spectrum. Green traces correspond to measurements by the OSA over three different spectral windows when the PZT is modulated by a slow ramp signal at 300 mHz. Squeezing is present over the entire spectrum, with a slight spectral dependence. The measured squeezing is 3.8 ± 0.4 dB around 1950 nm, 4.2 ± 0.2 dB around 2090 nm, and 4.9 ± 0.2 dB around 2200 nm. The slight spectral dependence is attributed to the wavelength dependence of the coupling efficiency of our adiabatic coupler (supplementary materials, section 5.5.4). We measured the squeezing bandwidth to be 25.1 THz. The bandwidth is expected to increase to 36.4 THz, as confirmed by the optical parametric generation (OPG) from the squeezer OPA in Fig. 5.3D. The measured squeezing bandwidth is mostly limited by the slight mismatch of measurement OPA gain in the wings of the spectrum, as evident from its OPG signal. Because of this difference in the gain spectrum, the measurement

OPA does not amplify the squeezed vacuum over its entire generation bandwidth to macroscopic levels, leading to a reduced measured squeezing bandwidth. These measurements indicate that our generated squeezed state can occupy a record-level time window of about four optical cycles (supplementary materials, section 5.5.3). This temporal window can be shortened further by engineering the dispersion and quasi-phase matching [29] and may lead to opportunities for studying quantum fields in the extremely short-pulse regime [30]. Our demonstrated squeezing bandwidth allows the definition of few-optical-cycle temporal bins in time-multiplexed CV quantum information processors [6, 7]. As a result, such ultra-short time bins can be defined in a dense manner for which centimeter-scale on-chip delay lines can be used for large-scale cluster states on a chip.

5.4 Conclusion

We have demonstrated few-cycle vacuum squeezing and its all-optical measurements in the LN nanophotonic platform. Our on-chip all-optical loss-tolerant broadband measurements through high-gain phase-sensitive amplification enabled squeezing measurements over more than 25 THz of bandwidth while providing measurement purification against the detection losses as high as $L_{\text{overall}}^{\text{off-chip}} \sim 7$ dB. Combined with the recent advances such as high-speed electro-optic modulators and integrated single-photon detectors [23], we envision that our results may enable scalable ultrafast all-optical quantum information processors in LN nanophotonic platform.

5.5 Supplementary Information

5.5.1 Experimental Setup

The experimental setup for the generation and all-optical measurement of the squeezed state is shown in Fig. 5.4. The Squeezer OPA and Measurement OPA are pumped by a mode-locked Yb-fiber laser (Menlo Systems Orange A) generating ~75-fs-long pulses centered at ~1045 nm at a repetition rate of 250 MHz. The pump laser is first split into two paths, namely Pump 1 and Pump 2 in Fig. 5.4. The first beam (labeled as Pump 2) is sent to a delay stage with a micrometer arm used for fine adjustments for temporal overlap; coarse adjustments are done by tuning the position of the delay stage. Depending on the measurement at hand, the second beam

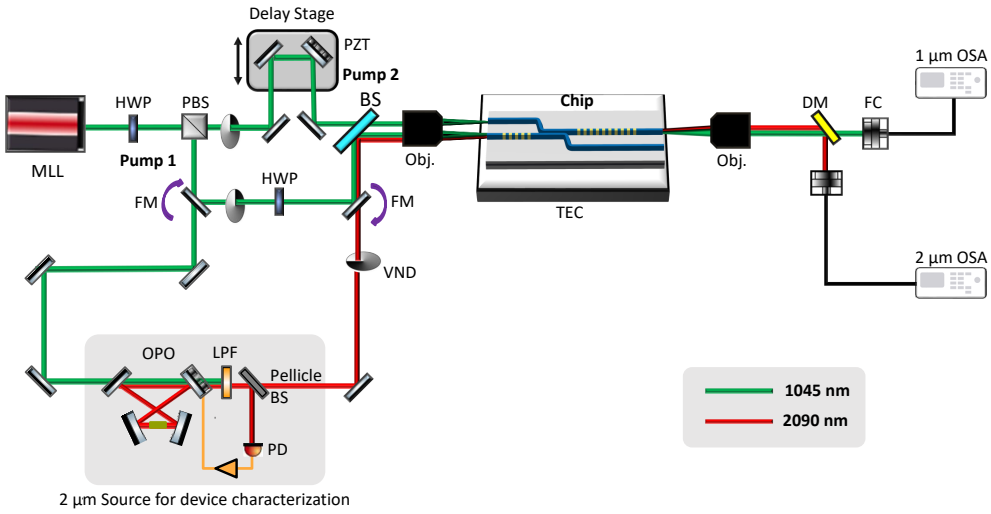

Figure 5.4: **Experimental schematic for all-optical squeezing measurements**. The pump laser is first split into two paths, namely Pump 1 and Pump 2, used for pumping the Squeezer OPA and Measurement OPA, respectively. The relative phase between the pumps is modulated by the PZT mounted on the delay stage in the Pump 2 arm. At the output of the nanophotonic chip, the amplified squeezed signal and Measurement OPA pump are separated using a dichroic mirror, and then are detected by optical spectrum analysers (OSAs) for spectral measurements. PBS: Polarizing beamsplitter, HWP: Half-wave plate, DM: Dichroic mirror, Obj.: Reflective objective, VND: Variable neutral-density filter, FC: Fiber Coupler, OSA: Optical spectrum analyzer, PD: Photodetector, OPO: Optical parametric oscillator, FM: Flip Mirror.

(labeled as Pump 1) is either guided to the chip setup or to a synchronously pumped degenerate optical parametric oscillator (SPDOPO) used for generating pulses at 2090 nm [31]. For squeezing measurements, both Pump 1 and Pump 2 are spatially overlapped at a 50:50 beamsplitter (BS), and then are focused to and coupled out of the nanophotonic chip using high NA reflective objectives (Newport: 50102-02). Pump powers are controlled using two variable neural density (VND) filters mounted on both the arms. The relative phase between the Pump 1 and Pump 2 pulses is modulated by the piezoelectric transducer (PZT) mounted on the delay stage. At the output of the chip, the amplified squeezed vacuum and Measurement OPA pump are first separated using a dichroic mirror (DM) with high transmission around 1045 nm and high reflectance around 2090 nm, and then are sent to two different optical spectrum analysers (Yokogawa AQ6370D and Yokogawa AQ6375B) for spectrum measurements at 2 nm resolution.

For linear characterization of our device and classical gain measurements of

the OPAs, we use the SPDOPO output centered at 2090 nm [31]. Pump 1 is used for pumping the SPDOPO, which is locked using a “dither and lock" technique, implemented with a Red Pitaya FPGA board [32, 33]. A variable ND filter is added to the output of the OPO to control the 2090 nm power. For OPA measurements, a well-attenuated SPDOPO signal is spatially overlapped with Pump 2 at a dichroic mirror mounted in place of the 50:50 BS. A discussion on device characterization and OPA gain measurements is provided in Sections 5.5.4 & 5.5.7.

5.5.2 Shot-noise calibration measurements

In this section, we discuss our shot-noise calibrations in greater detail. As discussed in the main text, the design of our adiabatic coupler and its fabrication imperfections couples ~20% of the Squeezer OPA pump to the high-gain Measurement OPA waveguide, which then interferes with Pump 2, resulting in a gain modulation in the Measurement OPA. In order to accurately determine the amount of squeezing, we measure this gain modulation by characterizing the interference of the these two pumps in the Measurement OPA and removing its effect from the squeezing measurements. Fig. 5.2A is an example of a Pump 1 and Pump 2 interference fringe (green trace) acquired by an OSA in zero span mode at 1100 nm. While keeping the Squeezer OPA Pump 1 blocked, we increase (decrease) the Measurement OPA Pump 2 power to the maxima (minima) levels of the interference fringe, which corresponds to the blue (red) trace in Fig. 5.2A. These two power levels of Pump 2 result in the “shot-noise maximum” and “shot-noise minimum” shown in Fig. 5.2B in the main text. We measure the pump interference in zero span mode at 1100 nm (the red arrow in the pump spectrum in Fig. 5.2C) to calibrate our shot-noise measurements to ensure that our calibration is not affected by any nonlinear effects in the Measurement OPA. This is confirmed by the linear transmission measurements, shown in Fig. 5.2B, at 1100 nm for the Measurement OPA Pump 2 power levels varying in the range of power levels of the recorded interference fringe.

To further verify our shot-noise calibrations, we recreate the interference pattern seen in Fig. 5.5A off-chip and inject it into the Measurement OPA arm while keeping the Squeezer OPA Pump 1 blocked. In Fig. 5.5D, we show the transmission measured in zero-span mode at 1100 nm. The interference fringe (green trace) is shown along with the maximum (blue) and minimum (red) power levels of Pump 2. In Fig. 5.5E, we show the OSA output for these traces when it was set to zero-span mode at 2090 nm. We can see that the maximum and minimum power levels of the green trace in Fig. 5.5E stays within the maximum and minimum amplified shot-noise levels. This is in stark contrast with the squeezing measurements (Fig. 5.2A and Fig. 5.3 in the main text) where the green trace goes below/above the shot-noise minima/maxima, which is due to the amplification of the squeezed and anti-squeezed quadratures of the original squeezed state generated in the Squeezer OPA.

Next, we calibrate the shot-noise at various values of Pump 2 energy levels. In conventional balanced homodyne detection (BHD), it is a common practice to verify the linearity of the shot-noise by adding the linear losses or by increasing the local oscillator (LO) strength. This verification test ensures that the BHD detection

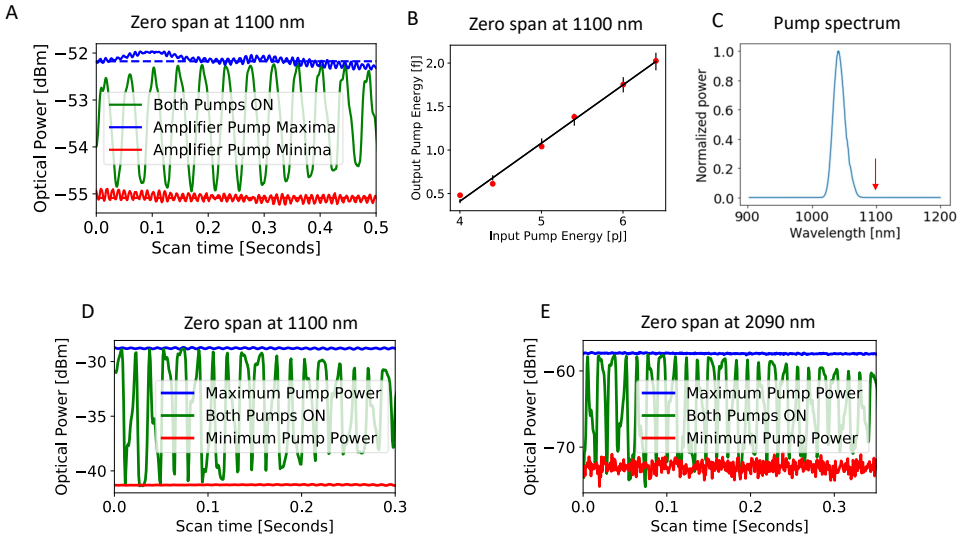

Figure 5.5: **Shot-noise calibration measurements**. **(A)** The green trace shows the interference fringe between Pump 1 and Pump 2, measured from the Measurement OPA. The red and blue traces correspond to the minimum and maximum power levels of Pump 2 when Pump 1 is blocked. **(B)** Linear transmission measurements from the measurement amplifier in zero span at 1100 nm. **(C)** Input pump spectrum normalized in linear units. **(D)** Measured fringes when the Pump 1 and Pump 2 interference is created off-chip with the squeezer pump 1 blocked. **(E)** Measured amplified shot-noise levels for different Pump 2 power levels in Fig. D.

system does not add any measurement noise, and the measured quadrature variances are truly due to the vacuum fluctuations. Mathematically, the measured quadrature variance of vacuum fields is

$$\triangle^2 \hat{X}_\phi \propto |\alpha|^2 \langle \hat{X}_\phi^2 \rangle_{\rho_v} \tag{5.2}$$

where ρ_v is the vacuum state with $\langle \hat{X}_\phi^2 \rangle_{\rho_v} = 1/4$. As a result, by adding the losses (i.e., $\alpha \rightarrow \sqrt{\eta}\alpha$ for $\eta < 1$) or by increasing the strength of the LO (i.e., $\alpha \rightarrow \sqrt{k}\alpha$, for $k > 1$), one can verify the linearity of the measured shot-noise, thereby confirming that the BHD does not add any noise during measurements and the measured noise is the shot-noise limit.

Likewise, one can calibrate the shot-noise of an all-optical measurement in a similar manner as BHD. In our all-optical measurements with high-gain OPAs, the roles of the beamsplitter and LO in HD are played by the Measurement OPA and its pump (Pump 2). In this case, the measured quadrature variance of the sufficiently amplified selected vacuum quadrature is given by

$$\triangle^2 \hat{X}_\phi \propto G \langle \hat{X}_\phi^2 \rangle_{\rho_v} \tag{5.3}$$

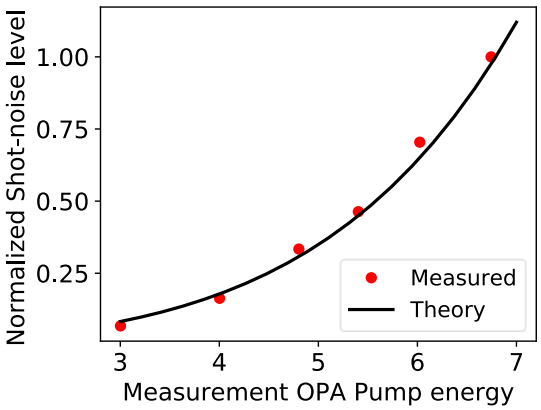

Figure 5.6: Shot-noise level measurements at various values of pump energy.

where $G = e^{2L\eta\sqrt{P}}$ is the gain of the Measurement OPA; L is the length of the Measurement OPA, η is the nonlinear efficiency, and P is the Pump 2 strength. As a result, the amplified shot-noise level (i.e., the noise of the high-gain OPA) grows exponentially with the Pump 2 (LO) strength. We verified this by measuring the amplified shot-noise at various values of Pump 2 energy, as shown in Fig. 5.6. Our measured normalized shot-noise level (red points) agrees well with the expected exponential behavior (black curve), as shown in the plot below. A good agreement with the expected amplified shot-noise solely due to the phase-sensitive amplification of the vacuum state confirms that the noise added by the Measurement OPA is negligible as compared to the amplified shot-noise. We then ensured that the Measurement OPA has sufficient gain. For a *direct* squeezing measurement, it is important for the Measurement OPA to amplify the selected quadrature such that it entirely dominates the energy of the amplified field, and the attenuated quadrature can be considered negligible. The desired and experimentally measured gain levels are discussed in depth in Sec. 5.5.5 (see in particular Fig. 5.11).

5.5.3 Numerical Simulation Methods

In this section, we detail the methods used in our numerical simulations. To simulate the short-pulse nonlinear dynamics in our devices, we solve a nonlinear envelope equation (NEE) in the frequency domain using a split-step Fourier method [34], where the nonlinear step is integrated using a fourth-order Runge-Kutta method. We obtained the NEE by ignoring counter-propagating modes, which are usually phase mismatched, and assuming a constant nonlinear coefficient across the entire simulation bandwidth. The NEE is given by:

$$\frac{\partial A}{\partial z} = -i\left[\beta(\omega) - \beta_0 - \frac{\Omega}{v_{ref}} - i\frac{\alpha}{2}\right]A - \frac{i\omega\varepsilon_0 X_0}{8}d(z)\,\mathcal{F}_\Omega\left\{a^2 e^{j\phi(z,t)} + 2aa^* e^{-j\phi(z,t)}\right\}, \quad (5.4)$$

where $A(z,\omega)$ and $a(z,t)$ are the complex amplitude of the field during propagation in the frequency and time domain, $\phi(z,t) = \omega_0 t - (\beta_0 - \omega_0/v_{ref})z$, β_0 is the waveguide propagation constant at frequency ω_0, $\Omega = \omega - \omega_0$ is the envelope frequency, α is the attenuation constant, $d(z) = \pm 1$ is the sign of the nonlinear coefficient that varies along the waveguide due to quasi-phase matching, $\mathcal{F}_\Omega$ is the Fourier transform in Ω-space, and X_0 is the effective nonlinear coefficient. The pump and signal pulses were assumed to have a transform-limited, hyperbolic-secant profile. We used a commercial software (Lumerical Inc.) to calculate the waveguide modes and dispersion parameters used in our numerical simulations.

In Fig. 5.7A, we show the simulated squeezer OPA gain when it is seeded with a weak coherent pulse ($|\alpha|^2 \ll 1$) centered at 2090 nm and the relative phase between the pump and weak signal is varied. For the pump pulse energy of $\sim$ 1 pJ, the simulated OPA gain of $\sim$ 10 dB agrees well with the measured gain (anti-squeezing) at the same pump energy levels. We now determine the shortest signal pulse that can be amplified by our Squeezer OPA in a phase sensitive manner. To determine that, we vary the pulse width of weak coherent pulse from 15 fs to 100 fs while keeping the average pulse energy constant for a given pump pulse ($\sim$ 75 fs) and monitor the Squeezer OPA in the time domain. Fig. 5.7b shows the ratio, $R = \tau_{\text{out}}/\tau_{\text{in}}$ of the FWHM widths of output and input pulses. Numerical simulations suggest that as we keep reducing the pulse width of the input pulse from 100 fs, the amplified output pulse width remains short until the input pulse width of $\sim$ 30 fs, which corresponds to $\sim$ 4 optical cycles. Beyond that point the output pulse width starts to broaden in the time domain, as evident from $R > 1$ in Fig. 5.7B. This may be attributed to stronger detrimental effects caused by a small group velocity dispersion (GVD) and group velocity mismatch (GVM) in our devices for shorter pulses. These effects can be minimized by a better management of GVD and GVM through dispersion engineering. As a result, we find that the shortest pulse that our Squeezer OPA can amplify while maintaining the pulse shape and offering high gain is $\sim$ 30 fs. The temporal and spectral evaluations of $\sim$ 30 fs weak coherent pulse seeding the OPA are shown in Fig. 5.7C and Fig. 5.7D, respectively. The input pulses are shown in blue traces and orange traces correspond to output pulses. Dashed yellow and blue lines in Fig. 5.7C show the FWHM ($|E|^2 = 1/2$) for determining the number of optical cycles. We see that the amplified pulse retains its shape and contains $\sim$ 4 cycles. Figure 5.7D shows the constant gain of $\sim$ 18 dB over the entire bandwidth for 4 pJ of pump energy. The simulated constant gain bandwidth agrees well with the measured bandwidth of the optical parametric generation (OPG) from the squeezer OPA. The OPG signal is produced by amplifying (anti-squeezing) a quadrature while attenuating (squeezing) the orthogonal quadrature of vacuum field. Therefore, our generated squeezed vacuum bandwidth supports only a few optical cycles. Ideally, to measure the squeezing over the entire bandwidth one needs to ensure that the Measurement OPA has the same gain bandwidth while having the sufficient gain to amplify the microscopic squeezed vacuum to macroscopic levels, which can be achieved by dispersion engineering in LN nanophotonics.

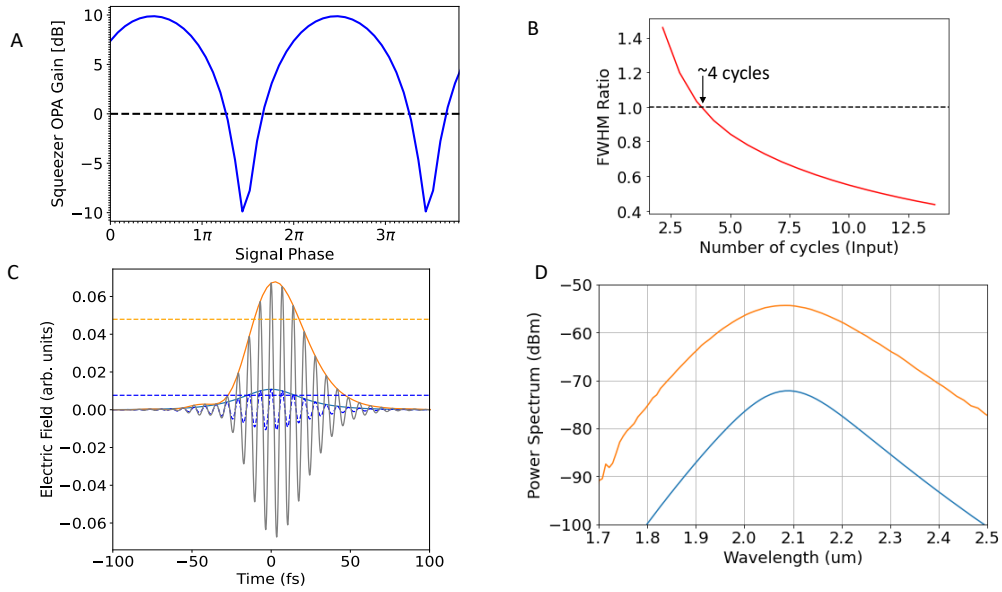

Figure 5.7: Numerical simulations. (A), Simulated Squeezer OPA gain as the signal phase is varied. (B), The ratio of FWHM bandwidths of output and input signal pulses for various values of input pulse widths. (C), The electric fields of input (solid blue) and output (solid orange) signal pulses. Dashed lines are at $|E|^2 = 1/2$ for determining the pulse widths at FWHM. (D), Spectrum of the weak coherent input and amplified output pulses.

5.5.4 Coupler design and characterization

In this section, we discuss our design for adiabatically tapered coupler. In our design, both waveguides are linearly tapered while keeping the gap constant throughout the coupling length as shown in Fig. 5.8A. Such a design offers a broadband coupling efficiency and is less susceptible to fabrication imperfections. Due to the adiabatic nature of the coupling process, such a coupler also relaxes the fixed beat length essential for a conventional non-tapered directional coupler and prohibits the Rabi-like oscillations of optical field between the pair of waveguides during propagation. The coupling efficiency of such a coupler given is by the Landau-Zener formula [35]:

$$\eta_c = 1 - \exp\left(\frac{-2\pi g^2}{\lambda}\frac{1}{\partial n_{\text{eff}}/\partial z.}\right) \tag{5.5}$$

The coupling strength is $g = (n_e - n_o)/2$, where n_e and n_0 are the refractive indices for the even and odd modes at the center of the coupler and $\partial n_{\text{eff}}/\partial z$ corresponds to the gradient in the refractive index along the propagation length. From Eq. 5.5, one can see that the coupling efficiency, η_c increases as the coupling strength, g increases. Due to the large difference in the spatial mode sizes as seen in Fig. 5.8B, the fundamental transverse-electric (TE) modes around 2090 nm of squeezed vacuum can be efficiently coupled from the squeezer waveguide to measurement amplifier waveguide, while the fundamental TE mode around 1045

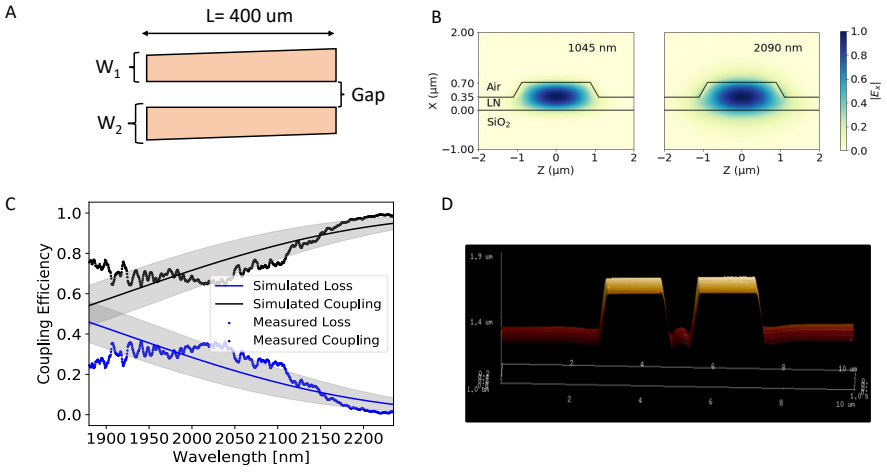

Figure 5.8: Design and characterization of adiabatically tapered coupler. (A), shows the design in which we keep the gap constant and adiabatically vary the waveguide widths (W_1 = 1668 nm and W_2 = 1768 nm) along the propagation length. (B), Calculated fundamental TE modes at 1045 nm and 2090 nm for the measured geometry. (C), Measured and simulated coupling efficiency. Solid black and blue curves correspond to numerically simulated coupling efficiency and losses, respectively. Shaded regions account for the fabrication uncertainty of ±10 nm in the etching depth. Black and blue dots show the measurements for coupling efficiency with an auxiliary beam centered around 2090 nm. (D), An AFM image of the coupler region.

nm of the squeezer pump mostly gets rejected. The numerically simulated coupling strengths around 1045 nm and 2090 nm are $O(10^{-4})$ and $O(10^{-3})$, respectively. Figure 5.8C shows the simulated (solid curves) and measured coupling efficiency and loss (dotted curves) over the measured squeezing bandwidth. The simulated coupling efficiency (solid black) and loss (solid blue) are obtained using using Eq. 5.5, where the effective refractive indices are calculated using the eigenmode solver in Lumerical. We measure the coupling efficiency of $\eta_c^{2090\text{ nm}} \sim 0.70$ using an auxiliary signal centered at 2090 nm generated by our SPDOPO and $\eta_c^{1045\text{ nm}} \sim 0.20$ around 1045 nm using the squeezer pump. The waveguide geometry for numerical simulations was obtained using atomic force microscopy (AFM). An image for the coupler region is shown in Fig. 5.8D. We measured the top widths of W_1 ~1668 nm and $W_2 \sim$ 1768 nm, etching depth of $\sim$ 380 nm, thin-film thickness of $\sim$ 713 nm, and sidewall angle of $\sim 57°$.

In the coupling region of L = 400 μm, the measured bottom gap in the coupler region is ~400 nm. While our measured coupling efficiency around 2 μm is ~70%, it can be significantly improved to ~100%, as suggested by our simulations. Figure 5.9 shows the numerically simulated coupling efficiencies for the signal at 2090 nm and pump at 1045 nm. For these simulations, we use the thin-film thickness of 700 nm

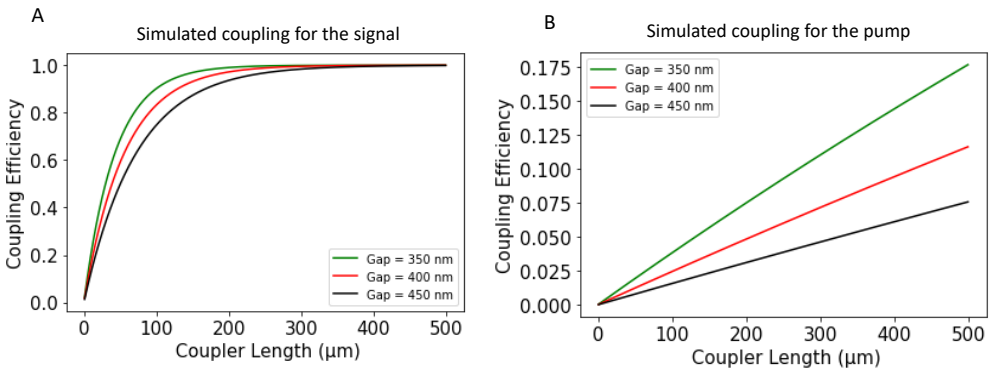

Figure 5.9: Simulated coupling efficiencies, (A) for the signal, (B) for the pump field.

and etching depth of 350 nm. Top widths of $W_1 = 1750$ nm and $W_2 = 1850$ nm and the waveguide ridge angle is $\sim 60°$. Three traces correspond to the three different values of bottom gaps of 350 nm, 400 nm, and 450 nm. For a coupler length of 300 μm, the coupling efficiencies for signal is >98% while < 5% of the pump is getting coupled when the coupler gap is of 450 nm. Considering the ultra-low loss propagation in LN nanophotonics and improved linear coupling of the coupler can lead to the measurements of squeezing levels suitable for fault-tolerant quantum information processors.

5.5.5 Quantum formalism for the generation and all-optical measurement of squeezed states

In this section, we derive the general formalism for the generation and all-optical measurement of quadrature squeezed vacuum using ultrashort-pulse phase-sensitive optical parametric amplifiers (OPAs). In our formulation, we define the single-mode field quadrature operators as $\hat{Q} := (\hat{a} + \hat{a}^\dagger)/\sqrt{2}$, $\hat{P} := (\hat{a} - \hat{a}^\dagger)/\sqrt{2}i$, and $\hbar = 1$ such that $\triangle Q \triangle P = 1/2$ for the vacuum state. In the interaction picture, the effective Hamiltonian for a spontaneous parametric down-conversion process in a $\chi^{(2)}$ waveguide OPA excited by a pulsed pump is given as [36, 37]

$$\hat{H} \propto \int \int d\omega_s d\omega_i S(\omega_s, \omega_i) \hat{a}_s^\dagger(\omega_s) \hat{a}_i^\dagger(\omega_i) + h.c., \tag{5.6}$$

where $S(\omega_s, \omega_i)$ describes the spectral correlations in signal and idler modes described by the photon creation operators $\hat{a}_s^\dagger(\omega_s)$ and $\hat{a}_i^\dagger(\omega_i)$, respectively and H.C. stands for the hermitian conjugate. By utilizing the Schmidt mode decomposition of the spectral correlation function $S(\omega_s, \omega_i) = \sum_m c_m \phi_m(\omega_s) \psi_m(\omega_i)$ with $\sum_m |c_m|^2 = 1$, one can rewrite the Hamiltonian as

$$H = \xi \sum_m (c_m \hat{A}_m^\dagger \hat{B}_m^\dagger + c_m^* \hat{A}_m \hat{B}_m), \tag{5.7}$$

where ξ determines the nonlinear interaction strength. $\hat{A}_m^\dagger$ and $\hat{B}_m^\dagger$ are broadband photon creation operators defined as [38]

$$\hat{A}_m^\dagger = \int d\omega_s \phi_m(\omega_s) \hat{a}_s^\dagger(\omega_s) \tag{5.8}$$

$$\hat{B}_m^\dagger = \int d\omega_i \psi_m(\omega_i) \hat{a}_i^\dagger(\omega_i), \tag{5.9}$$

The resultant unitary evolution operator under the Hamiltonian in Eq. 5.7 is then given as

$$\hat{U} = \exp\left(-\frac{i\xi t}{\hbar} \sum_m (c_m \hat{A}_m^\dagger \hat{B}_m^\dagger + c_m^* \hat{A}_m \hat{B}_m) \right), \tag{5.10}$$

For brevity, we define $r_m := -i\xi t c_m/\hbar = |r_m| e^{i\phi_m}$, which determines the nonlinear interaction strength of the m-th pairwise broadband spectral modes. The functions $\{\phi_m(\omega_s)\}$ and $\{\psi_m(\omega_i)\}$ form a complete set of orthonormal functions, i.e., $\int \phi_m^*(\omega_s)\phi_l(\omega_s) = \delta_{l,m}$ and $\int \psi_m^*(\omega_i)\psi_l(\omega_i) = \delta_{l,m}$. As a result, the Hamiltonian in Eq. 5.7 can be considered as the effective Hamiltonian of an ensemble of independent broadband two-mode squeezers, which further simplifies the unitary operator since we have $[\hat{A}_l, \hat{A}_m] = 0$ and $[\hat{B}_l, \hat{B}_m] = 0$. Thus, we get

$$\hat{U} = \bigotimes_m \exp(r_m \hat{A}_m^\dagger \hat{B}_m^\dagger - r_m^* \hat{A}_m \hat{B}_m). \tag{5.11}$$

We now consider the m-th mode with signal and idler broadband modes described by the photon annihilation operators $\hat{A}_m$ and $\hat{B}_m$, respectively. In this case, the unitary operator is

$$\hat{U} = \exp(r_m \hat{A}_m^\dagger \hat{B}_m^\dagger - r_m^* \hat{A}_m \hat{B}_m). \tag{5.12}$$

In the Heisenberg picture, the evolution of the broadband operators is given by the Bogoliubov transformation defined as (37)

$$\hat{A}_m \rightarrow \hat{A}_m \mathrm{cosh} r_m + e^{i\phi_m} \hat{B}_m^\dagger \mathrm{sinh} r_m \tag{5.13}$$

$$\hat{B}_m \rightarrow \hat{B}_m \mathrm{cosh} r_m + e^{i\phi_m} \hat{A}_m^\dagger \mathrm{sinh} r_m. \tag{5.14}$$

In the quadrature representation, for $\phi_m = 0$, Eqs. 5.13 and 5.14 can be written as

$$\hat{Q}_m^A \pm \hat{Q}_m^B \rightarrow (\hat{Q}_m^A \pm \hat{Q}_m^B) e^{\pm r_m} \tag{5.15}$$

$$\hat{P}_m^A \pm \hat{P}_m^B \rightarrow (\hat{P}_m^A \pm \hat{P}_m^B) e^{\mp r_m}, \tag{5.16}$$

where we have used $\hat{Q} = (\hat{a} + \hat{a}^\dagger)/\sqrt{2}$ and $\hat{P} = (\hat{a} - \hat{a}^\dagger)/\sqrt{2}i$ for the amplitude and phase quadratures of the quantum field. From Eqs. 5.15 & 5.16, we see that the sum (difference) of phase (amplitude) quadratures is squeezed and the difference (sum) of the phase (amplitude) quadratures is anti-squeezed. We define $\hat{Q}_\pm := \hat{Q}_m^A \pm \hat{Q}_m^B$ and $\hat{P}_\pm := \hat{P}_m^A \pm \hat{P}_m^B$. A simple calculation shows that $[\hat{Q}_\pm, \hat{P}_\mp] = 0$ and hence, they can be diagonalized simultaneously. Their shared eigenstate in the limit of $r_m \rightarrow \infty$ is the Einstein–Podolsky–Rosen (EPR) state with

$$\begin{aligned} \hat{Q}_-|\mathrm{EPR}\rangle &= 0, \\ \hat{P}_+|\mathrm{EPR}\rangle &= 0. \end{aligned} \tag{5.17}$$

In the finite squeezing limit, the EPR state serves as a crucial building block for many applications in continuous-variable quantum information processing [5, 6, 7, 8]. From Eq. 5.17, one can see that the operators $\hat{Q}_-$ and $\hat{P}_+$ are the nullifiers for the EPR state and have been widely used for their entanglement verification through the van Loock-Furusawa criterion in many frequency- or time-multiplexed CV cluster state experiments [39]. These nullifiers for each pair of modes are typically measured using multimode balanced homodyne detectors (BHD) with local oscillators (LO) tuned for each pair of frequency modes using electro-optic modulators (EOMs) [6, 7, 8, 10]. While the multimode homodyne measurements have been successful in small-scale experiments, it can be experimentally challenging when a large number of modes spanning over THz of bandwidth are involved. Moreover, the nullifier measurements are inherently limited by the electronic bandwidths of the EOMs, typically used for creating the LO sidebands to access the individual frequency modes of the quantum optical frequency comb [8].
In the photon-number basis, the two-mode squeezed state can be expressed as

$$|\psi\rangle^m_{A,B} = \sum_{n=0} C_{nn}|n_A, n_B\rangle, \tag{5.18}$$

where $c_{nn} = \tanh^n r_m/\cosh r_m$. As can be seen from Eq. 5.18, there are photon-number correlations between the signal and idler modes. The average photon-number is

$$\langle N^{A,B}_m\rangle = \mathrm{Tr}[\rho_{A,B}(\hat{N}^A_m + \hat{N}^B_m)] = 2\sinh^2 r_m. \tag{5.19}$$

So far, we have used single-mode operators for these derivations. We now adopt to frequency agnostic two-mode complex quadrature formalism [37, 38, 39, 40] where the two-mode complex quadrature operators can be defined as

$$\begin{aligned}\hat{X}_{A,B} &:= \hat{A} + \hat{B}^\dagger = (\hat{Q}_+ + i\hat{P}_-)/\sqrt{2}\\ \hat{Y}_{A,B} &:= i\hat{A}^\dagger - \hat{B} = (i\hat{Q}_- + \hat{P}_+)/\sqrt{2},\end{aligned} \tag{5.20}$$

Here, we have omitted the mode index m because the formalism is equally valid for any number of correlated frequency modes [19]. Similar to single-mode case, one can then define the generalized two-mode quadrature operator as

$$\hat{Z}_{A,B} = \cos\phi\hat{X}_{A,B} + \sin\phi\hat{Y}_{A,B}, \tag{5.21}$$

where $\hat{X}_{A,B}$ and $\hat{Y}_{A,B}$ can be thought as the amplitude and phase quadratures of the two-mode field. Using Eqs. 5.13, 5.14, 5.20, and 5.21, we can conclude that a two-mode OPA amplifies the amplitude quadrature $\hat{X}_{A,B}$ while attenuating the phase quadrature $\hat{Y}_{A,B}$ without any additional noise. Mathematically, we have

$$\hat{X}_{A,B} \to \hat{X}_{A,B}e^r \tag{5.22}$$

$$\hat{Y}_{A,B} \to \hat{Y}_{A,B}e^{-r}. \tag{5.23}$$

This is similar to a single-mode degenerate OPA where signal and idler photons are emitted into the same optical mode. In the single-mode case, the Hamiltonian can

be treated as an effective Hamiltonian of an ensemble of independent broadband single-mode squeezers [38]. The resulting unitary evolution can then be simplified as

$$\hat{U} = \bigotimes_{m=1} \exp[(r_m \hat{A}_m^{\dagger 2} - r_m^* \hat{A}_m^2)], \tag{5.24}$$

In the Heisenberg picture, the evolution of the broadband operators is given by the Bogoliubov transformation defined as [37]

$$\hat{A}_m \rightarrow \hat{A}_m \cosh r_m + e^{i\phi} \hat{A}_m^\dagger \sinh r_m. \tag{5.25}$$

Rewriting Eq. 5.25 in the quadrature representation for $\phi = 0$, we get

$$\hat{Q}_m \rightarrow \hat{Q}_m e^{r_m} \tag{5.26}$$

$$\hat{P}_m \rightarrow \hat{P}_m e^{-r_m} \tag{5.27}$$

From Eqs. 5.22, 5.23, 5.26, and 5.27, one can see that the two-mode complex quadrature representation puts the single-mode and two-mode OPAs at equal footing. In the two-mode complex quadrature representation, the total average photon-number turns out to be

$$\langle \hat{N}_{A,B} \rangle_\rho \propto e^{2r} \langle \hat{X}_{A,B}^\dagger \hat{X}_{A,B} \rangle_{\rho_{A,B}} + e^{-2r} \langle \hat{Y}_{A,B}^\dagger \hat{Y}_{A,B} \rangle_{\rho_{A,B}}, \tag{5.28}$$

where $\rho_{A,B}$ is the input state to the OPA. In the high-parametric gain regime $e^{2r} \gg 1$, the average photon-number is entirely dominated by the amplified quadrature and the attenuated quadrature can be considered negligible. The amplified quadrature power is in the macroscopic regime, i.e., it's sufficiently above the vacuum noise and can be directly measured with high-tolerance to losses due to off-chip coupling, mode-mismatching, and imperfect detection. From Eq. 5.28, we can see that the quadrature variance of the input state can be determined from a direct measurement of the average photon-number of the amplified quadrature. For the generation and all-optical measurement of squeezed vacuum states, one can cascade two such OPAs. The first low-gain OPA can be pumped to generate squeezed vacuum, which can then be measured by the second high-gain OPA, as shown in Fig. 5.10.

An ideal case is considered in Fig. 5.10a: OPA 1 is used to generate a squeezed vacuum state which is then amplified with a high-gain OPA 2. From hereon, We will call OPA 1 and OPA 2 as squeezer and measurement amplifiers, respectively. The squeezer phase, ϕ_1 is kept fixed while the measurement amplifier phase, ϕ_2 is modulated to amplify each quadrature of the squeezed vacuum state. The squeezer (measurement amplifier) gain is $G_{1(2)} = e^{2r_{1(2)}}$. In the Heisenberg picture, we find the evolution of annihilation operators after the first and second OPA. After OPA 1 in Fig. 5.10a, we get

$$\begin{aligned} \hat{a}_s' &= \hat{a}_s \cosh r_1 + e^{i\phi_1} \hat{a}_i^\dagger \sinh r_1 \\ \hat{a}_i' &= \hat{a}_i \cosh r_1 + e^{i\phi_1} \hat{a}_s^\dagger \sinh r_1. \end{aligned} \tag{5.29}$$

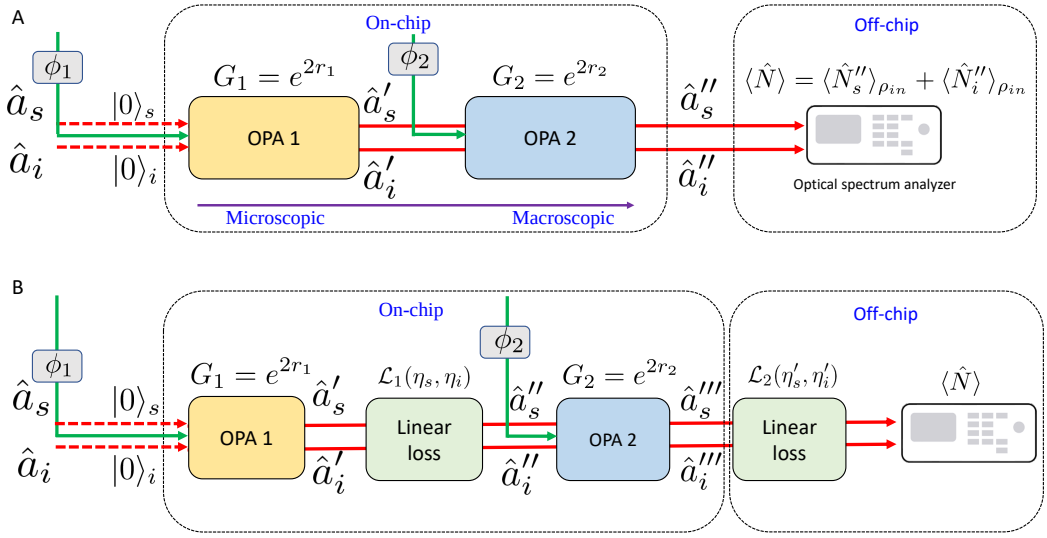

Figure 5.10: Generation and all-optical measurement of a squeezed vacuum state. (A), An ideal case where the squeezed vacuum is generated by OPA 1 and amplified by OPA 2 followed by a total power measurement of the signal and idler modes. (B) Lossy case where linear losses experienced by squeezed vacuum and amplified squeezed vacuum are considered. The green and red arrows show the pump and signal-idler modes, respectively. Dashed arrows show the initial vacuum for the signal and idler modes.

Likewise, after OPA 2

$$\begin{aligned}\hat{a}''_s &= \hat{a}'_s \cosh r_2 + e^{i\phi_2}\hat{a}'^{\dagger}_i \sinh r_2 \\ \hat{a}''_i &= \hat{a}'_i \cosh r_2 + e^{i\phi_2}\hat{a}'^{\dagger}_s \sinh r_2.\end{aligned} \tag{5.30}$$

As a result, the input operators for signal and idler modes evolve to

$$\begin{aligned}\hat{a}_s &\longrightarrow \hat{a}_s \cosh r_{\text{eff}} + e^{i\phi_1}\hat{a}^{\dagger}_i \sinh r_{\text{eff}} \\ \hat{a}_i &\longrightarrow \hat{a}_i \cosh r_{\text{eff}} + e^{i\phi_1}\hat{a}^{\dagger}_s \sinh r_{\text{eff}},\end{aligned} \tag{5.31}$$

where r_{eff} is the effective gain parameter given as

$$r_{\text{reff}} = \text{arctanh}\left[\frac{\sinh r_1 \cosh r_2 + e^{i\triangle\phi}\sinh r_2 \cosh r_1}{\cosh r_1 \cosh r_2 + e^{i\triangle\phi}\sinh r_1 \cosh r_2}\right], \tag{5.32}$$

where $\triangle\phi = \phi_1 - \phi_2$. The average photon-number is

$$\langle\hat{N}\rangle = \text{Tr}[|0_s, 0_i\rangle\langle 0_s, 0_i|\ \hat{N}] = 2\sinh^2|r_{\text{eff}|}. \tag{5.33}$$

In order to measure the squeezing, we need to compare the quadrature variances with the vacuum state. To determine the vacuum variances, we block the squeezer

(OPA 1) pump and measure the average photon-number of the amplified vacuum (optical parametric generation) from OPA 2. Mathematically, we can set $r_1 = 0$ and $\phi_1 = 0$ in Eq. 5.32. As a result, the average photon-number of amplified vacuum state is

$$\langle \hat{N}_v \rangle = 2\sinh^2 r_2. \tag{5.34}$$

Thus, Eq. 5.34 determines the amplified shot-noise level, i.e., the variance of the amplitude vacuum quadrature. It is worth emphasizing the average-photon number of the amplified vacuum does not depend on the phase of the Measurement OPA pump, as seen from Eq. 5.34. This is due to the uniform phase distribution of the vacuum state. However, the high-gain amplification by the Measurement OPA is performed in a phase-sensitive manner, i.e., the selected vacuum quadrature is amplified at macroscopic levels while attenuating the orthogonal quadradure, resulting in ellipse-shaped phase-space distributions shown in Fig. 5.1B and Fig. 5.1C in the main text, which are not distinguishable by power measurements.

For determining the squeezing, we need to compare the amplified vacuum variance with the amplified squeezed quadrature variance. Thus, we set $\triangle\phi = \pi$. In this case, r_{eff} in Eq. 5.32 is: $r_{\text{eff}} = r_- = |r_2 - r_1|$. Therefore, for average photon-number measurements both the OPAs can be treated as a single OPA with effective gain r_-, leading to

$$\langle \hat{N}_- \rangle = 2\sinh^2 r_-. \tag{5.35}$$

Likewise, we set $\triangle\phi = 0$ for measuring the anti-squeezed quadrature. In this case, anti-squeezed quadrature of the squeezed vacuum state from OPA 1 is being amplified by the Measurement OPA. The average photon-number in this case is

$$\langle \hat{N}_+ \rangle = 2\sinh^2 r_+, \tag{5.36}$$

where we define $r_+ = |r_1 + r_2|$. As a result, the anti-squeezing (S_+) and squeezing (S_-) can be calculated as

$$S_\pm[\text{dB}] = 10\log_{10}\left[\frac{\langle N_\pm \rangle}{\langle N_\text{v} \rangle}\right] = 10\log_{10}\left[\frac{\sinh^2 r_\pm}{\sinh^2 r_2}\right]. \tag{5.37}$$

For $e^{2r_2} \gg e^{2r_1} \gg 1$, $S_\pm[\text{dB}] \rightarrow 10\log_{10}(e^{2r_1})$. It is worth emphasizing that such an all-optical measurement scheme allows one to measure the quantum fields over the entire optical bandwidths since both the generation and measurement use the same nonlinear process.

We now include experimental imperfections due to linear losses and non-unity detection efficiencies in our model. Losses are modeled by setting up fictitious beamsplitters with losses modeled with non-unity transmission coefficients. On-chip losses on squeezed vacuum are modeled by two beamsplitters denoted by $\mathcal{L}_1(\eta_s, \eta_i)$, and off-chip coupling losses and imperfect detection are modeled by $\mathcal{L}_2(\eta'_s, \eta'_i)$, as shown in Fig. 5.10b, where (η_s, η_i) and (η'_s, η'_i) determine the transmission coefficients of beamsplitters placed in the path of signal and idler modes.

Similar to ideal case, we employ the Heisenberg picture to find the evolution of input annihilation operators. Due to on-chip loss $\mathcal{L}_1(\eta_s, \eta_i)$, the operators $\hat{a}'_s$ and $\hat{a}'_i$

transform to

$$\hat{a}_s'' = \sqrt{\eta_s}\hat{a}_s' + \sqrt{1-\eta_s}\hat{a}_s^v$$
$$\hat{a}_i'' = \sqrt{\eta_i}\hat{a}_i' + \sqrt{1-\eta_i}\hat{a}_i^v, \tag{5.38}$$

where $\hat{a}_s^v$ and $\hat{a}_i^v$ are the vacuum modes coupled through the open ports of the beamsplitters for the signal and idler modes, respectively. After OPA 2, the operators evolve as

$$\hat{a}_s''' = \hat{a}_s''\cosh r_2 + e^{i\phi_2}\hat{a}_i''^{\dagger}\sinh r_2$$
$$\hat{a}_i''' = \hat{a}_i''\cosh r_2 + e^{i\phi_2}\hat{a}_s''^{\dagger}\sinh r_2. \tag{5.39}$$

Finally, we calculate the evolution under $\mathcal{L}_2(\eta_s', \eta_i')$

$$\hat{a}_s^f = \sqrt{\eta_s'}\hat{a}_s''' + \sqrt{1-\eta_s'}\hat{a}_s^v$$
$$\hat{a}_i^f = \sqrt{\eta_i'}\hat{a}_i''' + \sqrt{1-\eta_i'}\hat{a}_i^v \tag{5.40}$$

The average photon-number is then given as

$$\langle\hat{N}\rangle = \mathrm{Tr}[\eta_s'\hat{a}_s^{\dagger'''}\hat{a}_s''' + \eta_i'\hat{a}_i^{\dagger'''}\hat{a}_i'''] \tag{5.41}$$

Using Eqs. 5.29, 5.38, 5.39, 5.40, and 5.41, we can determine the loss-degraded total average photon-number for amplified squeezed quadrature ($\triangle\phi = \pi$) and amplified anti-squeezed quadrature ($\triangle\phi = 0$) as

$$\begin{aligned}\langle N_\pm\rangle = {} & \eta_s'[(\sqrt{\eta_s}\sinh r_1\cosh r_2 \pm \sqrt{\eta_i}\cos r_1\sinh r_2)^2 + (1-\eta_i)\sinh^2 r_2)] \\ & + \eta_i'[(\sqrt{\eta_i}\sinh r_1\cosh r_2 \pm \sqrt{\eta_s}\cos r_1\sinh r_2)^2 + (1-\eta_s)\sinh^2 r_2].\end{aligned} \tag{5.42}$$

By comparing with the average photon-number $\langle N_\mathrm{v}\rangle = (\eta_s' + \eta_i')\sinh^2 r_2$ of the amplified vacuum, we can calculate the measurable squeezing as

$$\begin{aligned}S_\pm[\mathrm{dB}] = 10\log_{10}\Bigg[& \frac{\eta_s'[(\sqrt{\eta_s}\sinh r_1\cosh r_2 \pm \sqrt{\eta_i}\cosh r_1\sinh r_2)^2 + (1-\eta_i)\sinh^2 r_2]}{(\eta_s' + \eta_i')\sinh^2 r_2} \\ & + \frac{\eta_i'[(\sqrt{\eta_i}\sinh r_1\cosh r_2 \pm \sqrt{\eta_s}\cosh r_1\sinh r_2)^2 + (1-\eta_s)\sinh^2 r_2]}{(\eta_s' + \eta_i')\sinh^2 r_2}\Bigg]\end{aligned} \tag{5.43}$$

For $\eta_s = \eta_i = \eta$ and $\eta_s' = \eta_i' = \eta'$, Eq. 5.43 can be simplified to

$$S_\pm[\mathrm{dB}] = 10\log_{10}\left[\frac{\eta\sinh^2 r_\pm + (1-\eta)\sinh^2 r_2}{\sinh^2 r_2}\right] \tag{5.44}$$

From Eq. 5.44, we can see that the measured squeezing only depends on losses on microscopic squeezed vacuum, i.e., losses before the high-gain amplification by the Measurement OPA. Therefore, our all-optical measurement offers tolerance

against the off-chip coupling losses and detection inefficiencies. The high-gain amplification prior to off-chip coupling makes the originally squeezed quadrature sufficiently above than the vacuum noise, thereby making it robust against the vacuum contamination due to linear losses. For $e^{2r_2} \gg e^{2r_1}$, Eq. 5.44 turns out to be

$$S_{\pm}[\text{dB}] = 10\log_{10}[\eta e^{\pm 2r_1} + (1-\eta)]. \tag{5.45}$$

The first term in Eq. 5.45 amounts to reduced squeezing due to losses on squeezed vacuum and the second term is the contribution from the vacuum noise. The measured squeezing degrades with increasing amount of losses, $L = 1-\eta$. However, the measured squeezing remains non-zero for $\eta > 0$ and having higher initial squeezing is always advantageous no matter how much the loss is. In Fig. 5.11A, we plot the required measurement amplifier gain for measuring several values of generated initial squeezing without any losses. We find that the larger amount of initial squeezing requires higher gain, and once the gain is sufficient (for instance >33 dB for ~11 dB squeezing), further increments in the gain do not have any significant effects on the measurements, as seen from the flat regions in Fig. 5.11A and B. Sufficient gain ensures that the measured power is entirely dominated by the selected amplified quadrature and the attenuated quadrature can be considered negligible. Note that the measured anti-squeezing levels do not change as dramatically as squeezing when the Measurement OPA gain is varied. Since the anti-squeezed quadrature of microscopic squeezed field is already amplified by the Squeezer OPA, it then requires lower gain to dominate the measured power, as compared to the originally squeezed quadrature.

Figure 5.11B shows the lossy case with the total losses of $L = 1 - \eta = 0.30$ on microscopic squeezed signal. As expected, the measurable squeezing degrades significantly as compared to anti-squeezing in the presence of losses. Figure 5.11C displays the experimentally measured (solid circles) squeezing and anti-squeezing at 2090 nm as the squeezer pump energy is varied. Our measured values agrees well with the expected amounts of squeezing and anti-squeezing levels in Fig. 5.11B. Finally, Fig. 5.11D shows the measured gain (red points) of the Measurement OPA as the pump pulse energy is increased. The black curve correspond to the expected exponential fit, which is in a good agreement with our measured gain.

We now consider the generalized case shown in Fig. 5.10B. In the high-gain regime when $e^{2r_2} \gg e^{2r_1}$, Eq. 5.43 can be simplified to

$$S_{\pm}[\text{dB}] = 10\log_{10}\Bigg[\underbrace{\frac{1}{4}(\sqrt{\eta_s}+\sqrt{\eta_i})^2 e^{\pm 2r_1}}_{\text{Loss-degraded squeezing}} + \underbrace{1 - \frac{\eta_s\eta_i' + \eta_i\eta_s'}{\eta_s' + \eta_i'}}_{\text{Added vacuum noise}} + \underbrace{\frac{1}{4}(\sqrt{\eta_s}-\sqrt{\eta_i})^2 e^{\mp 2r_1}}_{\text{Added noise due to asymmetric losses}}\Bigg] \tag{5.46}$$

In contrast to Eq. 5.45, Eq. 5.46 has an additional term proportional to $e^{\mp 2r_1}$ due to loss asymmetry in the signal and idler modes. Since this additional term mixes the anti-squeezing term e^{2r_1} to the reduced squeezing term, e^{2r_1}, leading to a further reduction in the amount of measurable squeezing. In fact, the loss asymmetry is more detrimental at higher initial squeezing levels. Interestingly, for $\eta_s = \eta_i = \eta$,

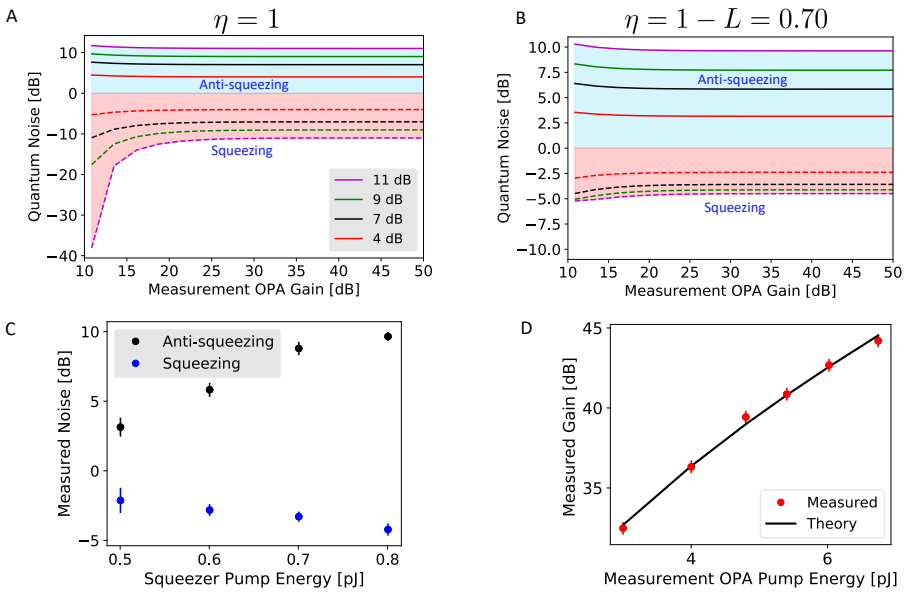

Figure 5.11: Required measurement amplifier gain for a given amount of squeezing. Measurement amplifier gain, (A) An ideal case without any experimental imperfections and ((B), realistic case with $L = 0.30$ optical losses experienced by the microscopic squeezed vacuum state. (C), Experimentally measured squeezing and anti-squeezing values as the squeezer pump energy is varied. (D) Gain measurements for the Measurement amplifier at various values of pump energy. Error bars are obtained from the statistics of the measurements.

the measured squeezing is independent of η_s' and η_i' provided that the measurement amplifier has sufficient gain.

Figure 5.12 displays the measured squeezing for a range of losses experienced by the signal and idler modes. The losses on signal and idler modes are $1-\eta_s$ and $1-\eta_i$, respectively. Figure 5.12A considers the case where the off-chip coupling losses and detection efficiencies of signal and idler modes are equal, i.e., $\eta_s' = \eta_i'$ in Fig. 5.10. In this case, the measured squeezing levels are completely independent of η_s' and η_i', as seen from Eq. 5.46. We can see that the measured squeezing is optimal along the diagonal, i.e., for $\eta_s = \eta_i$, and it degrades quickly with increasing asymmetry in losses for signal and idler modes. In fact, the squeezing can be entirely suppressed as seen from the measured squeezing along the anti-diagonal in Fig. 5.12A. It is worth emphasizing that the loss asymmetry is even more detrimental at higher levels of initial squeezing due to the larger contribution from e^{2r_1} term.

In Figure 5.12B, we consider unequal amount of losses for the signal and idler modes after the amplification. In particular, we choose $[\eta_s', \eta_i'] = [0.2, 0.5]$. Remarkably, the measured squeezing can be improved by carefully choosing η_s' and η_i' for a given amount of losses η_s and η_i on the squeezed vacuum state. This is evident in Fig. 5.12C which shows the difference of the cases "a" and "b". For $\eta_s > \eta_i$ in Fig. 5.12C, we have $\triangle S = S(\eta_s' = \eta_i') - S([\eta_s', \eta_i'] = [0.2, 0.5]) > 0$, thereby

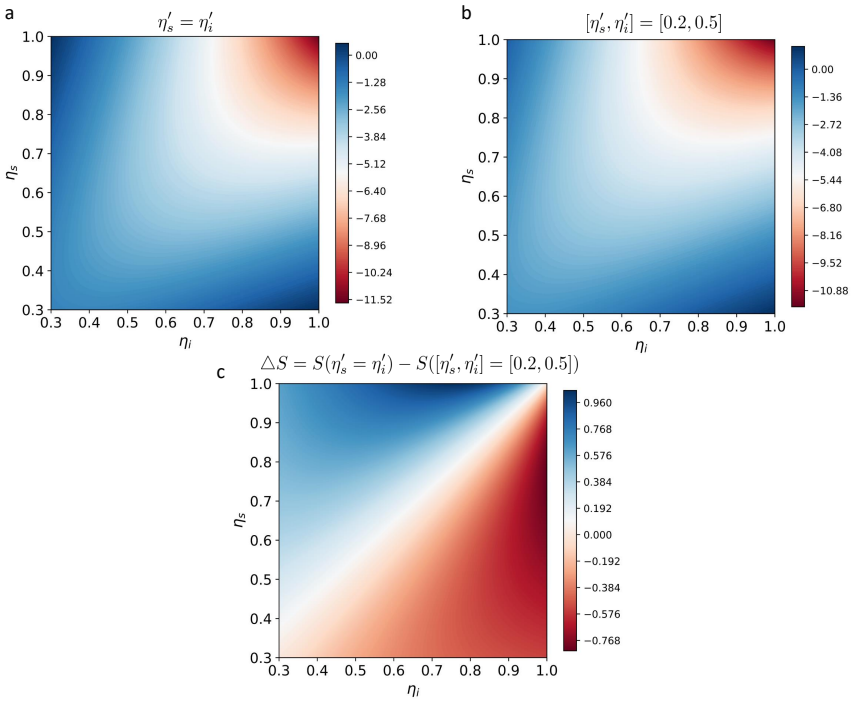

Figure 5.12: Squeezing degradation under photon loss. (A), When the output coupling losses and detection efficiencies are equal, i.e., $\eta_s' = \eta_i'$. (B), For $[\eta_s', \eta_i'] = [0.2, 0.5]$ and (C) displays the difference of "a" and "b".

confirming $S([\eta_s', \eta_i'] = [0.2, 0.5]) > S(\eta_s' = \eta_i')$. Therefore, a careful selection of well-calibrated losses on amplified squeezed vacuum allows one to restore the squeezing lost due to loss asymmetry in signal and idler modes. This is particularly beneficial for broadband squeezed signal where it is likely to have unequal amount of losses either due to spectral dependence of linear transmission rates or the detection efficiencies.

We now estimate the overall detection efficiency, which includes the off-chip coupling efficiency and the detector efficiency, in our experimental setup. A detailed discussion is provided in our previous work [41]; here we outline the essential steps. The measured average photon-number from a vacuum-seeded OPA is given as

$$\langle N \rangle_{\text{measured}} = \eta_1 \sinh^2 r, \tag{5.47}$$

where the gain parameter is: $r = 2L\sqrt{\eta_2 P}$ for a given pump power P and interaction length L. The overall detection efficiency is η_1, which includes the total optical losses due to coupling and imperfect detection experienced by the macroscopic OPG signal and η_2 quantifies the nonlinear interaction strength. In the high-gain regime, we have $\langle N \rangle_{\text{measured}} \sim \eta_1 e^{2L\sqrt{\eta_2 P}}/4$. We measured the macroscopic average photon-number generated from the Squeezer OPA for various levels of pump pulse energy. By fitting the data using Eq. 5.47, we extract the η_1 and η_2 parameters. We obtain the overall detection efficiency of $\eta_1 \approx 0.20$, which agrees well with our

previous estimations [41, 42]. The measured data and fit are shown in Fig. 5.2E of the main text.

Thus far we have considered the Measurement OPA to be an ideal OPA with the noise figure NF = 0 dB , i.e., during the amplification process no additional noise is being added by the OPA. We now turn our attention to the added noise by the Measurement OPA. We characterize the added excess noise using the phase-sensitive amplification efficiency, η_{OPA} parameter, which combines all the imperfections such as losses and the phase noise during the amplification process [43]. Since the imperfections in the the Measurement OPA degrade the amount of measured squeezing, η_{opa} can be treated as a linear loss channel, which brings in the vacuum noise, and can be modeled by a fictitious BS with transmission of η_{opa}. In this simplified model, the amplified quadrature is given by

$$\hat{X}' = \sqrt{G\eta_{\mathrm{OPA}}}\hat{X}^{\mathrm{in}} + \sqrt{G(1-\eta_{\mathrm{OPA}})}\hat{X}^{v}_{\mathrm{OPA}}, \tag{5.48}$$

where $\hat{X}^{v}_{\mathrm{OPA}}$ is the quadrature operator for the added vacuum noise. We then include the losses due to off-chip coupling and detection inefficiencies after the amplification. As a result, the loss-degraded amplified field quadrature is

$$\hat{X}' = \sqrt{\eta_l}(\sqrt{G\eta_{\mathrm{OPA}}}\hat{X}^{\mathrm{in}} + \sqrt{G(1-\eta_{\mathrm{OPA}})}\hat{X}^{v}_{\mathrm{OPA}}) + \sqrt{(1-\eta_l)}\hat{X}^{v}_{l}, \tag{5.49}$$

where η_l and $\hat{X}^{v}_{l}$ correspond to the overall losses after amplification and the vacuum quadrature, respectively. From Eq. 5.49, one can define the effective quadrature measurement efficiency as

$$\eta_{\mathrm{eff}} = \frac{G\eta_{\mathrm{OPA}}\eta_l}{G\eta_{\mathrm{OPA}}\eta_l + G(1-\eta_{\mathrm{OPA}})\eta_l + (1-\eta_l)} \tag{5.50}$$

We now consider the limiting cases of the Measurement OPA gain. Firstly, when the Measurement OPA has no gain, i.e., $G = 1$, the effective efficiency is $\eta_{\mathrm{eff}} = \eta_{OPA}\eta_l$. In this case, the Measurement OPA acts as a linear loss channel with transmission η_{OPA}, resulting in the overall loss of η_{eff}. Secondly, when $G \gg 1$ and $\eta_{\mathrm{OPA}} > \eta_l$, the effective detection efficiency of the quadrature measurement approaches the overall efficiency of the OPA, i.e., $\eta_{\mathrm{eff}} \to \eta_{\mathrm{OPA}}$. In the Fig. 5.13, we consider the effective quantum efficiency of our all-optical measurement for many values of NFs of $\{0, 1, 1.5, 3\}$ dB ($\eta_{\mathrm{OPA}} = \{1, 0.8, 0.7, 0.5\}$) at a given value for the overall detection efficiency of $\eta_l = 0.2$ after the amplification. Here we chose $\eta_l = 0.2$ because of our measured off-chip coupling efficiency. We find that the effective detection efficiency of all-optical measurement approaches to η_{OPA} for a sufficiently large gain. We note that the levels of gain were measured from our high-gain OPA, as shown in Fig. 5.11D.

As a result, we see the overall quantum efficiency of an all-optical measurement through a high-gain phase-sensitive OPA is ultimately determined by the NF of the OPA. While the measurement can be made tolerant against the losses after the high-gain amplification, the quantum efficiency is limited by the OPA NF and it is desirable to have NF $\to$ 0, particularly beneficial for measuring highly squeezed

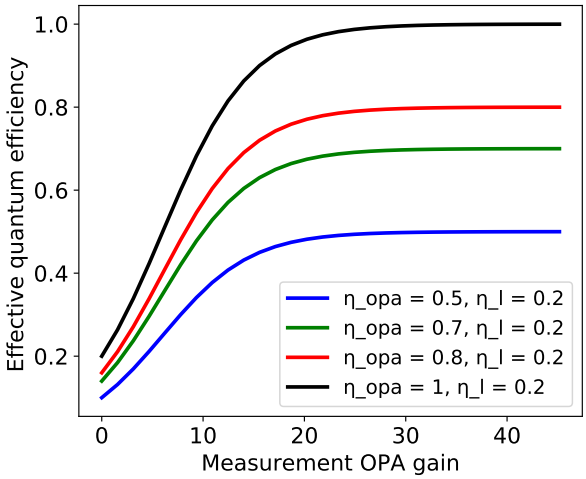

Figure 5.13: Effective efficiency for various values of η_{OPA} and η_l.

states, which are extremely sensitive to photon losses. In Fig. 5.14, we plot how the squeezing and anti-squeezing degrade as the photon loss ($L = 1 - \eta_{\text{effective}}$) increases. We see that 30 dB (blue) of initial squeezing degrades by ~20 dB with 10% photon loss, while 10 dB (red) squeezing only degrades by ~3 dB.

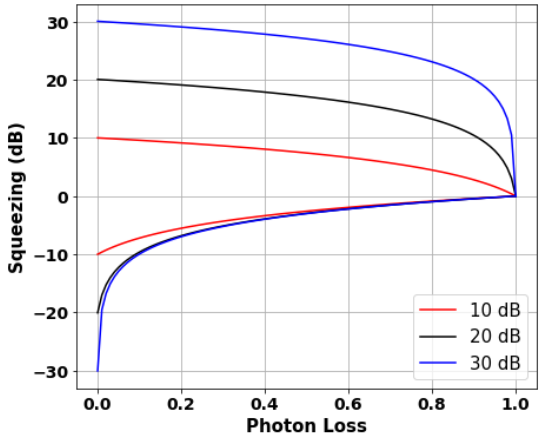

Figure 5.14: Squeezing degradation with the photon loss.

5.5.6 Device fabrication

Our devices are fabricated using a wafer with 700-nm-thick X-cut MgO-doped LN on 2-μm-thick SiO_2 from NANOLN. The fabrication process begins with periodically poling the chip. The poling electrodes (15 nm Cr/55 nm Au) were patterned using e-beam lithography, e-beam evaporation and metal lift-off. Then ~ 300 V pulses were applied across the electrodes resulting in periodic domain inversion

over the regions of 2.5 mm and 5.0 mm lengths for the Squeezer and Measurement OPAs, respectively. To account for fabrication imperfections, we varied the poling periods from 5.17 μm to 5.32 μm with a step size of 5 nm. The poling quality is inspected using second-harmonic microscopy, shown in Fig. 5.2A (iii) of the main text. Next, the device were patterned using e-beam lithography using hydrogen silsesquioxane (HSQ) as e-beam resist and 15 nm of Ti as an adhesion layer [42, 44]. The pattern was transferred to the LN layer by dry etching with Ar^+ plasma in an inductively-coupled plasma reactive-ion etcher (ICP-RIE). The remaining resists and side-wall re-deposition were removed by the buffered oxide etchant (BOE) and RCA cleaning. Finally, the waveguide facets were mechanically polished to improve the coupling efficiencies. The fabrication quality is inspected using SEM, example images are shown in Fig. 5.2A (i and ii) in the main text.

5.5.7 Measurement of the amplifier gain

In this section, we discuss our parametric gain measurements for the Measurement OPA with an auxiliary weak coherent signal generated by our 2 μm SPDOPO. We optimize the phase matching by ensuring the maximum amplification/deamplification experienced by the weak coherent pulse. To fine-tune the optimal phase matching, we tune the chip temperature using a thermoelectric cooling (TEC) plate set underneath the chip, and by coating the chip with a thin layer of organic material. The experimental setup for OPA measurements is shown in Fig. 5.4. We use pump 1 for pumping the SPDOPO and guide its output signal to the nanophotonic chip setup. After attenuating the OPO signal sufficiently, it is coupled to the measurement amplifier along with the Pump 2. Our measurements results are displayed in Fig. 5.15. The blue trace shows the measured spectrum of input weak coherent signal ($\sim$ 1 fJ) and the gray trace corresponds to the amplified signal with Pump 2 pulse energy of $\sim$ 6 pJ while the PZT is scanned using a ramp signal at 5 Hz. The ripples are due to phase-sensitive nature of the amplification process. For better visibility, we apply a median filter on the amplified signal trace, shown in red. The measured gain is >28 dB near 2090 nm, which is comparable to our previous work [42].

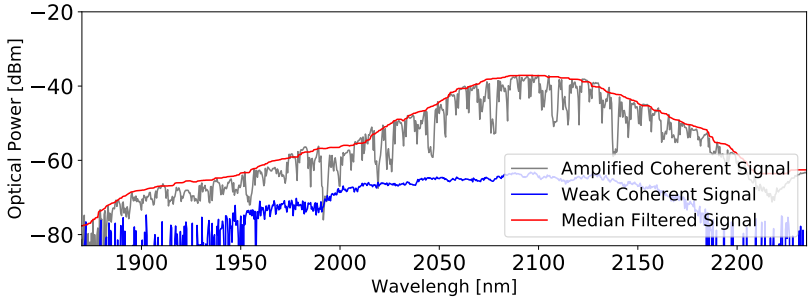

Figure 5.15: Classical measurement of the Measurement OPA gain. The blue and gray traces are for weak input signal and amplified output signal, respectively. The red trace is processed amplified signal trace using a median filter. The ripples are due to phase-sensitive amplification.

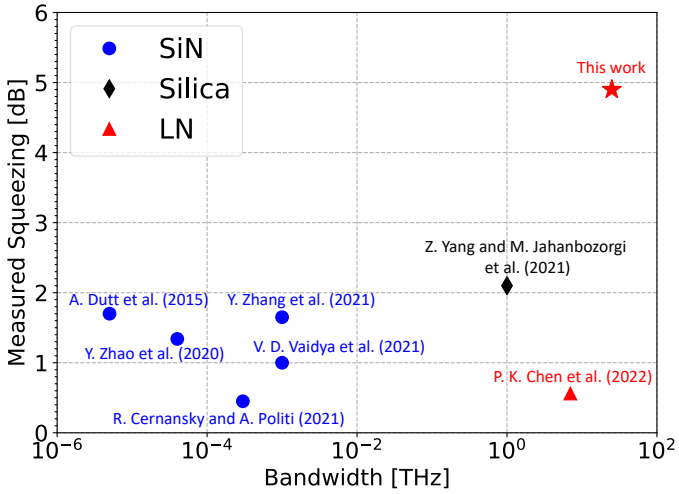

Figure 5.16: Performance comparison of measured squeezing levels and squeezing bandwidths on various nanophotonic platforms.

5.5.8 Squeezing in nanophotonics

Figure 5.16 compares our measured squeezing and bandwidth with state-of-the-art demonstrations in nanophotonic platforms including SiN and silica. These experimental demonstrations utilize relatively weaker $\chi^{(3)}$ nonlinearities and require microresonators for enhancement. Additionally, the squeezed light is typically detected using off-chip BHDs which impose limitations on the measured squeezing (due to off-chip coupling losses) and the accessible squeezing bandwidths. Our measured squeezing substantially surpasses these other works both in the magnitude and bandwidth.

In the table below, we present the references for state-of-the-art squeezing demonstrations in nanophotonics shown in Fig. 5.16.

Squeezing (inferred) [dB]	Platform	Bandwidth	Reference
1.7 (5)	SiN	5 MHz	[45]
1.0(4)	SiN	1 GHz	[11]
1.34(3)	SiN	40 MHz	[46]
1.65(8)	SiN	1 GHz	[47]
0.45 (1)	SiN	300 MHz	[48]
1.6(3.1)	Silica	1 THz	[49]
0.56(3)	LN	7 THz	[16]
4.9(11)	LN	25 THz	This work

Table 5.1: State-of-the-art demonstrations in nanophotonics squeezing.

5.5.9 Ultrafast quantum information processors in LN nanophotonics

In this section, we would like to highlight the importance of our ultra-short-pulse source of squeezed state and its all-optical measurement scheme for CV ultra-fast quantum information processing. Single-mode and two-mode squeezed vacuum states are used as the main building block for generating highly entangled large-scale cluster states, which serve as the quantum computing "substrate" for measurement-based quantum computing (MBQC) and have been generated using both time- and frequency-multiplexed architectures [6, 7, 8].

In time-multiplexed schemes, continuously generated squeezed vacuum states from continuous wave (CW) pumped optical parametric oscillator (OPOs) are divided into independent time bins, which are then entangled with each other using optical delays and linear optics to generate the large-scale cluster states [6, 7]. In such a configuration, the repetition rate of the time bins is limited by the bandwidth of the squeezer OPO, which is typically <100 MHz, resulting in few tens of nanosecond-scale temporal bins (~10 meters long). Consequently, to entangle thousands of these temporal modes, kilometer-scale optical delays are required, which are so far implemented with optical fibers in table-top experiments [6, 7] and are not suitable for on-chip integration. For these reasons, it is advantageous to shorten the lengths of these time bins and consequently the optical delays, which can be achieved by using ultra-short-pulse squeezed states (spanning over THz of bandwidths). This allows the definition of femtosecond-scale temporal bins, and one can entangle thousands of time bins with optical delays of few tens of centimeter-scale, which are amenable to on-chip integration.

Our demonstrated squeezing bandwidth of >25 THz and temporal confinement of few optical cycles is an important step towards realizing such large-scale cluster states in rapidly advancing LN nanophotonics. In MBQC with CV cluster states, quantum computation is typically performed with homodyne measurements and gate teleportation, which also requires homodyne measurements for feed-forward operations. Consequently, the electronic bandwidths of the homodyne detectors limit the clock rate of the quantum computation. Our high-gain OPAs can be used to perform all-optical loss-tolerant measurements and gate teleportation [50], thereby enabling ultrafast MBQC with CV cluster states.

References

[1] Thaddeus D Ladd et al. "Quantum computers". In: *Nature* 464.7285 (2010), pp. 45–53.

[2] Jeremy L O'brien, Akira Furusawa, and Jelena Vučković. "Photonic quantum technologies". In: *Nature Photonics* 3.12 (2009), pp. 687–695.

[3] Haocun Yu et al. "Quantum correlations between light and the kilogram-mass mirrors of LIGO". In: *Nature* 583.7814 (2020), pp. 43–47.

[4] Catxere A Casacio et al. "Quantum-enhanced nonlinear microscopy". In: *Nature* 594.7862 (2021), pp. 201–206.

[5] Akira Furusawa et al. "Unconditional quantum teleportation". In: *science* 282.5389 (1998), pp. 706–709.

[6] Warit Asavanant et al. "Generation of time-domain-multiplexed two-dimensional cluster state". In: *Science* 366.6463 (2019), pp. 373–376.

[7] Mikkel V Larsen et al. "Deterministic generation of a two-dimensional cluster state". In: *Science* 366.6463 (2019), pp. 369–372.

[8] Moran Chen, Nicolas C. Menicucci, and Olivier Pfister. "Experimental realization of multipartite entanglement of 60 modes of a quantum optical frequency comb". In: *Phys. Rev. Lett.* 112 (12 Mar. 2014), p. 120505. URL: http://link.aps.org/doi/10.1103/PhysRevLett.112.120505.

[9] Gregory S Kanter et al. "Squeezing in a LiNbO 3 integrated optical waveguide circuit". In: *Optics express* 10.3 (2002), pp. 177–182.

[10] Jonathan Roslund et al. "Wavelength-multiplexed quantum networks with ultrafast frequency combs". In: *Nature Photonics* 8.2 (2014), pp. 109–112.

[11] VD Vaidya et al. "Broadband quadrature-squeezed vacuum and nonclassical photon number correlations from a nanophotonic device". In: *Science advances* 6.39 (2020), eaba9186.

[12] Caterina Vigliar et al. "Error-protected qubits in a silicon photonic chip". In: *Nature Physics* 17.10 (2021), pp. 1137–1143.

[13] JM Arrazola et al. "Quantum circuits with many photons on a programmable nanophotonic chip". In: *Nature* 591.7848 (2021), pp. 54–60.

[14] Joel F Tasker et al. "Silicon photonics interfaced with integrated electronics for 9 GHz measurement of squeezed light". In: *Nature Photonics* 15.1 (2021), pp. 11–15.

[15] Usman A. Javid et al. "Ultrabroadband Entangled Photons on a Nanophotonic Chip". In: *Phys. Rev. Lett.* 127 (18 Oct. 2021), p. 183601. URL: https://link.aps.org/doi/10.1103/PhysRevLett.127.183601.

[16] Pao-Kang Chen et al. "Ultra-broadband quadrature squeezing with thin-film lithium niobate nanophotonics". In: *Optics Letters* 47.6 (2022), pp. 1506–1509.

[17] Daniel Peace et al. "Picosecond Pulsed Squeezing in Thin-Film Lithium Niobate Strip-Loaded Waveguides at Telecommunication Wavelengths". In: *arXiv preprint arXiv:2204.05694* (2022).

[18] Carlton M Caves. “Quantum limits on noise in linear amplifiers”. In: *Physical Review D* 26.8 (1982), p. 1817.

[19] Yaakov Shaked et al. “Lifting the bandwidth limit of optical homodyne measurement with broadband parametric amplification”. In: *Nature communications* 9.1 (2018), pp. 1–12.

[20] Naoto Takanashi et al. “All-optical phase-sensitive detection for ultra-fast quantum computation”. In: *Optics Express* 28.23 (2020), pp. 34916–34926.

[21] Gaetano Frascella et al. “Overcoming detection loss and noise in squeezing-based optical sensing”. In: *npj Quantum Information* 7.1 (2021), pp. 1–6.

[22] Zhichao Ye et al. “Overcoming the quantum limit of optical amplification in monolithic waveguides”. In: *Science advances* 7.38 (2021), eabi8150.

[23] Di Zhu et al. “Integrated photonics on thin-film lithium niobate”. In: *Advances in Optics and Photonics* 13.2 (2021), pp. 242–352.

[24] Luis Ledezma et al. “Intense optical parametric amplification in dispersion-engineered nanophotonic lithium niobate waveguides”. In: *Optica* 9.3 (2022), pp. 303–308.

[25] Marc Jankowski et al. “Ultrabroadband nonlinear optics in nanophotonic periodically poled lithium niobate waveguides”. In: *Optica* 7.1 (Jan. 2020), pp. 40–46. URL: http://www.osapublishing.org/optica/abstract.cfm?URI=optica-7-1-40.

[26] Yaowen Hu et al. “On-chip electro-optic frequency shifters and beam splitters”. In: *Nature* 599.7886 (2021), pp. 587–593.

[27] M. J. Werner et al. “Ultrashort pulsed squeezing by optical parametric amplification”. In: *Phys. Rev. A* 52 (5 Nov. 1995), pp. 4202–4213. URL: https://link.aps.org/doi/10.1103/PhysRevA.52.4202.

[28] J Eli Bourassa et al. “Blueprint for a scalable photonic fault-tolerant quantum computer”. In: *Quantum* 5 (2021), p. 392.

[29] DB Horoshko and MI Kolobov. “Towards single-cycle squeezing in chirped quasi-phase-matched optical parametric down-conversion”. In: *Physical Review A* 88.3 (2013), p. 033806.

[30] Matthias Kizmann et al. “Subcycle squeezing of light from a time flow perspective”. In: *Nature Physics* 15.9 (2019), pp. 960–966.

[31] Rajveer Nehra. *Few-cycle vacuum squeezing in Nanophotonics*. June 2022. URL: https://figshare.com/articles/journal_contribution/Few-cycle_vacuum_squeezing_in_nanophotonics/20100140/1.

[32] Marc Jankowski et al. “Temporal Simultons in Optical Parametric Oscillators”. In: *Phys. Rev. Lett.* 120 (5 Feb. 2018), p. 053904. URL: https://link.aps.org/doi/10.1103/PhysRevLett.120.053904.

[33] Alireza Marandi et al. “Coherence properties of a broadband femtosecond mid-IR optical parametric oscillator operating at degeneracy”. In: *Opt. Express* 20 (2012), pp. 7255–7262.

[34] Marcelo Alejandro Luda et al. “Compact embedded device for lock-in measurements and experiment active control”. In: *Review of Scientific Instruments* 90 (2019), p. 023106.

[35] Xiang Guo, Chang-Ling Zou, and Hong X Tang. “70 dB long-pass filter on a nanophotonic chip”. In: *Optics express* 24.18 (2016), pp. 21167–21176.

[36] Xiang Guo et al. “Parametric down-conversion photon-pair source on a nanophotonic chip”. In: *Light: Science & Applications* 6.5 (2017), e16249–e16249.

[37] Wojciech Wasilewski et al. “Pulsed squeezed light: Simultaneous squeezing of multiple modes”. In: *Phys. Rev. A* 73 (6 June 2006), p. 063819. URL: https://link.aps.org/doi/10.1103/PhysRevA.73.063819.

[38] Carlton M. Caves and Bonny L. Schumaker. “New formalism for two-photon quantum optics. I. Quadrature phases and squeezed states”. In: *Phys. Rev. A* 31 (5 May 1985), pp. 3068–3092. URL: https://link.aps.org/doi/10.1103/PhysRevA.31.3068.

[39] Andreas Christ et al. “Probing multimode squeezing with correlation functions”. In: *New Journal of Physics* 13.3 (2011), p. 033027.

[40] Peter Van Loock and Akira Furusawa. “Detecting genuine multipartite continuous-variable entanglement”. In: *Physical Review A* 67.5 (2003), p. 052315.

[41] Leon Bello et al. “Broadband complex two-mode quadratures for quantum optics”. In: *Optics Express* 29.25 (2021), pp. 41282–41302.

[42] Gordon H.Y. Li et al. In: *Nanophotonics* 12.5 (2023), pp. 847–855. URL: https://doi.org/10.1515/nanoph-2022-0137.

[43] Asuka Inoue et al. “Towards a multi-core ultra-fast optical quantum processor: 43-GHz bandwidth real-time amplitude measurement of 5-dB squeezed light using modularized optical parametric amplifier with 5G technology”. In: *arXiv preprint arXiv:2205.14061* (2022).

[44] Qiushi Guo et al. “Femtojoule femtosecond all-optical switching in lithium niobate nanophotonics”. In: *Nature Photonics* 16.9 (Sept. 2022), pp. 625–631. URL: https://doi.org/10.1038/s41566-022-01044-5.

[45] Avik Dutt et al. “On-chip optical squeezing”. In: *Physical Review Applied* 3.4 (2015), p. 044005.

[46] Yun Zhao et al. “Near-Degenerate Quadrature-Squeezed Vacuum Generation on a Silicon-Nitride Chip”. In: *Phys. Rev. Lett.* 124 (19 May 2020), p. 193601. URL: https://link.aps.org/doi/10.1103/PhysRevLett.124.193601.

[47] Y Zhang et al. “Squeezed light from a nanophotonic molecule”. In: *Nature communications* 12.1 (2021), pp. 1–6.

[48] Robert Cernansky and Alberto Politi. “Nanophotonic source of quadrature squeezing via self-phase modulation”. In: *APL Photonics* 5.10 (2020), p. 101303.

[49] Zijiao Yang et al. “A squeezed quantum microcomb on a chip”. In: *Nature Communications* 12.1 (2021), pp. 1–8.

[50] Timothy C Ralph. “All-optical quantum teleportation”. In: *Optics letters* 24.5 (1999), pp. 348–350.

Chapter 6

MULTI-OCTAVE FREQUENCY COMB FROM AN ULTRA-LOW-THRESHOLD NANOPHOTONIC PARAMETRIC OSCILLATOR

Ryoto Sekine[†], Robert M. Gray[†], Luis Ledezma, Selina Zhou, Qiushi Guo, and Alireza Marandi. "Multi-Octave Frequency Comb from an Ultra-Low-Threshold Nanophotonic Parametric Oscillator," *arXiv:2309.04545*, (2023).
R.S. conceived the project, designed and fabricated the device, performed part of the optical characterization, and lead the writing of the manuscript.
[†] denotes equal contributions

6.1 Abstract

Ultrabroadband frequency combs coherently unite distant portions of the electromagnetic spectrum. They underpin discoveries in ultrafast science and serve as the building blocks of modern photonic technologies. Despite tremendous progress in integrated sources of frequency combs, achieving multi-octave operation on chip has remained elusive mainly because of the energy demand of typical spectral broadening processes. Here we break this barrier and demonstrate multi-octave frequency comb generation using an optical parametric oscillator (OPO) in nanophotonic lithium niobate with only femtojoules of pump energy. The energy-efficient and robust coherent spectral broadening occurs far above the oscillation threshold of the OPO and detuned from its linear synchrony with the pump. We show that the OPO can undergo a temporal self-cleaning mechanism by transitioning from an incoherent operation regime, which is typical for operation far above threshold, to an ultrabroad coherent regime, corresponding to the nonlinear phase compensating the OPO cavity detuning. Such a temporal self-cleaning mechanism and the subsequent multi-octave coherent spectrum has not been explored in previous OPO designs and features a relaxed requirement for the quality factor and relatively narrow spectral coverage of the cavity. We achieve orders of magnitude reduction in the energy requirement compared to the other techniques, confirm the coherence of the comb, and present a path towards more efficient and wider spectral broadening. Our results pave the way for ultrashort-pulse and ultrabroadband on-chip nonlinear photonic systems for numerous applications.

6.2 Introduction

Broadband optical frequency combs are among the great achievements of modern optics [1, 2]. Recently, increasing efforts are focused on the realization of broadband frequency combs in nanophotonic platforms [3, 4, 5] with applications including dual-comb spectroscopy [6], optical communications [7], optical frequency synthesis [8, 9], and laser ranging [10]. However, the spectral coverage of

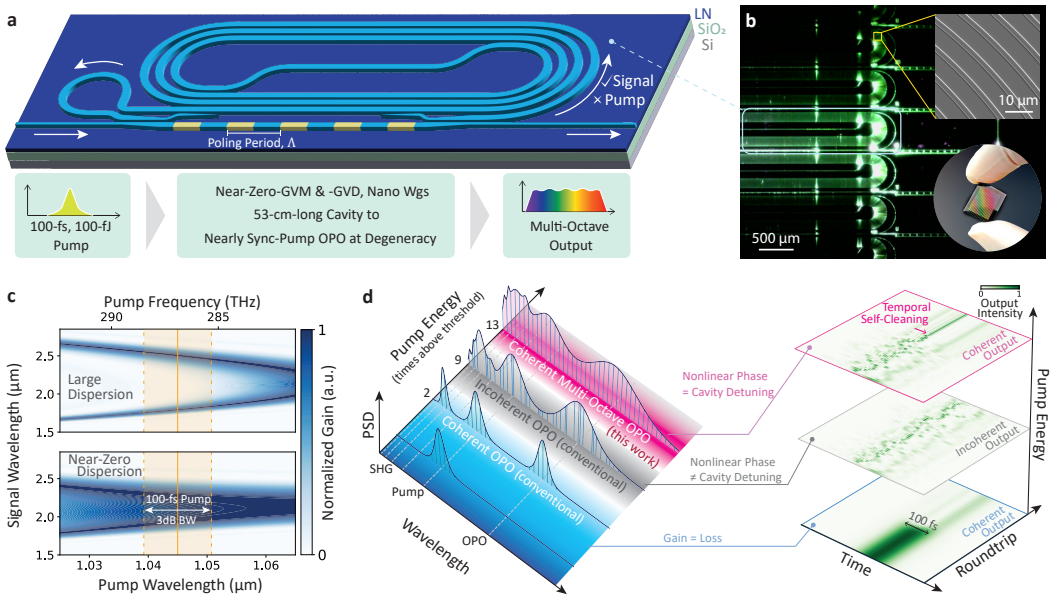

Figure 6.1: **Principle and design of the multi-octave nanophotonic OPO**. **a,** Illustration of the sync-pumped OPO on thin-film lithium niobate with key features highlighted. **b,** Microscope image of several devices when the one in the center is pumped at 1 μm. The chip glows green due to second harmonic generation (SHG). The top inset is a scanning electron microscope image of the spiral region and the bottom is a picture of the entire chip containing 16 OPOs. **c,** Illustration showcasing how short pump pulses can take advantage of near-zero-dispersion-engineered OPAs. The simulated gain profiles are shown in the top for a waveguide with 60 fs^2/mm half-harmonic GVD and 26 fs/mm GVM and in the bottom for a near-zero-dispersion waveguide. The solid orange line marks the center wavelength of the pump and the orange shaded regions mark the 3-dB bandwidth (BW) of the 100-fs source. **d,** Depiction of the different regimes of operation of the OPO as a function of pump pulse energy, along with the roundtrip-to-roundtrip temporal output of the OPO in each regime.

integrated frequency comb sources remains far behind their table-top counterparts using high-pulse-energy lasers and discrete components, which have recently surpassed six-octave spectra [11, 12]. Such multi-octave frequency combs are valuable for applications such as ultrashort pulse synthesis[13], attosecond science[14], and bio-chemical sensing and imaging [15, 16, 17].

Integrated sources of short-pulse frequency combs typically generate picojoules or femtojoules of pulse energies [2, 4, 18, 19, 20] and their spectral coverage barely reaches an octave [21, 22]. This has necessitated further spectral broadening stages for many applications, which so far have been realized strictly using table-top systems with discrete amplifiers and components [1, 23, 8]. A femtojoule-level multi-octave coherent spectral broadening mechanism has so far been beyond the reach of current photonic technologies, and hence, a path towards a fully integrated

multi-octave frequency comb has remained elusive.

Substantial spectral broadening is typically achieved by passing femtosecond or picosecond pulses with 0.1-10 nJ of energy through waveguides, crystals or fibers with quadratic ($\chi^{(2)}$) or Kerr ($\chi^{(3)}$) nonlinearity with various designs [24, 1, 25, 26, 27, 28]. Among these schemes, waveguides with quadratic nonlinearity are becoming increasingly more efficient, especially because of the recent progress on quasi-phase matching and dispersion engineering [29, 24, 26] and show superior performances over their cubic counterparts. However, to reach an octave of coherent spectrum and beyond they still need 10's of picojoules of energy[29], which is far beyond the current capability of integrated frequency comb sources.

Resonant enhancement of spectral broadening is expected to improve the energy requirements. However, such experiments have so far remained below an octave [30, 31, 23]. This is mainly because of the overly constrained dispersion requirements of cubic coherent spectral broadening schemes especially when combined with high-Q requirements. In fact, even linear components in nanophotonics with multi-octave spectral response are still challenging to design and realize [32]. In contrast, quadratic nonlinearity not only leads to lower energy requirements in single-pass configurations, but it also offers a wider range of nonlinear processes for ultrawide coherent spectral broadening resulting from nonlinear interactions of distant portions of the spectrum[11, 12]. However, a proper resonator design is necessary to enable an operation regime where a sequence of quadratic nonlinear processes can yield coherent spectral broadening towards multi-octave operation.

A promising path towards such a multi-octave nonlinear resonator is based on synchronously (sync-) pumped degenerate OPOs, which so far have been successfully used in bulk optics for efficient phase-locked down-conversion via half-harmonic generation of broadband frequency combs [15, 33, 34, 35]. Recent studies indicate the potential of sync-pumped OPOs for extreme pulse shortening and spectral broadening while preserving the coherence properties of the pump [36]. However, lack of dispersion engineering in bulk nonlinear crystals, low parametric gain bandwidths, and multi-picojoule thresholds have put limitations on their applicability for compact and ultrabroadband frequency comb applications. Recent developments of dispersion-engineered optical parametric amplifiers (OPAs) [37] and narrowband sync-pumped OPOs [38] in lithium niobate nanophotonics promise a path towards overcoming these limitations and accessing a new regime of ultrabroadband ultra-low-energy nonlinear optics that has not been accessible before.

In this work, in sharp contrast to previous realizations of nonlinear photonic resonators, we judiciously design and realize an on-chip sync-pumped OPO featuring a low-finesse resonator which couples only frequencies near the half-harmonic of the pump while leaving the pump and its high-harmonics non-resonant. It is near-zero dispersion engineered for the pump and its half-harmonic. The nanophotonic sync-pumped OPO operates with a record-low threshold of ~18 fJ. Due to its low-energy, intense, phase-sensitive amplification, we discovered an operation regime of the OPO where the nonlinear phase compensates the cavity detuning, yielding temporal self cleaning and a multi-octave coherent spectrum. We measured a 2.6

octave frequency comb at ~121 fJ of pump energy and experimentally confirmed its coherence. We numerically replicate the broadband nonlinear dynamics associated with such a multi-octave broadening and provide design guidelines for even broader outputs.

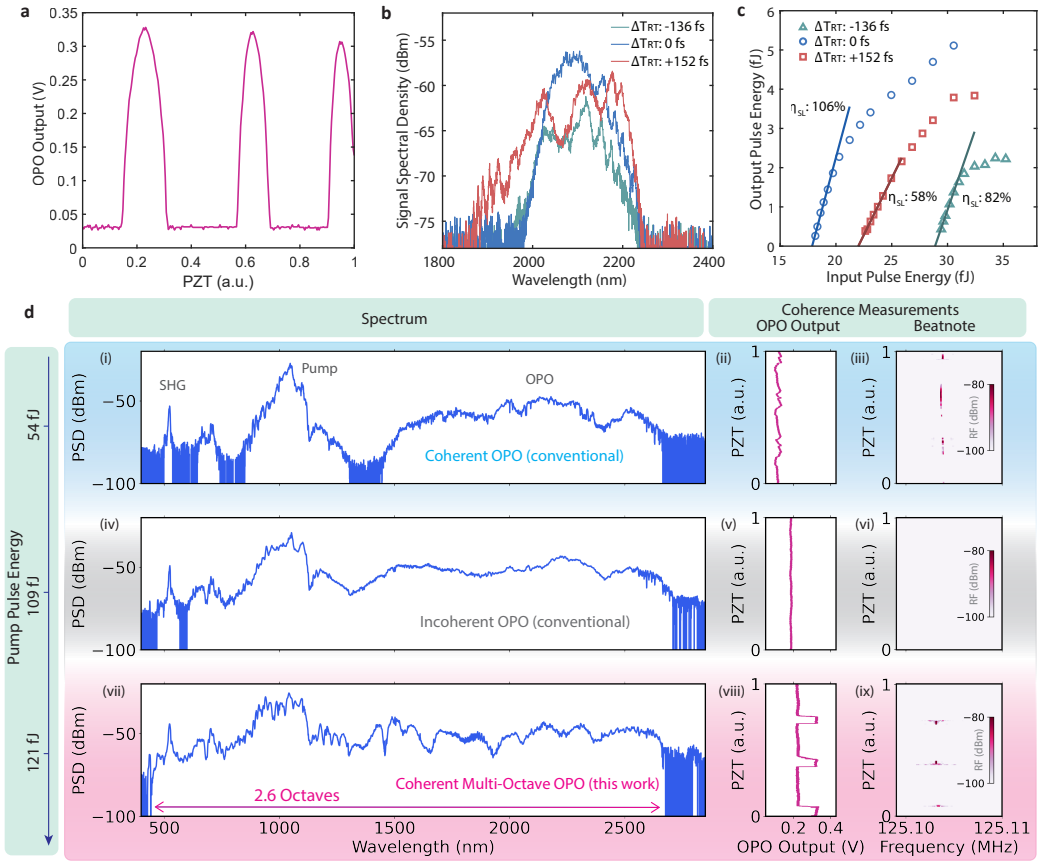

Figure 6.2: **OPO characterization. a,** Oscillation peaks of the OPO near-threshold as the pump repetition rate is modulated by a piezoelectric transducer (PZT) in the pump laser cavity at 600 Hz. **b,** Signal spectrum at 35 fJ of pump energy for three different roundtrip detunings and **c,** the corresponding OPO signal growth as a function of pump energy for different oscillation peaks and their slope efficiencies, η_{SL}. **d**, Output spectra, OPO oscillation peaks, and beatnote measurements from the OPO cavity at 54 fJ, 109 fJ, and 121 fJ of pump. The OPO oscillation peaks (ii), (v), (viii) were taken under the same detector amplification settings. The RF beatnotes (iii), (vi), (ix) were taken between a free space and on-chip OPO that share the same pump, the rep rate of which is tuned over time.

6.3 Operating Principle and Design

Figure 6.1a illustrates the design of the on-chip sync-pumped OPO, with the fabricated device shown in Fig. 6.1b. The input/output couplers are designed to allow resonance only around the half-harmonic of the pump (see supplementary

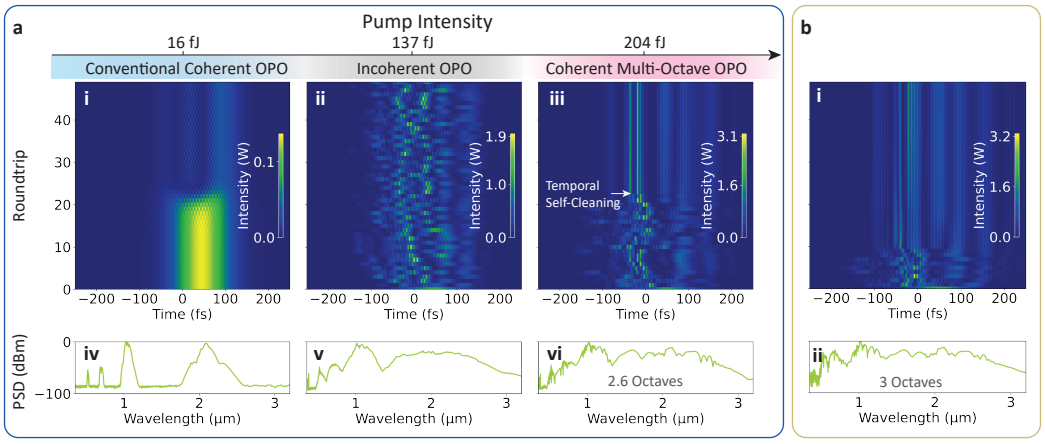

Figure 6.3: **Simulation results showing different operation regimes of the nanophotonic OPO**. **a**, Transition from (i) near-threshold coherent operation to (ii) incoherent operation and (iii) back to coherent operation when the pump energy is increased. The roundtrip temporal evolution (i-iii) and output spectra (iv-vi) are shown for three different pump intensities using experimental parameters and at a cavity detuning of -10.5 fs. **b**, A three-octave coherent OPO. The same experimental parameters are used except that the last one mm of the PPLN was replaced with a chirped poling period. The pump pulse energy was at 250 fJ.

section 6.7.1), and the cavity is designed to be minimally dispersive for these wavelengths. To phase and frequency lock the OPO, the OPO is nearly sync-pumped at degeneracy, requiring a cavity round-trip time of 4 ns for a pump comb with a 250 MHz repetition rate. With the effective index of our nanophotonic lithium niobate waveguides (wgs), this amounts to a 53-cm-long-cavity.

To achieve the ultra-high, ultra-broad, phase-sensitive gain at fJ pump pulse energies that enables coherent broadband comb generation, the OPO includes a 10.8 mm OPA with proper dispersion engineering and quasi phase matching (QPM). Specifically, we target minimizing the group velocity dispersion (GVD) of the pump and signal, as well as the group velocity mismatch (GVM) between the pump and signal [37]. Figure 6.1d illustrates the large gain bandwidth that can be accessed when coupling a 100-fs pump to a near-zero dispersion engineered waveguide, as opposed to one with large dispersion that is favored for broadly tunable OPOs[39, 38]. The designs for the poling period, cavity length, and couplers for sync-pumped operation can be found in the Supplementary, Section 6.7.1.

Figure 6.1d illustrates the different regimes of operation of this nanophotonic OPO. At low pump pulse energies, the OPO goes above threshold when the gain overcomes the loss inside the cavity. This is conventionally the regime where OPOs are operated to yield coherent outputs phase-locked to the pump[34]. At higher pump pulse energies a degenerate OPO is known to transition to an unstable operation regime where the phase-locked operation diminishes[40, 41]. Here however, we find that far above threshold, the OPO can undergo a transition to the phase-locked

regime as a result of the nonlinear phase being compensated by the cavity. This is emphasized in the accompanying time domain plots as a temporal self-cleaning mechanism, where after a finite number of roundtrips the output pulse intensity is seen to stabilize with ultrashort features in the multi-octave case. This emergence of coherence and ultra-short pulse formation is reminiscent of condensation and thermalization occurring in other nonlinear multimode systems[42, 43].

6.4 Experimental Results

In Fig. 6.2a-c, we show the near-threshold performance of the nanophotonic OPO. Scanning the repetition rate of the pump by 600 Hz, we observe the oscillation peaks of the OPO as depicted in Fig. 6.2a. These peaks are characteristic of doubly-resonant operation[34]. We can actively lock the pump repetition rate to the center of each of these peaks, and the near-threshold signal spectra of three such peaks at distinct detunigs between the pump repetition period and cavity round-trip time, ΔT_{RT}, are shown in Fig. 6.2b. In Fig. 6.2c we show the measured input-output pulse energy growth of these same peaks. We can extrapolate the threshold and slope efficiencies, η_{SL}, and define the peak with the lowest threshold as the zero cavity detuned state. For this peak we estimate an OPO threshold of ~18 fJ.

In Fig. 6.2d, we show three characteristic output spectra of the OPO. At 54 fJ of pump we observe conventional OPO behavior. The pump, half-harmonic and second-harmonic are all spectrally broadened, and there is noticeable sum frequency generation (SFG) between the pump and half harmonic. At 109 fJ of pump, we observe continuous spectra from 600 nm to 2710 nm, and at 121 fJ we observe continuous spectra from 443 nm to 2676 nm. The dip at 2.8 μm is associated with the OH absorption peak in the LN and/or the buffer layer[39, 44], and kinks near 680 nm and 1135 nm are due to mode crossings (see Supplementary Section 6.7.2). It is also worth noting that the spectra at 121 fJ has some distinctive signatures on the long wavelength side of the spectrum that are absent in the 109 fJ pumped cases.

To characterize the coherence of the OPO at these pump pulse energies, we interfere the chip output with that of a free-space OPO pumped by the same laser using a filter centered around 2.1 μm. When operated in a coherent regime, a degenerate OPO above threshold can have two possible CEO frequencies which differ by half of the pump repetition rate, $f_{\text{rep}}/2$, depending on the oscillation peak[34]. When the on-chip OPO has a different CEO from the free-space OPO, upon spatially and temporally overlapping their outputs, beatnotes at $f_{\text{rep}}/2$ should be observed. For the coherence measurements in Fig. 6.2d, we scan the rep rate of the pump over time. At 54 fJ of pump, Fig. 6.2d(ii) shows that the on-chip OPO exhibits features at certain detunings, which are reflected by the $f_{\text{rep}}/2$ beatnotes between the OPOs in Fig. 6.2d(iii). The lack of these signatures both in the OPO power and beatnotes at 109 fJ of pump, indicate that the on-chip OPO has transitioned from a coherent to incoherent regime. At 121 fJ however, the OPO peak structures and RF beatnote reappear, signifying the reemergence of a coherent operating regime.

The coherence of the second-harmonic portions of these spectra were confirmed

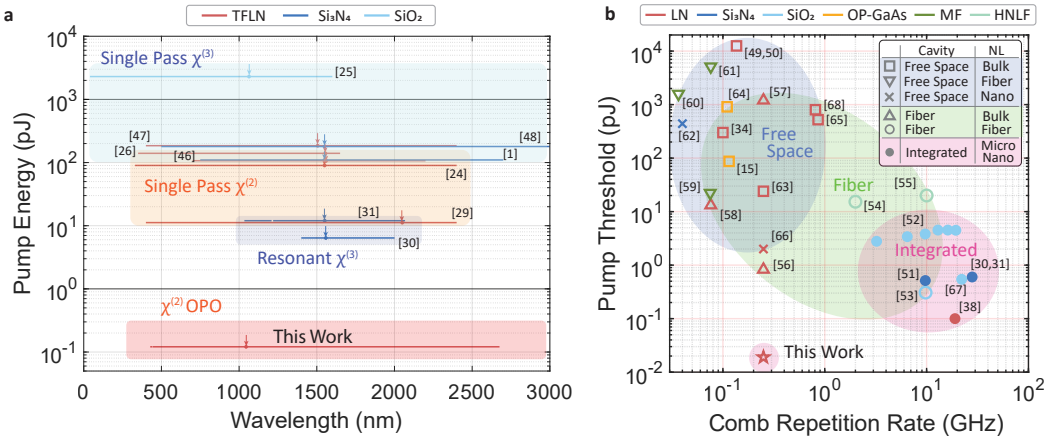

Figure 6.4: **Performance comparison of (a), integrated spectral broadening, and (b), frequency comb sync-pumped OPOs**. **a**, Wavelength coverage and pump pulse energies of integrated frequency comb spectral broadening schemes. The arrows indicate the pump wavelength. **b**, Comb repetition rates and pump threshold energies of sync-pumped OPOs. The marker shapes denote the different cavity and nonlinear (NL) element compositions for each OPO, the categories being free space, fiber, integrated and bulk, fiber, nanophotonic respectively. In both figures, the top legend denotes the material of the nonlinear element. Abbreviations, TFLN: thin-film lithium niobate, OP: orientation patterned, MF: microstructured fiber, HNLF: highly nonlinear fiber.

using a spectrally broadened output of the pump by a photonic crystal fiber. We interfere this broadened pump with the second-harmonic portion of the on-chip OPO and observe beatnotes of the resultant carrier-envelope offset frequency, f_{CEO}, along with the pump repetition rate at 250 MHz for all of the pump pulse energies in Fig. 6.2d, irrespective of the detuning (see Supplementary Section 6.7.2E for details). In particular, at 121 fJ of pump, because both the half-harmonic and second harmonic combs are coherent with respect to the pump and all frequency portions of our spectrum are generated through parametric processes of these three combs[29], we conclude that the continuous 2.6 octave spectrum in Fig. 6.2d is coherent. We could even lock the rep rate of the pump to keep the OPO oscillating in this state, and in Supplementary Section 6.7.2E we show the beatnote signal being maintained over time.

To explain the dynamics of this OPO far above threshold and how coherence can be established over such a broad spectrum, we turn to numerical simulations. To capture the multi-octave nonlinear interactions occurring in the OPO, we modeled the electric field in the nanophotonic cavity as a single envelope in frequency domain which is evolved using the split-step Fourier method for propagation in the PPLN region and a linear filter for the cavity feedback (see Supplementary Section 6.7.3A for details). In Fig. 6.3a, we show how this captures distinct regimes of operation when using parameters matching that of the experiment. At 16 fJ the OPO goes above threshold and stabilizes after ~20 roundtrips. At this point, all the frequency

translated components (OPO, SHG, SFG of the pump and OPO) are coherent with respect to the pump and they remain unchanged from roundtrip to roundtrip. As the pump pulse energy is increased, fewer roundtrips are required for the OPO to form, and at 137 fJ of pump (~9× above threshold) we see that the OPO output is incoherent.

At roughly 204 fJ of pump (~13× above threshold), however, the the half-harmonic is seen to acquire a π phase shift through the nonlinear interaction with the pump in each single-pass through the PPLN region. This can be compensated by detuning the cavity by an odd number of OPO peaks, or by adding a constant phase offset of π between the pump and cavity, corresponding to the carrier-envelope offset phase, ϕ_{CEO}, of the pump (see Supplementary Section 6.7.3B). The former case is shown in Fig. 6.3a(iii) and shows a two octave coherent continuous comb that stabilizes after roughly twenty roundtrips with temporal features as short as 4 fs (see Supplementary Section 6.7.3C). The output spectrum is also very similar to the detuned 121 fJ experimental result of Fig. 6.2d.

In simulation, we further investigate how to extend the coherent operation of the OPO to even broader spectra. By replacing the last one mm of the PPLN region with a chirped poling period for efficient second harmonic and sum-frequency generation, we achieve a coherent three-octave continuous frequency comb with ~250 fJ of pump energy as shown in Fig. 6.3b.

6.5 Conclusion and Discussion

In Fig. 6.4 we compare our results with other integrated spectral broadening schemes and sync-pumped OPOs. The figure highlights how our nanophotonic OPO design and its operation regime enable orders-of-magnitude improvement in the energy efficiency of coherent spectral broadening. Our work represents the lowest threshold sync-pumped OPO which is enabled by its near-zero-dispersion design. This ultralow-threshold operation enabled accessing a previously unexplored operation regime of the OPO far above threshold, where ultrabroad coherent spectral broadening is established as a consequence of the balance between cavity detuning and nonlinear phase shift.

In summary, we have experimentally demonstrated a nearly sync-pumped nanophotonic OPO operating in the near zero-GVM, zero-GVD, fs-pumped, high-gain low-finesse regime resulting in an ultra-broadband coherent output with only ~121 fJ of energy. The 2.6 octave frequency comb enables unprecedented opportunities for on-chip applications including wavelength division multiplexing[7], dual-comb spectroscopy[45], and frequency synthesis[5]. We show the OPO transitions from an incoherent to coherent operation regime and demonstrate a path towards much broader frequency comb sources in the femtojoule regime.

6.6 Methods

Device fabrication. Our device was fabricated on 700-nm-thick X-cut MgO-doped thin-film lithium nioabte on a SiO_2/Si substrate (NANOLN). Following the procedure in [37], we pattern Cr/Au poling electrodes with 16 fixed poling periods ranging

from 4.955-5.18 μm using lift-off and and apply a voltage to periodically flip the ferroelectric domains. Upon poling we remove the electrodes and subsequently etch the waveguides using Ar-milling and Hyrdogen Silsesquioxane (HSQ) as the etch mask. Finally, the waveguide facets are mechanically polished to allow for butt coupling. Each OPO has a footprint of 0.5 mm $\times$ 13 mm.

Optical measurements. The measurements were performed using a Menlo Orange HP10 Yb mode-locked laser (MLL) centered at 1045 nm. It outputs 100-fs-long pulses at 250 MHz with a $\pm$1 MHz tuning range. Light was coupled to and from the chip using Newport 50102-02 reflective objectives, chosen for their minimal chromatic aberration. All of the results in this paper were performed on a device with 5.075 μm poling period at 26°C, regulated by a thermoelectric cooler (TEC). The lowest OPO threshold was obtained from a pump repetition rate of 250.1775 MHz, which we define as the zero detuned state. This device has a total throughput loss of 43.4 dB, and following the methodology in [37], we measured the input and output coupling losses to be 35.7 dB and 7.7 dB respectively. For the results in Fig. 6.3d, the spectra were collected by two different optical spectrum analyzers (OSA), specifically a Yokogawa AQ6374 (350-1750nm) and AQ6376 (1500-3400 nm). The OSAs were operated with High3 sensitivity except for the case of 121 fJ of pump, where High2 was used. The RF spectra in Fig. 6.2d were collected by an electronic spectrum analyzer (Rhode & Schwarz FSW) using an InGaAs high speed photodiode (DSC2-40S). The SHG beatnotes were taken using a high-speed silicon avalanche photodiode (Menlo Systems APD210).

Numerical simulations. We used commercial software (Lumerical Inc.) to solve for the waveguide modes shown in Sections 6.7.1 and 6.7.2 of the Supplementary that allowed us to dispersion engineer and quasi-phase-match our device. For the nonlinear optical simulation, we solved an analytical nonlinear envelope equation as described in Section 6.7.3 of the Supplementary. The simulations were performed with no constant phase offset between the pump and cavity unless specifically mentioned otherwise. This parameter effectively acts as a carrier-envelope offset phase of the pump, ϕ_{CEO}. As the simulations were performed with a time window of 1.7 ps, it should be mentioned that a large portion of the short wavelength side of the spectrum walked out of the time window of our simulation. For example, the simulated GVM between our simulation reference frame at the half-harmonic signal wavelength of 2090 nm and the second harmonic of the pump at 522 nm is 721 fs/mm. As a result, the up-converted portions of the spectrum in simulation tend to be smaller than what was measured experimentally. In these simulations we have only incorporated the effects of $\chi^{(2)}$ nonlinearity and have not considered the effects of $\chi^{(3)}$. Especially given the low pulse energies and low-finesse nature of our cavity, we believe this to be a good approximation, yet it could be one additional reason for small discrepancies between experiment and simulation.

6.7 Supplementary Information

6.7.1 Chip Design

A. OPO Design

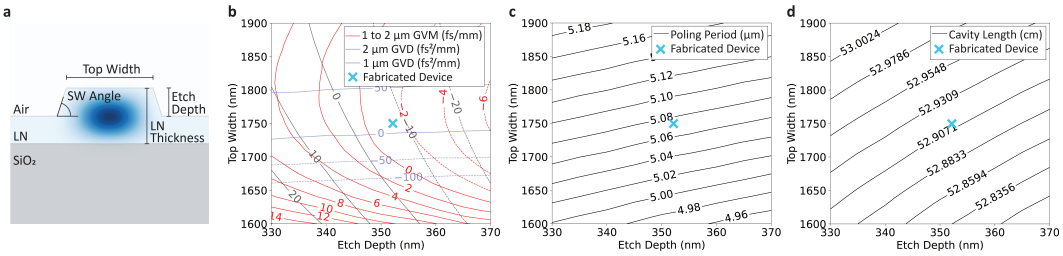

Figure 6.5: **Key OPO design parameters as a function of waveguide geometry. a,** Parameters for tuning spatiotemporal confinement of pulses propagating through our nanophotonic waveguides. An example fundamental TE mode at 1 μm is shown in the core of the waveguide. **b,** Dispersion profile **c,** Phase-matched poling period, and **d,** Optimal sync-pumping cavity length as a function of waveguide top width and etch depth variations. The actual measured dimensions of our fabricated device are indicated by the cross.

The spatiotemporal profile of pulses propagating through our nanophotonic waveguides can be sculpted by a few key fabrication parameters. Labeled in Fig. 6.5a, these are the lithium niobate (LN) thickness, etch depth, top width, and sidewall angle. All of these parameters directly affect the effective index of the waveguide which, in turn, determines the near-zero dispersion geometry, quasi-phase-matching poling period, and required cavity length for synchronous pumping of our OPO, as shown in Figs. 6.5b-d. We fabricated our device with a constant poling period of 5.075 μm and a cavity length of 52.92 cm, and we measured a waveguide etch depth and top width of 352 nm and 1753 nm respectively. These dimensions are marked by crosses in Fig. 6.5b-d and show that we successfully engineered our device to be close to optimal parameters for phase-matched operation with near-zero GVM and GVD. The resulting simulated effective index, n_{eff}, and fabricated poling period are shown in Fig. 6.6, along with the simulated bending loss as a function of bend radius and wavelength. The dotted blue line in Fig. 6.6c at 77 μm indicates the minimum bend radius used in fabricating the spiral, showing small bending loss for wavelengths shorter than 3.3 μm at all points in the spiral.

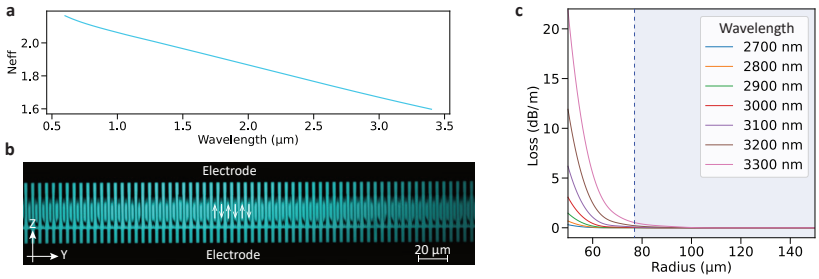

Figure 6.6: **Additional OPO parameters given the waveguide geometry shown in Fig. 6.5. a,** Effective index of the waveguide **b,** Second harmonic microscope image of the periodic poling pre-waveguide patterning, and **c,** Simulated propagation loss as a function of bend radius for different signal wavelengths. The dotted blue line is at 77 μm, the minimum bend radius employed when designing the OPO cavity.

B. Input/Output Coupler Design

The input and output couplers of the OPO, as defined in Fig. 6.7a, are symmetrically identical and take the adiabatic shape depicted in Fig. 6.7b, where the parameters for w_1, w_2, gap, and L are 1753 nm, 1900 nm, 980 nm, and 750 μm respectively. Adiabatic couplers were chosen for their broadband response and comparative fabrication insensitivity compared to other coupler geometries. The fundamental TE mode profiles at 1 μm and 2 μm for the waveguide design with top width w_2 are shown in Fig. 6.7c. Pulses propagating through this adiabatic coupler follow the coupled mode equations,

$$\begin{cases} \dfrac{da_1}{dz} = -j\kappa e^{j\Delta\beta z} a_2(z) \\ \dfrac{da_2}{dz} = -j\kappa e^{-j\Delta\beta z} a_1(z) \end{cases} \tag{6.1}$$

where a_1 and a_2 are the amplitudes of the modes in each waveguide, κ is the coupling coefficient between the waveguides, and $\Delta\beta = |\beta_1 - \beta_2|$ is the phase mismatch between the two waveguides. Solving eq. (6.1) for our geometry, we obtain the power coupling curve in Fig. 6.7d. We see that only signal wavelengths above 2 μm experience significant coupling. In Fig. 6.7e we compare the spectral output of our OPO (device with coupler and cavity) against that from an adjacent straight waveguide without any couplers but sharing the same poling and waveguide parameters. We find that the simulated dips and peaks in the adiabatic coupler are reflected in the measured spectra from the nanophotonic OPO but are absent from the periodically poled straight waveguide, matching our theoretically predicted coupler response.

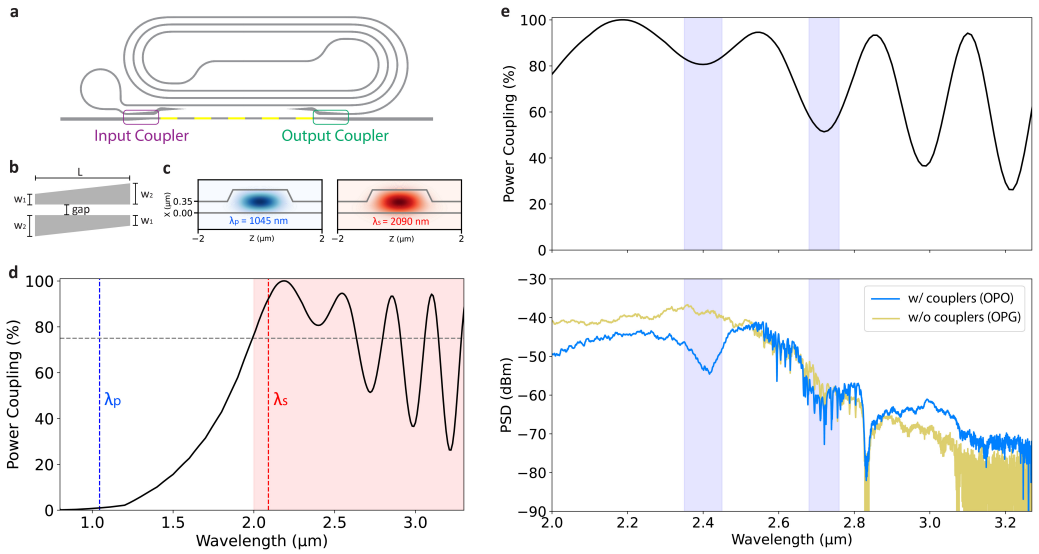

Figure 6.7: **OPO coupler design. a,** Definition of the input/output coupler and **b,** an illustration of the output coupler adiabatic design. Here, the widths and gaps refer to those at the top of the waveguide. **c,** The waveguide fundamental TE modes at 1 μm and 2 μm. **d,** The simulated coupler response using the fabricated waveguide geometry. **e,** Comparing the theoretical coupler behavior to measured spectra at 380 fJ of pump for otherwise identical devices with and without couplers.

6.7.2 Chip Characterization

A. Experimental Setup

Our experimental setup is shown in Fig. 6.8. The detector in the PID loop allows the repetition rate of the pump comb to be locked to disparate oscillation peaks of the OPO while the spectra is being collected on an optical spectrum analyzer (OSA). The synergistic features of the pump and OPO that enable multi-octave frequency comb generation are emphasized in the figure.

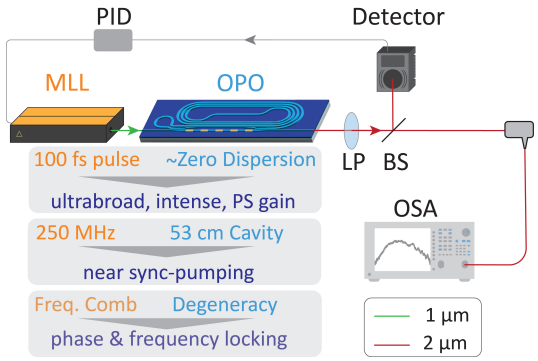

Figure 6.8: **Experimental Setup**. Abbreviations, PS: phase sensitive, MLL: mode locked laser, LP: long pass, BS: beam splitter.

B. Extended Experimental Data to Three Octave Spectra

Using the experimental setup shown in Fig. 6.8, we investigated the output spectra of the OPO at different pump pulse energies, a subset of which was shown in Fig. 6.2d of the main text. In Fig. 6.9a, we show the extension to even higher pump pulse energies. At 380 fJ of pump, we observe three-octave-spanning spectra from 362 nm to 3261 nm. The beatnote analysis with a free space OPO shown in Fig. 6.9b however, following the procedure in Supplementary Section 6.7.2E1, indicates that the OPO here is incoherent.

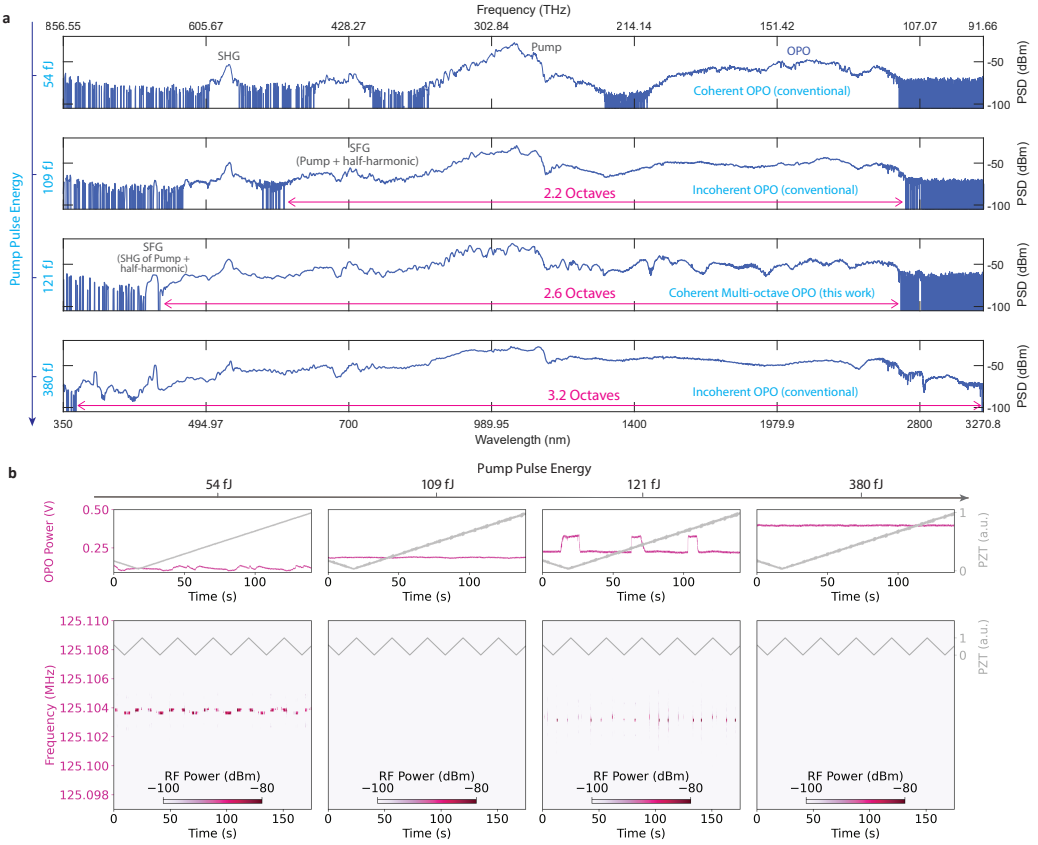

Figure 6.9: **Extended Measurements to** $\sim 20\times$ **above threshold**. **a** Output spectra from the OPO cavity up to 380 fJ of pump pulse energy. **b** For the same energies, the top panels show the OPO oscillation peaks as the pump rep rate is scanned by a PZT. The bottom panels show the RF beatnote between a free space and on-chip OPO that share the same pump, the rep rate of which is tuned over time at 63.58 mHz.

C. Molecular Absorption Features

For the measured spectra above 2.5 μm in Fig. 6.9a, we observe features that appear to be from spectral absorption lines coming from ambient molecules.

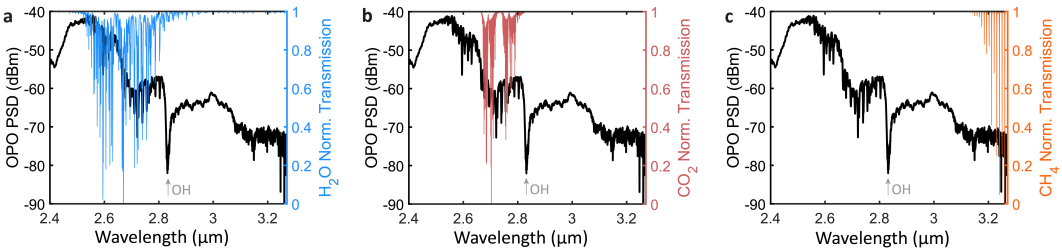

Figure 6.10: **Absorption features of atmospheric molecules compared to the OPO spectra measured at 380 fJ of pump**. The spectral lines were taken from the HITRAN database[69].

In Fig. 6.10, we compare the experimental OPO spectra to the spectral lines of H_2O, CO_2, and CH_4. The overlap between water and the OPO's spectral features is especially close, likely because H_2O is the strongest absorber in this spectral region at atmospheric concentrations. We calculate that 9 % of the 3 μm mode inside the spiral region is evanescent, suggesting that with the 53 cm spiral, on-chip sensing may be possible. Here, however, we expect that the absorption primarily occurs between the output of the chip and the detector as none of the systems in this experiment were purged. Furthermore, these absorption features result from ambient molecules existing in the lab as no gas cells were prepared.

As noted in the main text, the notch at 2.83 μm is due to an OH absorption peak in the LN and/or SiO_2 substrate buffer layer. Studies of the absorption of SiO_2 employed as a buffer layer for Si waveguides[70, 71, 72] indicate that the SiO_2 bottom-cladding will become prohibitively narrow around 2.8 μm and above 3.5 μm. For current thin-film lithium (TFLN) niobate devices with a SiO_2 buffer and Si substrate, the upper absorption appears to set in around 3.25 μm [73]. Wavelengths between, 2.8-3.8 μm, however have been measured on TFLN waveguides on a sapphire substrate[74], suggesting a path towards making a multi-octave frequency comb with even longer wavelength components.

D. Mode Crossings

In Fig. 6.9, there are spectral kinks at 680 nm and 1135 nm evident over all pump pulse energies. These correspond to the two mode crossings shown in Fig. 6.11a. M1 is the mode crossing between the fundamental TE mode and second order TM mode (Fig. 6.11b) whereas M2 is the mode crossing between the fundamental TE and TM modes (Fig. 6.11c). Indeed, these mode crossings, as well as the OH absorption discussed in Section IIB, are even evident in the spectra measured from a straight waveguide with the same waveguide geometry and poling period as the OPO and plotted in Fig. 6.11d. As this straight waveguide does not have a cavity, its half-harmonic spectra is due to optical parametric generation (OPG).

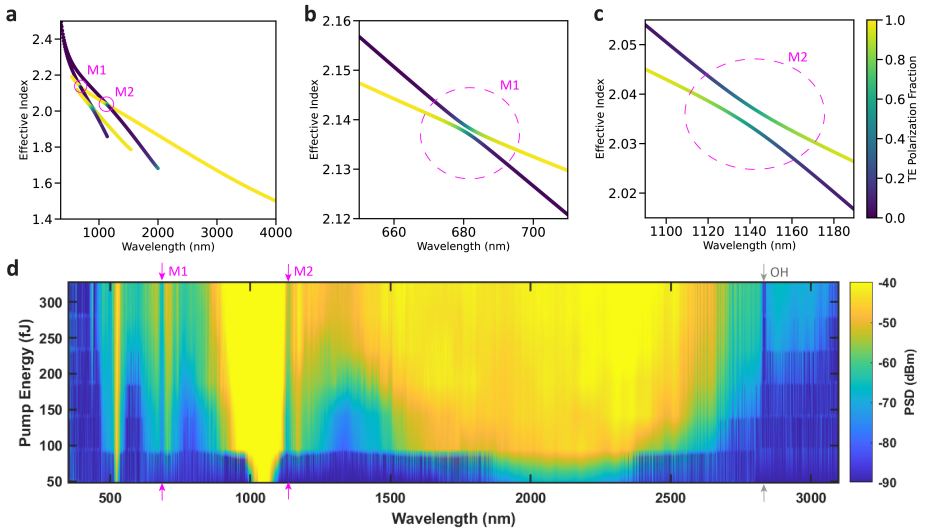

Figure 6.11: **Simulated mode crossings compared to measured straight waveguide spectra**. **a,** Simulated modes at the periodically poled region of the chip. The mode crossings experienced by the fundamental TE mode are marked as M1 and M2. Close-ups of these are shown in **b** and **c** respectively. **d,** The measured power spectral density of a periodically poled nanophotonic waveguide with no OPO cavity as a function of pump pulse energy. The locations of M1 (680 nm) and M2 (1135 nm) are indicated by arrows.

E. Beatnote Measurement

1. Down-Conversion Beatnote

The coherence of the down-converted portion of the comb around the half-harmonic was investigated using the experimental setup in Fig. 6.12a. The output of an on-chip and free space OPO pumped by the same laser were interfered. Depending on the detuning peak l of each OPO, we expect to see different signatures in their radio frequency (RF) spectrum and interference patterns. Here, the dimensionless detuning parameter $l = 2f_s\Delta T_{RT}$, where ΔT_{RT} is the mismatch between the cavity roundtrip time and pump repetition period, and f_s is the signal frequency. While OPOs with even l have comb lines aligned with that of the pump, OPOs with odd l have comb lines shifted by $f_{\text{rep}}/2$ [34, 75]. This is illustrated in Fig. 6.12b. As a result, when one of the OPOs has even l while the other has odd l, the temporally and spatially overlapped OPO outputs show an f_{CEO} beatnote at $f_{\text{rep}}/2$, as shown in the RF spectrum measurement in Fig. 6.12c(i). Furthermore, in this case where the two combs have different f_{CEO} frequencies, we do not expect to see interference fringes as the delay between the two coherent OPO outputs is scanned. As shown by the orange trace in Fig. 6.12c(ii), no fringe is observed.

In the case that the OPOs are coherent and share the same even or odd detuning parameter, and thus the same f_{CEO}, however, we do not expect and did not observe a beatnote at $f_{\text{rep}}/2$. Furthermore, since the combs share an f_{CEO}, we expect to

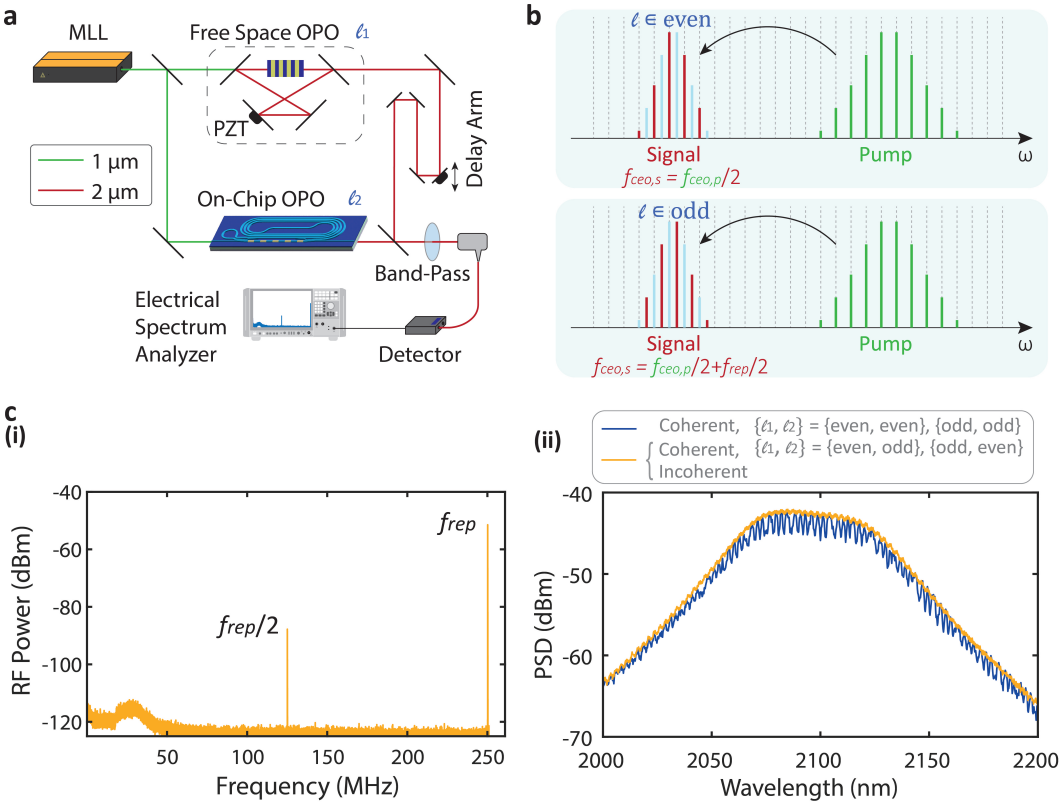

Figure 6.12: **OPO beatnote measurement. a,** Experimental setup. **b,** Illustration of the two f_{CEO} states possible for the OPO comb depending on the detuning peak, l, being even or odd. **c,** (i) RF beatnote and (ii) spectral overlap, showing interference fringes (blue) as the relative output delay between the OPOs is scanned in the case where they share an f_{CEO} in the temporal self-cleaning regime.

see an interference fringe as their relative delay is scanned. This is indeed what we measured, as shown by the blue curve in Fig. 6.12c(ii). At 109 fJ and 380 fJ of pump, where the down-converted portion of the nanophotonic OPO output is incoherent, we observed neither a $f_{\mathrm{rep}}/2$ beatnote nor the blue interference fringe of Fig. 6.12c(ii).

Finally, the pump rep rate can be locked to features in the OPO output signal. In Fig. 6.13, we show that we can indeed lock to, and stabilize the on-chip OPO output to the 2.6 octave comb state in the temporal self-cleaning regime.

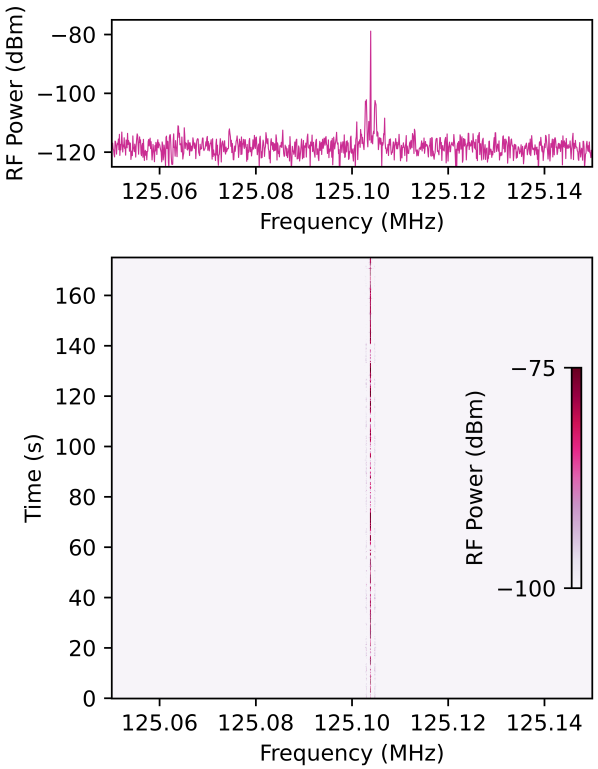

Figure 6.13: **OPO beatnote locked in the Temporal Self-Cleaning Regime.** The pump here is at 121 fJ, and the pump rep rate is locked to the OPO peak structures seen in the OPO oscillation peaks in Fig. 6.2d(viii) of the main text. The top panel shows the $f_{\text{rep}}/2$ beatnote at a representative time, and the bottom panel shows the beatnote persist over time. The dither signals of the free-space and on-chip OPO cavity locks cause the two sets of side fringes to the main $f_{\text{rep}}/2$ beatnote.

2. Up-Conversion Beatnote

The coherence of the up-converted portion of the pump was investigated using similar methodologies to [35, 29]. Specifically, a spectrally broadened portion of the pump was interfered with the second harmonic portion of the on-chip OPO, as illustrated in Fig. 6.14a. The spectral overlap for three of the pump pulse energies mentioned in Fig. 6.2d of the main text are shown in Fig. 6.14b, with the corresponding beatnotes presented in Figs. 6.14c-e. In each case we confirmed the beatnotes correspond to the f_{CEO} by recording its shift as the pump f_{CEO} is tuned. We conclude that the up-converted porion of the pump reamins coherent irrespective of the pump pulse energy or cavity detuning, which is as expected[35, 29].

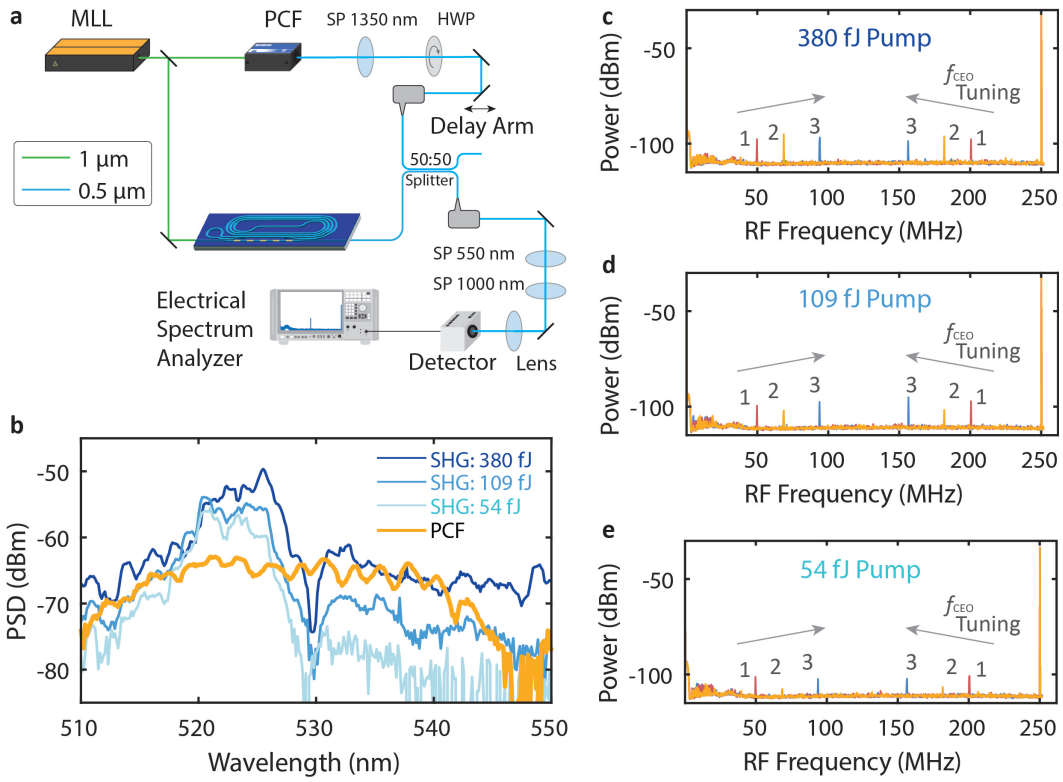

Figure 6.14: **SHG beatnote measurement.** **a,** Experimental setup. **b,** Spectral overlap between the chip SHG outputs and the PCF. Sample beatnotes measured at **c,** 380 fJ, **d,** 109 fJ, and **e,** 54 fJ with the different colors corresponding to different pump f_{CEO}s. Abbreviations, SP: short pass, PCF: photonic crystal fiber (Menlo Systems), HWP: half wave plate.

6.7.3 OPO Simulations

A. Method

We model the ultrabroad spectral dynamics of the nanophotonic OPO by representing the total electric field in the nanophotonic waveguide using a single envelope in the frequency domain [76, 37],

$$\mathbf{E}(x, y, \omega) = A(z, \Omega)\mathbf{e}(x, y, \omega)e^{-i(\beta_0 - \omega_0/v_{\mathrm{ref}})z}, \tag{6.2}$$

where ω and $\Omega = \omega - \omega_0$ are the optical and envelope angular frequencies, ω_0 is the simulation center frequency, β_0 is the waveguide propagation constant at ω_0, v_{ref} is the simulation reference frame velocity, x and y are the transversal waveguide coordinates, $\mathbf{e}(x, y, \omega)$ is the mode transversal field distribution, and $A(z, \omega)$ is the complex amplitude of the field that evolves during propagation. In our OPO simulation, ω_0 is chosen to be the center of the half-harmonic signal at 2090 nm, and v_{ref} is the group velocity of the half-harmonic. $A(z, \omega) = A(z, \Omega)e^{-i\omega_0 t}$ is a rapidly-varying envelope which contains the phase factor $e^{-i\beta(\omega)z}$ acquired during linear propagation. Additionally, $A(z, \omega)$ is an analytic signal, meaning it only contains positive frequencies ($A(z, \omega < 0) = 0$).

Our simulation models each round-trip in the OPO in two parts. The first accounts for the nonlinear propagation in the poled region of the waveguide, while the second consists of a linear filter which models the round-trip evolution in the spiral resonator [77]. The output of this round-trip evolution is fed back as a seed for the subsequent nonlinear propagation. The first round-trip is seeded by white noise for all frequencies besides the pump, which is taken to be an 80-fs pulse with a sech pulse profile, centered at 1045 nm.

We find a uni-directional equation of motion describing the nonlinear propagation of $A(z,\Omega)$ by ignoring counter-propagating terms (which are usually phase mismatched) and assuming a constant nonlinear coefficient and mode overlap integral, both of which are weak functions of frequency away from any material resonances. No limitations are placed upon the maximum spectral bandwidth of the simulation. The resulting propagation equation is,

$$\frac{\partial A}{\partial z} = -i\left[\beta(\omega) - \beta_0 - \frac{\Omega}{v_{\text{ref}}} - i\frac{\alpha}{2}\right]A - \frac{i\omega\epsilon_0 X_0}{8}d(z) \mathcal{F}_\Omega\left\{a^2(z,t)e^{j\phi(z,t)} + 2a(z,t)a^*(z,t)e^{-j\phi(z,t)}\right\}, \quad (6.3)$$

where $d(z) = \pm 1$ is the sign of the quadratic nonlinear coefficient that is modulated in quasi-phase matching, α is the propagation loss coefficient, $a(z,t)$ is the time domain representation of $A(z,\Omega)$, $\phi(z,t) = \omega_0 t - (\beta_0 - \omega_0/v_{\text{ref}})z$, $\mathcal{F}_\Omega$ is the Fourier transform in the Ω variable. The effective nonlinear coefficient X_0 is defined as:

$$X_0 = \sum_{ijk} \chi^{(2)}_{ijk} \int e^*_i(\omega_1) e_j(\omega_2) e_k(\omega_1 - \omega_2)\, \mathrm{d}S\,, \quad (6.4)$$

where $\chi^{(2)}_{ijk}$ is the quadratic nonlinear susceptibility tensor, and j, k, l denote Cartesian components.

The nonlinear propagation in each round-trip involves solving the evolution equation (6.3) using the split-step Fourier technique over the length of the poled waveguide, L = 10.8 mm. The nonlinear step employs the fourth-order Runge-Kutta method in the interaction picture (RK4IP) [78].

Propagation in the spiral resonator is modeled through application of a linear feedback function to the output of the poled region. In particular, the signal fed back to the input of the poled region for the $(n+1)^{th}$ round-trip, $A^{n+1}_{in}(0,\omega)$, is related to the field out of the poled region on the n^{th} round-trip, $A^n_{out}(L,\omega)$, by the expression:

$$A^{n+1}_{in}(0,\omega) = A^n_{out}(L,\omega)R(\omega)e^{-j(D_{RT}(\omega)L_{RT} + \Delta T_{RT}\omega + \phi_0)} \quad (6.5)$$

Here, $R(\omega)$ is the frequency-dependent coupling factor of the designed adiabatic couplers, $D_{RT} = \beta(\omega) - \beta_0 - \frac{\Omega}{v_{\text{ref}}} - i\frac{\alpha_{RT}}{2}$ is the complex dispersion operator describing propagation in the round-trip waveguide with parameters defined as above for the poled waveguide, L_{RT} = 518.4 mm is the length of the round-trip cavity, ΔT_{RT} is the detuning parameter which accounts for any timing mismatch between the

pump repetition period and cavity round-trip time, and ϕ_0 is a constant phase offset, which effectively represents the carrier-envelope offset phase, ϕ_{CEO}, of the pump. In addition to this fed back signal, a new pump pulse is also injected, centered at t = 0 on the fast time axis.

Simulations are conducted on a Fourier grid of size 4096 with a bandwidth of 2.4 PHz. The corresponding time window is 1.7 ps. To avoid wrapping in the time window during the nonlinear propagation, a Tukey filter padded with zeros on the edges is applied in the time domain after each nonlinear step. Additionally, before application of the linear filter, all frequency components which will walk out of the time window over the course of the 518-mm propagation in the spiral resonator are filtered out. This has the undesirable effect of effectively reducing the simulated power in frequency modes which are far from the reference frequency (and thus experience significant walk-off with respect to the reference velocity of the simulation), but it ensures the validity of the simulated nonlinear interaction.

In this context we consider nonlinear phase to be the phase accumulated in the PPLN section of the resonator due to the nonlinear process (excluding the linear phase accumulation). We explicitly focus on a narrow spectral range around the pump and its half-harmonic for the spectral analysis and around the peak intensities for the pump and half-harmonic in the temporal analysis.

B. OPO Dynamics under Different Conditions

As discussed in the main text, the ultrabroadband OPO enters different regimes of operation high above threshold. An extended version of the regimes shown in the main text is shown in Fig. 6.15a. Whether our near-zero dispersion OPO can reach the coherent multi-octave state denoted as (iii) in the figure, largely depends on the pump energy, cavity detuning (shown in Fig. 6.15b), and effective pump carrier-envelope-offset phase, ϕ_{CEO}. We find that the dynamics of our OPO largely depend on whether it has an even or odd detuning peak, l, and whether its relative ϕ_{CEO} is 0 or π. We will dive into each of these cases in more depth below.

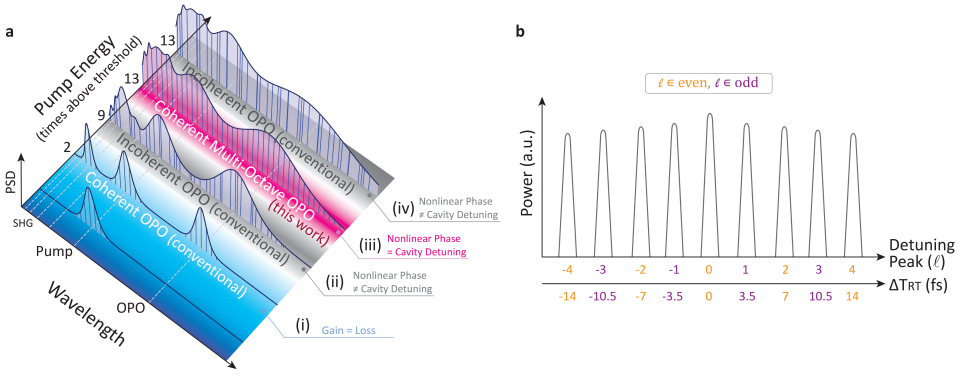

Figure 6.15: **a**, Extended regimes of operation of the nanophotonic OPO and **b**, OPO resonances labeled in terms of detuning peak (l), and cavity roundtrip detuning (ΔT_{RT}).

1. $l \in$ **even,** $\phi_{\mathrm{CEO}} = 0$

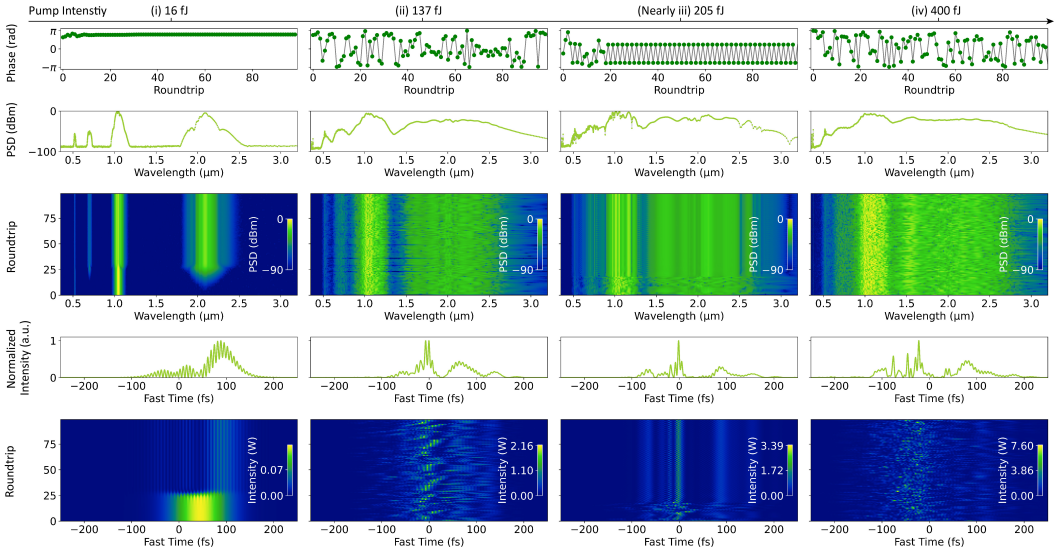

Figure 6.16: **OPO Characterization:** $l = 2$**,** $\phi_{\mathrm{CEO}} = 0$.

When $l \in$ even and $\phi_{\mathrm{CEO}} = 0$, we find that while the OPO nearly reaches a coherent, mutli-octave comb, it never quite manages to. In the cases of $l = \{2, 0, -2\}$ in Figs. 6.16-6.18, this is emphasized by the label (Nearly iii). In all of these cases we see that in regime (i) near threshold, the roundtrip-to-rountrip phase of the coherent OPO remains fixed once the OPO goes above threshold. After transitioning though an incoherent state in regime (ii), the OPO phase is seen to flip roundtrip-to-roundtrip by π in pump regime (iii). These periodic oscillations suggest that perhaps in this state the OPO is composed of two coherent non-degenerate combs, the beating of which creates the observed phase fluctuations as well as the roundtrip-to-roundtrip power fluctuations observed in the time- and frequency-domain plots of the OPO evolution. At even higher pump energies, the OPO enters the completely saturated, incoherent regime of (iv).

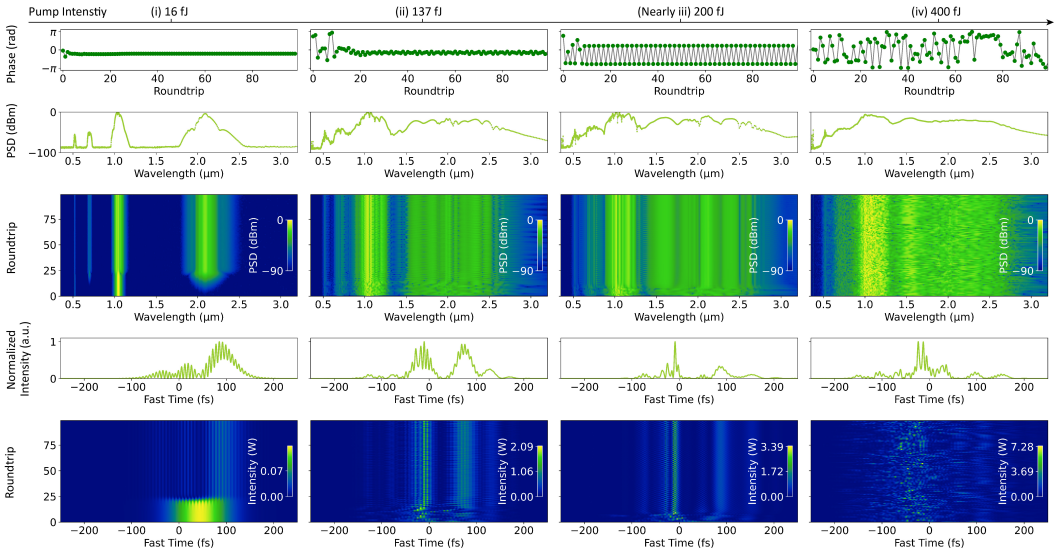

Figure 6.17: **OPO Characterization:** $l = 0$**,** $\phi_{\text{CEO}} = 0$.

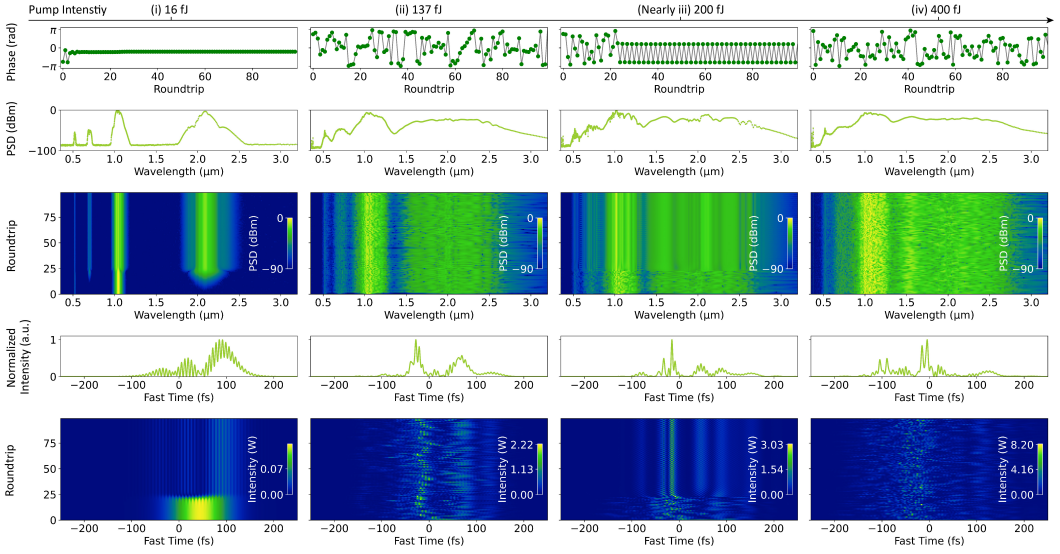

Figure 6.18: **OPO Characterization:** $l = -2$**,** $\phi_{\text{CEO}} = 0$.

2. $l \in$ **odd,** $\phi_{\mathrm{CEO}} = 0$

The roundtrip-to-roundtrip π phase flips in the ~200 fJ-pumped cases when $l \in$ even and $\phi_{\mathrm{CEO}} = 0$ suggest that if the cavity phase can be detuned by π, a multi-octave coherent comb can be sustained. One way of obtaining such a detuning is to select OPO peaks where $l \in$ odd while maintaining $\phi_{\mathrm{CEO}} = 0$, and in Figs. 6.19-6.22, we show the dynamics of the cases where $l = \{3, 1, -1, -3\}$. As expected, near threshold, i.e. in regime (i), these OPOs show roundtrip-to-roundtrip π phase flips. In regime (iii), however, we find that the OPO demonstrates temporal self-cleaning and is able to stabilize, showing a fixed roundtrip-to-roundtrip phase.

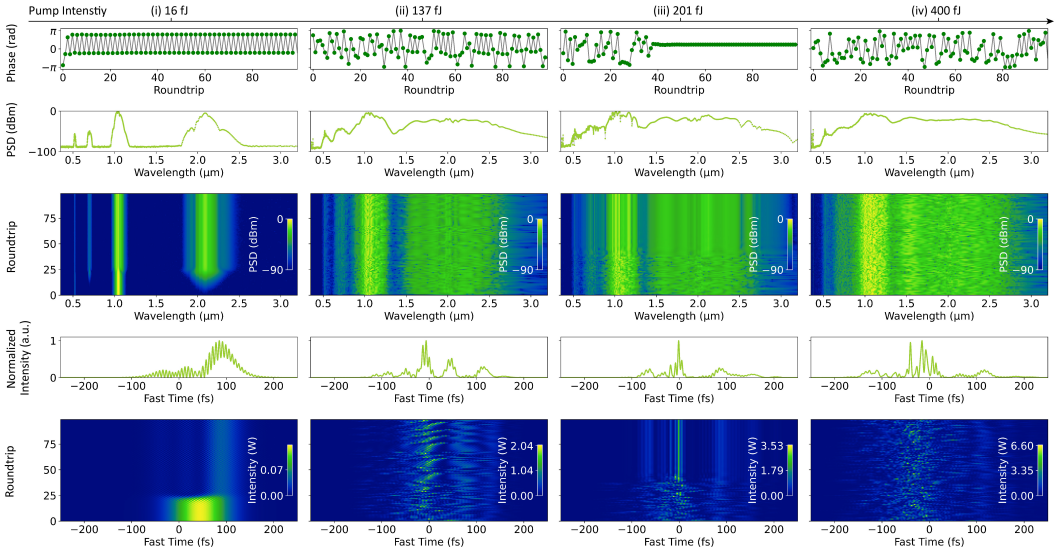

Figure 6.19: **OPO Characterization:** $l = 3$**,** $\phi_{\mathrm{CEO}} = 0$.

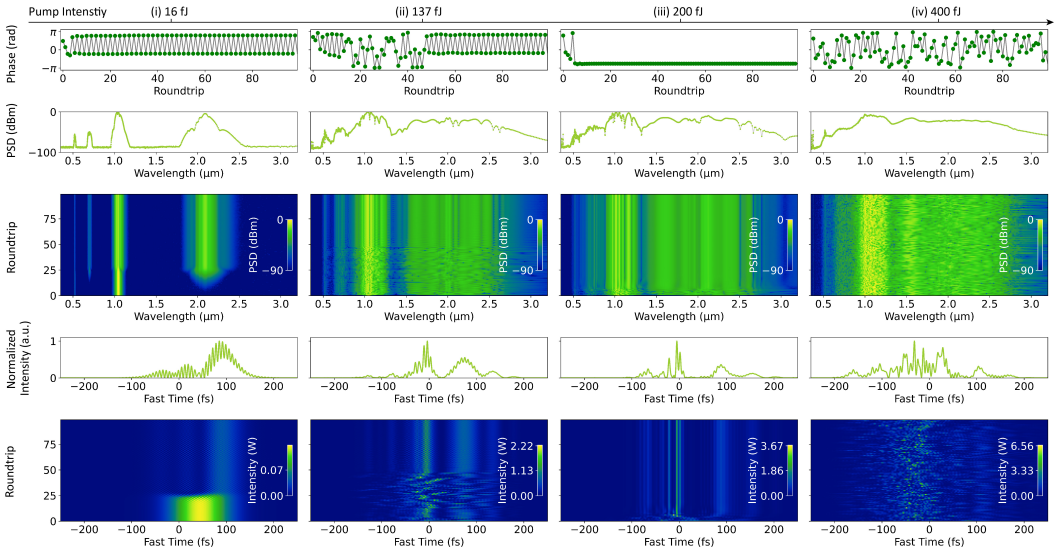

Figure 6.20: **OPO Characterization:** $l = 1$**,** $\phi_{\text{CEO}} = 0$.

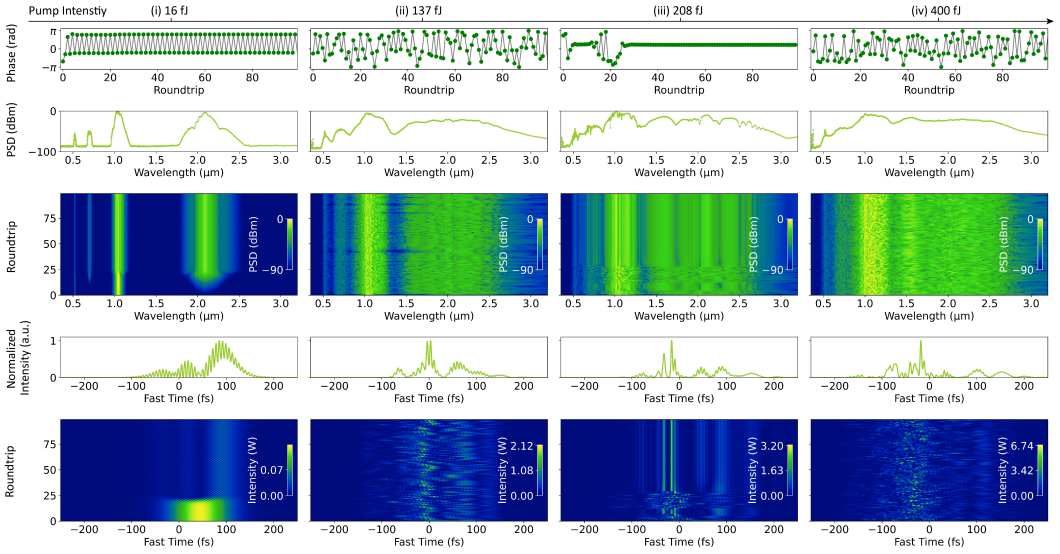

Figure 6.21: **OPO Characterization:** $l = -1$**,** $\phi_{\text{CEO}} = 0$.

The coherence of the two octave spectra in regime (iii) can be further verified by means of calculating the $g^{(1)}$ coherence over pairs of output pulses as well as by directly inspecting the overlap of the half-harmonic, pump, second harmonic, and sum-frequency generated combs. As can be seen in the top panel of Fig. 6.23a, we see through measurement of the $g^{(1)}$ coherence between pairs of pulses taken from the last 15 roundtrips of our simulation, the device displays over two octaves of coherent spectra. This can be further verified by looking at the the actual comb lines of the two-octave comb. The full comb spectrum, as well as a close-up of the comb lines corresponding to different harmonic combs, shifted by the nearest multiple of

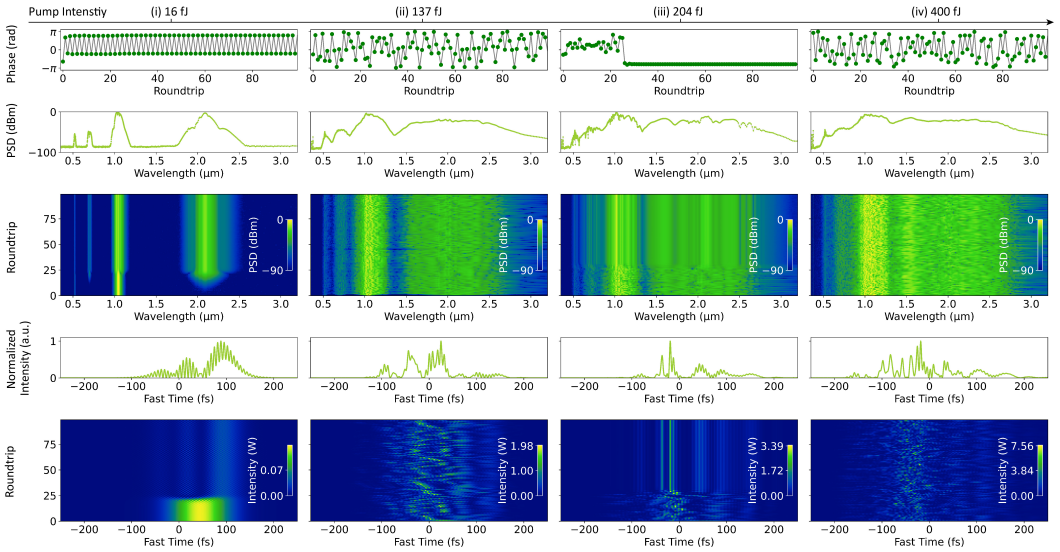

Figure 6.22: **OPO Characterization:** $l = -3$**,** $\phi_{\mathrm{CEO}} = 0$.

f_{rep} which centers them at zero, are shown in Fig. 6.23b. The good overlap between the comb lines is a further indication that the combs share an $\mathrm{f_{CEO}}$ and are thus coherent. Note that the second harmonic comb at 500 nm is not expected to share an $\mathrm{f_{CEO}}$ with the other harmonics except in the case where the pump comb at 1 μm has an $\mathrm{f_{CEO}}$ of 0, which is generally assumed in our simulation.

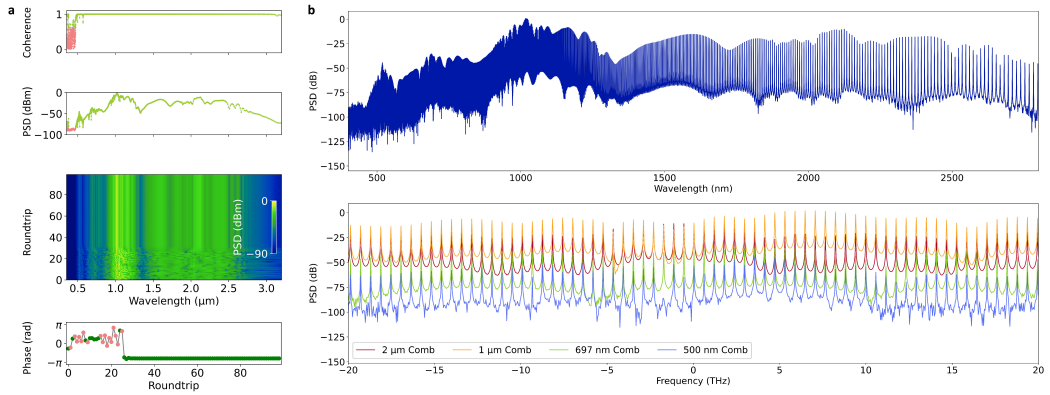

Figure 6.23: **Further characterization of the coherence of regime (iii) for** $l = -3$**,** $\phi_{\mathrm{CEO}} = 0$. **a**, $g^{(1)}$ coherence as a function of wavelength, PSD, and roundtrip spectra, where points with simulated coherence greater than 0.6 are denoted by a light green dot, with the rest colored in pink. For the roundtrip phase plot, points where the difference in phase compared to the prior roundtrip is smaller than $\pi/6$ are plotted in green with the other points marked in pink. **b**, Simulated comb lines at the output. The 2-μm, 1-μm, 69-nm, and 500-nm combs correspond to the half-harmonic, pump, sum-frequency generation of the pump and half-harmonic, and second harmonic of the pump respectively.

3. $l \in$ **even,** $\phi_{\text{ceo}} = \pi$

Along with picking an odd detuning peak, a roundtrip phase of π can be directly added in the case where $l \in$ even, corresponding to an effective pump carrier-envelope-offset phase $\phi_{\text{CEO}} = \pi$. The results of this are shown in Figs. 6.24-6.26 for $l = \{2, 0, -2\}$. Similar to the case of $l \in$ odd with $\phi_{\text{CEO}} = 0$, the OPO shows roundtrip-to-roundtrip phase flips at low powers of regime (i) and enters the oscillatory state of regime (ii) until ultimately landing in a steady-state at 200 fJ of pump. One qualification here is that, since the phase is added to the signal rather than the pump in simulation, the coherence between the pump and higher harmonics is also preserved, though this would not be true experimentally for a pump with non-zero ϕ_{CEO}, as discussed in Supplementary Section 6.7.3C.

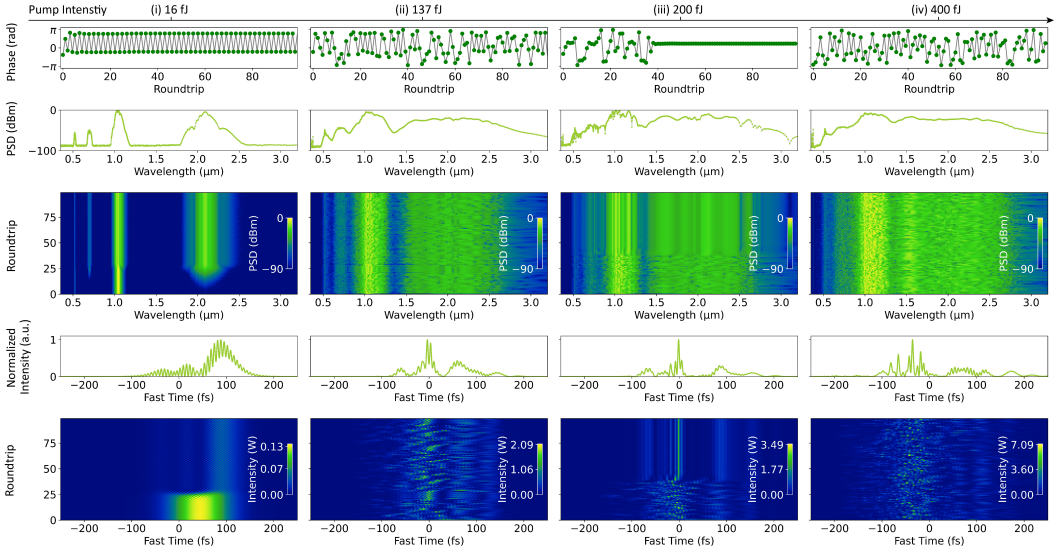

Figure 6.24: **OPO Characterization: Peak 2,** $\phi_{\text{CEO}} = \pi$.

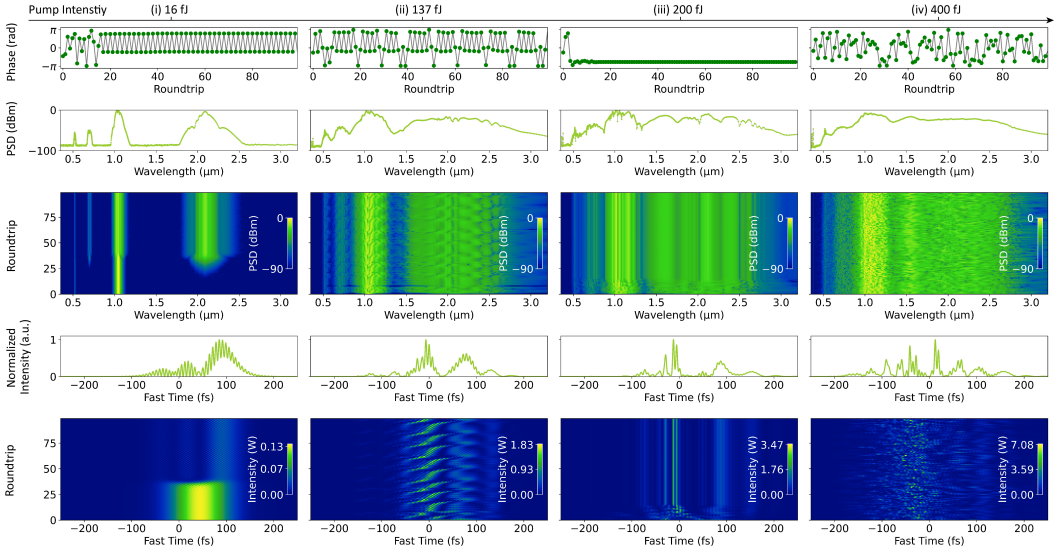

Figure 6.25: **OPO Characterization: Peak 0,** $\phi_{\text{CEO}} = \pi$.

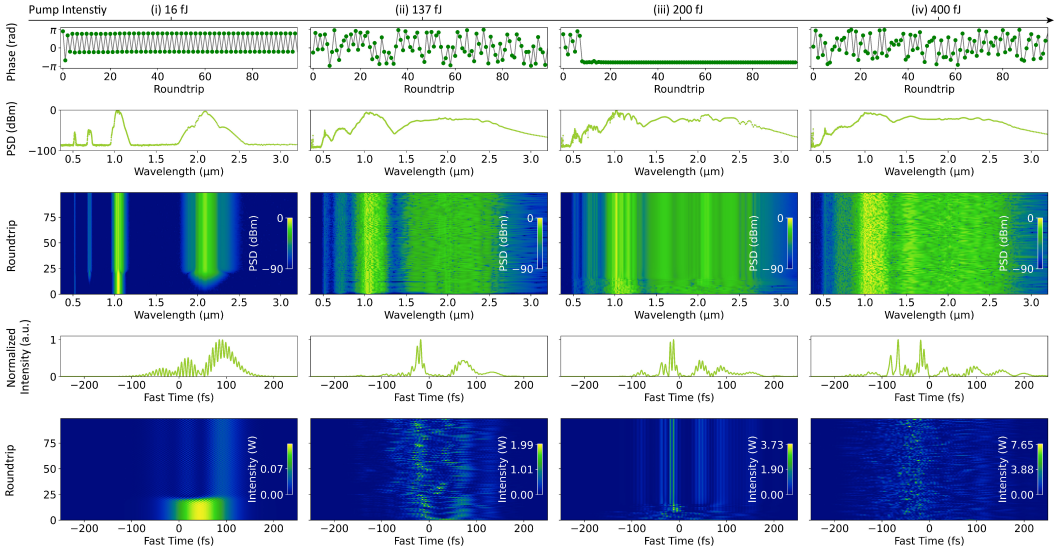

Figure 6.26: **OPO Characterization: Peak -2,** $\phi_{\text{CEO}} = \pi$.

C. Temporal Self-Cleaning

1.Mechanism

In Fig. 6.2d of the main text, we experimentally demonstrated that as the input pump pulse energy is increased, our OPO transitions from a conventional operational regime, where it is coherent, to an incoherent one, but then it recovers its coherence at higher pump pulse energies with an appropriate cavity detuning. In Fig. 6.27, we show the intensity and phase propagation of the pump and half-harmonic in the periodically poled region of the cavity at ~200 fJ of pump (i.e. in the TSC regime). The evolution of the half-harmonic phase in a(ii) clearly shows a phase flip from $-\pi \rightarrow 0$ in locations where the half-harmonic has substantial intensity.

In Supplementary Section 6.7.2B, we showed that this π phase flip in the half-harmonic in each single-pass through the PPLN can be compensated by detuning the cavity by an odd number of OPO peaks (Section IIB2), or by adding a constant phase offset of π between the pump and cavity, corresponding to the carrier-envelope offset phase, ϕ_{CEO}, of the pump (Section IIB3). Fig. 6.22 is an example of the former. Near threshold (16 fJ), the OPO output experiences a π phase flip in every roundtrip, but it is able to stabilize to a constant phase output in the case of 204 fJ of pump. An example of the latter approach of choosing an even detuning peak but ϕ_{CEO} of π, is Fig. 6.24. Again, we observe that in the TSC regime of 200 fJ of pump, the output phase can stabilize after ~40 cavity roundtrips. These examples show that compensating the single pass phase accumulation in the PPLN by appropriately detuning the cavity, or ϕ_{CEO}, is the key to operating in the TSC regime. Thus, the pump pulse energy of where TSC occurs is dependent on the OPO dispersion and nonlinear gain that induces π phase flips between the half-harmonic and the pump.

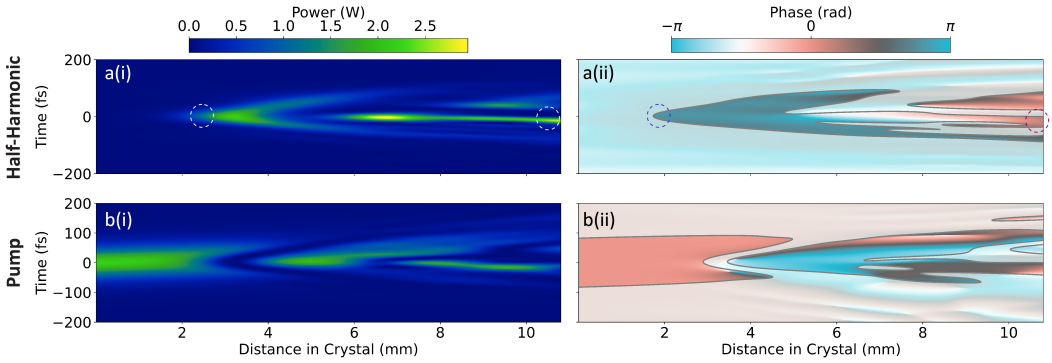

Figure 6.27: **Intensity and phase evolution inside the crystal for the half-harmonic (top) and pump (bottom) of regime (iii) for $l = -3$, $\phi_{\mathrm{ceo}} = 0$.** For a(ii) and b(ii), the phase of regions with intensity greater than ~ 0.2 W are encircled, and phases of locations with lower intensities are made more transparent.

2. Short Pulse Formation

As mentioned in the main text, the temporal self-cleaning mechanism of the coherent multi-octave OPO can lead to ultrafast features at the output of the OPO. In Fig. 6.28, we explicitly show the simulated temporal output of this regime for the cases

of $l = \{-3, -1, 1, 3\}$ with $\phi_{\mathrm{CEO}} = 0$. Features as narrow as 4.2 fs can be observed, suggesting that the coherent multi-octave comb regime can in the future be leveraged for extreme pulse compression and single/few-cycle pulse synthesis.

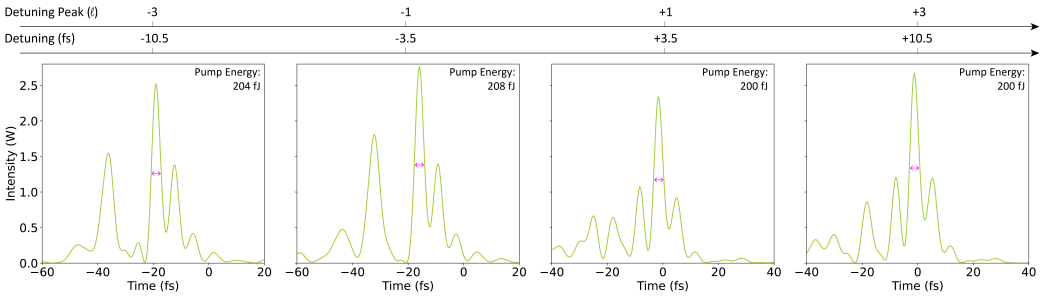

Figure 6.28: **Temporal output of the two-octave combs at different detunings**. In each case, the pink line showing the 3 dB bandwidth of the central feature is ~ 4.2 fs. Here, $\phi_{\mathrm{CEO}} = 0$.

D. Extension to a Three Octave Comb

By employing a chirped poling period targeting energy transfer to the second harmonic and sum frequency generation terms, we can even induce three octaves of coherent spectra. In particular, the poling period in the last 1 mm of the 10.8-mm poled region is assumed to vary smoothly between the period required for quasi-phase-matched OPA between the pump at 1 μm and signal at 2 μm to phase matching the interaction between the pump at 1 μm and its second harmonic at 500 nm. Extended characterization of the results, discussed in Fig. 6.3b of the main text, are shown in Fig. 6.29. Of note is that this high-harmonic generation process acts as an effective loss for the 2 μm signal, resulting in a slightly higher threshold for the OPO and larger pump power requirement to reach the temporal self-cleaning regime. At 248 fJ of pump, however, a multi-octave comb is observed, with the additional high-harmonic processes enabling formation of a coherent three-octave spectrum (Fig. 6.29a-b) by filling the spectral gap between the second harmonic at 500 nm and sum-frequency component at 697 nm.

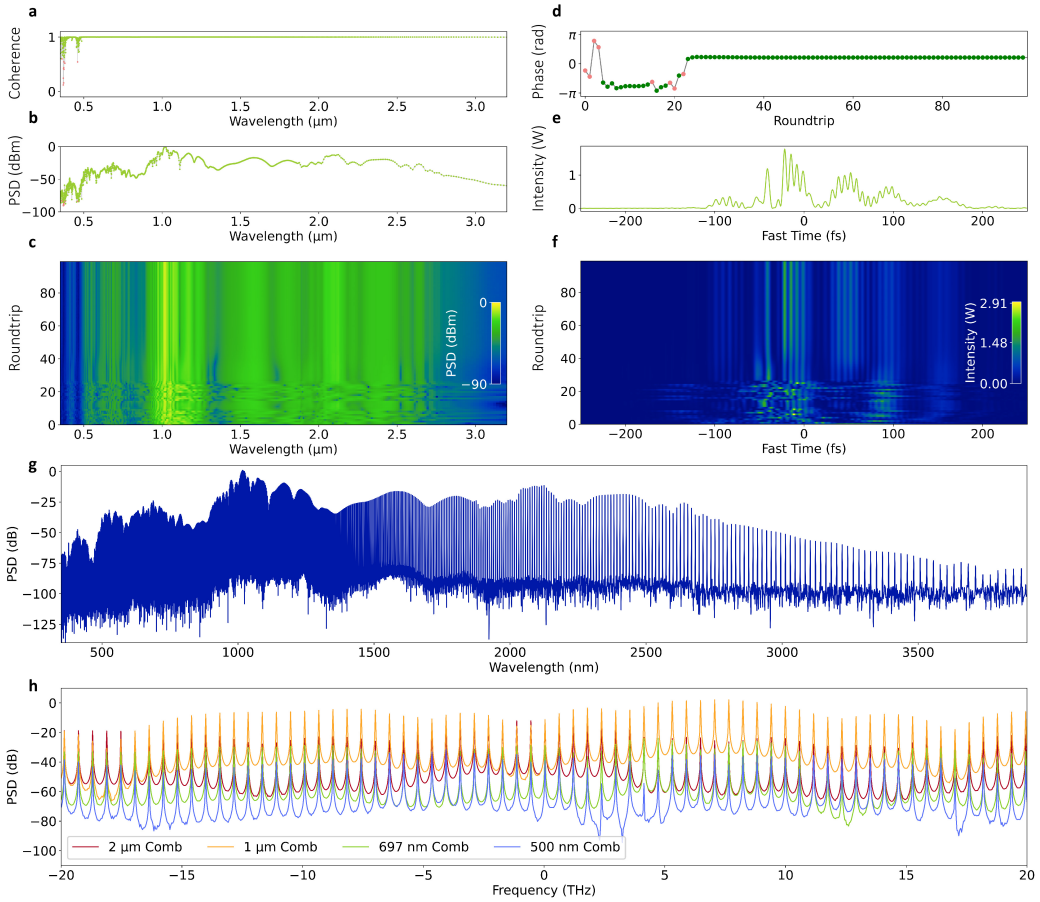

Figure 6.29: **Three Octave Comb Characterization at** $l = 3$**,** $\phi_{\text{CEO}} = 0$. Coherence and normalized output spectrum of a simulated OPO with additional duty cycle variations in the poling period to yield a three-octave coherent frequency comb with 248 fJ of pump.

References

[1] David R. Carlson et al. "Ultrafast electro-optic light with subcycle control". In: *Science* 361.6409 (2018), pp. 1358–1363. URL: https://www.science.org/doi/abs/10.1126/science.aat6451.

[2] Scott A. Diddams, Kerry Vahala, and Thomas Udem. "Optical frequency combs: Coherently uniting the electromagnetic spectrum". In: *Science* 369.6501 (2020), eaay3676. URL: https://www.science.org/doi/abs/10.1126/science.aay3676.

[3] Tobias J. Kippenberg et al. "Dissipative Kerr solitons in optical microresonators". In: *Science* 361.6402 (2018), eaan8083. URL: https://www.science.org/doi/abs/10.1126/science.aan8083.

[4] Lin Chang, Songtao Liu, and John E. Bowers. "Integrated optical frequency comb technologies". In: *Nature Photonics* 16.2 (Feb. 2022), pp. 95–108. URL: https://doi.org/10.1038/s41566-021-00945-1.

[5] Alexander L. Gaeta, Michal Lipson, and Tobias J. Kippenberg. "Photonic-chip-based frequency combs". In: *Nature Photonics* 13.3 (Mar. 2019), pp. 158–169. URL: https://doi.org/10.1038/s41566-019-0358-x.

[6] Myoung-Gyun Suh et al. "Microresonator soliton dual-comb spectroscopy". In: *Science* 354.6312 (2016), pp. 600–603. URL: https://www.science.org/doi/abs/10.1126/science.aah6516.

[7] Pablo Marin-Palomo et al. "Microresonator-based solitons for massively parallel coherent optical communications". In: *Nature* 546.7657 (June 2017), pp. 274–279. URL: https://doi.org/10.1038/nature22387.

[8] Daryl T. Spencer et al. "An optical-frequency synthesizer using integrated photonics". In: *Nature* 557.7703 (May 2018), pp. 81–85. URL: https://doi.org/10.1038/s41586-018-0065-7.

[9] Minh A. Tran et al. "Extending the spectrum of fully integrated photonics to submicrometre wavelengths". In: *Nature* 610.7930 (Oct. 2022), pp. 54–60. URL: https://doi.org/10.1038/s41586-022-05119-9.

[10] Johann Riemensberger et al. "Massively parallel coherent laser ranging using a soliton microcomb". In: *Nature* 581.7807 (May 2020), pp. 164–170. URL: https://doi.org/10.1038/s41586-020-2239-3.

[11] Daniel M. B. Lesko et al. "A six-octave optical frequency comb from a scalable few-cycle erbium fibre laser". In: *Nature Photonics* 15.4 (Apr. 2021), pp. 281–286. URL: https://doi.org/10.1038/s41566-021-00778-y.

[12] Ugaitz Elu et al. "Seven-octave high-brightness and carrier-envelope-phase-stable light source". In: *Nature Photonics* 15.4 (Apr. 2021), pp. 277–280. URL: https://doi.org/10.1038/s41566-020-00735-1.

[13] A. Wirth et al. "Synthesized Light Transients". In: *Science* 334.6053 (2011), pp. 195–200. URL: https://www.science.org/doi/abs/10.1126/science.1210268.

[14] P. B. Corkum and Ferenc Krausz. “Attosecond science”. In: *Nature Physics* 3.6 (June 2007), pp. 381–387. URL: https://doi.org/10.1038/nphys620.

[15] A. V. Muraviev et al. “Massively parallel sensing of trace molecules and their isotopologues with broadband subharmonic mid-infrared frequency combs”. In: *Nature Photonics* 12.4 (Apr. 2018), pp. 209–214. URL: https://doi.org/10.1038/s41566-018-0135-2.

[16] Nathalie Picqué and Theodor W. Hänsch. “Frequency comb spectroscopy”. In: *Nature Photonics* 13.3 (Mar. 2019), pp. 146–157. URL: https://doi.org/10.1038/s41566-018-0347-5.

[17] Chein-I Chang. *Hyperspectral Imaging*. Springer US, 2003. URL: https://doi.org/10.1007/978-1-4419-9170-6.

[18] Mengjie Yu et al. “Integrated femtosecond pulse generator on thin-film lithium niobate”. In: *Nature* 612.7939 (Dec. 2022), pp. 252–258. URL: https://doi.org/10.1038/s41586-022-05345-1.

[19] Qiushi Guo et al. *Mode-locked laser in nanophotonic lithium niobate*. 2023.

[20] Brian Stern et al. “Battery-operated integrated frequency comb generator”. In: *Nature* 562.7727 (Oct. 2018), pp. 401–405. URL: https://doi.org/10.1038/s41586-018-0598-9.

[21] Martin H. P. Pfeiffer et al. “Octave-spanning dissipative Kerr soliton frequency combs in Si3N4 microresonators”. In: *Optica* 4.7 (July 2017), pp. 684–691. URL: https://opg.optica.org/optica/abstract.cfm?URI=optica-4-7-684.

[22] Qing Li et al. “Stably accessing octave-spanning microresonator frequency combs in the soliton regime”. In: *Optica* 4.2 (Feb. 2017), pp. 193–203. URL: https://opg.optica.org/optica/abstract.cfm?URI=optica-4-2-193.

[23] Ewelina Obrzud et al. “A microphotonic astrocomb”. In: *Nature Photonics* 13.1 (Jan. 2019), pp. 31–35. URL: https://doi.org/10.1038/s41566-018-0309-y.

[24] Tsung-Han Wu et al. *Visible to Ultraviolet Frequency Comb Generation in Lithium Niobate Nanophotonic Waveguides*. 2023.

[25] Dong Yoon Oh et al. “Coherent ultra-violet to near-infrared generation in silica ridge waveguides”. In: *Nature Communications* 8.1 (Jan. 2017), p. 13922. URL: https://doi.org/10.1038/ncomms13922.

[26] Markus Ludwig et al. *Ultraviolet astronomical spectrograph calibration with laser frequency combs from nanophotonic waveguides*. 2023.

[27] John M. Dudley, Goëry Genty, and Stéphane Coen. “Supercontinuum generation in photonic crystal fiber”. In: *Rev. Mod. Phys.* 78 (4 Oct. 2006), pp. 1135–1184. URL: https://link.aps.org/doi/10.1103/RevModPhys.78.1135.

[28] Sergey Vasilyev et al. “Multi-octave visible to long-wave IR femtosecond continuum generated in Cr:ZnS-GaSe tandem”. In: *Opt. Express* 27.11 (May 2019), pp. 16405–16412. URL: https://opg.optica.org/oe/abstract.cfm?URI=oe-27-11-16405.

[29] Marc Jankowski et al. “Ultrabroadband nonlinear optics in nanophotonic periodically poled lithium niobate waveguides”. In: *Optica* 7.1 (Jan. 2020), pp. 40–46. URL: https://opg.optica.org/optica/abstract.cfm?URI=optica-7-1-40.

[30] Miles H. Anderson et al. “Photonic chip-based resonant supercontinuum via pulse-driven Kerr microresonator solitons”. In: *Optica* 8.6 (June 2021), pp. 771–779. URL: https://opg.optica.org/optica/abstract.cfm?URI=optica-8-6-771.

[31] Miles H. Anderson et al. “Zero dispersion Kerr solitons in optical microresonators”. In: *Nature Communications* 13.1 (Aug. 2022), p. 4764. URL: https://doi.org/10.1038/s41467-022-31916-x.

[32] Sean Molesky et al. “Inverse design in nanophotonics”. In: *Nature Photonics* 12.11 (Nov. 2018), pp. 659–670. URL: https://doi.org/10.1038/s41566-018-0246-9.

[33] Peter L. McMahon et al. “A fully programmable 100-spin coherent Ising machine with all-to-all connections”. In: *Science* 354.6312 (2016), pp. 614–617. URL: https://www.science.org/doi/abs/10.1126/science.aah5178.

[34] Alireza Marandi et al. “Coherence properties of a broadband femtosecond mid-IR optical parametric oscillator operating at degeneracy”. In: *Opt. Express* 20.7 (Mar. 2012), pp. 7255–7262. URL: https://opg.optica.org/oe/abstract.cfm?URI=oe-20-7-7255.

[35] Alireza Marandi et al. “Cascaded half-harmonic generation of femtosecond frequency combs in the mid-infrared”. In: *Optica* 3.3 (Mar. 2016), pp. 324–327. URL: https://opg.optica.org/optica/abstract.cfm?URI=optica-3-3-324.

[36] Arkadev Roy et al. “Temporal walk-off induced dissipative quadratic solitons”. In: *Nature Photonics* 16.2 (Feb. 2022), pp. 162–168. URL: https://doi.org/10.1038/s41566-021-00942-4.

[37] Luis Ledezma et al. “Intense optical parametric amplification in dispersion-engineered nanophotonic lithium niobate waveguides”. In: *Optica* 9.3 (Mar. 2022), pp. 303–308. URL: https://opg.optica.org/optica/abstract.cfm?URI=optica-9-3-303.

[38] Arkadev Roy et al. *Visible-to-mid-IR tunable frequency comb in nanophotonics*. 2022.

[39] Luis Ledezma et al. “Octave-spanning tunable infrared parametric oscillators in nanophotonics”. In: *Science Advances* 9.30 (2023), eadf9711. URL: https://www.science.org/doi/abs/10.1126/sciadv.adf9711.

[40] Ryan Hamerly et al. “Reduced models and design principles for half-harmonic generation in synchronously pumped optical parametric oscillators”. In: *Phys. Rev. A* 94 (6 Dec. 2016), p. 063809. URL: https://link.aps.org/doi/10.1103/PhysRevA.94.063809.

[41] S. Mosca et al. “Modulation Instability Induced Frequency Comb Generation in a Continuously Pumped Optical Parametric Oscillator”. In: *Phys.*

Rev. Lett. 121 (9 Aug. 2018), p. 093903. URL: https://link.aps.org/doi/10.1103/PhysRevLett.121.093903.

[42] Logan G. Wright et al. "Physics of highly multimode nonlinear optical systems". In: *Nature Physics* 18.9 (Sept. 2022), pp. 1018–1030. URL: https://doi.org/10.1038/s41567-022-01691-z.

[43] K. Krupa et al. "Spatial beam self-cleaning in multimode fibres". In: *Nature Photonics* 11.4 (Apr. 2017), pp. 237–241. URL: https://doi.org/10.1038/nphoton.2017.32.

[44] M. Leidinger et al. "Comparative study on three highly sensitive absorption measurement techniques characterizing lithium niobate over its entire transparent spectral range". In: *Opt. Express* 23.17 (Aug. 2015), pp. 21690–21705. URL: https://opg.optica.org/oe/abstract.cfm?URI=oe-23-17-21690.

[45] Nathalie Picqué and Theodor W. Hänsch. "Frequency comb spectroscopy". In: *Nature Photonics* 13.3 (Mar. 2019), pp. 146–157. URL: https://doi.org/10.1038/s41566-018-0347-5.

[46] Yoshitomo Okawachi et al. "Chip-based self-referencing using integrated lithium niobate waveguides". In: *Optica* 7.6 (June 2020), pp. 702–707. URL: https://opg.optica.org/optica/abstract.cfm?URI=optica-7-6-702.

[47] Mengjie Yu et al. "Coherent two-octave-spanning supercontinuum generation in lithium-niobate waveguides". In: *Opt. Lett.* 44.5 (Mar. 2019), pp. 1222–1225. URL: https://opg.optica.org/ol/abstract.cfm?URI=ol-44-5-1222.

[48] David R. Carlson et al. "Photonic-Chip Supercontinuum with Tailored Spectra for Counting Optical Frequencies". In: *Phys. Rev. Appl.* 8 (1 July 2017), p. 014027. URL: https://link.aps.org/doi/10.1103/PhysRevApplied.8.014027.

[49] Ben Spaun et al. "Continuous probing of cold complex molecules with infrared frequency comb spectroscopy". In: *Nature* 533.7604 (May 2016), pp. 517–520. URL: https://doi.org/10.1038/nature17440.

[50] B. J. Bjork et al. "Direct frequency comb measurement of OD + CO → DOCO kinetics". In: *Science* 354.6311 (2016), pp. 444–448. URL: https://www.science.org/doi/abs/10.1126/science.aag1862.

[51] Wenle Weng et al. "Gain-switched semiconductor laser driven soliton microcombs". In: *Nature Communications* 12.1 (Mar. 2021), p. 1425. URL: https://doi.org/10.1038/s41467-021-21569-7.

[52] Yiqing Xu et al. "Harmonic and rational harmonic driving of microresonator soliton frequency combs". In: *Optica* 7.8 (Aug. 2020), pp. 940–946. URL: https://opg.optica.org/optica/abstract.cfm?URI=optica-7-8-940.

[53] Ewelina Obrzud, Steve Lecomte, and Tobias Herr. "Temporal solitons in microresonators driven by optical pulses". In: *Nature Photonics* 11.9 (Sept. 2017), pp. 600–607. URL: https://doi.org/10.1038/nphoton.2017.140.

[54] Takahiro Inagaki et al. “Large-scale Ising spin network based on degenerate optical parametric oscillators”. In: *Nature Photonics* 10.6 (June 2016), pp. 415–419. URL: https://doi.org/10.1038/nphoton.2016.68.

[55] Preetpaul S. Devgan et al. “10-GHz dispersion-managed soliton fiber-optical parametric oscillator using regenerative mode-locking: erratum”. In: *Opt. Lett.* 30.13 (July 2005), pp. 1743–1743. URL: https://opg.optica.org/ol/abstract.cfm?URI=ol-30-13-1743.

[56] Arkadev Roy et al. “Non-equilibrium spectral phase transitions in coupled nonlinear optical resonators”. In: *Nature Physics* 19.3 (Mar. 2023), pp. 427–434. URL: https://doi.org/10.1038/s41567-022-01874-8.

[57] Kirk A. Ingold et al. “Fiber-feedback optical parametric oscillator for half-harmonic generation of sub-100-fs frequency combs around 2μm”. In: *Opt. Lett.* 40.18 (Sept. 2015), pp. 4368–4371. URL: https://opg.optica.org/ol/abstract.cfm?URI=ol-40-18-4368.

[58] Carsten Langrock and M. M. Fejer. “Fiber-feedback continuous-wave and synchronously-pumped singly-resonant ring optical parametric oscillators using reverse-proton-exchanged periodically-poled lithium niobate waveguides”. In: *Opt. Lett.* 32.15 (Aug. 2007), pp. 2263–2265. URL: https://opg.optica.org/ol/abstract.cfm?URI=ol-32-15-2263.

[59] Jay E. Sharping et al. “Optical parametric oscillator based on four-wave mixing in microstructure fiber”. In: *Opt. Lett.* 27.19 (Oct. 2002), pp. 1675–1677. URL: https://opg.optica.org/ol/abstract.cfm?URI=ol-27-19-1675.

[60] Yujun Deng et al. “Broadly tunable femtosecond parametric oscillator using a photonic crystal fiber”. In: *Opt. Lett.* 30.10 (May 2005), pp. 1234–1236. URL: https://opg.optica.org/ol/abstract.cfm?URI=ol-30-10-1234.

[61] Jay E. Sharping et al. “Octave-spanning, high-power microstructure-fiber-based optical parametric oscillators”. In: *Opt. Express* 15.4 (Feb. 2007), pp. 1474–1479. URL: https://opg.optica.org/oe/abstract.cfm?URI=oe-15-4-1474.

[62] Ming Gao et al. “Optical Parametric Oscillator Based on Silicon Nitride Waveguides”. In: *Optica Advanced Photonics Congress 2022*. Optica Publishing Group, 2022, JTh4A.3. URL: https://opg.optica.org/abstract.cfm?URI=BGPPM-2022-JTh4A.3.

[63] Alireza Marandi et al. “Network of time-multiplexed optical parametric oscillators as a coherent Ising machine”. In: *Nature Photonics* 8.12 (Dec. 2014), pp. 937–942. URL: https://doi.org/10.1038/nphoton.2014.249.

[64] Oliver H. Heckl et al. “Three-photon absorption in optical parametric oscillators based on OP-GaAs”. In: *Opt. Lett.* 41.22 (Nov. 2016), pp. 5405–5408. URL: https://opg.optica.org/ol/abstract.cfm?URI=ol-41-22-5405.

[65] D.T. Reid et al. “Widely tunable, near- to mid-infrared femtosecond and picosecond optical parametric oscillators using periodically poled $LiNbO_3$ and $RbTiOAsO_4$”. In: *IEEE Journal of Selected Topics in Quantum Electronics* 4.2 (1998), pp. 238–248.

[66] Ryoto Sekine et al. “Sync-Pumped Femtosecond OPO Based on Dispersion-Engineered Nanophotonic PPLN with 3-Octave Spectrum”. In: *Conference on Lasers and Electro-Optics*. Optica Publishing Group, 2022, SM5K.2. URL: https://opg.optica.org/abstract.cfm?URI=CLEO_SI-2022-SM5K.2.

[67] Jiang Li et al. “Efficiency of pulse pumped soliton microcombs”. In: *Optica* 9.2 (Feb. 2022), pp. 231–239. URL: https://opg.optica.org/optica/abstract.cfm?URI=optica-9-2-231.

[68] Kent C. Burr et al. “Broadly tunable mid-infrared femtosecond optical parametric oscillator using all-solid-state-pumped periodically poled lithium niobate”. In: *Opt. Lett.* 22.19 (Oct. 1997), pp. 1458–1460. URL: https://opg.optica.org/ol/abstract.cfm?URI=ol-22-19-1458.

[69] I.E. Gordon et al. “The HITRAN2016 molecular spectroscopic database”. In: *Journal of Quantitative Spectroscopy and Radiative Transfer* 203 (2017). HITRAN2016 Special Issue, pp. 3–69. URL: https://www.sciencedirect.com/science/article/pii/S0022407317301073.

[70] Richard A Soref, Stephen J Emelett, and Walter R Buchwald. “Silicon waveguided components for the long-wave infrared region”. In: *Journal of Optics A: Pure and Applied Optics* 8.10 (Aug. 2006), p. 840. URL: https://dx.doi.org/10.1088/1464-4258/8/10/004.

[71] Steven A. Miller et al. “Low-loss silicon platform for broadband mid-infrared photonics”. In: *Optica* 4.7 (July 2017), pp. 707–712. URL: https://opg.optica.org/optica/abstract.cfm?URI=optica-4-7-707.

[72] Hongtao Lin et al. “Mid-infrared integrated photonics on silicon: a perspective”. In: *Nanophotonics* 7.2 (2018), pp. 393–420. URL: https://doi.org/10.1515/nanoph-2017-0085.

[73] Arkadev Roy et al. *Visible-to-mid-IR tunable frequency comb in nanophotonics*. 2022.

[74] Jatadhari Mishra et al. “Ultra-broadband mid-infrared generation in dispersion-engineered thin-film lithium niobate”. In: *Opt. Express* 30.18 (Aug. 2022), pp. 32752–32760. URL: https://opg.optica.org/oe/abstract.cfm?URI=oe-30-18-32752.

[75] Marc Jankowski. “Pulse formation and frequency conversion in dispersion-engineered nonlinear waveguides and resonators”. PhD thesis. Stanford University, Sept. 2020.

[76] C. R. Phillips et al. “Supercontinuum Generation in Quasi-Phasematched Waveguides”. In: *Optics Express* 19.20 (Sept. 2011), pp. 18754–18773. (Visited on 02/18/2019).

[77] Marc Jankowski et al. “Temporal simultons in optical parametric oscillators”. In: *Physical review letters* 120.5 (2018), p. 053904.

[78] Johan Hult. “A Fourth-Order Runge–Kutta in the Interaction Picture Method for Simulating Supercontinuum Generation in Optical Fibers”. In: *Journal of Lightwave Technology* 25.12 (Dec. 2007), pp. 3770–3775.

Chapter 7

LARGE-SCALE TIME-MULTIPLEXED NANOPHOTONIC PARAMETRIC OSCILLATORS

Robert M. Gray†, **Ryoto Sekine**†, Luis Ledezma, Gordon H. Y. Li, Selina Zhou, Arkadev Roy, Midya Parto, and Alireza Marandi, "Large-scale time-multiplexed nanophotonic parametric oscillators," *arXiv:2405.17355*, (2024).
R.S. designed and fabricated the device, assisted the measurements, and contributed to developing the all-to-all coupled network architecture.
† denotes equal contributions

7.1 Abstract

Arrays of nonlinear resonators offer a fertile ground for a wide range of complex phenomena and opportunities for advanced photonic sensing and computing. Recently, significant attention has focused on studying coupled resonators in special-purpose configurations either on chips or in table-top experiments. However, a path to realizing a large-scale programmable network of nonlinear photonic resonators remains elusive because of the challenges associated with simultaneously achieving strong nonlinearity, independent operation of the resonators, and programmability of the couplings. In this work, we break these barriers by realizing large-scale, time-multiplexed optical parametric oscillators (OPOs) on a single lithium niobate nanophotonic chip. We show independent operation of 70 identical OPOs in an ultrafast nanophotonic circuit. The OPOs exhibit an ultra-low threshold of a few picojoules, substantially surpassing the strength of nonlinearity of other platforms. Using our ultrafast nanophotonic circuit, a network of N OPOs with programmable all-to-all couplings requires only a few additional components. The time-multiplexed nanophotonic OPOs can enable myriad applications, including ultrafast classical and quantum information processing.

7.2 Introduction

Nonlinear resonators are emerging as one of the most versatile building blocks for a wide range of photonic systems benefiting applications in quantum information processing [1, 2], stochastic computing [3, 4], metrology [5, 6], and spectroscopy and sensing [7, 8], among others. Coupled nonlinear resonators further promise broad potentials, which have been showcased through a variety of table-top experiments, for instance using optical parametric oscillators (OPOs) [9, 10, 11, 12] and lasers [13, 14]. However, in nanophotonics, demonstrations of coupled nonlinear resonators remain in the small-scale regime [15, 16, 17, 18] or suffer from limited programmability [19, 20].

OPOs using quadratic nonlinearity are one of the most promising nonlinear photonic resonators, with a long history as table-top tunable sources in hard-to-

access wavelength ranges [21]. More recently, OPOs have been used for a wide range of applications spanning from frequency comb spectroscopy [22] to sensing [23], quantum information processing [24], and computing [25, 26, 27]. Advances in thin-film lithium niobate have enabled realization of nanophotonic OPOs [28, 29, 30] with substantial miniaturization and threshold enhancement due to the sub-micron modal confinement. Synchronous pumping of dispersion-engineered nanophotonic OPOs with ultrashort pulses is particularly important because it leads to ultralow-threshold operation [31] enabling opportunities for energy-efficient ultrabroad comb sources [32] and quantum information processing [33].

Ultrafast nanophotonic OPOs not only benefit from ultra-low-energy operation, they also enable large-scale time-domain multiplexing (TDM) for realization of programmable OPO networks. Time-multiplexed resonator networks have been demonstrated on table-top experiments for a wide range of studies in optical computing [34, 26, 11], topological photonics [35, 36], and non-equilibrium phase transitions [12], among others. Compared with other multiplexing schemes for realizing nonlinear resonators, such as spatial and spectral multiplexing [37], TDM benefits from scalability, and the strength of nonlinearity [14].

Here, we demonstrate the first nanophotonic realization of large-scale time-multiplexed OPOs in lithium niobate (LN). By leveraging a large parametric gain and dispersion engineering, we achieve simultaneous oscillation of as many as 70 independent OPOs at a 17.5 GHz repetition rate, limited primarily by the speeds of our pump repetition rate and detection electronics. We verify the independence of the oscillators through an interferometric measurement at the output of the chip which confirms the vacuum-seeded randomness of each oscillator.

7.3 Results

The on-chip time-multiplexed OPO system is schematically depicted in Fig. 7.1A. The temporally separated resonators, equivalent to the N independent resonators shown in Fig. 7.1B, share the same optical path length and long periodically poled section. High gain provided by the periodically poled region ensures a low on-chip threshold pulse energy of a few pJ for the ps pulses used in the experiment. Adiabatic tapers couple more than 96% of the signal light into the resonator while ensuring very little coupling ($\leq 2\%$) for the pump. Finally, dispersion engineering of the waveguide geometry ensures near-zero group velocity mismatch between the pump and signal during the nonlinear interaction to achieve a high gain and gain bandwidth as well as near-zero group velocity dispersion for the signal in the roundtrip, which preserves the short-pulse operation necessary for maintaining the independence of the oscillators.

We operate in both the non-degenerate (Fig. 7.1C) and degenerate (Fig. 7.1D) regimes by adjusting the pump frequency detuning with respect to the cavity. In the non-degenerate regime, pump photons are split into signal and idler photons at different frequencies, and their phase relationship is given by:

$$\phi_p - \phi_s - \phi_i = \frac{\pi}{2}, \tag{7.1}$$

where ϕ_p, ϕ_s, and ϕ_i are the pump, signal, and idler phase, respectively. Taking the pump phase as determined, this relationship leaves the signal and idler phases free, constraining only their sum. Thus, as illustrated in the phase space diagram of Fig. 7.1C, wherein the radial coordinate represents the pulse amplitude and the angle represents the phase, the phases are random and may take on any value.

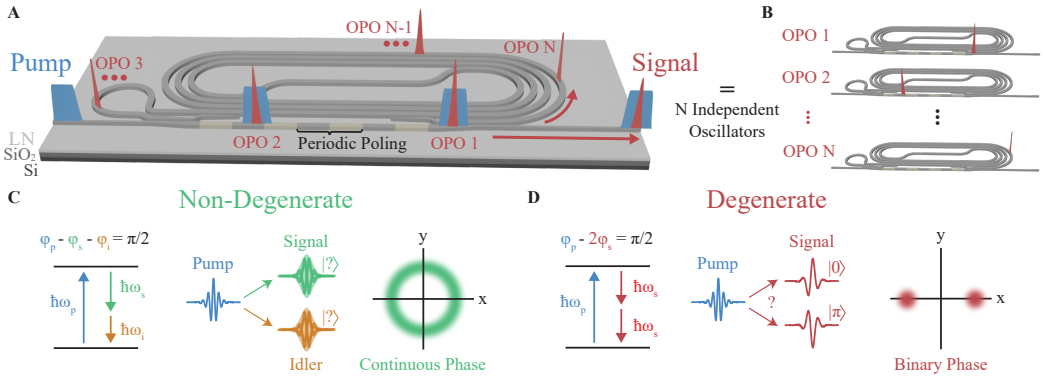

Figure 7.1: **Time-multiplexed nanophotonic OPOs.** (**A**) Schematic of the device based on thin-film lithium niobate. N pulses in a long cavity are equivalent to (**B**) N independent time-multiplexed oscillators. (**C**) In the non-degenerate regime, the pump photons split into signal and idler photons at different frequencies. In this case, the phase of each is unconstrained, as shown in the signal phase space diagram. (**D**) In the degenerate regime, the pump photons split into indistinguishable signal photons at the half-harmonic of the pump, resulting in a binary phase for the signal.

By contrast, in the degenerate regime, the signal and idler both resonate at the half-harmonic of the pump and thus are indistinguishable from one another. In this case, equation 1 consolidates to:

$$\phi_p - 2\phi_s = \frac{\pi}{2}, \tag{7.2}$$

such that signal phase is restricted to one of two phase states (Fig. 7.1D), which we refer to as $|0\rangle$ and $|\pi\rangle$.

Figure 7.2 shows the measurement protocol for ensuring independence of the N oscillators in the time-multiplexed OPO cavity. The measurement setup is shown in Fig. 7.2A and is described in further detail in Supplementary Information Section 1. The cavity is pumped by ps pulses at 1045 nm generated by an electro-optic (EO) comb with a variable repetition rate. TDM is achieved through selecting a pump repetition period, T_{rep}, that is a harmonic of the cavity roundtrip time, T_{RT}, meaning $T_{rep} = T_{RT}/N$, such that N OPOs are made to oscillate simultaneously in the long spiral cavity. In our system, the 53-cm spiral results in a round-trip time of 4 ns and corresponding 250-MHz FSR. The signal is coupled into an unbalanced Mach-Zehnder interferometer (MZI), the output of which is collected on a photodetector, which allows for measurement of the relative phases of the output pulse train. A 92:8 splitter placed before the MZI additionally sends a fraction of the signal to

a reference photodetector for normalizing the measurement. The inset shows a microscope image (left) and SEM image (right) of a portion of the long spiral resonator.

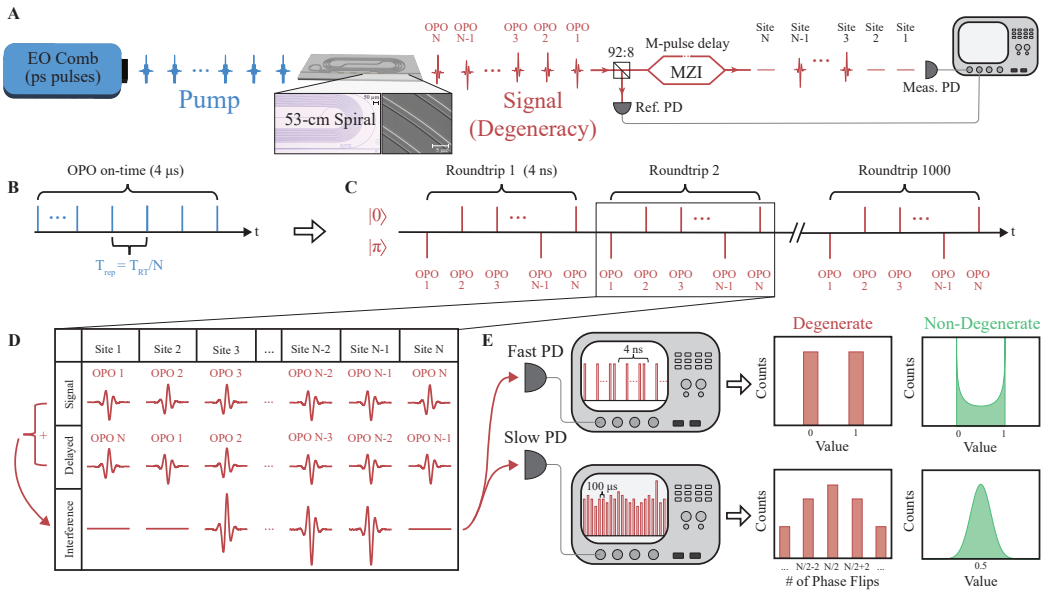

Figure 7.2: **Measurement of independent oscillators.** (**A**) Schematic of the measurement setup. The nanophotonic chip is pumped by the output of an EO comb which provides ps pulses at GHz repetition rates. The output is passed through a fiber interferometer with an M-pulse delay for characterizing the relative phases of the output pulses. The inset shows microscope (left) and SEM (right) images of a segment of the spiral resonator. (**B**) Illustration of the pump pulse train, with 4-μs on-time. (**C**) Example signal pulse train at degeneracy, showing the binary phase of the output. Each OPO iteration contains a repeating 4-ns random pattern of $|0\rangle$ and $|\pi\rangle$. (**D**) Principle of the interferometric measurement of the OPO signal, illustrated with a 1-pulse delay. (**E**) Expected outputs for pulse-to-pulse (fast) and average (slow) measurements. EO, electro-optic; PD, photodetector.

Figures 7.2B and 7.2C illustrate an example of the pump and signal pulse trains, respectively. The pump (Fig. 7.2B) consists of a train of ps pulses to pump N time-multiplexed OPOs which are kept on for 1000 roundtrips (4 μs). The resulting signal (Fig. 7.2C) is composed of a train of N pulses with phases sampled randomly from the allowed phase states of the system. In the depicted case of degeneracy, they are sampled from the binary states $|0\rangle$ and $|\pi\rangle$.

Figure 7.2D depicts the passage of the signal through the MZI for each measurement. Here, a 1-pulse delay is assumed for simplicity. The top row shows the signal arm while the middle row shows the delayed arm. Their recombination results in the interference signal shown in the bottom row, which is finally sent to the measurement detector. In our experiment, this measurement is repeated every 100 μs by turning the OPOs off and sending another 4-μs set of pump pulses for collecting statistics. As shown in Fig. 7.2E, we have employed both a fast detector

for shot-to-shot measurement of the resulting intensity in each pulse site and a slow detector for averaging over the MZI output for each 4-μs set of pump pulses.

Each time the OPOs are turned on, each independent OPO signal takes a random phase. In the case of fast detector measurements (Fig. 7.2E, top) and degenerate operation, the corresponding normalized pulse peak intensity distribution taken across many OPO iterations should resemble a Bernoulli distribution with a 50% probability for obtaining either 0 or 1, such that the probability mass function (PMF) is given by:

$$f(x) = \begin{cases} 0.5 & x = 0, \\ 0.5 & x = 1, \\ 0 & \text{otherwise.} \end{cases} \tag{7.3}$$

By contrast, in the non-degenerate case where the signal can take on an arbitrary phase, the expected theoretical distribution is given by the probability density function (PDF):

$$f(x) = \begin{cases} \frac{1}{\pi\sqrt{x(1-x)}} & 0 \leq x < 1, \\ 0 & \text{otherwise.} \end{cases} \tag{7.4}$$

In the case of slow detector measurements (Fig. 7.2E, bottom), the average value of the MZI signal over the 4-ns pulse train should be considered. Such a measurement is helpful for obtaining statistics over a larger number of OPO iterations as well as for improving measurement SNR in the case where the OPO repetition rate approaches the detection bandwidth of the fast measurement system. In this case, the PMF for the degenerate case is expected to be:

$$f(x) = \begin{cases} \frac{1}{2^{N-1}}\binom{N}{k} & k \text{ even}, \\ 0 & \text{otherwise}, \end{cases} \tag{7.5}$$

where $k \in 0, 1, ..., N$ is the number of phase flips between consecutive pulses in the train of N pulses. Meanwhile, for large N, the non-degenerate system should tend towards a normal distribution. More information regarding the expected outputs can be found in Supplementary Section 2.

We first measure the case where N = 40, meaning the repetition rate of the pump is set to be 10 GHz, the results of which are presented in Fig. 7.3. Figures 7.3A-D contain the results of the interferometric measurement on a 25-GHz fast detector, with Figs. 7.3A-B showing the output when the laser is detuned to degeneracy while Figs. 3C-D show the output in the non-degenerate case. Figures 7.3A and 7.3C show examples of the directly measured interference pulse trains. The y-axis shows the detector voltage, normalized such that 0 and 1 roughly correspond to the cases of constructive and destructive interference between the arms of the MZI, respectively. As expected theoretically, the MZI output is binary in the case of degeneracy (Fig. 7.3A). This is further confirmed by the histogram of the peak pulse intensities over 30 OPO iterations shown in Fig. 7.3B, where we observe two well-separated lobes

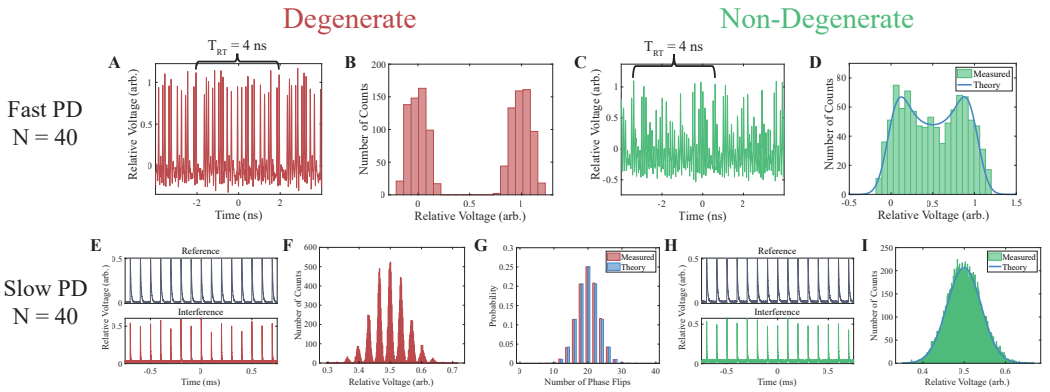

Figure 7.3: **Interference measurements for N = 40.** (**A**-**D**) Fast detector measurements in the degenerate (A-B) and non-degenerate (C-D) regimes. Examples of the measured interference pulse trains are shown in (A) and (C). Histograms of the measured peak pulse intensities over 30 degenerate (B) and 25 non-degenerate (D) interference measurements show good agreement with theoretical expectations. (**E**-**I**) Slow detector measurements in the degenerate (E-G) and non-degenerate (H-I) regimes. Example data out of the slow detector is shown in (E) and (H). The reference trace (top) is sampled from the OPO output before the MZI and is used for intensity noise correction of the interference trace (bottom). Histograms of the resulting corrected traces are shown in (F) and (I). As expected theoretically, discrete peaks are observed in the degenerate case (F), whereas a continuous distribution is seen in the the non-degenerate case (I). The discrete peaks in the degenerate case are binned for comparison with theory (G), showing good agreement.

around 1 and 0 with nearly equal probability. As discussed in Supplementary Section 2, one key difference between our measurement and theory is the addition of detector noise which results in the measured distribution looking like the convolution of the expected theoretical distribution with a Gaussian. Meanwhile, the MZI output in the non-degenerate regime can take on any value between 0 and 1 (Fig. 7.3C). By taking the histogram of the pulse peaks over 25 OPO iterations, we obtain the distribution shown in Fig. 7.3D. As expected, the measured distribution is bimodal, and it agrees well with the theoretical fit.

The independence of the pulses is further confirmed through the slow detector measurements shown in Fig. 7.3E-I. Figure 7.3E shows a snippet of the detected signal in the degenerate case. The reference measurement is acquired directly after the chip output and is used for intensity noise correction, while the interference data is taken after the MZI. Both are measured using a 1 MHz detector such that each of the observed peaks correspond to one OPO iteration. The histogram of Fig. 7.3F contains the peak values from the intensity-noise-corrected interference trace over 2 s of data, corresponding to 19,999 OPO iterations. Here, the observance of a discretization in the measured values confirms operation in the degenerate regime. Further comparison between the measurement and the expected theoretical distribution in Fig. 7.3G shows strikingly good agreement, verifying the independence

of the OPOs in the time-multiplexed system.

The corresponding non-degenerate measurement is shown in Figs. 7.3H-I. Figure 7.3H shows a snippet of the data in this case. In contrast to the degenerate case, the interference output is not discretized, an observation confirmed by the histogram shown in Fig. 7.3I. Again, the histogram consists of 2 s of data. A Gaussian fit over the histogram shows good agreement between the measured data and the theoretically expected distribution.

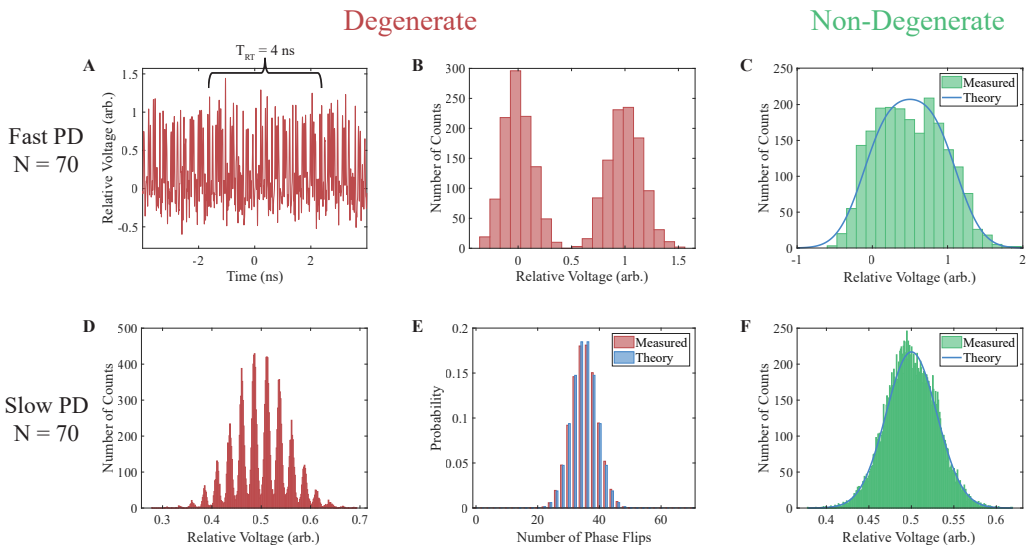

Figure 7.4: **Extension to N = 70.** (**A**) Example interference pulse train on the fast detector in the degenerate case. (**B**) Histogram of peak pulse intensities over 30 degenerate OPO iterations, exhibiting the expected Bernoulli distribution. (**C**) Corresponding histogram of fast detector measurements in the non-degenerate regime and theoretical fit. (**D**) Histogram of slow detector measurements in the degenerate regime. (**E**) Theoretical comparison after binning the distribution from (D), showing close agreement. (**F**) Histogram of non-degenerate interference data and corresponding Gaussian fit.

One advantage of the TDM scheme is the ability to change the number of sites without significant additional overhead, making computation of problems of different sizes readily achievable. We demonstrate this by pushing our system to N = 70 at a pump repetition rate of 17.5 GHz. Our current measurement is limited by the modulators used in the EO comb and bandwidth of our fast photodetector. However, as faster nanophotonic pump sources become available, we believe the current time-multiplexed system will be capable of supporting much larger Ns and significantly faster pump rates.

Figure 7.4 presents the results for pumping with N = 70. As can be seen in the raw data of Fig. 7.4A measured with the fast detector, pumping near the limits of our electronics results in a reduced signal-to-noise compared to the case of N = 40. However, the histogram of fast detector measurements at degeneracy over 30

OPO iterations depicted in Fig. 7.4B again shows a clear Bernoulli distribution, in accordance with the theory. This stands in contrast with the non-degenerate case of Fig. 7.4C, which also agrees well with the theoretical fit. Here, the bimodality is less prevalent because of the relatively larger detector noise. The slow detector measurements in Figs. 7.4D-F further confirm that independence is maintained. At degeneracy, discrete values are again observed in the histogram (Fig. 7.4D), and the distribution is shown in Fig. 7.4E to match the theoretically expected distribution. Likewise, the non-degenerate measurement shown in Fig. 7.4F agrees well with the Gaussian fit.

7.4 Outlook

In this work, we have demonstrated a large-scale system of time-multiplexed OPOs in lithium niobate nanophotonics and shown the independence of the oscillators in both the degenerate and non-degenerate regimes through interferometric measurements of the device output. The addition of programmable couplings between the oscillators will allow for exploration of a multitude of fundamental phenomena and enable large-scale, all-optical information processing. Towards this end, we propose the architecture illustrated in Fig. 7.5A. Here, the main cavity consisting of N time-multiplexed OPOs is accompanied by a secondary memory cavity with N + 1 sites. The cavities are coupled such that pulses in the main and memory cavities can interact, and the strength of the coupling is set through MZI-based intensity modulators using fast electro-optic modulators (EOMs). A second pump and periodically poled region in the memory cavity is used to compensate the roundtrip loss.

In general, information processing requires a mixture of both linear and nonlinear operations. In this architecture, linear operations, such as multiply-accumulate operations or dot products, are achieved through arbitrary all-to-all couplings which may be implemented over N + 1 roundtrips of the memory cavity. In the first roundtrip, pulses from the main cavity are coupled to the memory cavity through the right MZI channel. In the subsequent N roundtrips, couplings occur as illustrated in the connectivity diagrams of Fig. 7.5B from the memory cavity back to the main cavity through the left MZI channel. The memory cavity may then be emptied of pulses to allow the next coupling cycle to begin. Meanwhile, all-optical nonlinear functions [38] may be applied by modulating the pump in the main cavity. Such a system, therefore, offers a flexible platform for studying systems of coupled nonlinear resonators and highlights the importance of our demonstrated time-multiplexed OPO as a first step towards achieving integrated ultrafast, energy-efficient, and scalable all-optical information processing systems.

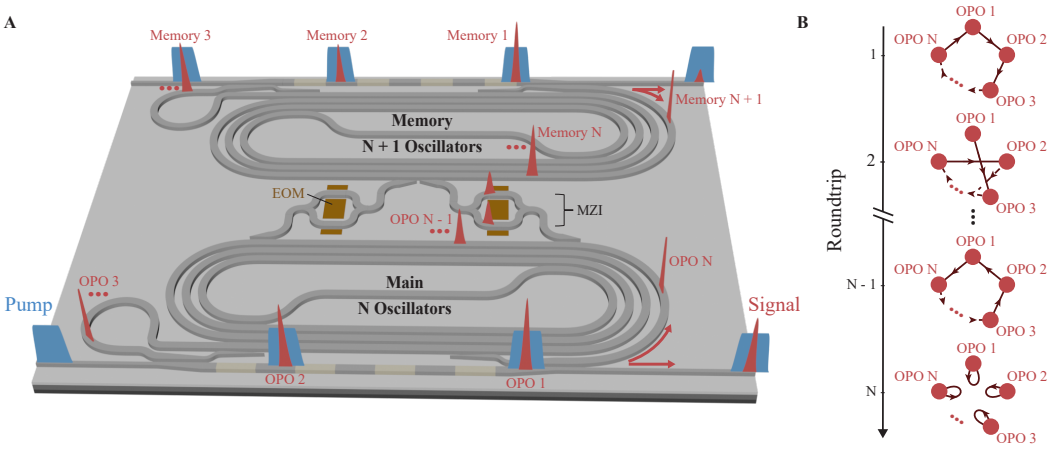

Figure 7.5: **Time-multiplexed architecture for programmable all-to-all coupled nonlinear resonators.** (**A**) The main resonator (bottom) with N time-multiplexed OPOs is coupled to a secondary memory cavity (top), designed to have N + 1 sites. Losses in the memory cavity are compensated by a secondary pump and poled region. EOMs in the coupling regions are used to program an MZI-based intensity modulator, which can be used to tune the strength of the coupled pulse. (**B**) Connectivity diagrams showing how arbitrary couplings are achieved over N roundtrips. EOM, electro-optic modulator; MZI, Mach-Zehnder interferometer.

References

[1] Warit Asavanant et al. “Generation of time-domain-multiplexed two-dimensional cluster state”. In: *Science* 366.6463 (2019), pp. 373–376.

[2] Mikkel V Larsen et al. “Deterministic generation of a two-dimensional cluster state”. In: *Science* 366.6463 (2019), pp. 369–372.

[3] Alireza Marandi et al. “All-optical quantum random bit generation from intrinsically binary phase of parametric oscillators”. In: *Optics express* 20.17 (2012), pp. 19322–19330.

[4] Charles Roques-Carmes et al. “Biasing the quantum vacuum to control macroscopic probability distributions”. In: *Science* 381.6654 (2023), pp. 205–209.

[5] Ewelina Obrzud et al. “A microphotonic astrocomb”. In: *Nature Photonics* 13.1 (2019), pp. 31–35.

[6] Daryl T Spencer et al. “An optical-frequency synthesizer using integrated photonics”. In: *Nature* 557.7703 (2018), pp. 81–85.

[7] Zhaowei Zhang, Tom Gardiner, and Derryck T Reid. “Mid-infrared dual-comb spectroscopy with an optical parametric oscillator”. In: *Optics letters* 38.16 (2013), pp. 3148–3150.

[8] Liron Stern et al. “Direct Kerr frequency comb atomic spectroscopy and stabilization”. In: *Science advances* 6.9 (2020), eaax6230.

[9] Peter L McMahon et al. “A fully programmable 100-spin coherent Ising machine with all-to-all connections”. In: *Science* 354.6312 (2016), pp. 614–617.

[10] Yutaka Takeda et al. “Boltzmann sampling for an XY model using a non-degenerate optical parametric oscillator network”. In: *Quantum Science and Technology* 3.1 (2017), p. 014004.

[11] Toshimori Honjo et al. “100,000-spin coherent Ising machine”. In: *Science advances* 7.40 (2021), eabh0952.

[12] Arkadev Roy et al. “Non-equilibrium spectral phase transitions in coupled nonlinear optical resonators”. In: *Nature Physics* 19.3 (2023), pp. 427–434.

[13] Geva Arwas et al. “Anyonic-parity-time symmetry in complex-coupled lasers”. In: *Science advances* 8.22 (2022), eabm7454.

[14] Christian Leefmans et al. “Topological temporally mode-locked laser”. In: *arXiv preprint arXiv:2209.00762* (2022).

[15] Arghadeep Pal et al. “Linear and Nonlinear Coupling of Twin-Resonators with Kerr Nonlinearity”. In: *arXiv preprint arXiv:2404.05646* (2024).

[16] Mian Zhang et al. “Electronically programmable photonic molecule”. In: *Nature Photonics* 13.1 (2019), pp. 36–40.

[17] Jae K Jang et al. “Synchronization of coupled optical microresonators”. In: *Nature Photonics* 12.11 (2018), pp. 688–693.

[18] Yoshitomo Okawachi et al. “Demonstration of chip-based coupled degenerate optical parametric oscillators for realizing a nanophotonic spin-glass”. In: *Nature communications* 11.1 (2020), p. 4119.

[19] Miguel A Bandres et al. “Topological insulator laser: Experiments”. In: *Science* 359.6381 (2018), eaar4005.

[20] Sunil Mittal et al. “Topological frequency combs and nested temporal solitons”. In: *Nature Physics* 17.10 (2021), pp. 1169–1176.

[21] Malcolm H Dunn and Majid Ebrahimzadeh. “Parametric generation of tunable light from continuous-wave to femtosecond pulses”. In: *Science* 286.5444 (1999), pp. 1513–1517.

[22] AV Muraviev et al. “Massively parallel sensing of trace molecules and their isotopologues with broadband subharmonic mid-infrared frequency combs”. In: *Nature Photonics* 12.4 (2018), pp. 209–214.

[23] Robert M Gray et al. “Cavity-soliton-enhanced mid-IR molecular sensing”. In: *arXiv preprint arXiv:2301.07826* (2023).

[24] Shunya Konno et al. “Logical states for fault-tolerant quantum computation with propagating light”. In: *Science* 383.6680 (2024), pp. 289–293.

[25] Zhe Wang et al. “Coherent Ising machine based on degenerate optical parametric oscillators”. In: *Physical Review A* 88.6 (2013), p. 063853.

[26] Alireza Marandi et al. “Network of time-multiplexed optical parametric oscillators as a coherent Ising machine”. In: *Nature Photonics* 8.12 (2014), pp. 937–942.

[27] Yoshihisa Yamamoto et al. “Coherent Ising machines—optical neural networks operating at the quantum limit”. In: *npj Quantum Information* 3.1 (2017), p. 49.

[28] Timothy P McKenna et al. “Ultra-low-power second-order nonlinear optics on a chip”. In: *Nature Communications* 13.1 (2022), p. 4532.

[29] Juanjuan Lu et al. “Ultralow-threshold thin-film lithium niobate optical parametric oscillator”. In: *Optica* 8.4 (2021), pp. 539–544.

[30] Luis Ledezma et al. “Intense optical parametric amplification in dispersion-engineered nanophotonic lithium niobate waveguides”. In: *Optica* 9.3 (2022), pp. 303–308.

[31] Arkadev Roy et al. “Visible-to-mid-IR tunable frequency comb in nanophotonics”. In: *Nature Communications* 14.1 (2023), p. 6549.

[32] Ryoto Sekine et al. “Multi-Octave Frequency Comb from an Ultra-Low-Threshold Nanophotonic Parametric Oscillator”. In: *arXiv preprint arXiv:2309.04545* (2023).

[33] Ryotatsu Yanagimoto et al. “Mesoscopic ultrafast nonlinear optics–The emergence of multimode quantum non-Gaussian physics”. In: *arXiv preprint arXiv:2311.13775* (2023).

[34] Gordon HY Li et al. “Photonic elementary cellular automata for simulation of complex phenomena”. In: *Light: Science & Applications* 12.1 (2023), p. 132.

[35] Christian Leefmans et al. “Topological dissipation in a time-multiplexed photonic resonator network”. In: *Nature Physics* 18.4 (2022), pp. 442–449.

[36] Midya Parto et al. “Non-Abelian effects in dissipative photonic topological lattices”. In: *Nature Communications* 14.1 (2023), p. 1440.

[37] Tomoki Ozawa and Hannah M Price. “Topological quantum matter in synthetic dimensions”. In: *Nature Reviews Physics* 1.5 (2019), pp. 349–357.

[38] Gordon HY Li et al. “All-optical ultrafast ReLU function for energy-efficient nanophotonic deep learning”. In: *Nanophotonics* 12.5 (2023), pp. 847–855.

Chapter 8

OUTLOOK

In this dissertation, we have developed the nanophotonic PPLN platform and demonstrated its potential to offer new information processing opportunities at the device, circuit, and system levels. However, we have only begun to explore the possibilities this platform offers. With the foundational work now in place, we are well-positioned to address more ambitious challenges. In this chapter, I aim to provide a glimpse of the future advancements and applications that this platform may enable.

8.1 Large Scale Information Processors

8.1.1 Coupled OPO Networks

Perhaps one of the most salient applications of parametric $\chi^{(2)}$ photonics is in analog optical computing. While electronics-based von Neumann machines, from smart watches to supercomputers, have revolutionized our way of life and can seemingly do anything – from streaming the Tour de France to putting a man on the moon – we are starting to understand the limitations of digital computers. For example, electronic supercomputers cannot operate at THz clock rates, compute as energy efficiently as the human brain, or take advantage of quantum parallelism. These new capabilities are becoming ever more desirable and relevant given the computation problems of today. Indeed, since 2012 the amount of computation required to train prominent AI problems has doubled every 3.4 months[1] (in comparison Moore's law has a two year doubling period) and we are fast approaching the regime where we simply do not have enough resources to provide the level of computation required to solve increasingly difficult challenges[2]. Furthermore, there is an ever growing sphere of computationally tractable and yet environmentally unsustainable tasks[3]. A recent study has shown that training a natural language processing (NLP) model from scratch emits as much CO_2 as five cars in their lifetimes[4]. In other words, although electronics can in principle provide universal computing, their practical performance is limited by hardware, architecture, and the available resources, effectively rendering some real-life tasks unsolvable.

To address some of these problems, photonic computers based on second-order nonlinearities have been recently proposed. In particular, all-optical computers can potentially operate in THz rates[5] and exhibit aJ activation functions[6]. These features provide valuable resources for certain artificial neural network problems, especially those involving analog and time-dependent optical signals obtained for instance from lidars. In addition, by harnessing the rich physics arising in photonic platforms, new paradigms of unconventional computing can be explored. Examples of these include NP-hard solvers such as coherent Ising machines and optical quantum information processors (see Section 8.1.2).

It is worth-while noting that many legitimate concerns about the scalability of

optical computers have been raised in the past[7, 8, 9], and these are perhaps the reason why optical computers, table-top implementations of which already existed in the 1980s[10], have yet to hit mainstream commercialization. We argue however, that the landscape has recently changed. First, with the recent progress in $\chi^{(2)}$ integrated photonics, we finally have access to strong on-chip nonlinearities, the necessary ingredient for all-optical activation functions and switches – essential building blocks for computers. Furthermore, due to the much larger nonlinearities provided by $\chi^{(2)}$ processes as compared to $\chi^{(3)}$ photonics, many applications such as all-optical switching can be realized in single-pass devices[11], without the need of high-Q cavities. Combined with the success in building linear operation solvers[12], we finally have the toolkit to perform both linear[13, 14] and nonlinear[15, 16, 17] operations on the same integrated material platform. Secondly, we have reached technological advancement to exploit time[18, 19], wavelength[20, 21], and spatial division multiplexing[22, 23] to devise non-von Neumann computer architectures tailored to the strengths and limitations of photonics. Thus, despite the comparatively large footprint of $\chi^{(2)}$ nonlinear elements compared to electronic transistors, we now know that with a single nonlinear optical element coupled to linear waveguides one can perform meaningful computation, such as reservoir computers[24, 25] and 100,000-node ising machines[26]. Finally, and perhaps the most importantly, even the silicon industry has realized the need of exploring so-called *More than Moore* architectures[27], and as such there is a large societal/industrial impetus to explore alternative unconventional computing schemes.

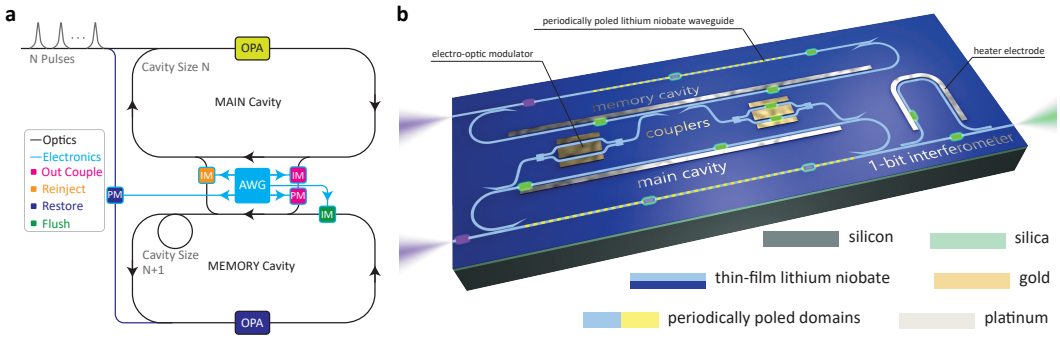

Figure 8.1: **OPO Network Information Processor**. **a** architecture and **b** illustration of a coupled OPO processor chip. The latter was adapted from [28].

Nanophotonic PPLN has reached a level of maturity where we can now explore all-optical information processors that demonstrate the clear advantages of optics. In Chapter 7, we introduced one such architecture – a scalable and flexible framework for time-multiplexed photonic computing. As depicted in Fig. 8.1a, this system comprises two synchronously-pumped pulsed OPOs with high-speed programmable couplings between the cavities. One OPO functions as the main cavity where the computation occurs, while the other serves as a memory cavity to facilitate inter-pulse interactions. Both linear and nonlinear operations can be performed by precisely controlling the pump pulses and the forward/backward couplings be-

tween the two cavities. This architecture enables all-optical computation that is not limited by electronic bandwidth, can be scaled to accommodate arbitrary problem sizes without relying on impractical numbers of delay lines, and allows fully programmable all-to-all connections between pulses. The architecture is particularly well-suited for tackling computational problems such as combinatorial optimization, neuromorphic computing, and cellular automata. Given its scalability with all-to-all connectivity, its ability to operate at optical computation rates, and its capacity to harness the rich dynamics of OPOs [29, 30, 31], we believe this system is the perfect platform to demonstrate the advantages of information processing with optics.

While this architecture is ambitious from both fabrication and measurement perspectives, significant progress is being made toward its realization. One major challenge was integrating high-speed RF electronics in a manner compatible with QPM, but this hurdle has largely been mitigated. Further simplification of the experimental setup can be achieved by transitioning to 775 nm and 1550 nm wavelengths, allowing the 1-bit delay in Figure 8.1b to be replaced with a homodyne measurement scheme and utilizing high-speed detectors with significantly better signal-to-noise ratios (SNR). Recently, substantial progress has been made toward phase matching 1550 nm nanophotonic PPLN waveguides.

In this network, the problem size N is primarily defined by the length of the memory cavity and the problem encoding speed, with the latter constrained by the bandwidth of the switch used in the encoding scheme. Using realistic current technology, we can conceive of memory cavities 1 meter long and employing EOMs operating at 100 GHz, allowing for a problem size N of 1k. If on-chip losses can be reduced to enable 10-meter-long resonators and 10 THz switches, as discussed in Chapter 4, problem sizes approaching a million are possible. Notably, even as the problem size N scales, the number of components required in this platform remains fixed.

8.1.2 Quantum Information Processors

Quantum information processing (QIP) has been widely explored using discrete variables with qubits, on many physical platforms such as superconducting circuits, photonics, trapped ions, quantum dots, nuclear spins, and neutral atoms. In our nanophotonic PPLN platform we are interested in another universal paradigm for QIP that makes use of continuous variables (CV) - in this case the amplitude and phase quadratures of the quantized electromagnetic field. The key interest in CVQIP comes primarily from its unprecedented potential to generate massively entangled quantum states (cluster states) at room temperature using optical parametric oscillators (OPOs). These have been demonstrated to possess long coherence times.

Compared to other CVQIP approaches, nanophotonic PPLN is appealing for several reasons. First, the large quadratic nonlinearity combined with the tight mode confinement in nanophotonic waveguides, allows for record levels of on-chip squeezing. Second, these squeezed state can be achieved over large bandwidths, which are beneficial for all-optical ultrafast quantum computation, quantum communication, and quantum metrology. Finally, the fact that these states are prepared

on-chip enables the quantum states to be generated and processed within the same photonic integrated circuit (PIC) without experiencing on-chip to off-chip coupling losses.

One of the most fundamental quantum states of light is squeezed vacuum, in which noise in one of the quadratures is less than the standard quantum noise limit. Significant progress has been made in the generation of optical squeezed vacuum and its utilization for numerous applications. However, it remains challenging to generate, manipulate, and measure such quantum states in nanophotonics with performances required for a wide range of scalable quantum information systems. In Chapter 5, we demonstrated how this challenge can be overcome in lithium niobate nanophotonics by utilizing ultrashort-pulse phase-sensitive amplifiers for both generation and all-optical measurement of squeezed states on the same chip. We generate a squeezed state spanning over more than 25 THz of bandwidth supporting only a few optical cycles, and measure a maximum of 4.9 dB of squeezing ($\sim$11 dB inferred). This level of squeezing surpasses the requirements for a wide range of quantum information systems. Our results on generating and measuring few-optical-cycle squeezed states in nanophotonics enables a practical path towards scalable quantum information systems with THz clock rates and open opportunities for studying non-classical nature of light in the sub-cycle regime.

While the study of Gaussian states is of great significance in understanding the dynamcis of Bose gases and the theory of optical coherence, from a computation perspective they yield no advantage and can be efficiently simulated by classical resources. To implement universal quantum computation using CVs, it is widely believed that non-Gaussian states are required. While the generation of non-Guassian states has generally been challenging, leveraging the record level of squeezing in TFLN, we hope to generate, process, and study non-Gaussian states beginning with Cat States. Indeed, as discussed in [32], if we can further lower the loss in our waveguides we may be able to breach the $g/\kappa \rightarrow 1$ barrier to access the strong coupling regime in the near future, the implications of which have been explored in detail[32, 33, 34]. Furthermore, our recent progress towards demonstrating time-multiplexed coupled OPO networks may become a fertile playground for quantum information processing.

Beyond information processing in the strict sense of CVQIP, I am excited about the potential of our newly developed capabilities to generate, manipulate, and measure quantum states of light for enhanced sensing and metrology. Some of these applications are being explored by the Scott Cushing group at Caltech.

8.1.3 Ultrashort Pulse Synthesizers

Using the techniques described in this dissertation, we can develop an ultra-short-pulse synthesizer at the few- to single-cycle level on an integrated photonic chip. An example of such as circuit is shown in Fig. 8.2. This system achieves pulse compression and amplification, sub-cycle control, and wavelength conversion through precise dispersion and quasi-phase-matching (QPM) engineering, paired with controllable ultrafast nonlinearity on-chip, in both cavity and single-pass configurations.

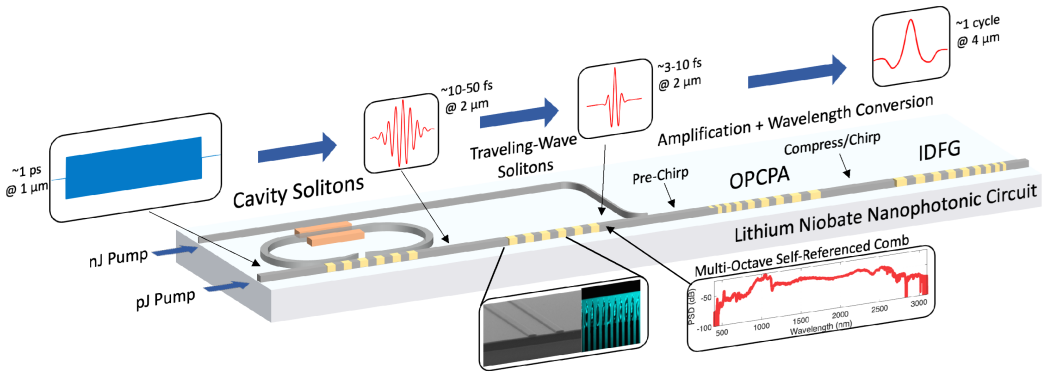

Figure 8.2: **On-Chip Photonic Ultra-Short-Pulse Synthesizer**. Taken from US provisional patent (CIT-9055-P).

Extreme pulse compression is achieved via a combination of a multi-octave optical parametric oscillator (OPO), quadratic cavity soliton, and traveling-wave quadratic soliton. Further pulse synthesis and amplification are performed through on-chip optical parametric chirped pulse amplification (OPCPA). Wavelength conversion, including into the mid-infrared (mid-IR) region, is achieved using intrapulse difference frequency generation (IDFG). While ultrafast optical schemes have traditionally required meter-scale setups and nanojoule- to microjoule-level pulse energies, we are excited by the prospect of bringing these setups to millimeter-scale nanophotonic chips and picojoule- to femtojoule-level pulse energies. This advancement enables new information processing opportunities in fields such as attosecond physics, spectroscopy, and communications.

Over the past few years many parts of the pulse synthesizer in Fig. 8.2 have been developed in isolation. Here we will describe design details of the IDFG unit. IDFG benefits from requiring few components, being intrinsically carrier-envelope phase (CEP) stable, and ability to produce sub- to few-cycle output pulses. Figure 8.3a illustrates a simple design of a nano-waveguide on LN for IDFG. Unlike typical optical parametric amplification (OPA), IDFG only requires one input frequency comb, and in contrast to optical parametric oscillators (OPOs), it only requires a single pass through a nonlinear element. There are inherent advantages of bringing IDFG to a nanophotonic platform. Not only will the smaller mode confinement allow for significantly lower pump pulse energies, but the ability to dispersion engineer enables significantly more control of the DFG pulse shape. Lower group velocity dispersion (GVD) at the output pulse wavelength keeps the generated pulse from widening, and control over the group velocity mismatch (GVM) between the signal and idler pulses enables us to shape the output idler pulse[36]. Combined, these capabilities not only unlock novel use cases for IDFG on an integrated platform, but may also allow us to observe new physics in extreme dispersion regimes. Significant amount of dispersion engineering in LN nanophotonics [35] makes it an ideal platform for IDFG.

In Fig. 8.3b we show how tuning waveguide parameters on a TFLN on sap-

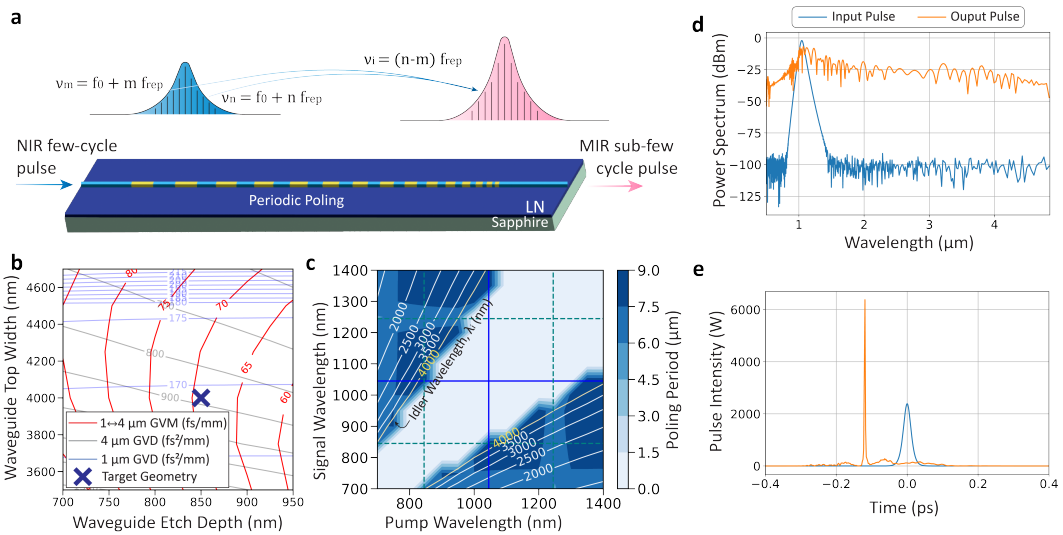

Figure 8.3: **IDFG**. (a) Concept of IDFG on thin film lithium niobate on sapphire. (b) Dispersion parameters of nanophotonic PPLN as a function of waveguide top width and etch depth for a 950 nm thick film. (c) Idler wavelengths and necessary poling periods for IDFG between various wavelengths of the pump, where the blue lines indicate the pump center wavelength. (d) Frequency spectra and (e) time domain simulations of IDFG in a waveguide with 8 mm of 8 μm poling to generate a MIR frequency comb, using the single envelope approach described in [35], suggesting the potential of generating single-cycle mid-IR pulses in nanophotonic LN.

phire substrate enables dispersion control between the 1 μm pump and 4 μm idler wavelengths in numerical simulation. The geometry indicated by the cross on the figure can support up to 4.8 μm modes, and as shown in Fig. 8.3c, by using various poling periods and pump wavelengths, a large range of mid-IR idler wavelengths can be generated. In Fig. 8.3d,e we show the simulated output spectra of an IDFG waveguide pumped with only 68 pJ of 25-fs pulses centered at 1 μm with a 250-MHz repetition rate. These simulation results suggest that single-cycle mid-IR optical pulses can be generated using IDFG in LN nanophotonics with further performance improvements expected from using more complicated dispersion engineering geometries and apodized periodic poling structures.

8.2 New Lasers ↔ New Nonlinear Optics

The fields of lasers and nonlinear optics have always been closely intertwined, with advancements in one often catalyzing breakthroughs in the other. This relationship dates back to the invention of the Ruby laser by Maiman in 1960, which enabled Franken to observe second harmonic generation. The subsequent development of more stable, high-power lasers improved conversion efficiencies in non-

linear optics. Conversely, nonlinear optics provided wavelength tuning capabilities to fixed-wavelength lasers, and as evidenced in the timeline in Fig. 1.1, nonlinear photonic concepts such as Q-switching, mode-locking, and OPCPA soon enabled the creation of higher power lasers.

The latest advancements in the nonlinear optical platforms of nanophotonic PPLN continue this tradition. We are already seeing demonstrations of fast RF modulations enabling a new class of on-chip mode-locked lasers. Efforts to achieve passive mode-locking as well as add broad tunability to gain media are actively being pursued. Dispersion engineering in this context can facilitate femtosecond-scale ultrashort pulse sources with compact footprints. In terms of wavelength tuning, we have already begun to see demonstrations of on-chip electrically pumped OPOs, where commercially available DBRs are co-packaged with our latest on-chip OPOs. This advancement opens up numerous exciting opportunities for applications in sensing, spectroscopy, and metrology.

Although these new light sources have mostly been limited to lab-scale demonstrations so far, historically, new light sources have often been followed by a surge of start-ups aiming to commercialize these technologies. With the emergence of start-ups focused on nanophotonic PPLN, it will be fascinating to see if these companies can overcome the "valley of death" and address the challenges of packaging and volume-scale manufacturing, thereby advancing the maturity and commercial viability of nanophotonic PPLN.

References

[1] Danny Hernandez and Tom B. Brown. *Measuring the Algorithmic Efficiency of Neural Networks*. 2020.

[2] Ryan Hamerly. "The future of deep learning is photonic: Reducing the energy needs of neural networks might require computing with light". In: *IEEE Spectrum* 58.7 (2021), pp. 30–47.

[3] David Patterson et al. *Carbon Emissions and Large Neural Network Training*. 2021.

[4] Emma Strubell, Ananya Ganesh, and Andrew McCallum. *Energy and Policy Considerations for Deep Learning in NLP*. 2019.

[5] P.R. Prucnal and B.J. Shastri. *Neuromorphic Photonics*. CRC Press, 2017. URL: https://books.google.com/books?id=VbvODgAAQBAJ.

[6] Gordon H. Y. Li et al. *All-optical ultrafast ReLU function for energy-efficient nanophotonic deep learning*. 2022.

[7] David A. B. Miller. "Are optical transistors the logical next step?" In: *Nature Photonics* 4.1 (Jan. 2010), pp. 3–5. URL: https://doi.org/10.1038/nphoton.2009.240.

[8] Robert W. Keyes. "Optical Logic-in the Light of Computer Technology". In: *Optica Acta: International Journal of Optics* 32.5 (), pp. 525–535.

[9] Robert W. Keyes. "What Makes a Good Computer Device?" In: *Science* 230.4722 (1985), pp. 138–144. URL: https://www.science.org/doi/abs/10.1126/science.230.4722.138.

[10] Demetri Psaltis and Nabil Farhat. "Optical information processing based on an associative-memory model of neural nets with thresholding and feedback". In: *Opt. Lett.* 10.2 (Feb. 1985), pp. 98–100. URL: http://opg.optica.org/ol/abstract.cfm?URI=ol-10-2-98.

[11] Qiushi Guo et al. *Femtojoule, femtosecond all-optical switching in lithium niobate nanophotonics*. 2021.

[12] Nicholas C. Harris et al. "Quantum transport simulations in a programmable nanophotonic processor". In: *Nature Photonics* 11.7 (July 2017), pp. 447–452. URL: https://doi.org/10.1038/nphoton.2017.95.

[13] Yaowen Hu et al. "On-chip electro-optic frequency shifters and beam splitters". In: *Nature* 599.7886 (Nov. 2021), pp. 587–593. URL: https://doi.org/10.1038/s41586-021-03999-x.

[14] Cheng Wang et al. "Integrated lithium niobate electro-optic modulators operating at CMOS-compatible voltages". In: *Nature* 562.7725 (Oct. 2018), pp. 101–104. URL: https://doi.org/10.1038/s41586-018-0551-y.

[15] Luis Ledezma†, **Ryoto Sekine**†, Qiushi Guo†, Rajveer Nehra, Saman Jahani, and Alireza Marandi. "Intense optical parametric amplification in dispersion-engineered nanophotonic lithium niobate waveguides". In: *Optica* 9.3 (Mar. 2022), pp. 303–308. URL: https://opg.optica.org/optica/abstract.cfm?URI=optica-9-3-303.

[16] Gordon H.Y. Li†, **Ryoto Sekine**†, Rajveer Nehra†, Robert M. Gray†, Luis Ledezma, Qiushi Guo, and Alireza Marandi. "All-optical ultrafast ReLU function for energy-efficient nanophotonic deep learning". In: *Nanophotonics* 12.5 (2023), pp. 847–855. URL: https://doi.org/10.1515/nanoph-2022-0137.

[17] Qiushi Guo†, **Ryoto Sekine**†, Luis Ledezma†, Rajveer Nehra, Devin J. Dean, Arkadev Roy, Robert M. Gray, Saman Jahani, and Alireza Marandi. "Femtojoule femtosecond all-optical switching in lithium niobate nanophotonics". In: *Nature Photonics* 16.9 (Sept. 2022), pp. 625–631. URL: https://doi.org/10.1038/s41566-022-01044-5.

[18] Xingyuan Xu et al. "11 TOPS photonic convolutional accelerator for optical neural networks". In: *Nature* 589.7840 (Jan. 2021), pp. 44–51. URL: https://doi.org/10.1038/s41586-020-03063-0.

[19] Xingyuan Xu et al. "Photonic Perceptron Based on a Kerr Microcomb for High-Speed, Scalable, Optical Neural Networks". In: *Laser & Photonics Reviews* 14.10 (2020), p. 2000070. URL: https://onlinelibrary.wiley.com/doi/abs/10.1002/lpor.202000070.

[20] J. Feldmann et al. "All-optical spiking neurosynaptic networks with self-learning capabilities". In: *Nature* 569.7755 (May 2019), pp. 208–214. URL: https://doi.org/10.1038/s41586-019-1157-8.

[21] J. Feldmann et al. "Parallel convolutional processing using an integrated photonic tensor core". In: *Nature* 589.7840 (Jan. 2021), pp. 52–58. URL: https://doi.org/10.1038/s41586-020-03070-1.

[22] Santosh Kumar, He Zhang, and Yu-Ping Huang. "Large-scale Ising emulation with four body interaction and all-to-all connections". In: *Communications Physics* 3.1 (June 2020), p. 108. URL: https://doi.org/10.1038/s42005-020-0376-5.

[23] J. Bueno et al. "Reinforcement learning in a large-scale photonic recurrent neural network". In: *Optica* 5.6 (June 2018), pp. 756–760. URL: http://opg.optica.org/optica/abstract.cfm?URI=optica-5-6-756.

[24] Y. Paquot et al. "Optoelectronic Reservoir Computing". In: *Scientific Reports* 2.1 (Feb. 2012), p. 287. URL: https://doi.org/10.1038/srep00287.

[25] L. Larger et al. "Photonic information processing beyond Turing: an optoelectronic implementation of reservoir computing". In: *Opt. Express* 20.3 (Jan. 2012), pp. 3241–3249. URL: http://opg.optica.org/oe/abstract.cfm?URI=oe-20-3-3241.

[26] Toshimori Honjo et al. "100,000-spin coherent Ising machine". In: *Science Advances* 7.40 (2021), eabh0952. URL: https://www.science.org/doi/abs/10.1126/sciadv.abh0952.

[27] Sankar Basu et al. "Nonsilicon, Non-von Neumann Computing—Part I [Scanning the Issue]". In: *Proceedings of the IEEE* 107.1 (2019), pp. 11–18.

[28] Gordon Li et al. *Time-multiplexed photonic computer*. US20240061316A1. 2023. URL: https://patents.google.com/patent/US20240061316A1/en.

[29] Arkadev Roy. “Parametrically-driven nonlinear optical resonators and their networks for sensing and computing”. PhD thesis. California Institute of Technology, 2023.

[30] Yoshihisa Yamamoto et al. “Coherent Ising machines—optical neural networks operating at the quantum limit”. In: *npj Quantum Information* 3.1 (2017), pp. 1–15. URL: https://www.nature.com/articles/s41534-017-0048-9 (visited on 02/16/2022).

[31] Tatsuhiro Onodera et al. “Nonlinear quantum behavior of ultrashort-pulse optical parametric oscillators”. In: *Phys. Rev. A* 105 (3 Mar. 2022), p. 033508. URL: https://link.aps.org/doi/10.1103/PhysRevA.105.033508.

[32] Ryotatsu Yanagimoto et al. “Mesoscopic ultrafast nonlinear optics – The emergence of multimode quantum non-Gaussian physics”. In: (2023).

[33] Ryotatsu Yanagimoto et al. “Temporal trapping: a route to strong coupling and deterministic optical quantum computation”. In: *Optica* 9.11 (Nov. 2022), pp. 1289–1296. URL: https://opg.optica.org/optica/abstract.cfm?URI=optica-9-11-1289.

[34] Ryotatsu Yanagimoto et al. “Onset of non-Gaussian quantum physics in pulsed squeezing with mesoscopic fields”. In: *Optica* 9.4 (Apr. 2022), pp. 379–390. URL: https://opg.optica.org/optica/abstract.cfm?URI=optica-9-4-379.

[35] Luis Ledezma et al. “Intense optical parametric amplification in dispersion-engineered nanophotonic lithium niobate waveguides”. In: *Optica* 9.3 (Mar. 2022), pp. 303–308. URL: https://opg.optica.org/optica/abstract.cfm?URI=optica-9-3-303.

[36] G. Imeshev et al. “Pulse shaping by difference-frequency mixing with quasi-phase-matching gratings”. In: *J. Opt. Soc. Am. B* 18.4 (Apr. 2001), pp. 534–539. URL: https://opg.optica.org/josab/abstract.cfm?URI=josab-18-4-534.